THE KINEMATICS OF MASSIVE STARS AND CIRCUMSTELLAR MATERIAL IN THE CARINA NEBULA

by

Megan Michelle Kiminki

A Dissertation Submitted to the Faculty of the

DEPARTMENT OF ASTRONOMY

In Partial Fulfillment of the Requirements
For the Degree of

DOCTOR OF PHILOSOPHY
WITH A MAJOR IN ASTRONOMY AND ASTROPHYSICS

In the Graduate College

THE UNIVERSITY OF ARIZONA

2017

THE UNIVERSITY OF ARIZONA
GRADUATE COLLEGE

As members of the Dissertation Committee, we certify that we have read the dissertation prepared by Megan Michelle Kiminki, titled The Kinematics of Massive Stars and Circumstellar Material in the Carina Nebula and recommend that it be accepted as fulfilling the dissertation requirement for the Degree of Doctor of Philosophy.

Nathan Smith — Date: 27 June 2017

Daniel Marrone — Date: 27 June 2017

Kaitlin Kratter — Date: 27 June 2017

Catharine Garmany — Date: 27 June 2017

Marcia Rieke — Date: 27 June 2017

Final approval and acceptance of this dissertation is contingent upon the candidate's submission of the final copies of the dissertation to the Graduate College.

I hereby certify that I have read this dissertation prepared under my direction and recommend that it be accepted as fulfilling the dissertation requirement.

Dissertation Director: Nathan Smith — Date: 27 June 2017

STATEMENT BY AUTHOR

This dissertation has been submitted in partial fulfillment of the requirements for an advanced degree at the University of Arizona and is deposited in the University Library to be made available to borrowers under rules of the Library.

Brief quotations from this dissertation are allowable without special permission, provided that an accurate acknowledgement of the source is made. Requests for permission for extended quotation from or reproduction of this manuscript in whole or in part may be granted by the head of the major department or the Dean of the Graduate College when in his or her judgment the proposed use of the material is in the interests of scholarship. In all other instances, however, permission must be obtained from the author.

SIGNED: Megan Michelle Kiminki

ACKNOWLEDGEMENTS

This dissertation would not exist without the invaluable guidance and encouragement of my advisor, Nathan Smith. Thank you for taking on a nervous third-year with an interest in massive stars.

I would also like to thank the members of my committee: Dan Marrone, for a listening ear when I needed it; Katy Garmany, for jumping in with extraordinary enthusiasm; Kaitlin Kratter, for the single most useful tip on writing an introduction; Marcia Rieke, for helping out at the last minute; George Rieke, for the advising that got me through my prelim; and Josh Eisner, who also couldn't be there at the end but offered support along the way.

We would all have been lost without the tireless work of Michelle Cournoyer, program coordinator extraordinaire.

Many thanks are owed to my collaborators and most especially to Megan Reiter, who—among many other things—reminded me that talking science can be fun. I will be forever grateful to Jay Anderson for sharing his code and teaching me the secrets of aligning *HST* images. I am also indebted to the Yale SMARTS team, particularly Emily MacPherson, for scheduling my CHIRON observations, and the telescope operators at CTIO who carried out those observations.

Thank you to my fellow Steward grad students for your friendship and support. Michelle Wilson, office- and trailer-mate—we made it! Vanessa Bailey and Amanda Ford were there when the going got rough. Kate Follette has been an amazing role model and landlord. Johanna Teske's enthusiasm about all my endeavors, both inside and outside of academia, helped so much. And Nick Ballering introduced me to BibTeX, which no dissertation-writer should ever have to do without.

Thank you to my dad, for reading all my papers, and to my mom, for always being proud of me. Most of all, thank you to Dan, the most wonderful partner anyone could ever ask for.

Support for the research in this dissertation was provided by NASA grants GO-13390 and GO-13791 from the Space Telescope Science Institute, which is operated by the Association of Universities for Research in Astronomy (AURA) under NASA contract NAS 5-26555. This work is based on observations made with the NASA/ESA *Hubble Space Telescope* and obtained from the Data Archive at the Space Telescope Science Institute, and on observations made at Cerro Tololo Inter-American Observatory, National Optical Astronomy Observatory (NOAO Proposal IDs 2014B-0235 and 2015B-0141), which is operated by AURA under a cooperative agreement with the National Science Foundation.

DEDICATION

For Dan, my strength.
For Ian, my joy.
For the one on the way.

TABLE OF CONTENTS

TABLE OF CONTENTS – *Continued*

LIST OF FIGURES

LIST OF TABLES

ABSTRACT

This dissertation presents the results of three related projects, each focusing on an aspect of the massive stars in the Carina Nebula and how they impact their surroundings. First, I use the proper motions of dense gas ejected by η Carinae to show that this luminous blue variable (LBV) has experienced major eruptions not just once but three times in the past millennium. The three eruptions show distinctly different symmetries: the thirteenth-century event was essentially one-sided, while the sixteenth-century event and the nineteenth-century Great Eruption were bipolar but not aligned with each other. These observations provide new constraints to theoretical models of η Car and LBVs. In the second project, I constrain the proper motions of five other massive stars in the Carina Nebula. Each of these five has a stellar wind bow shock, but I find that none are runaway stars. In two cases, the bow shocks, which face a cluster that is driving large-scale flows of ionized gas, point at right angles to the motion of their stars. In the other three cases, both feedback-driven gas flows and stellar motion may be factors in setting bow shock orientation. The third section of this dissertation is a survey of the radial velocities of the Carina Nebula's full O-star population, combining new spectroscopy with a thorough review of values from the literature. The radial velocity distribution supports a common distance to the region's various clusters and subclusters. Comparison to molecular gas velocities shows that feedback from the Trumpler 16 cluster (home to η Car), has accelerated a dense cloud toward us and possibly triggered additional massive-star formation. Comparison to ionized gas velocities shows that the feedback-driven expansion of the H II region is not spherical and is likely constrained by an unseen dense cloud on the far side.

CHAPTER 1

INTRODUCTION

Massive stars are big, bright, and critical to the Universe. Although their lives are short in astronomical terms, massive stars pump enormous amounts of energy and momentum into their surroundings, shining 10^4–10^6 times brighter than our Sun. At death, they explode, distributing heavy elements into the interstellar medium (ISM) and briefly rivaling the luminosity output of entire galaxies. Yet despite the importance of massive stars, many aspects of their environments and their evolution remain poorly understood.

A "massive" star is one that will, in the eventual course of its evolution, ignite non-degenerate carbon burning in its core, kicking off a several-hundred-year sequence that leads to a core-collapse supernova. Such an end requires a minimum initial mass of 8–10 $M_\odot$ (e.g., Smartt, 2009; Ibeling and Heger, 2013; Woosley and Heger, 2015). While on the main sequence, these are OB stars, a term that covers the full range of O spectral types and the earliest (hottest) B spectral types (B0–B3). Once off the main sequence, massive stars can take on many different spectral types: red and blue supergiants, yellow hypergiants, luminous blue variables, and classical Wolf-Rayet stars. The overwhelming majority of massive stars belong to binary or higher-order multiple systems (Garmany et al., 1980; Mason et al., 2009; Chini et al., 2012; Sana et al., 2012, 2013, 2014; Kobulnicky et al., 2014; Moe and Di Stefano, 2017), and many will interact or even merge with their companions over the course of their lives (Sana et al., 2012; de Mink et al., 2014). These systems are not spread randomly across a galaxy, but instead group together in clusters and associations.

This dissertation concentrates on the massive stars of the Carina Nebula, a large star-forming region in the southern-hemisphere sky. This chapter presents the scientific context for my research, exploring what is known (and unknown) about the lives

and influence of massive stars. Section 1.1 describes the processes by which massive stars impart feedback to their environment and introduces the concept of triggered star formation. Section 1.2 provides a tour of the Carina Nebula and an overview of η Carinae, its most famous member. Section 1.3 discusses OB associations: what they are and how they might form. Section 1.4 closes out the chapter with an outline of the three research projects that make up the body of this dissertation.

1.1 Feedback from Massive Stars

The energy and momentum transferred from astronomical objects to their environment is known as feedback. Not all feedback is stellar in origin—the supermassive black holes of active galactic nuclei can provide their fair share in certain contexts (e.g., Fabian, 2012)—but stellar feedback acts in every galaxy on every scale. Feedback contributes to the dispersal of protoplanetary disks (Johnstone et al., 1998; Störzer and Hollenbach, 1999; Adams et al., 2004; Balog et al., 2007, 2008); shapes molecular gas into pillars and globules (Frieman, 1954; Reipurth, 1983; Lefloch and Lazareff, 1994; Williams et al., 2001; Mizuta et al., 2006; Mackey and Lim, 2010; Gritschneder et al., 2010; Tremblin et al., 2012); regulates the efficiency of star formation (e.g., Whitworth, 1979; Mac Low and Klessen, 2004; Fall et al., 2010; Hopkins et al., 2011; Agertz and Kravtsov, 2015); blows superbubbles in galactic disks (Mac Low and McCray, 1988; Heiles, 1990; Krause and Diehl, 2014); and powers multi-kpc galactic outflows (Chevalier and Clegg, 1985; Murray et al., 2005; Veilleux et al., 2005; Nath and Silk, 2009; Murray et al., 2011; Creasey et al., 2013). On an even larger scale, feedback from massive stars was a dominant contributor to the reionization of the Universe (e.g., Fan et al., 2006; Hassan et al., 2017).

1.1.1 Feedback mechanisms

Ionizing radiation, stellar winds, and supernovae: the typical introductory statement on the importance of massive stars lists these three feedback processes, each of

which makes several different contributions to the overall feedback budget. Below, I provide an overview of the physics of each of these mechanisms and their effects on the ISM. I also address a fourth feedback channel, protostellar outflows, that arises during the formation of stars of all masses.

Ionizing radiation:

A photon with energy $E \geq 13.6$ eV (equivalent to wavelength $\lambda \leq 912$ Å) is capable of unbinding the electron of a hydrogen atom. The rate at which stars emit ionizing photons is a strong function of their effective temperature. For instance, an O3 star with $T_{\rm eff} \approx 45,000$ K produces approximately 16 times as much ionizing flux as an O8 star with $T_{\rm eff} \approx 35,000$ K (Martins et al., 2005). The ionizing contribution from stars with spectral types later than about B2 ($T_{\rm eff} \approx 20,000$ K; Drilling and Landolt, 2000) is generally considered negligible. Perhaps conveniently for astronomers, the boundary in initial mass between stars that do and do not emit much ionizing radiation is essentially equivalent to the boundary between stars that do and do not end their lives as core-collapse supernovae.

Thanks to their ionizing radiation, massive stars are surrounded by bubbles of ionized gas known as H II regions. The size of an H II region is determined by the balance between ionization and recombination (Strömgren, 1939), but the situation is not static. The ionized gas has a temperature of $\sim 10^4$ K, much warmer than the cool ($\lesssim 100$ K), neutral gas around it. The gas inside an H II region therefore has a much higher thermal pressure than its surroundings and will expand until pressure balance is reestablished. It pushes out on the denser material around it, thereby doing work on the ISM. H II region expansion occurs at about the speed of sound within it, ~ 10 km s^{-1}.

In ionized gas, the recombination rate per unit volume is a function of the square of the particle density, so as an H II region expands due to its thermal pressure, the total number of recombinations decreases and more ionizing photons reach its boundaries. Consequently, the ionization front eats it way further into the surrounding neutral material. In what is known as the "rocket effect," (Oort and Spitzer,

1955; Bally and Scoville, 1980; Bertoldi and McKee, 1990), the newly photoionized and heated gas expands back into the lower density of the H II region's interior, transferring an equal and opposite amount of momentum to its natal neutral cloud. The neutral dense gas can thereby be accelerated to velocities of 10–20 km s^{-1} or even more, depending on the amount of mass it has lost. In models, the rocket effect is not often distinguished from the general thermal expansion of H II regions; where they are treated separately, the rocket effect may be the more important factor in the transfer of momentum (Dale, 2017).

Photons of all wavelengths can also transfer momentum directly to the ISM when they are scattered or absorbed by particles in their path. Under the right conditions, this direct radiation pressure could drive the expansion of an H II region at velocities greater than the sound speed of ionized gas (Dale et al., 2012, 2013a). It may be a significant component of feedback in massive starburst regions (Krumholz and Matzner, 2009), particularly during the early stages of their development (Silich and Tenorio-Tagle, 2013), and in the extreme star-forming environments of ultraluminous infrared galaxies (ULIRGs; Murray et al., 2010). However, in typical local H II regions, direct radiation pressure seems to be unimportant compared to the thermal pressure of ionized gas (Lopez et al., 2014), although its significance depends on how "direct radiation pressure" is defined and measured. Lopez et al. (2011) adopted a straightforward definition of pressure as energy density, and concluded that direct radiation pressure is the dominant form of feedback in the interior of the giant H II region 30 Doradus. Pellegrini et al. (2011, see also Povich 2012) disagreed, arguing that radiation pressure can only be relevant where it can act on dense gas (i.e., at the edges of H II regions rather than in their optically thin interiors).

Further radiation pressure comes from dust heated by stellar radiation: dust particles re-radiate their energy in the infrared, where it can be absorbed or scattered by additional dust. If the cloud around an H II region has a sufficiently high dust opacity, the "trapped" infrared light may make a noticeable contribution to the total radiation pressure in the region (Hopkins et al., 2011; Krumholz and Thompson,

2012). But as with direct radiation pressure, the relative importance of this effect is debated. Krumholz and Matzner (2009) argue that infrared radiation will never be completely trapped, and the simulations of Skinner and Ostriker (2015) find that its effect on H II region pressures is only significant when the dust abundance is highly enhanced or the metallicity is greater than solar. Lopez et al. (2011, 2014) observed that infrared radiation pressure in H II regions is never greater than the thermal pressure of photoionized gas, at least at the sub-solar metallicities of the Magellanic Clouds.

Stellar population synthesis (SPS) models combine stellar evolutionary tracks, star formation histories, and initial mass functions to compute the total expected ionizing flux (and stellar wind energy and supernova rate) of a particular stellar population at a particular metallicity. These values are then used as input to galaxy-scale simulations (e.g., Hopkins et al., 2014). Most SPS models, like the popular `Starburst99` code (Leitherer et al., 1999, 2014), consider only single stars and avoid the "free-parameter heaven" (Gallagher, 1989) of binary interactions. But some models, notably `BPASS` (Eldridge et al., 2008, 2011; Eldridge and Stanway, 2009, 2012), have begun to explore the effects of binary evolution on the predicted outputs. Mergers and mass accretion produce stars that are hotter and brighter than expected for their age (Eldridge and Stanway, 2009; Stanway et al., 2016, see also van Bever and Vanbeveren 1998; Schneider et al. 2014), while mass loss through Roche-lobe overflow results in fewer red supergiants and more Wolf-Rayet stars (e.g., Eldridge et al., 2008). SPS models that include binaries thus produce higher ionizing fluxes for longer times and are better able to reproduce the observed spectral line ratios of high-redshift galaxies (Eldridge and Stanway, 2012; Stanway et al., 2014).

Stellar winds:

In the atmospheres of hot stars, the absorption and scattering of ultraviolet photons by metal ions transfers momentum from radiation to matter, driving a stellar wind (Lucy and Solomon, 1970; Castor et al., 1975). In main-sequence O-type stars, wind-driven mass-loss rates amount to 10^{-9}–10^{-6} $M_\odot$ yr^{-1} (de Jager et al.,

1988; Vink et al., 2001; Smith, 2014). It was recently recognized that the standard observational diagnostics of O-star winds were overestimating mass-loss rates by up to an order of magnitude because they failed to account for inhomogeneities ("clumps") in the wind (Bouret et al., 2005; Fullerton et al., 2006; Puls et al., 2006). As a consequence, there is currently a great deal of uncertainty about the importance of main-sequence winds in massive-star evolution and feedback (see Puls et al., 2008; Smith, 2014). Most stellar evolutionary codes, including the Geneva models (Ekström et al., 2012; Georgy et al., 2013) and the `PARSEC` tracks (Bressan et al., 2012; Tang et al., 2014; Chen et al., 2015), have not yet revised their applied mass-loss rates to reflect the new data.

Regardless of their exact mass-loss rates, the winds of main-sequence O-type stars are fast, reaching velocities of 1000–3000 km s^{-1} (Kudritzki and Puls, 2000, and references therein). At the interface between the stellar wind and surrounding ISM, layers of gas in both wind and ISM are shock-heated to temperatures of 10^6–10^7 K. The hot gas subsequently expands due to its high thermal pressure, but it may not be a substantial factor in the dynamics of massive star-forming regions (e.g., Dale et al., 2013b, 2014; Geen et al., 2015). Diffuse X-ray emission from wind-shocked hot gas has been detected in many such regions (Townsley et al., 2006, 2011a; Güdel et al., 2008; Lopez et al., 2014), but the observed X-ray luminosities and associated thermal pressures are much lower than what would be expected from simple models of wind-blown bubbles (Harper-Clark and Murray, 2009; Lopez et al., 2011, 2014, although see Pellegrini et al. 2011). The hot gas may be escaping through inhomogeneities in the surrounding dense gas (Harper-Clark and Murray, 2009) and/or losing heat through turbulent mixing with cooler material (Rosen et al., 2014).

As massive stars evolve off the main sequence, their winds and mass-loss rates evolve, too. The defining features of Wolf-Rayet spectra are their broad, strong emission lines originating in strong stellar winds. As in main-sequence OB stars, these winds are line-driven and reach terminal velocities of 1000s km s^{-1}, but their mass-loss rates are orders of magnitude higher at 10^{-5}–10^{-4} $M_\odot$ yr^{-1} (Vink and de Koter,

2005; Crowther, 2007; Puls et al., 2008). Increased shock-heating when Wolf-Rayet winds "turn on" is clearly discernible in models of cluster feedback evolution (Rogers and Pittard, 2014). Red supergiants, on the other hand, drive an entirely different sort of stellar wind: dust forms in their cool, extended atmospheres and is accelerated outward by radiation pressure (Gehrz and Woolf, 1971). Although their mass-loss rates are comparable to those of Wolf-Rayet stars (de Jager et al., 1988; van Loon et al., 2005; Mauron and Josselin, 2011), the winds of red supergiants have much slower velocities (10–20 km s^{-1}) and do not shock-heat the surrounding ISM to the same kinds of high temperatures.

Supernovae:

Of the $\sim 10^{53}$ erg of energy released in a single core-collapse supernova, 99% is in the form of neutrino emission (Colgate and White, 1966) that passes through the ISM with essentially no effect. Most of the remaining $\sim 10^{51}$ erg is the kinetic energy of the supernova ejecta, while $\sim 10^{49}$ erg is emitted as radiation (e.g., Chevalier, 1977). Exploding outward at 10^4 km s^{-1}, the ejecta rapidly sweep up the surrounding ISM and shock-heat gas to temperatures on the order of 10^7 K. Dynamically, supernova-shocked hot gas behaves like wind-shocked hot gas, and it expands due to its high thermal pressure. In star-forming regions that are old enough to have experienced supernovae, the relative contributions of winds and supernovae to the X-ray-emitting hot gas can be difficult to separate (e.g., Townsley et al., 2011a,b).

Even the most massive stars, burning through their nuclear fuel hottest and fastest, live for at least 3 Myr or so. Consequently, supernovae cannot be a major source of feedback during the early development of stellar clusters (see discussions in Krumholz and Matzner, 2009; Fall et al., 2010), although they may act to trigger star formation in neighboring molecular clouds (see Section 1.1.2). On galactic scales, however, the effect of supernova feedback is enhanced by the time delay. Supernovae generally explode into diffuse, warm H II bubbles created by stellar radiation, where the supernova shock loses less energy to radiative cooling than it would in a dense medium (Thornton et al., 1998; Cho and Kang, 2008). The hot gas

tends not to remain confined in the H II cavity; rather, it escapes into the galactic halo through low-density holes carved by prior feedback (e.g., Hopkins et al., 2012; Rogers and Pittard, 2013). Galactic simulations have begun to account for this coupling between the various forms of feedback, finding that the observed properties of galactic outflows and hot halo gas are only reproduced when supernovae go off in diffuse environments (e.g., Wise et al., 2012; Creasey et al., 2013; Gatto et al., 2015; Girichidis et al., 2016).

Protostellar outflows:

Protostars of all masses launch bipolar outflows during the accretion phase of star formation (Lada, 1985; Welch et al., 1985; Parker et al., 1991; Bontemps et al., 1996; Bally, 2016). Unsurprisingly, massive protostars have the highest mass-loss rates and kinetic energies (Shepherd and Churchwell, 1996). Outflows drive turbulence in the ISM (Li and Nakamura, 2006; Matzner, 2007) and are the dominant feedback mechanism in low-mass star-forming regions (e.g., Matzner and McKee, 2000). However, even massive protostellar outflows inject relatively little energy and momentum compared to the radiation and winds of main-sequence massive stars, and so protostellar outflows are generally neglected in studies of feedback in massive clusters (e.g., Lopez et al., 2011, 2014).

Nevertheless, protostellar outflows may still play an important, albeit indirect, role in the feedback from massive star-forming regions: they may be a key factor in setting stellar masses. In many simulations, outflows act to disperse protostellar envelopes, reducing accretion rates onto young stars and lowering their final masses (Adams and Fatuzzo, 1996; Matzner and McKee, 2000; Myers, 2008; Li et al., 2010; Wang et al., 2010; Federrath et al., 2014). Alternatively, if accretion onto massive protostars is limited by radiation pressure, outflows might increase accretion rates and promote massive-star formation by opening low-density channels through which radiation can escape (Krumholz et al., 2005a; Cunningham et al., 2011).

1.1.2 Triggered star formation

To first order, massive stars have a negative effect on the star formation rate around them. As described above, their feedback destroys and/or disperses the dense molecular gas from which stars form. In certain circumstances, however, massive-star feedback can induce gravitational collapse in dense gas and thereby trigger star formation. There are two primary mechanisms by which triggering might occur, both involving the shock front that precedes the expanding ionization front of an H II region. Similar processes can occur at the shock front of a supernova.

The first type of triggered star formation is the collect-and-collapse model (Elmegreen and Lada, 1977; Whitworth et al., 1994; Hosokawa and Inutsuka, 2005; Dale et al., 2007a). As the shock and ionization fronts propagate into a molecular cloud, a shell of dense, cool gas accumulates between them. Eventually, the density of the shell becomes sufficiently high for it to fragment into self-gravitating cores, beginning the process of star formation. Early models of this process (Elmegreen and Lada, 1977; Whitworth et al., 1994) indicated that collect-and-collapse triggering favored the formation of massive stars. But more recent hydrodynamic simulations of triggered star formation (Dale et al., 2007b; Dale and Bonnell, 2012) do not find an overproduction of massive stars compared to spontaneous (non-triggered) star formation.

The second type of triggered star formation is known as radiation-driven implosion (RDI; Sandford et al., 1982; Bertoldi, 1989; Kessel-Deynet and Burkert, 2003; Bisbas et al., 2011). In this model, existing dense clumps within a molecular cloud are compressed by the passage of the shock front and become unstable to gravitational collapse. Because the gas does not have to be first swept up into a shell, RDI can occur more quickly than collect-and-collapse triggering ($<$ 1 Myr versus 1–3 Myr) and on smaller spatial scales ($<$ 1 pc versus 5–20 pc).

A multitude of observational studies have found signs that collect-and-collapse and/or RDI triggering have occurred around massive star-forming regions (e.g., Lada et al., 1978; Sugitani et al., 1991; Sugitani and Ogura, 1994;

Sugitani et al., 2002; Deharveng et al., 2003; Karr and Martin, 2003; Oey et al., 2005; Zavagno et al., 2007; Deharveng et al., 2009; Ohlendorf et al., 2013; Walch et al., 2015, and see compilation in Dale et al. 2015). The usual cited evidence is a concentration of young stars in pillars or cometary clouds or otherwise along the edges of H II regions. Based on the association of massive young stellar objects with H II bubbles, Kendrew et al. (2012) and Thompson et al. (2012) estimate that 20–30% of the Milky Way's massive stars formed via triggered star formation. In addition, our own Solar System may be the product of triggering. The daughter species of ^{26}Al, ^{60}Fe, and other short-lived radioactive isotopes have been detected in meteorites (e.g., Lee et al., 1976a,b; Tachibana and Huss, 2003), indicating that a supernova occurred relatively close in time and space to the birth of the Sun (Hester and Desch, 2005; Tachibana et al., 2006). The Sun's formation may have been triggered by the supernova itself (Cameron and Truran, 1977; Krebs and Hillebrandt, 1983; Cameron et al., 1995; Vanhala and Boss, 2002; Gritschneder et al., 2012), by the supernova progenitor star (Hester and Desch, 2005), or by a series of several stellar generations (Gounelle and Meynet, 2012).

Yet despite its probable importance as a mechanism of star formation, definitive evidence for triggering remains elusive (see Dale et al., 2015). Our Sun could have formed spontaneously and had its protostellar disk "polluted" by a coincidental nearby supernova (Chevalier, 2000; Ouellette et al., 2007; Parker and Dale, 2016). The young stars observed at the edges of H II regions could have formed spontaneously and simply been revealed when their natal dense gas was dispersed by feedback. In the simulations of Dale et al. (2012, 2013a), observed proximity to an ionization front or pillar increases the chances that any given star was triggered, but does not guarantee it. Dale et al. (2013a) also found that age gradients (i.e., when the youngest stars are farthest from the initial feedback source) occur in both triggered and spontaneous stellar populations. Since triggered stars are expected to inherit the outward velocities of their feedback-accelerated natal gas, it has been proposed that stellar kinematics might offer a way to distinguish between triggered and spontaneous populations (e.g., Elmegreen, 2011, but see Dale et al. 2012, 2015).

1.2 The Carina Nebula

The effects of stellar feedback are on striking display in the Carina Nebula,[1] also known as NGC 3372 or the Great Nebula in Carina. This region is home to upwards of 200 massive stars, including more than 70 O-type stars (Gagné et al., 2011; Alexander et al., 2016) and the luminous blue variable η Carinae (η Car; see Section 1.2.2). Together, those massive stars pump out nearly 10^{51} ionizing photons per second along with 10^5 $L_\odot$ in wind energy (Smith, 2006a), powering a giant H II region that is expanding at $\pm$15–20 km s^{-1} about the observed mean gas velocity (Gardner et al., 1970; Deharveng and Maucherat, 1975; Huchtmeier and Day, 1975; Walborn and Hesser, 1975; Azcarate et al., 1981; Walsh, 1984; Brooks et al., 2001; Smith et al., 2004; Damiani et al., 2016). The Carina Nebula complex, which extends more than 30 pc in diameter (e.g., Smith et al., 2000), also contains about 3×10^5 $M_\odot$ of molecular gas (Yonekura et al., 2005; Rebolledo et al., 2016). A further $\sim 10^6$ $M_\odot$ of neutral atomic gas is present in photodissociation regions warmed by non-ionizing radiation (Smith and Brooks, 2007; Preibisch et al., 2012). New stars are born in the Carina Nebula at an estimated rate of 0.01–0.02 $M_\odot$ yr^{-1} (Smith et al., 2010c; Povich et al., 2011a; Gaczkowski et al., 2013), making up $\sim 1\%$ of the ongoing star formation in the Milky Way (Murray and Rahman, 2010; Robitaille and Whitney, 2010; Chomiuk and Povich, 2011; Licquia and Newman, 2015).

The large size of the Carina Nebula is especially apparent when compared to the nearest massive star-forming region, the Orion Nebula Cluster (ONC). The ONC contains just 20 massive stars (Muench et al., 2008), with a total ionizing luminosity two orders of magnitude below that of the Carina Nebula (Smith, 2006a). While the Carina Nebula is not quite as extreme as starburst clusters like NGC 3603 (Moffat et al., 2002), the Arches Cluster (Figer et al., 2002), and 30 Doradus (Doran et al., 2013; Walborn et al., 2014), it offers our closest and least obscured

[1] Not to be confused with the Carina Dwarf, a faint dwarf spheroidal galaxy in orbit around the Milky Way (Cannon et al., 1977).

opportunity to study a starburst-like feedback-rich environment.

Below, I provide a tour of the clusters, pillars, and other scientifically interesting features in the Carina Nebula. For a map, the reader is referred to Figures 3.1 and 4.1 in this dissertation and to the review by Smith and Brooks (2008).

1.2.1 Structure and stellar content

Trumpler 16:

The densest stellar populations in the Carina Nebula are found in Trumpler (Tr) 14 and Tr 16, the pair of clusters at the center of the complex. Tr 16, the home of η Car, is slightly more massive than its neighbor. Its stellar population is clumped into more than a half-dozen subclusters, with no single group dominating in terms of size and location (Wolk et al., 2011). Tr 16 is believed to be ~ 3 Myr old, based primarily on the fact that the extremely massive η Car (see Section 1.2.2) has evolved off the main sequence but has not yet exploded (e.g., Massey and Johnson, 1993; Smith, 2006a). There has been some suggestion from analyses of color-magnitude diagrams that Tr 16's lower-mass stellar population first started forming 6–10 Myr ago (DeGioia-Eastwood et al., 2001; Tapia et al., 2003).

The distance to η Car, 2.3 kpc, is known quite precisely from fits to the three-dimensional expansion of its circumstellar Homunculus Nebula (Allen and Hillier, 1993; Davidson et al., 2001; Smith, 2006b). It is also quite clear that η Car is inside Tr 16—rather than in the foreground or background—because η Car's light is reflected by other gas in the cluster (Walborn and Liller, 1977) and because η Car blocks only the receding component of the nebular emission from Tr 16's H II region (Allen, 1979). Prior to the η Car measurements, Tr 16's distance was derived from main-sequence fitting, usually coming out in the 2.2–3.2 kpc range (Feinstein et al., 1973; Walborn, 1973; The et al., 1980a,b; Tapia et al., 1988; Massey and Johnson, 1993; Tapia et al., 2003) but occasionally reported to be as high as 4.0 kpc (Carraro et al., 2004). More recent references, including this dissertation, adopt the 2.3 kpc from η Car, but the matter is still not entirely settled. Hur et al. (2012) argue for a photometric distance of 2.9 kpc.

The spread in distances found for Tr 16 (and the other components of the Carina Nebula, as described below) may be partially the result of the effect of stellar feedback on dust grains. Accurate photometric distances depend on a correct accounting of how much light at various wavelengths has been absorbed and scattered by intervening dust. The ratio of total-to-selective extinction, $R_V = A_V/E(B-V)$, is observed to be 4–5 in the Carina Nebula (Herbst, 1976; Forte, 1978; The et al., 1980a,b; Smith, 1987; Tovmassian et al., 1994; Carraro et al., 2004; Povich et al., 2011b; Mohr-Smith et al., 2017), compared to the normal interstellar value of ~ 3.1 (e.g., Rieke and Lebofsky, 1985). High values of R_V are attributed to larger-than-average grain sizes (Cardelli et al., 1989; Draine, 2003), which are often generically explained as coming from grain growth in dense environments. In massive star-forming regions, it seems more likely that small grains have been preferentially destroyed and/or blown out by shocks and high-energy radiation (McCall, 1981; Smith, 1987; Cardelli and Clayton, 1988).

Trumpler 14:

The Carina Nebula's second major cluster, Tr 14, lies about 15′ (10 pc at 2.3 kpc) to the northwest of Tr 16. It has a more compact, spherical structure than its neighbor, with a well-defined central core (Ascenso et al., 2007; Feigelson et al., 2011). Its most massive member is HD 93129Aa, the primary star in a close binary system (Nelan et al., 2004, 2010) whose spectrum defined first the O3 supergiant (Walborn, 1971) and then the O2 supergiant spectral types (Walborn et al., 2002b). HD 93129Aa alone contributes about 10% of the total ionizing flux of the Carina Nebula (Smith, 2006a). Tr 14's stellar population also includes three main-sequence O3.5 stars (Walborn et al., 2002b; Nelan et al., 2004; Smith, 2006a), each weighing in at around 50 $M_\odot$. It is widely agreed that Tr 14 is between 0.5 and 2 Myr old and hence slightly younger than Tr 16, based on isochrone fitting (Morrell et al., 1988; Penny et al., 1993; Vazquez et al., 1996; Carraro et al., 2004; Rochau et al., 2011) and the fact that Tr 14 is more closely associated with molecular gas (de Graauw et al., 1981; Brooks et al., 2003; Tapia et al., 2003). Parts of its

lower-mass population may be up to 5 Myr old (Tapia et al., 2003; Ascenso et al., 2007).

Most photometric studies of the region have concluded that Tr 14 is at the same distance as Tr 16, regardless of exactly what distance they calculated that to be (Feinstein et al., 1973; Walborn, 1982a,b; Turner and Moffat, 1980; The et al., 1980a,b; Tapia et al., 1988; Cudworth et al., 1993; Massey and Johnson, 1993; Tovmassian et al., 1994; Tapia et al., 2003; Walborn, 1995; Hur et al., 2012). From observations of ^{12}CO, de Graauw et al. (1981) concurred, sketching a model of a single elongated H II region enclosed by a partial shell of molecular gas. Although occasional analyses have argued otherwise—Walborn (1973) and Morrell et al. (1988) argued that Tr 14 is a kpc or so further away than Tr 16, while Carraro et al. (2004, who found an unusually high distance for Tr 16) saw Tr 14 as the closer cluster—it seems most likely that the two clusters are closely related. Smith et al. (2003a) and Smith (2006a) propose that Tr 14 is more distant than its neighbor, but only by 10–20 pc, since proplyds and dense pillars seen in silhouette near Tr 14 point toward Tr 16 and η Car (see also Smith et al., 2010a).

Bochum 11, Collinder 228, and the South Pillars:

Early far-infrared observations did not find any evidence of ongoing star formation around Tr 14 and Tr 16 (Harvey et al., 1979; Ghosh et al., 1988), and so for decades it was assumed that the Carina Nebula's current star formation rate was negligible. That view changed dramatically when wide-field mid-infrared imaging revealed the South Pillars, a complex of dusty pillars extending 20–30 pc south of Tr 16 (Smith et al., 2000; Rathborne et al., 2004). The heads and bright edges of the pillars face Tr 16, indicating that they were sculpted by feedback from that cluster's massive stars. The South Pillars are replete with star formation, with $>$ 1000 protostars and pre-main-sequence stars detected in *Spitzer* and *Herschel* surveys (Smith et al., 2010c; Povich et al., 2011b; Gaczkowski et al., 2013). Particularly striking is the "Treasure Chest," a very young ($<$ 0.1 Myr) cluster emerging from the head of one of the large pillars (Hägele et al., 2004; Rathborne et al., 2004;

Smith et al., 2005b). Dozens of protostellar jets, some bent by direct massive-star feedback or by photoevaporative flows off the molecular pillars, have also been detected across the region (Smith, 2004; Smith et al., 2010a; Ohlendorf et al., 2012; Reiter and Smith, 2013, 2014; Hartigan et al., 2015).

In addition to the extensive pre-main-sequence population, the South Pillars contain about half of the Carina Nebula's massive stars. There are two named open clusters, Bochum 11 (Bo 11) and Collinder 228 (Cr 228). Bo 11, approximately 30′ (20 pc at 2.3 kpc) southeast of Tr 16, has been poorly studied aside from its five O-type stars. Isochrone analysis gives it an age of 3–5 Myr (Fitzgerald and Mehta, 1987; Patat and Carraro, 2001; Preibisch et al., 2011a), but it has also been reported as much younger ($\leq$ 1 Myr; Smith and Brooks, 2008).

Cr 228 is formally centered 24′ (16 pc at 2.3 kpc) southwest of Tr 16 (Wu et al., 2009), but the name is often applied to the general distributed massive-star population in the South Pillars. Although a few analyses put it somewhat in the foreground (Feinstein et al., 1976; Forte, 1978; Carraro and Patat, 2001), most studies concluded that it shares a common distance with Tr 14 and/or Tr 16 (Herbst, 1976; Turner and Moffat, 1980; Tapia et al., 1988; Tovmassian et al., 1994; Massey et al., 2001). Sometimes it was even treated as a continuous extension of Tr 16, with their apparent separation merely an artifact of the dark dust lane that cuts across the Carina Nebula (Walborn, 1973, 1995; Smith, 2006a; Smith and Brooks, 2008). Analysis of its X-ray-detected stellar population indicates that it is distinct from Tr 16, and that it is a collection of loose subclusters rather than a single coherent group (Feigelson et al., 2011). Its age is poorly constrained, with estimates ranging from 2 Myr (Massey et al., 2001) to 8 Myr (Carraro and Patat, 2001).

The ongoing star formation in the South Pillars looks very much like it was triggered by feedback from Tr 14 and Tr 16 (Smith et al., 2010c; Gaczkowski et al., 2013), but whether that triggering has resulted in the formation of new massive stars is unclear. On the one hand, there is a late-type O star in the Treasure Chest, still mostly surrounded by its natal pillar (Smith et al., 2005b). On the other hand, Gaczkowski et al. (2013) detected no protostars with masses $\gtrsim$ 20 $M_\odot$ anywhere in

the South Pillars, leading them to conclude that the current round of star formation is primarily limited to low- and intermediate-mass objects. The massive stars in Bo 11 and Cr 228, with their relatively uncertain ages, provide no definitive evidence either way.

The WNH stars:

The massive-star population of the Carina Nebula also includes three late-type hydrogen- and nitrogen-rich Wolf-Rayet stars, known as WNH stars. Classical Wolf-Rayet stars, including typical nitrogen-rich WN stars, are post-main-sequence helium-burning objects that have lost most or all of their hydrogen envelopes (e.g., Crowther, 2007). In contrast, WNH stars are the late main-sequence forms of very massive stars (Crowther et al., 1995; Smith and Conti, 2008; Gräfener et al., 2011)—the Wolf-Rayet designation is just the result of their high mass-loss rates producing emission-line-dominated spectra. Together, the three WNH stars in the Carina Nebula contribute nearly one-quarter of the total ionizing flux of the region (Smith, 2006a).

One might expect these very bright, massive sources to be at the centers of large clusters, but, rather puzzlingly, they are not. WR 25 (HD 93162) is on the outskirts of Tr 16, and WR 24 (HD 93131) is in the main subgroup of Cr 228. Most peculiarly, WR 22 (HD 92740) is on the far western side of the region, about 30′ (20 pc at 2.3 kpc) from Tr 16 and well separated from other massive stars. Walborn (1995) suggested that WR 22 and WR 24 originated in Tr 16 and migrated out over their 2-Myr lifetimes, which would require them to have moderate tangential velocities of ~ 10 km s^{-1}.

Bochum 10, Collinder 232, and Trumpler 15:

There are a few other named components of the Carina Nebula that should be mentioned. Tr 15 is a modest-sized cluster about 12′ (8 pc at 2.3 kpc) to the north of Tr 14. It is a bit older than the central clusters, with an age of 5–10 Myr (Carraro, 2002; Wang et al., 2011) or more (Tapia et al., 2003). Its relation-

ship to the rest of the Carina Nebula was not always clear (Thé and Vleeming, 1971; Walborn, 1973; Morrell et al., 1988), although photometric analyses tended to suggest that it was at a similar distance (The et al., 1980a,b; Tapia et al., 1988; Carraro, 2002; Tapia et al., 2003). Feigelson et al. (2011) and Wang et al. (2011) confirmed its association to the rest of the region through the detection of a bridge of X-ray-bright young stars between Tr 14 and Tr 15.

Cr 232 is a small cluster centered on two O-type stars about halfway between Tr 14 and Tr 16 on the north side. Walborn (1995) argued that it was not a physical group, just an alignment of sources in the haloes of the larger clusters. However, it appears as a distinct concentration of X-ray-detected stars (Feigelson et al., 2011), confirming the hypothesis of Carraro et al. (2004) that it is a real, if sparse, stellar aggregate.

Finally, Bo 10 is a loose open cluster, around 7 Myr old (Feinstein, 1981; Fitzgerald and Mehta, 1987), located roughly 40′ (25 pc at 2.3 kpc) to the northwest of Tr 14. Bo 10 seems to be at about the same distance as the rest of the Carina Nebula (Fitzgerald and Mehta, 1987; Patat and Carraro, 2001), but is not interacting with it in any way. Because of its size, its separation from the main clusters, and its relatively older stellar population, Bo 10 is often excluded from studies of the Carina Nebula, and it is not discussed any further in this dissertation.

1.2.2 The luminous blue variable η Carinae

The most massive and most famous stellar system in the Carina Nebula is η Carinae, a remarkable binary star at the heart of Tr 16. The primary star has a current mass of $\geq$ 90 $M_\odot$ (Davidson and Humphreys, 1997; Hillier et al., 2001), and is orbited by a hot (Pittard and Corcoran, 2002; Mehner et al., 2010), $\sim$ 30-$M_\odot$ companion on a highly eccentric, 5.5-year orbit (Damineli, 1996; Damineli et al., 1997, 2000; Corcoran et al., 2001; Whitelock et al., 2004; Madura et al., 2012). The stars themselves are well-hidden inside the bipolar Homunculus Nebula (Thackeray, 1949; Gaviola, 1950; Morse et al., 1998; Steffen et al., 2014), which has the highest apparent brightness at 10 and 20 μm of any object outside our Solar System

(Westphal and Neugebauer, 1969). The dusty Homunculus has a mass of 10–15 $M_\odot$ (Smith et al., 2003c; Smith and Ferland, 2007), and another 2–4 $M_\odot$ (Weis, 2012) or more (Gomez et al., 2010) of clumpy ejecta are seen out to nearly half a parsec from the stars. The ejecta are rich in helium and nitrogen, elements churned up from the primary star's interior during its post-main-sequence evolution (Davidson et al., 1982, 1986; Dufour et al., 1997; Smith and Morse, 2004).

η Car belongs to a class of stars called luminous blue variables (LBVs). As the name indicates, LBVs are bright, hot (at least when quiescent), and prone to dramatic photometric variations. In "normal" LBVs, also known as S Doradus variables, mass-loss rates rise to 10^{-5}–10^{-4} $M_\odot$ yr^{-1} while the star cools and expands, causing it to brighten at visual wavelengths while maintaining a relatively constant bolometric luminosity (Humphreys and Davidson, 1994; van Genderen, 2001). Exactly what causes these episodes, which last for years or decades, is unknown. A star in radiative equilibrium cannot exceed its Eddington luminosity (Eddington, 1916), the point at which the outward push of radiation pressure is just balanced by the inward pull of gravity. Single-star models of LBVs invoke super-Eddington continuum-driven winds (Quinn and Paczynski, 1985; Owocki et al., 2004; Owocki and Shaviv, 2016), possibly initiated by dynamical or opacity-induced instabilities inside the star (Maeder, 1983; de Jager, 1984; Lamers and Fitzpatrick, 1988; Glatzel and Kiriakidis, 1993; Stothers and Chin, 1993; Glatzel, 1994).

What happened to η Car was much more extreme and even less well understood. Its Homunculus was ejected in the 1840s (Currie et al., 1996; Smith and Gehrz, 1998; Morse et al., 2001), around the time it temporarily became the second-brightest star in the night sky (Innes, 1903; Davidson and Humphreys, 1997; Frew, 2004; Smith and Frew, 2011). This Great Eruption released 10^{50} erg of kinetic energy (Smith et al., 2003c; Smith, 2008), or about 10% of the kinetic energy produced by a core-collapse supernova. Only one even vaguely comparable stellar eruption, the seventeenth-century outburst of P Cygni (de Groot and Lamers, 1992; Smith and Hartigan, 2006), has been directly observed in our Galaxy. Analogous extragalactic events are referred to as "supernova impostors" (e.g., Humphreys et al.,

1999; Van Dyk et al., 2005; Smith et al., 2011, 2016).

The cause of giant eruptions like η Car's remains a mystery. The energy requirements seem too high to be explained by S Doradus-like variability, although modified single-star models cannot be ruled out. Binary interaction is another possibility, particularly because nineteenth-century observations η Car's color and luminosity indicate that the primary star's radius was comparable to the periastron separation between the two components (see Smith, 2011). It has been proposed that tidal forces spun up the primary star to the point of instability (Cassinelli, 1999), that the secondary star accreted mass from the primary (Soker, 2007; Kashi and Soker, 2010), or even that the two stars physically collided (Iben, 1999; Smith, 2011). Alternatively, the Great Eruption might have been the merger of the inner binary in a triple system (Gallagher, 1989; Iben, 1999; Morris and Podsiadlowski, 2009; Podsiadlowski, 2010; Portegies Zwart and van den Heuvel, 2016) or caused by a dynamical exchange between a close binary and an outer third companion (Livio and Pringle, 1998).

Another major question about LBVs, both normal and eruptive, is where they fit into our schema of massive-star evolution. The traditional single-star view is that all very massive stars go through an LBV phase. They shed their hydrogen envelopes and emerge as classical Wolf-Rayet stars (Humphreys and Davidson, 1994), which then live for another 0.5 Myr or so (e.g., Meynet and Maeder, 2005) before exploding as Type Ib/c supernovae. That paradigm has been challenged by observations of Type IIn supernovae (Schlegel, 1990; Filippenko, 1997), which show signs of interaction with recently ejected circumstellar material (e.g., Benetti et al., 1998; Chugai et al., 2004; Hoffman et al., 2008; Smith et al., 2008; Chatzopoulos et al., 2011; Stritzinger et al., 2012; Zhang et al., 2012). In a few cases, LBV-like eruptions from a massive star have been directly observed months or years before its supernova (Mauerhan et al., 2013; Ofek et al., 2013). This has led to the proposal that LBVs are a final stage, rather than an intermediate step, in the evolution of certain massive stars (Kotak and Vink, 2006; Gal-Yam et al., 2007; Smith et al., 2007, 2010b; Kiewe et al., 2012; Groh et al., 2013; Justham et al., 2014; Smith, 2014). Further support for this scenario comes from the spatial distribution of

LBVs: with the notable exception of η Car, they are more isolated than Wolf-Rayet stars, the opposite of what would be expected if the former evolved into the latter (Smith and Tombleson, 2015; Smith, 2016, but see Humphreys et al. 2016).

After the decade-long Great Eruption, η Car faded below its pre-nineteenth-century visual luminosity (Davidson and Humphreys, 1997; Frew, 2004). It experienced a Lesser Eruption, much less dramatic than the first, around 1890 (Ishibashi et al., 2003; Smith, 2005), and ejected 0.1 $M_\odot$ into a "Little Homunculus" (Ishibashi et al., 2003; Smith, 2005). It then remained largely unnoticed until a sudden jump in magnitude around 1950 (de Vaucouleurs and Eggen, 1952) and has been slowly brightening ever since (see Frew, 2004). Today, its multi-wavelength photometric and spectroscopic variations are mostly tied to its binary cycle, with every periastron approach generating a flurry of observational activity (e.g., Feast et al., 2001; Whitelock et al., 2004; Gull et al., 2006; van Genderen et al., 2006; Nielsen et al., 2007; Davidson et al., 2015).

When it was on the main sequence, η Car provided about 20% of the Carina Nebula's ionizing luminosity. At the moment, though, it contributes almost no ionizing photons, as its high-energy radiation is absorbed by its dense stellar wind (Hillier et al., 2001; Smith et al., 2003b) and the dusty Homunculus. Its contribution to the Carina Nebula's feedback budget will spike again when—possibly in the very near future—it goes supernova.

1.3 OB Associations

Massive stars rarely live alone or even in isolated binary pairs; as in the Carina Nebula, they tend to be found in groups of various sizes. Stellar groups that are gravitationally bound overall are called clusters, while unbound groups are called associations (Ambartsumian, 1947, 1955). OB associations (i.e., associations containing at least a handful of massive stars; Blaauw, 1964; Garmany, 1994) range from 10–15 pc to $>$ 200 pc across, with typical sizes around 80–100 pc (Garmany and Stencel, 1992; Magnier et al., 1993; Bresolin et al., 1996; Ivanov, 1996; Bresolin et al., 1998;

Gouliermis et al., 2003), and often encompass multiple subgroups (Blaauw, 1964). They may be the birthplaces of the majority of stars in the Galaxy (Miller and Scalo, 1978; Briceño et al., 2007).

Different authors have applied various criteria to determine whether a stellar group is a bound cluster or an unbound association. Some use a cutoff in stellar mass density (e.g., Lada and Lada, 1991), requiring that an association be vulnerable to disruption by galactic tidal forces (< 0.1 $M_\odot$ pc^{-3}; Bok, 1934) or by the gravity of a passing interstellar cloud (< 1 $M_\odot$ pc^{-3}; Spitzer, 1958). Gieles and Portegies Zwart (2011) proposed a dynamical definition such that the crossing time of an association is greater than its age. The scale on which these criteria are applied is relevant, as associations sometimes contain one or more bound clusters within their borders (e.g., Garmany and Stencel, 1992). In practice, the words "association" and "cluster" are often used semi-interchangeably (e.g., Massey et al., 1995), and Battinelli and Capuzzo-Dolcetta (1991) note that a substantial fraction of Galactic "open clusters" are probably gravitationally unbound.

The Carina Nebula is a perfect example of the ambiguities involved in the definitions of clusters and associations. Throughout this dissertation, I adopt the common terminology for the subcomponents of the Carina Nebula complex: Tr 14 and Tr 16 are "massive clusters," Bo 11 and Cr 228 are "open clusters," and so forth. But only the relatively compact Tr 14 is known to be gravitationally bound (Gieles and Portegies Zwart, 2011). The whole Carina Nebula complex, as described in Section 1.2.1, is characterized in the literature as a young association or a "cluster of clusters" (Smith et al., 2010c; Feigelson et al., 2011). Formally, it is only part of the Car OB1 association, which extends several more degrees to the west (Ruprecht, 1966; Humphreys, 1978). Car OB1 also includes Gum 31 (NGC 3324; Clariá, 1977; Carraro et al., 2001; Ohlendorf et al., 2013; Preibisch et al., 2014), NGC 3293 (Balona et al., 1997; Baume et al., 2003; Freyhammer et al., 2005; Dufton et al., 2006; Kaltcheva and Golev, 2012), and IC 2581 (Kaltcheva and Golev, 2012). Gum 31 seems to be associated with the molecular gas complex that surrounds the Carina Nebula (Smith et al., 2000; Ohlendorf et al., 2013; Rebolledo et al., 2016;

Zeidler et al., 2016), but does not show signs of interaction with the main complex. The relationships between NGC 3293, IC 2581, and the rest of Car OB1 are unclear.

There are two leading models to explain the formation of unbound associations (see also the discussion in Briceño et al., 2007). The first is the oft-cited "most stars form in clusters" paradigm, based on near-infrared observations suggesting that most star formation occurs in embedded clusters (Lada and Lada, 1991, 2003). When the massive stars in these clusters emerge onto the main sequence, their feedback disperses the remaining gas within a few Myr (e.g., Tenorio-Tagle et al., 1986). The dynamically sudden reduction in the cluster's gravitational potential leaves it unbound (Tutukov, 1978; Hills, 1980; Goodwin, 1997; Boily and Kroupa, 2003; Bastian and Goodwin, 2006; Goodwin and Bastian, 2006), resulting in an expanding OB association that may retain a smaller still-bound cluster at its core (Lada et al., 1984; Kroupa et al., 2001; Fall et al., 2005).

The competing view is that stars are not preferentially born in bound clusters. Rather, they form in a hierarchical distribution across a wide range of stellar densities (Elmegreen and Efremov, 1996, 1998; Bastian et al., 2007; Bressert et al., 2010), tracing the fractal density structure of turbulent molecular clouds (Larson, 1995; Elmegreen and Elmegreen, 2001; Bonnell et al., 2003; Gutermuth et al., 2011). Bound clusters result from star formation in the highest-density regions (Kruijssen, 2012) and from the mergers of subclusters (Bonnell et al., 2003). Unbound associations arise directly out of lower-density regions of gas (e.g., Clark et al., 2005) and never pass through a stage where they are globally bound. Recent observations of the spatial and kinematic substructure—and lack of overall expansion—in the massive Cygnus OB2 cluster support this model for its formation (Wright et al., 2014, 2016).

Triggered star formation (see Section 1.1.2) could be important in either scenario of association formation. Within some OB associations, there is a clear age sequence from one subgroup to the next (e.g., Blaauw, 1964; Sargent, 1979; Preibisch and Mamajek, 2008; Ortega et al., 2009). The collect-and-collapse model (Elmegreen and Lada, 1977) was developed to explain these age sequences, with

each subgroup triggering the formation of the next after a few Myr. Smith et al. (2010c) propose that a more continuous process of triggering is operating in the Carina Nebula's South Pillars, producing an expanding OB association as the next generation of stars is formed from feedback-accelerated gas.

1.4 Dissertation Overview

This dissertation is a three-part study of the Carina Nebula's massive stars and their interactions with the ISM on various scales. The results are important for understanding the origin and evolution of specific stars and structures in the region, and for making direct connections between massive stars and the observational effects of their feedback.

Chapter 2 focuses on the eruptive history of η Carinae. I present proper motions of that star's outer ejecta, measured from more than two decades of *Hubble Space Telescope (HST)* imaging, and show that it experienced multiple major mass-loss events prior to the Great Eruption of the 1840s.

Chapter 3 looks at five massive stars with stellar wind bow shocks, arc-shaped features that arise when the relative velocity between a star and the ISM is supersonic (Baranov et al., 1971; van Buren and McCray, 1988). Bow shocks often indicate fast-moving stars, but they may also mark the direction of feedback-driven gas flows (e.g., Povich et al., 2008; Sexton et al., 2015). I use a decade of *HST* imaging to constrain the proper motions of these five stars, comparing their velocity vectors to the orientations of their bow shocks.

Chapter 4 is a radial velocity survey of the Carina Nebula's full O-star population, combining archival data with new observations from the CHIRON spectrograph on the CTIO/SMARTS 1.5-m telescope. I compare the radial velocity distributions of the various clusters to the motions of the region's molecular clouds and to the expansion of its giant H II region.

Chapter 5 summarizes my conclusions and discusses potential pathways for future research.

CHAPTER 2

ANCIENT ERUPTIONS OF η CARINAE: A TALE WRITTEN IN PROPER MOTIONS[†]

We analyze eight epochs of *Hubble Space Telescope* Hα+[N II] imaging of η Carinae's outer ejecta. Proper motions of nearly 800 knots reveal that the detected ejecta are divided into three apparent age groups, dating to around 1250 A.D., to around 1550 A.D., and to during or shortly before the Great Eruption of the 1840s. Ejecta from these groups reside in different locations and provide a firm constraint that η Car experienced multiple major eruptions prior to the 19$^{\rm th}$ century. The 1250 and 1550 events did not share the same axisymmetry as the Homunculus; the 1250 event was particularly asymmetric, even one-sided. In addition, the ejecta in the S ridge, which have been associated with the Great Eruption, appear to predate the ejection of the Homunculus by several decades. We detect essentially ballistic expansion across multiple epochs. We find no evidence for large-scale deceleration of the observed knots that could power the soft X-ray shell by plowing into surrounding material, suggesting that the observed X-rays arise instead from fast, rarefied ejecta from the 1840s overtaking the older dense knots. Early deceleration and subsequent coasting cannot explain the origin of the older outer ejecta—significant episodic mass loss prior to the 19$^{\rm th}$ century is required. The timescale and geometry of the past eruptions provide important constraints for any theoretical physical mechanisms driving η Car's behavior. Non-repeating mechanisms such as the merger of a close binary in a triple system would require additional complexities to explain the observations.

[†]This chapter has been previously published as Kiminki et al. (2016).

2.1 Introduction

One of the most remarkable stars in our Galaxy, η Carinae has been puzzling astronomers for over 150 years. In the mid-nineteenth century, it became increasingly variable, then peaked temporarily as the second brightest star in the sky (Innes, 1903; Davidson and Humphreys, 1997; Frew, 2004; Smith and Frew, 2011) before slowly fading over more than a decade. During this Great Eruption, η Car ejected an estimated 10–15 $M_\odot$ into the well-known bipolar Homunculus nebula (Smith et al., 2003c). A second, Lesser Eruption followed in 1890 (Innes, 1903; Humphreys et al., 1999; Frew, 2004), but only ejected ~ 0.1 $M_\odot$ (Ishibashi et al., 2003; Smith, 2005).

η Car belongs to a class of stars known as luminous blue variables (LBVs, Humphreys and Davidson, 1994), very massive, unstable, post-main-sequence stars characterized by luminous mass-loss events. Even among LBVs, η Car is unusual and its parameters are extreme. In its current quiescent state, η Car is substantially more luminous than most other known LBVs (e.g., van Genderen, 2001; Smith and Tombleson, 2015). It is one of only two Galactic LBVs that has been observed in a giant eruption. The other is P Cygni, whose largest eruption involved significantly less energy and mass loss, similar to η Car's Lesser Eruption (Smith and Hartigan, 2006). Moreover, η Car has a massive binary companion in an eccentric 5.5-year orbit (Damineli, 1996; Damineli et al., 1997, 2000; Corcoran et al., 2001; Whitelock et al., 2004), and is located in the rich cluster Trumpler 16, home to dozens of O-type stars (Smith, 2006a). In contrast, most LBVs are relatively isolated and lack O-type neighbors (Smith and Tombleson, 2015).

The mechanism of η Car's Great Eruption—which released roughly 10^{50} ergs of kinetic energy (Smith et al., 2003c; Smith, 2008)—remains a mystery. Many theories treat it as part of single-star evolution, invoking super-Eddington radiation-driven winds (Davidson, 1971; Maeder, 1983; de Jager, 1984; Lamers and Fitzpatrick, 1988; Stothers and Chin, 1993; Glatzel and Kiriakidis, 1993; Glatzel, 1994; Humphreys and Davidson, 1994; Shaviv, 2000; Owocki et al., 2004). However, the source of the increased bolometric luminosity in these sce-

narios is unclear. Alternatively, the eccentric orbit of η Car's companion has been taken to imply that the Great Eruption was influenced by periastron interactions between the two binary components. Based on nineteenth-century observers' estimates of the primary star's color and brightness, its radius must have been much larger than at present, large enough that its companion would significantly interact or even physically collide (Iben, 1999; Smith, 2011). A speculative idea is that the collision mixed fresh nuclear fuel to greater depths, causing a sudden burst of increased nuclear burning (Smith, 2011). It has also been proposed that periastron tidal interactions spun up the primary to unstable rates, leading to a burst of mass loss (Cassinelli, 1999), or that the Great Eruption was fueled by accretion from the primary onto its companion (Soker, 2007; Kashi and Soker, 2010). Still other theories postulate a hierarchical triple system, in which the close inner pair either merged (Gallagher, 1989; Iben, 1999; Morris and Podsiadlowski, 2009; Podsiadlowski, 2010; Portegies Zwart and van den Heuvel, 2016) or underwent a dynamical exchange with the outer companion (Livio and Pringle, 1998).

Models of the driving cause of the Great Eruption must also incorporate the outer ejecta, a collection of irregular condensations found out to nearly half a parsec outside the Homunculus (Thackeray, 1950; Walborn, 1976; Meaburn et al., 1996; Smith and Morse, 2004; Weis, 2012). These outer ejecta (Figure 2.1) are highly nitrogen-rich, suggesting a substantial degree of CNO processing (Davidson et al., 1986; Smith and Morse, 2004). They contain a minimum mass of 2–4 $M_{\odot}$ (Weis, 2012), with dust observations suggesting a much larger total mass (Gomez et al., 2010). The various models for the Great Eruption produce different explanations for the outer ejecta. The merger model of Portegies Zwart and van den Heuvel (2016), for instance, predicts that the outer ejecta were formed after the formation of the Homunculus.

The proper motions of the outer ejecta provide concrete constraints on η Car's mass-loss history. The bright S condensation and the "jet"-shaped N bow (see Figure 2.1) have motions consistent with having been ejected during the Great Eruption (Walborn et al., 1978; Ebbets et al., 1993; Currie et al., 1996; Morse et al.,

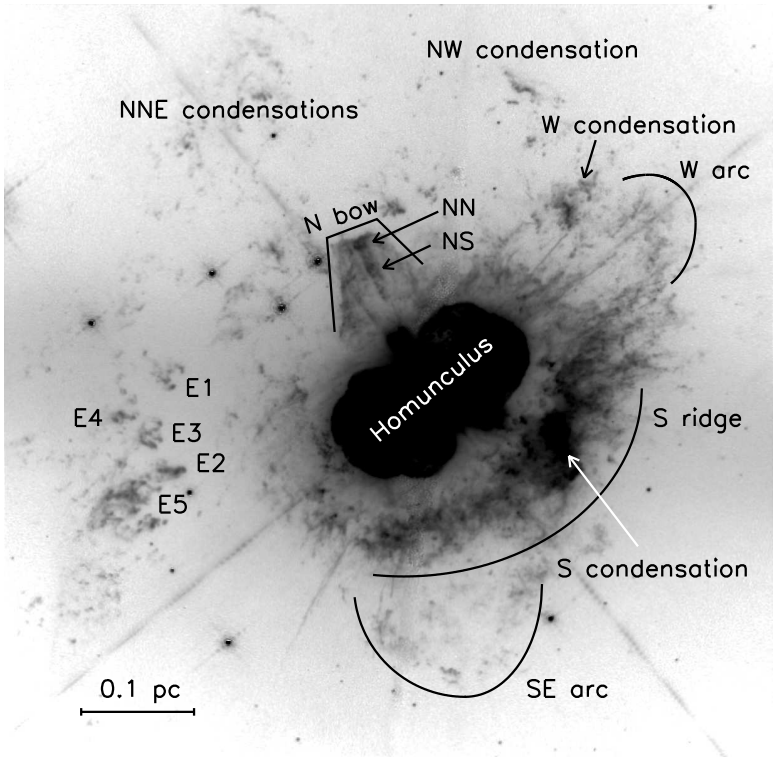

Figure 2.1: *HST* WFPC2 image of η Car in the F658N filter, which captures intrinsic and scattered [N II] λ6584 emission along with redshifted Hα emission (Morse, 1999; Morse et al., 2001). Prominent features are labeled according to the convention of Walborn (1976) and Weis (2012).

2001). Some results have suggested, however, that the extended S ridge is up to one hundred years older (Walborn et al., 1978; Morse et al., 2001). The age of the E condensations is even less clear: Walborn et al. (1978) found transverse velocities of 300–400 km s^{-1}, indicating ejection dates in the mid-1400s, but Walborn and Blanco (1988) determined ten years later that the same features had slowed dramatically, suggesting they were from the Great Eruption after all. While the motions of the outer condensations have hinted at prior mass-loss events, a single ejection date around the time of the Great Eruption could not be ruled out.

In this paper, we measure the proper motions of η Car's outer ejecta to unprecedented accuracy, using 16 different baselines over 21 years of *Hubble Space Telescope* (*HST*) data. The depth and resolution of the *HST* images allow us to re-evaluate the origins of the N, E, and S features, and, for the first time, measure motions of

Table 2.1: *HST* data log.

Instrument	Camera	Date	Filter	Exp. Time (s)	Program ID
WFPC2	WF3	1993 Dec 31	F658N	2×200	5188
WFPC2	WF3	1997 Jul 11	F658N	2×200	7253
WFPC2	WF3	1999 Jun 12	F658N	2×200	8178
WFPC2	WF3	2001 Jun 4	F658N	2×200	9226
WFPC2	WF3	2003 Aug 8	F658N	2×100	9775
WFPC2	WF3	2008 Sept 6	F658N	2×100	11500
ACS	WFC	2005 Jul 18	F658N[a]	2×500	10241
ACS	WFC	2014 Aug 4	F658N[a]	2×520	13390

[a]Note that the bandpass of the ACS 658N filter is different from that of the WFPC2 filter of the same name (see discussion in Section 2.2.2).

the fainter NNE, NW, and SE condensations. We find no evidence of widespread deceleration, and show that while some of the outer ejecta come from the Great Eruption (or the lead-up to it), many features require at least one prior mass-loss event centuries earlier. Our data, image registration, and approach to measuring proper motions are described in Section 2.2; the results are presented in Section 2.3. We discuss the implications of our results on models of η Car in Section 2.4 and conclude with a summary in Section 2.5.

2.2 Observations and Analysis

2.2.1 *HST* ACS

We obtained new Hα+[N II] images of η Car and the surrounding Tr 16 cluster on 2014 Aug 4, using the Wide Field Channel (WFC) of the Advanced Camera for Surveys (ACS) on *HST* (program ID 13390; see Table 2.1). These observations were designed to replicate our observations of 2005 Jul 18 (Smith et al., 2010a) as closely as possible, in pointing and position angle, in order to minimize position-dependent uncertainties when measuring proper motions. The Homunculus and central star are heavily saturated in these exposures, which were each 500–520 s long. In both epochs, observations were made as a series of 205×400 arcsec^2 "footprints," each consisting of three pairs of `CR-SPLIT` dithers in a linear offset

pattern designed to fill in the ACS chip gaps. η Car and its outer ejecta were observed in a single footprint; the rest make up a mosiac of Tr 16 and neighboring Tr 14 (see Smith et al., 2010a). All data were processed by the standard *HST* ACS pipeline, which does bias subtraction and flat-fielding and corrects for charge transfer efficiency (CTE) to produce an image with the designation "`flc`." The pipeline also produces a "`drc`" image that has been additionally corrected for geometric distortion and dither-combined via AstroDrizzle.

We transformed both epochs of ACS data to a common distortion-free reference frame via a modified version of the method used in Anderson et al. (2008a,b), Anderson and van der Marel (2010), and Sohn et al. (2012, see also Reiter et al. 2015a,b). An initial reference frame, aligned with the y axis pointing north and with a pixel scale of 50 mas pixel^{-1}, was constructed using the astrometric solutions in the headers of the `drc` images to match stars that appear in overlapping images. However, the resampling performed by AstroDrizzle makes the `drc` images unsuitable for direct high-accuracy positional measurements. Instead, we performed point spread function (PSF) fitting on the undrizzled `flc` images using the program `img2xym_WFC.09x10` (Anderson and King, 2006), which uses a library of spatially dependent effective PSFs. We then applied the geometric distortion corrections of Anderson (2006) to the measured stellar positions.

Next, we iteratively mapped the stellar positions from the `flc` images to the reference frame by:

1. identifying the high signal-to-noise stars (typically several hundred per image) in common between each `flc` image and the reference frame;

2. computing the six-dimensional linear transformation from the distortion-corrected positions of the `flc` images to the reference frame; and

3. replacing each existing reference-frame stellar position with the average of that star's transformed, distortion-corrected `flc` positions.

After three iterations, the internal accuracy of the reference frame was < 0.02 pixels

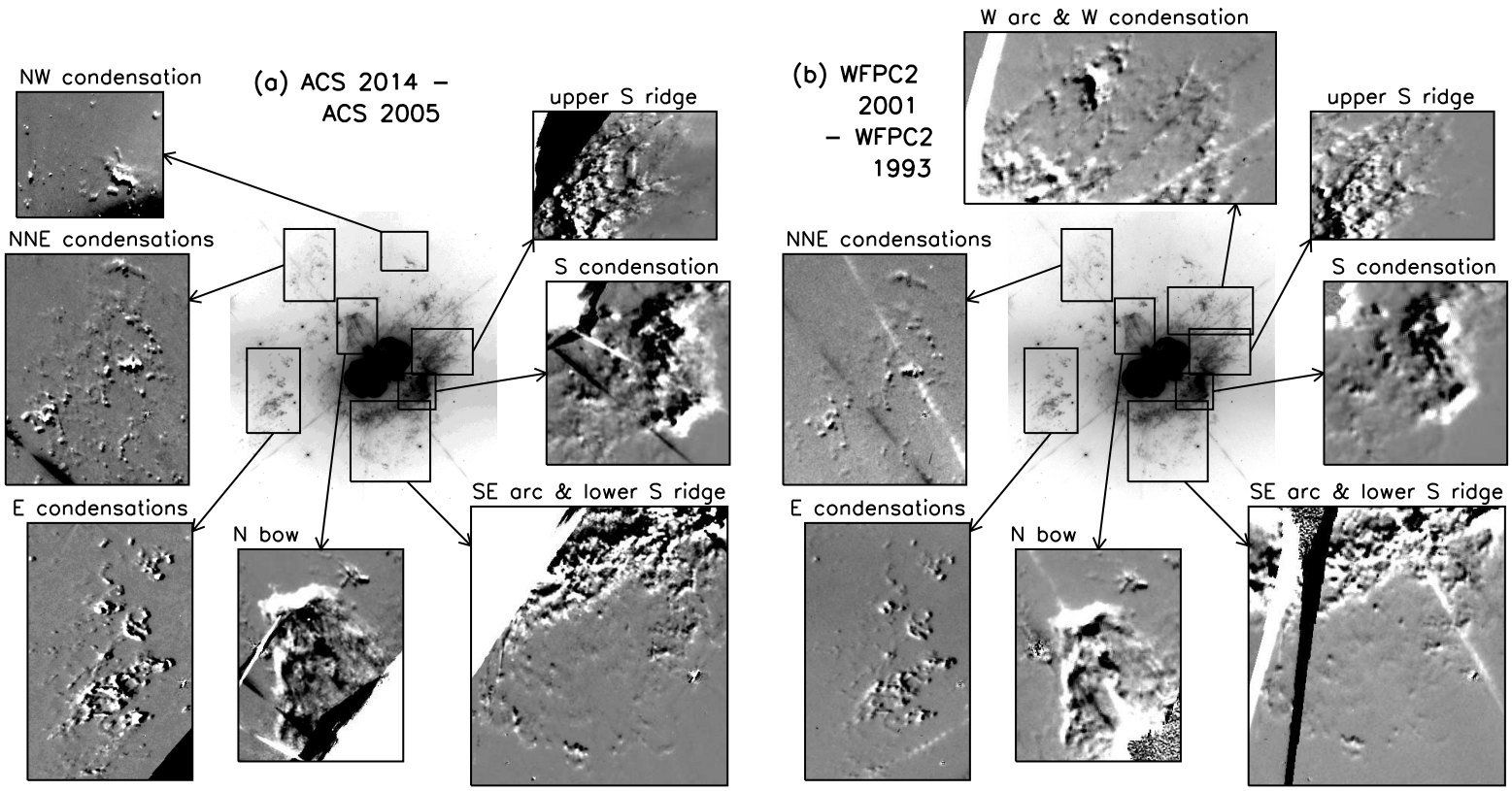

Figure 2.2: (a) Difference images showing the outward motion of η Car's ejecta over the 9-year baseline between ACS images. Dark patches are where the various condensations were in 2005; bright patches are places into which that material had moved by 2014. The central image is the same one shown in Figure 2.1 and is included to orient the reader. (b) Same as (a) but for the 7-year baseline between the WFPC2 1993 and 2001 images. The W and NW condensations are not shown in the ACS (left) and WFPC2 (right) panels, respectively, because they are contaminated by bleeding from the saturated Homunculus in the relevant epochs. Animated GIFs showing the motion of each feature across all 8 epochs are available in the online supplementary material to Kiminki et al. (2016).

(1 mas, or 1.2 km s^{-1} over this 9-year baseline at the distance of η Car) across a single footprint.

Using the final linear transformations determined by this process, we resampled the `flc` images from each epoch into the reference frame using the algorithm described in Anderson et al. (2008b), scaling each image to a total exposure time of 500 s. The end result was a single stacked image at each epoch for each observed footprint. With both epochs of data on the same reference frame, the positions of ejecta features in the stacked images could be directly compared. Figure 2.2 presents difference images (stacked image from 2014 minus stacked image from 2005) for named regions of interest in η Car's outer ejecta. In these images, material has moved from the dark patches into the corresponding bright areas. It is immediately qualitatively apparent that some features have greater transverse velocities than others; the N bow, for instance, is rapidly overtaking the small feature to its immediate northwest. Notably, there are no pronounced changes in condensation morphology or brightness from 2005 to 2014.

The proper motions of well-defined knots in the ejecta around η Car were measured in the stacked images. "Well-defined" features are those that are (1) not contaminated by or confused with the saturated Homunculus or diffraction spikes in either epoch and (2) sufficiently isolated for a defined knot or feature to be identified. A total of 620 such features were identified in the ACS images. To measure the proper motion of each, we subtracted a median-filtered image (filtered using a kernal size of 12 pixels) in order to suppress the local diffuse Hα background. We then extracted the knot using a box size optimized for that feature; Figure 2.3 illustrates the boxes used for the features in and around the E condensations. We used our implementation of the modified cross-correlation technique developed by Currie et al. (1996), Hartigan et al. (2001), and Morse et al. (2001, see also Reiter and Smith 2014; Reiter et al. 2015a,b) to determine the difference in position between the two epochs. In brief, the box containing the feature of interest was compared to the second image and an array was generated containing the total of the square of the difference between two images for each shift. The minimum of this array corre-

Table 2.2: Baselines used for proper motion measurements.

Baseline	Instrument	Δt (years)	# Features	Median σ (km s^{-1})
1993–1997	WFPC2	3.524068	694	8.5
1993–1999	WFPC2	5.443602	704	7.0
1993–2001	WFPC2	7.422813	712	5.4
1993–2003	WFPC2	9.599420	714	4.8
1993–2008	WFPC2	14.680967	698	3.9
1997–1999	WFPC2	1.919534	703	14.3
1997–2001	WFPC2	3.898745	742	7.7
1997–2003	WFPC2	6.075352	713	6.3
1997–2008	WFPC2	11.156898	686	4.6
1999–2001	WFPC2	1.979211	716	12.1
1999–2003	WFPC2	4.155818	684	8.0
1999–2008	WFPC2	9.237365	679	4.6
2001–2003	WFPC2	2.176607	633	13.0
2001–2008	WFPC2	7.258153	666	5.5
2003–2008	WFPC2	5.081546	648	7.6
2005–2014	ACS	9.046256	620	2.7

sponds to the shift that best matches the two images. Angular displacements were converted to km s^{-1} assuming a distance of 2.3 kpc (Smith, 2006b). To estimate the uncertainty on the offset, we repeated the procedure using a variety of box sizes. The median proper motion uncertainty for features measured in the ACS images is 2.7 km s^{-1}.

2.2.2 *HST* WFPC2

To supplement our proper motion measurements from the 2005–2014 ACS baseline, we searched the *HST* archive for additional deep images of η Car taken with an F658N filter. Six epochs of observations from the Wide-Field Planetary Camera 2 (WFPC2) met our requirements: the images had to be deep enough for the outer ejecta to be visible, and η Car had to be centered on one of the Wide Field chips (the field of view of the Planetary Camera chip is too small). The dates and program IDs for these data are given in Table 2.1. We retrieved the longest exposures available

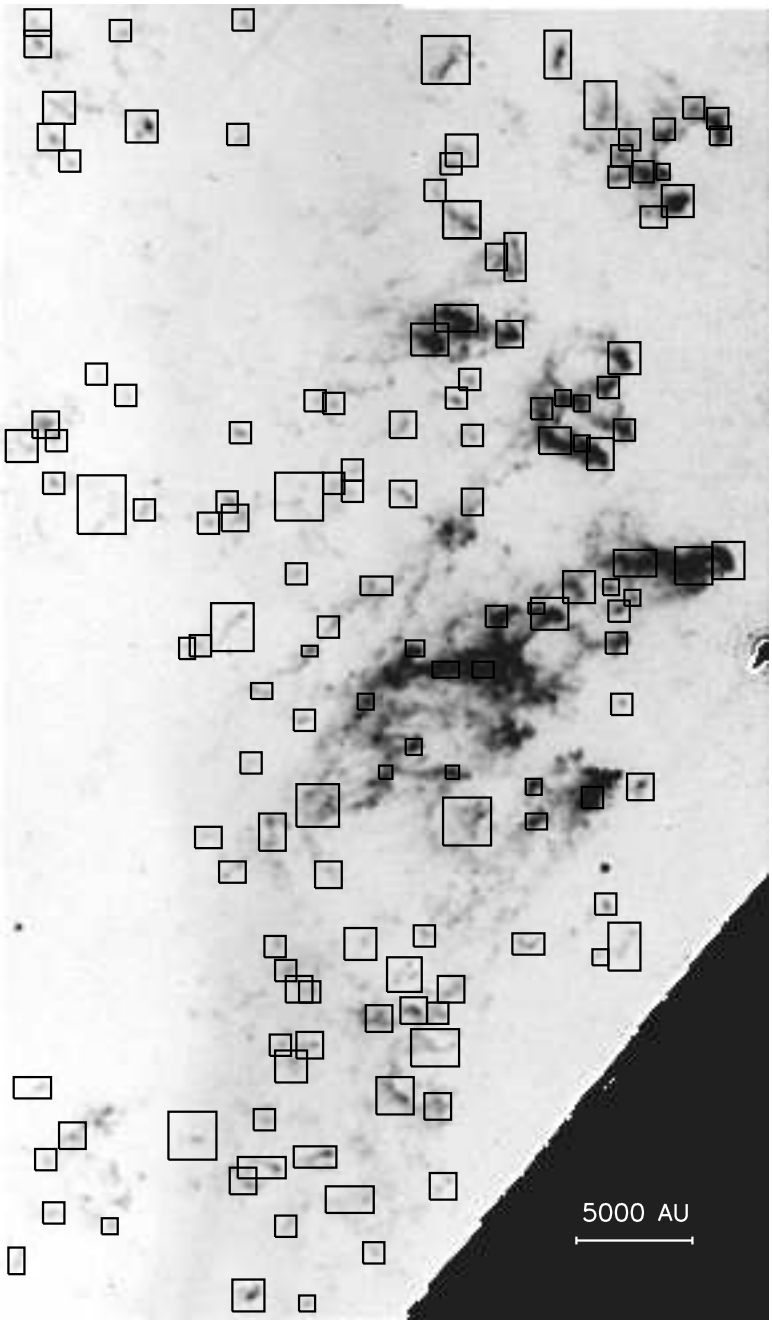

Figure 2.3: Close-up of the region around the E condensations in the 2005 ACS F658N image, showing the boxes used to measure proper motions via modified cross-correlation. The saturated strip in the lower right is bleeding from the saturated Homunculus.

at each epoch: a pair of 200-s exposures from each of 1993, 1997, 1999, and 2001, and a pair of 100-s exposures from each of 2003 and 2008. η Car itself and much of the Homunculus are saturated in these images, although the bleeding is much less extensive than in the ACS images, which have both longer exposure times and a wider filter bandpass (see below). All of the data had been reprocessed by the final version of the *HST* WFPC2 pipeline, which produces images designated "`c0m`" that have been bias-subtracted, dark-corrected, and flat-fielded.

Note that there are important differences between the WFPC2 F658N filter and the ACS filter of the same name. The former covers a narrow wavelength range (FWHM 38 Å) roughly centered on [N II]λ6584, capturing emission from that line with Doppler shifts from approximately -615 to +1130 km s^{-1}. The latter is broader (FWHM 72 Å), capturing [N II] emission with radial velocities up to $\pm$1600 km s^{-1} as well as significant Hα emission. Although most of the same ejecta features seen in the ACS images are identifiable in the WFPC2 images, there is no way to guarantee that the knot shapes are unaffected by the differences in filter bandpass. Consequently, we do not measure proper motions directly between WFPC2 and ACS images. We use only WFPC2–WFPC2 and ACS–ACS baselines. In addition, the fastest known ejecta are Doppler-shifted out of one or both filters and are not detected. The WFPC2 F658N filter would not, for instance, pick up the -875 km s^{-1} blueshifted emission just outside the southeast lobe of the Homunculus (Currie et al., 2002), even if the Homunculus were not saturated in our images. Both filters miss the -3200 km s^{-1} blueshifted ejecta detected further out by Smith (2008). Our images thus exclude the fastest-moving material from the Great Eruption and therefore do not exclude the possibility of additional recent mass-loss episodes. We note, however, that since few of the ejecta seen in the ACS images drop out in the WFPC2 images (and those that do are relatively faint and not detected in the shortest exposures), few to none of the dense knots measured in our images have radial velocities of $\pm$1000–1500 km s^{-1}.

We took the same approach to aligning and stacking the WFPC2 data as we did with the ACS images. We used a modified version of the `img2xym` program

(Anderson and King, 2006) to measure stellar positions in the c0m images, employing a library of spatially dependent effective WFPC2 PSFs from Anderson and King (2000). The measured positions were then corrected for the 34th-row anomaly (Anderson and King, 1999) and for geometric distortion (Anderson and King, 2000). We identified 6–10 isolated, low-proper-motion stars in common between each WFPC2 image and the ACS-based reference frame, and used those stars to derive a six-parameter linear transformation between each distortion-corrected WFPC2 frame and the reference frame. Unlike with the ACS data, we did not iterate on the process: we took the ACS-based reference frame as final. The internal accuracy of the alignment and stacking procedure is < 0.06 reference-frame pixels (3 mas) for the first four epochs. The shorter, lower signal-to-noise 2003 and 2008 exposures had greater positional uncertainties of up to 0.2 reference frame pixels (10 mas).

Using the calculated transformations, the WFPC2 c0m images were resampled and stacked into a single image at each epoch, aligned with the ACS-based reference frame. The c0m images, which have a plate scale of 99.6 mas pixel^{-1}, were oversampled during stacking so that the output image matched the 50-mas pixels of the ACS images. An example of the results is shown in the right panel of Figure 2.2, which shows difference images for the major named regions of η Car's outer ejecta for the 1993–2001 baseline. Although the resolution is somewhat lower compared to the ACS images, much detail is still apparent. Animated GIFs of each region, made from all eight epochs of aligned data, are available in the online supplementary material.

The proper motions of the features identified in the ACS images were measured in the WFPC2 images, using the modified cross-correlation technique described in Section 2.2.1, for every possible baseline among the six epochs (a total of 15 baselines). Some features were contaminated by diffraction spikes or saturation bleeds in some epochs; proper motions for these features were measured using only the epochs in which they were not contaminated. The baselines, number of features measured, and median proper motion uncertainties for each baseline are given in Table 2.2. The median proper motion uncertainties range from 3.9 to 14.3 km s^{-1},

and the magnitude of the uncertainty is highly negatively correlated with the length of the baseline (i.e., shorter baselines produce greater uncertainties). In the areas blocked by saturation bleeding in the ACS images, we used the 1993–2001 baseline (the longest baseline with 200-s exposures) to identify additional features which were then measured across the other WFPC2 baselines where possible. A small number of features in a gap that was saturated in 2001 are identified in the 1993–2003 baseline instead, then measured across other baselines where possible. In total, we measure the proper motions of 792 individual features in the ejecta of η Car. Each feature is measured in 1–16 baselines (including the 2005–2014 ACS baseline); on average, a feature is measured in 14 baselines.

2.2.3 Position of the central source

Owing to the heavy saturation of the Homunculus, we were unable to measure the position of η Car itself in any of our stacked images. Instead, we measure the centroid of the central star in an F631N WFPC2 Planetary Camera image from Morse et al. (1998). The centroid positions of five surrounding stars in this image were used to derive a linear transformation to our reference frame. We estimate that this transformation is accurate to $\sim$ 0.2 reference-frame pixels. Added in quadrature with the $\pm$0.5-pixel uncertainties in absolute knot positions, this means that the overall uncertainty in a knot's distance from η Car is $\sim$0.55 pixels (27 mas, or 60 A.U. at the distance of η Car). For a knot moving at 300 km s^{-1}, this translates to an uncertainty in its age of $\pm$0.9 years.

2.3 Results

2.3.1 *HST* proper motions over two decades

Figure 2.4 presents our results in aggregate: a histogram of the weighted mean proper motions of all measured features, along with proper motion histograms for the ejecta in each of the regions highlighted in Figure 2.2. The transverse velocities of η Car's outer ejecta range from 219 km s^{-1} to 1462 km s^{-1}, with a broad peak

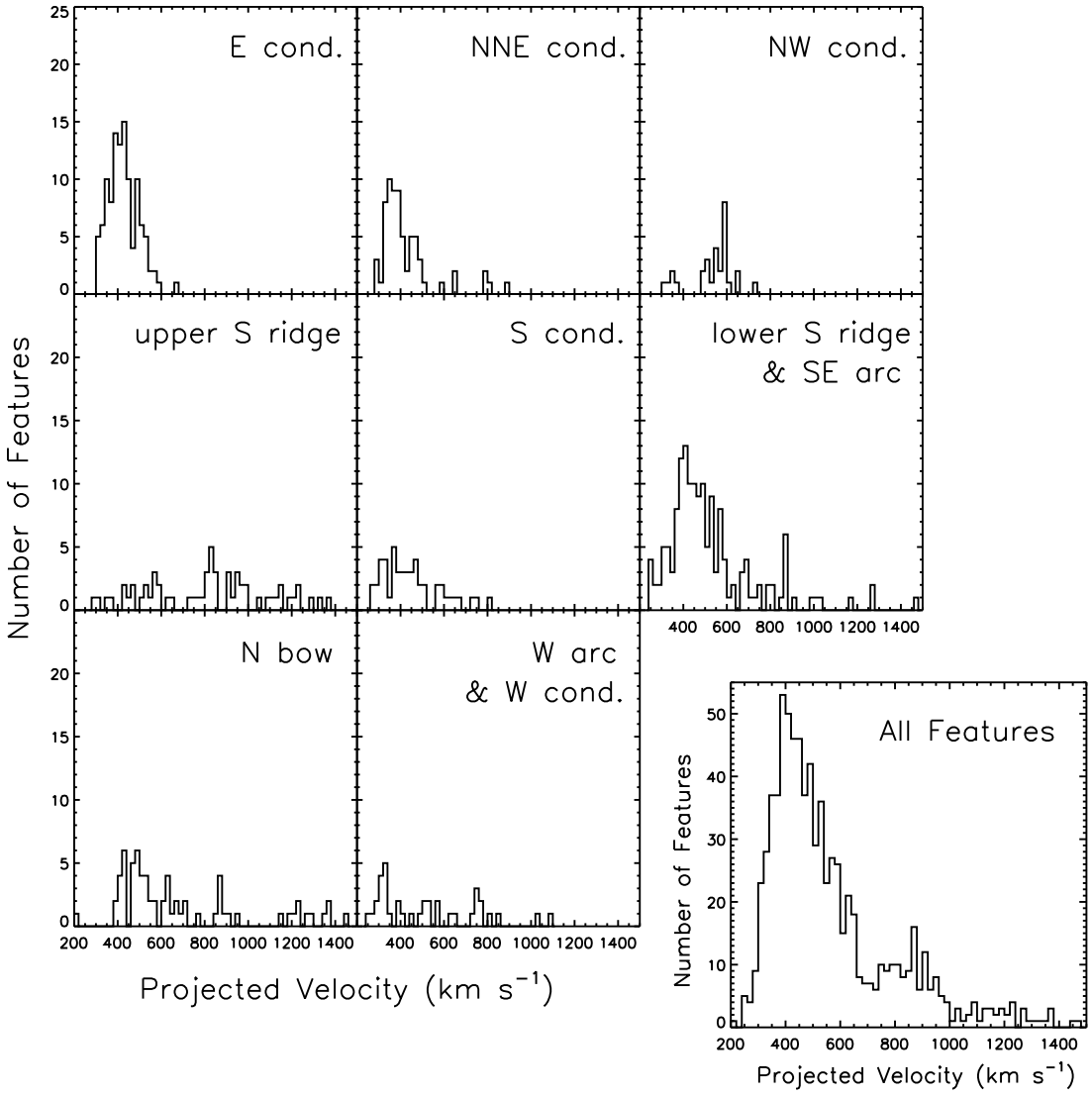

Figure 2.4: Histograms of the weighted mean proper motions of the outer ejecta, assuming a distance of 2.3 kpc. The regions are as shown in Figure 2.2; note that some of the regions slightly overlap. The bottom right panel shows the velocity histogram for all 792 measured features.

at 300–600 km s^{-1} and a secondary peak at 750–900 km s^{-1}. The highest proper motions are found in the N bow, the S ridge, and the parts of the W arc that overlap with the upper S ridge. The presence and location of speeds upward of 1000 km s^{-1} agrees with past observations of the S ridge and N bow (Walborn et al., 1978; Walborn and Blanco, 1988; Ebbets et al., 1993; Morse et al., 2001). The mix of speeds seen in the lower S ridge is also consistent with the results of Morse et al. (2001).

Our results for the E condensations (no high-proper-motion features; mean proper motion ~ 400 km s^{-1}) agree solidly with the results of Walborn et al. (1978), who used photographic plate images from 1950 to 1975. However, the observed motion in our *HST* images disagrees strongly with the deceleration hypothesis of Walborn and Blanco (1988), who added data from 1985 and found that the E condensations had dramatically slowed over 10 years. The Walborn and Blanco (1988) deceleration hypothesis predicts that the E features would have reached zero velocity by the end of the twentieth century, a hypothesis that our data definitively exclude.

With a total of 16 different baselines from two instruments, we can approach the question of acceleration/deceleration with unprecedented detail. Figure 2.5 plots the measured proper motions over time for three features representative of the E condensations and of the ejecta overall. The weighted mean transverse velocity of each feature is overplotted, along with a least-squares fit to the data. Although there is some variation among the proper motions, there are no overall trends with time. In a χ^2 test, the measured motions for all three features shown in Figure 2.5 are consistent with having been drawn from a distribution with constant transverse velocity.

This level of variance and (lack of) acceleration is found across all our data. Out of the 792 features for which proper motions were measured, only 50 (6%) have data that are inconsistent at the $p < 0.05$ level with being drawn from a constant velocity distribution. These 50 features occupy no special region of physical space or velocity space. The slopes of the least-squares fits to velocity versus time for these 50 features also fall inside the range of slopes found for the rest of the ejecta.

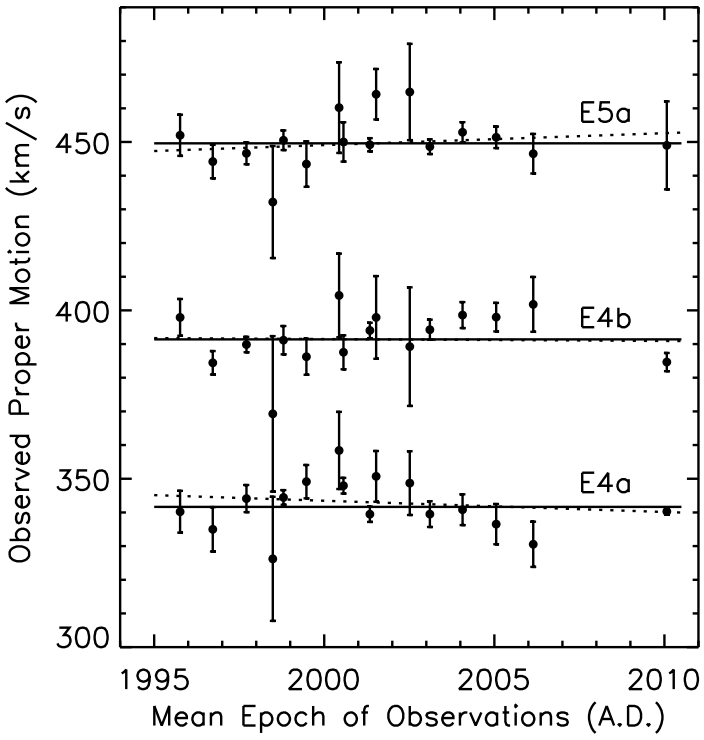

Figure 2.5: Proper motions measured over all possible baselines for three representative features among the E condensations. The points around 2010 are from the ACS 2005–2014 baseline, while the other measurements come from the various WFPC2–WFPC2 baselines. The largest uncertainties typically occur over the shortest baselines, e.g., 1997–1999. The solid lines are the weighted means of the measurements, and the dotted lines are least-squares fits to proper motion versus time for each ejecta feature.

If material were being significantly accelerated (from being hit by younger, faster material) or decelerated (from running into older material), we would expect to see some kind of spatial correlation of those changes in velocity, yet we do not. Thus, while we cannot rule out small amounts of acceleration or deceleration for individual features, the outer ejecta appear to be, on the whole, expanding ballistically. We therefore treat all velocities as constant unless otherwise noted, and use the weighted mean as the final proper motion for each feature.

As a last check on whether the assumption of constant velocities is appropriate, we extrapolate our observed positions of the outer ejecta back to 1950 and compare them to the ground-based photographic plate images of Thackeray (1950). We aligned the Thackeray (1950) images to a copy of our stacked ACS image that had been convolved with a broad PSF to approximately match the resolution of the older images. Figure 2.6 shows the predicted 1950 positions, with the observed 2005 positions overplotted for comparison. There is good agreement between our predicted positions and the observed features in 1950. Although one must be conscious of the limitations of photographic plate data, these data are consistent with ballistic motion of η Car's ejecta over the past 60 years. From the motion that we measure, however, we cannot rule out significant acceleration or deceleration that may have occurred earlier than 60 years ago.

2.3.2 Ages of the outer ejecta

Under the assumption that the constant velocities observed over the last 60 years apply over the lifetime of the ejecta, estimating ejection dates is trivial. Earlier episodes of acceleration or deceleration would affect the specific ejection dates deduced, but, as we discuss in Section 2.4.3, are unlikely to affect the overall relationships between groups of ejecta. Ejection date results are summarized in Figure 2.7: the magnitude and direction of each knot's proper motion are indicated by the length and orientation of its arrow, and the arrows are color-coded by apparent ejection date. Red arrows mark the most recently ejected material, i.e., material that was ejected around the time of the Great Eruption, while blue and purple arrows indicate the

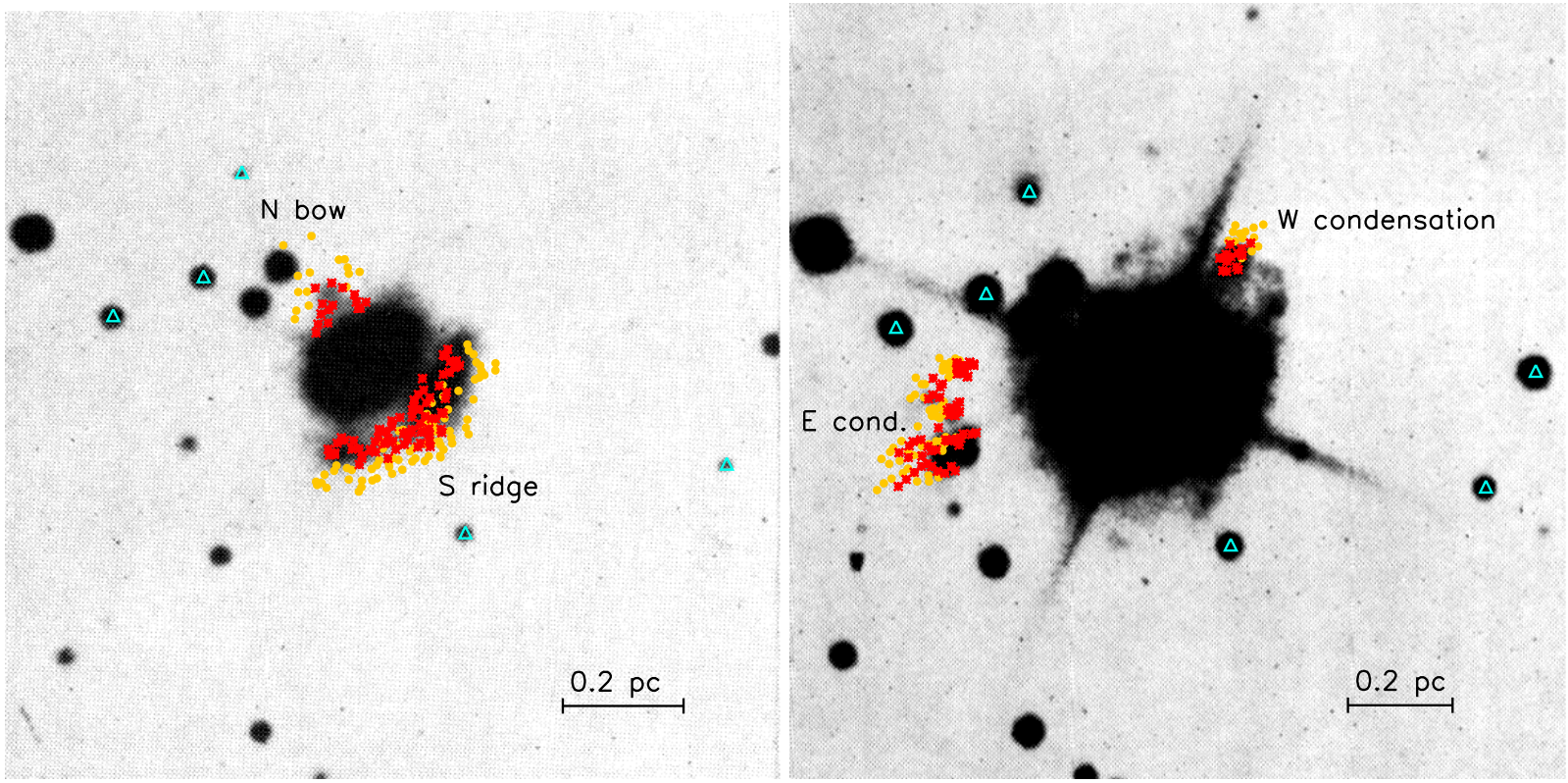

Figure 2.6: Left: red-sensitive photographic plate image of η Car and its surrounding nebulosity from Thackeray (1950). The predicted 1950 positions of the features we observe in the N bow and S ridge are plotted as red asterisks, while our observed 2005 positions of the same features are marked with yellow circles. The stars that were used to align this image with our reference frame are indicated with cyan triangles. Right: same as left, using a deeper image from Thackeray (1950) to show the observed current and predicted past positions of the E and W condensations.

oldest material. It can be seen in Figure 2.7 that all 792 measured features are moving nearly directly away from the central star.

There are several distinct groups of ejecta in Figure 2.7:

1. The N bow, S condensation, and S ridge (which extends nearly completely around the Homunculus) all date back to the early 1800s, consistent with prior results (Walborn et al., 1978; Ebbets et al., 1993; Morse et al., 2001). As we discuss below, the age of the S ridge suggests an origin during one of the precursor outbursts to the Great Eruption (seen as spikes in the historical light curve; Smith and Frew, 2011), before the ejection of the Homunculus.

2. The E blobs and many of the NNE condensations date back to an ejection event in the thirteenth century. This event was apparently highly asymmetric: there are no ejecta with this age to the south or west. (Note, however, that our *HST* ACS footprint for this reference frame cuts off in the far southwest. We address this issue further in Section 2.3.3.)

3. The SE arc, the W and NW condensations, and part of the W arc appear to date to an intermediate eruption in the sixteenth century. In the SE and W arcs, this material is being overtaken by faster-moving material from the Great Eruption. The lower S ridge is a mix of material of different ages, explaining why Morse et al. (2001) dated this region to half a century before the Great Eruption.

   One might surmise that the apparently intermediate ages of material in the SE and W arcs could result from the interaction between material from the 1200s and material from the 1800s. However, there are no newer ejecta around the NW condensation or the faint ejecta to the far north. As we discuss in Section 2.4.1, radial velocities also suggest that these ejecta are not connected to the thirteenth-century eruption. They also lie outside the soft X-ray shell, which traces strong current interactions between ejecta (see Section 2.4.2)

Figure 2.8 presents these data in an alternative form, plotting the transverse

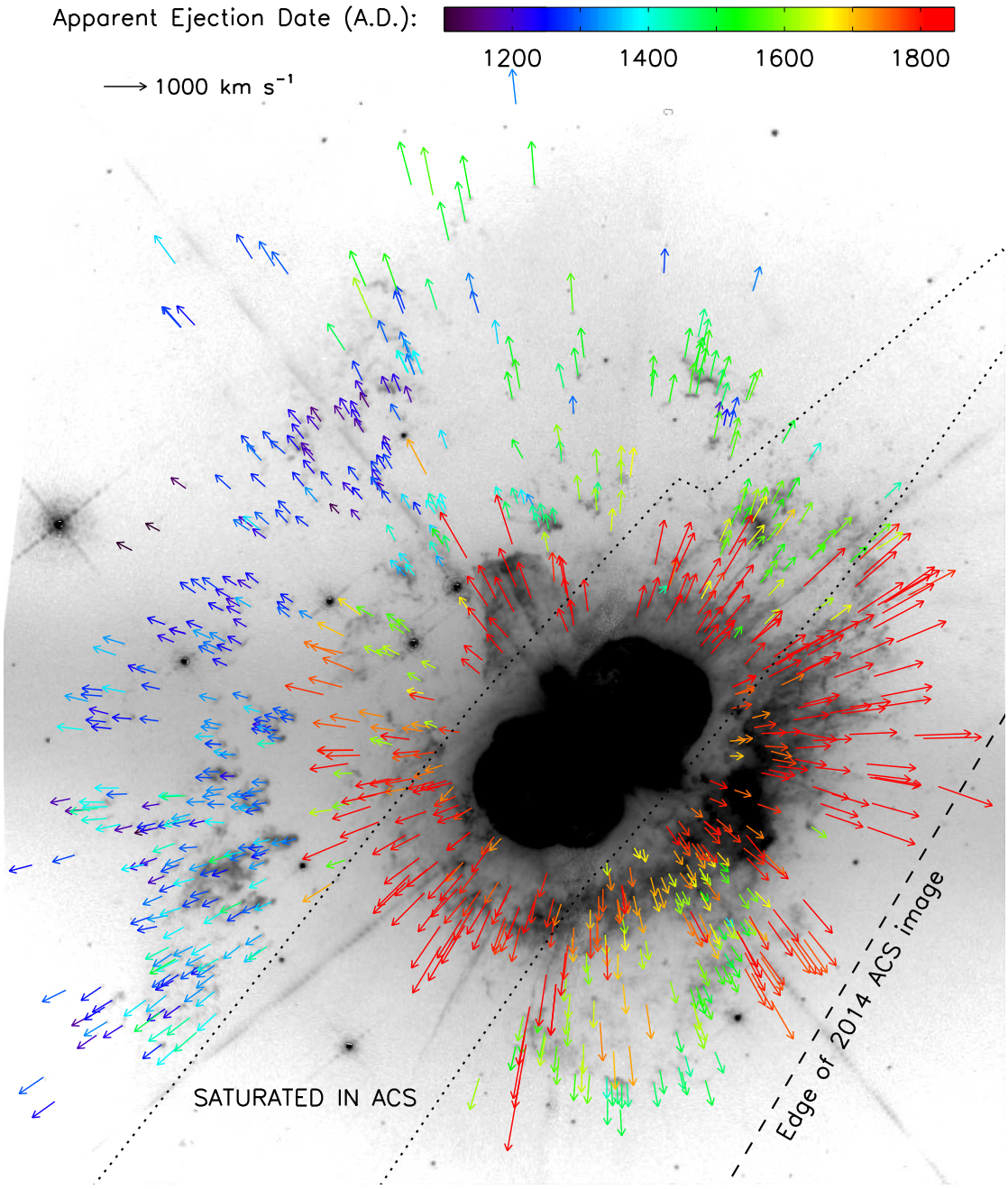

Figure 2.7: Vectors illustrating the observed proper motions of 792 features in the ejecta of η Car. The arrows are color-coded by the date of ejection from the central star, calculated assuming constant velocity. The region contaminated in the ACS images by bleeding from the highly saturated Homunculus is marked; features in this region were measured in WFPC2 data only. The background image is the same as in Figure 2.1.

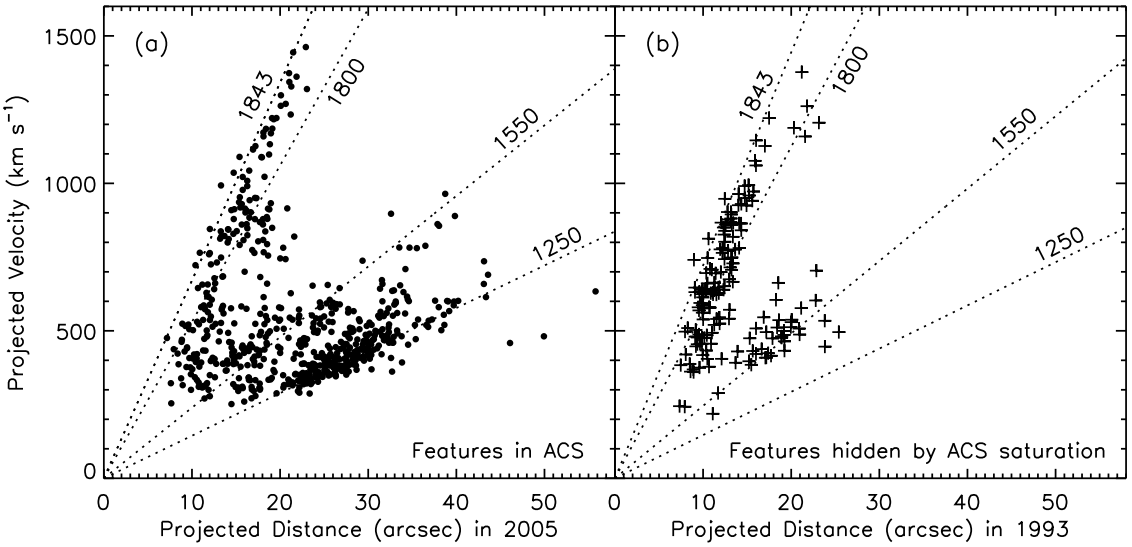

Figure 2.8: (a) Measured transverse velocity versus projected distance from the central star for all features measured over the ACS 2005–2014 baseline. The predicted positions of material ejected at the peak of the 1840s Great Eruption is marked, along with tracks for material ejected in 1250 A.D., 1550 A.D., and 1800 A.D., for reference. (b) Same as (a), but for features that were masked by saturation bleeds in the ACS images and were consequently only measured with WFPC2.

velocity of ejecta features versus their projected distance from η Car. Again, there is evidence for at least two eruptions, one in the early 1800s and another circa 1250 A.D. An intermediate eruption, circa 1550 A.D., is suggested but less obvious. As mentioned above, the sixteenth-century ages could in principle be the result of interaction between ejecta from the Great Eruption and the 1200s event. However, the intermediate-aged features appear in a fairly clear line in velocity–distance space (i.e., as a Hubble-like law) rather than being smeared between the points from the two other events.

An additional feature of interest in Figure 2.8 is that nearly all of the nineteenth-century features appear to have been ejected decades before 1843. Proper motions of the Homunculus date it to the mid-1840s (Currie et al., 1996; Smith and Gehrz, 1998; Morse et al., 2001); this is when the light curve of η Car reached its peak (Smith and Frew, 2011). There are two possibilities for why the S ridge and its

extended wings appear older: (1) its material experienced a period of deceleration as it interacted with circumstellar material early in its history before continuing to expand ballistically; or (2) it was ejected prior to the formation of the Homunculus. The second option is supported by the photometric record: the Great Eruption was preceded by a brightening in 1838 and a similar but poorly observed event in 1827 (see Smith and Frew, 2011, who found that these events align with the predicted periastron times of η Car's binary orbit). The data before 1827 are very sparse (or nonexistent) and leave open the possibility of additional prior periastron outbursts. The S ridge may have been ejected during one or more of these events rather than during the main peak of the Great Eruption. Its strong asymmetry may therefore be related to stellar collisions at periastron (Smith, 2011) associated with these early brightenings. The alternative explanation (an early deceleration episode) is plausible for the material at the edges of the bright S condensation, which appears in Figure 2.8 around 16–20″ and 500–700 km s^{-1}. We could be seeing the result of interaction between the S condensation (ejected during the Great Eruption) and the slightly older S ridge material.

Finally, Figure 2.9 presents histograms of the apparent ejection dates, both overall and for each of the regions in Figures 2.2 and 2.4. The differences in age between the various groups of features are clearly evident. The E and NNE condensations, for instance, are much older than the upper S ridge and S condensations. The mix of ages in the W arc and the lower S ridge is also apparent. As in Figure 2.8, the overall histogram of ejection dates shows two obvious distinct events, in the thirteenth and nineteenth centuries, as well as a smaller peak of features ejected in the late 1500s.

Overall, our proper motions of η Car's outer ejecta solidly confirm that there was at least one major mass-loss event prior to the Great Eruption, barring a strong deceleration event occurring sometime before 1950 (see Section 2.4.3). Assuming constant velocities, there is an approximately 600-year interval between the two most distinct eruptions. If the third eruption is included, then these major mass-loss events have occurred every ∼300 years.

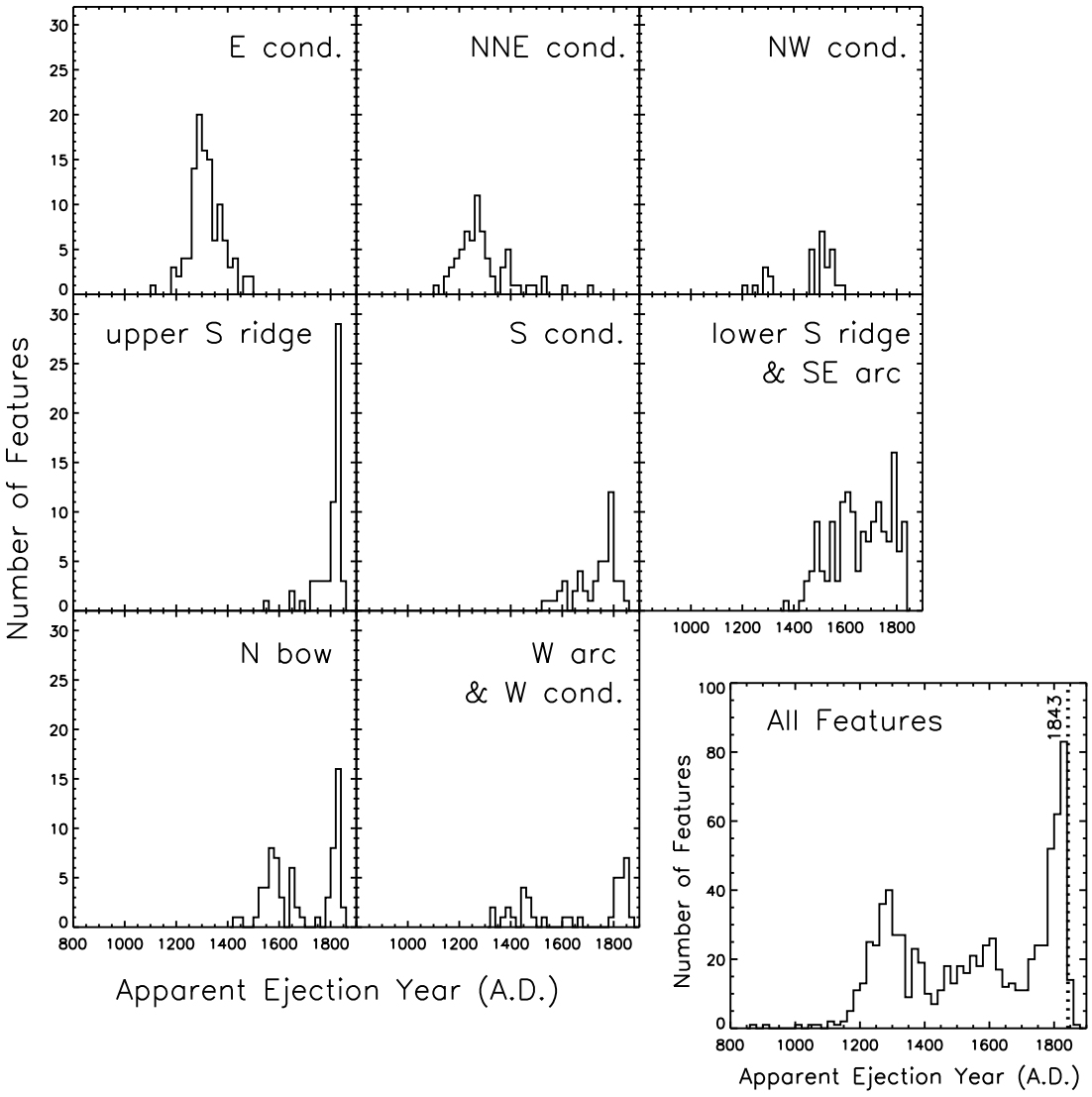

Figure 2.9: Histograms of the apparent ejection dates of η Car's outer ejecta, assuming constant velocity since ejection. The regions are as shown in Figure 2.2. The bottom right panel shows the ejection date histogram for all 792 measured features, with the peak of the Great Eruption in 1843 marked by a dotted line.

2.3.3 Asymmetry and the most distant ejecta

As mentioned above and as shown in Figure 2.7, the reference frame in which we identified and measured ejecta cuts off closer to η Car on the southwest than on any other side, complicating our assessment of asymmetry. We searched the adjacent ACS footprints (which together make up a mosaic of the Tr 16 cluster; see Smith et al., 2010a) for other possible ejecta. As shown in Figure 2.10, we found only four small features moving away from η Car, three to the south and one to the northwest. We were able to measure the proper motions of three of those features, although a relative zero-point uncertainty of several km s^{-1} exists between footprints because of their minimal overlap. For the same reason, there is also a several-pixel (100s mas) uncertainty in distance from the central source.

The knot to the northwest has a transverse velocity of $\sim$ 630 km s^{-1}, giving it an estimated ejection date of 1045 $\pm$ 15 A.D., assuming ballistic motion. The two knots that we were able to measure to the far south are traveling at 460–480 km s^{-1} and date to 900 $\pm$ 30 A.D. The four outer knots could thus come from a smaller, older mass-loss event or events. Given the systemic uncertainties described above, however, we cannot rule out an association with the thirteenth-century event.

Notably, there are no large-scale older ejecta similar to the E condensations on the west side of η Car. It would appear that the eruption in the 1200s was highly asymmetric, perhaps even one-sided, sending substantial mass to the east and northeast but little to no mass in other directions. The Great Eruption, despite producing the bipolar Homunculus, was also significantly asymmetric, ejecting more mass into the extended S ridge than into the distinctly shaped N bow. The sixteenth-century ejecta show some possible bipolarity, but are not aligned with the axis of the Homunculus.

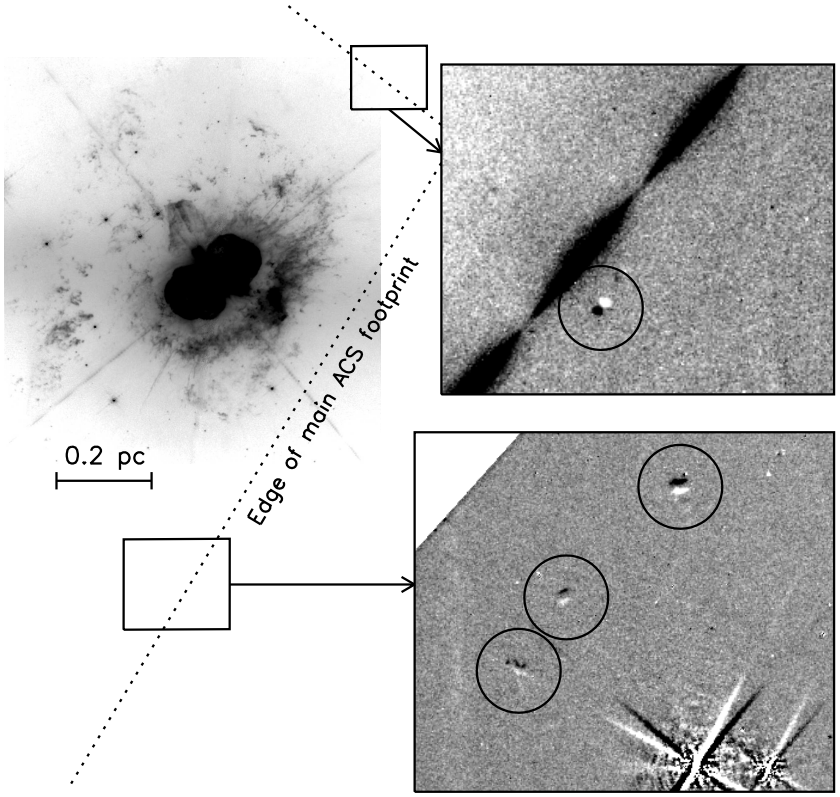

Figure 2.10: Difference images (ACS 2014 − ACS 2005) showing knots identified in images outside the primary observed footprint. The image from Figure 2.1 is shown as a reference; the small boxes indicate where the displayed features are located relative to η Car. The four knots showing motion over the 9-year baseline are circled.

2.4 Discussion

2.4.1 Comparison to radial velocities

To fill out the third dimension of the outer ejecta's motion, we turn to radial velocity studies in the literature. Weis et al. (2001) measured radial velocities of 90 distinct features in the outer ejecta, finding speeds from 100 km s^{-1} (in the SE arc) to 1960 km s^{-1} (in the upper part of the S ridge). The E condensations, the N bow, most of the NNE condensations, and the unnamed material on the east side of the Homunculus—including all of the ejecta that date back to the 1200s—are blueshifted. In contrast, the S ridge, S condensation, SE arc, W arc, W condensation, NW condensation, and some of the material to the far north are redshifted. The Homunculus itself is also aligned in this fashion, with a blueshifted southeast lobe and redshifted northwest lobe, tilted out of the plane of the sky by 48° (e.g., Davidson et al., 2001; Smith, 2006b).

The ejecta from the thirteenth-century eruption are traveling *toward us* at an angle of 20–40° out of the plane of the sky, depending on whether we use the radial velocities of Meaburn et al. (1987) and Smith and Morse (2004) or those of Weis et al. (2001, who present only the highest-magnitude velocities for each feature). The ejecta that appear to date from the 1500s, however, are traveling *away from us*, tilted up to 30° from the plane of the sky. The dividing line between the two proper motion groups on the north side of η Car closely follows the dividing line between blue- and redshifted material seen by Weis et al. (2001). With the intermediate-aged material in a completely different part of three-dimensional space than the oldest ejecta, it becomes much more likely that the intermediate-aged features are from a distinct eruption rather than the result of past acceleration/deceleration from ejecta interactions.

2.4.2 Relationship to X-ray emission and the extremely fast ejecta

η Car is encircled by an elongated partial ring or shell of soft X-ray emission that extends from just south of the S condensation, over the W arc, and around to the

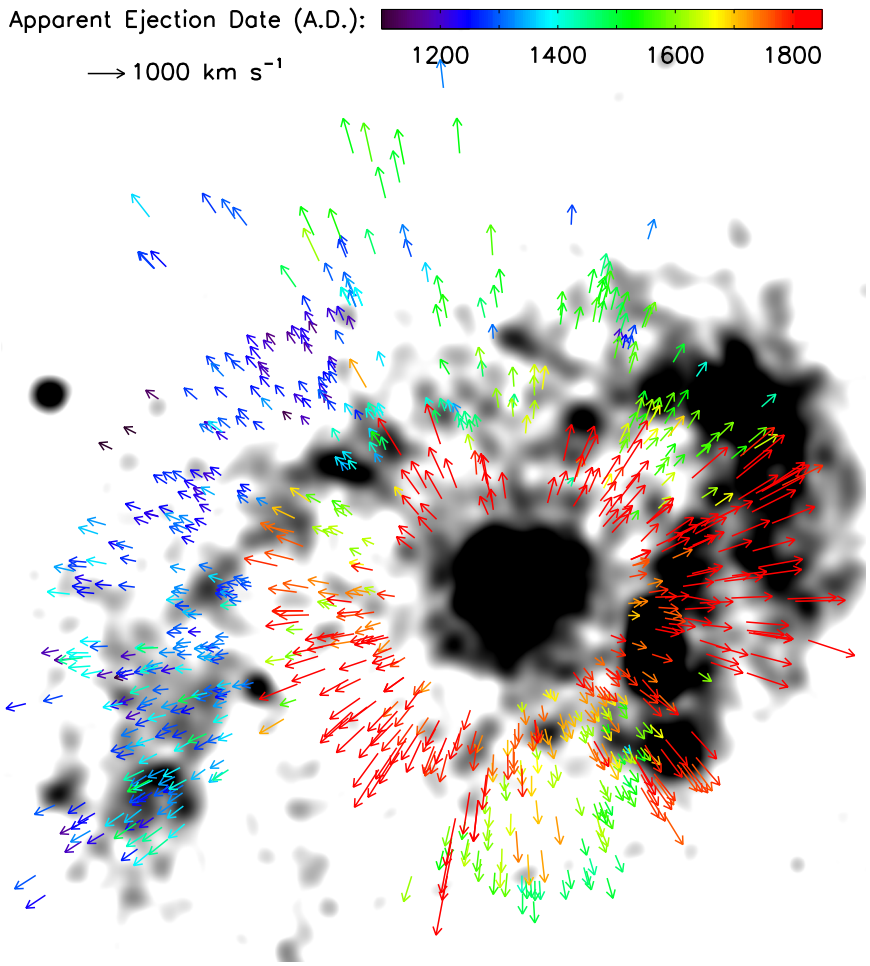

Figure 2.11: Similar to Figure 2.7, with the scaled and color-coded proper motion vectors overplotted on a soft X-ray *Chandra* image of η Car and its surroundings. This X-ray image (Seward et al., 2001) covers the energy range 0.5–1.5 keV and was adaptively smoothed as in Smith and Morse (2004).

E condensations (Chlebowski et al., 1984; Seward et al., 2001). Figure 2.11 shows a *Chandra X-ray Observatory* image of η Car and its surroundings (Seward et al., 2001), with the proper motion velocity vectors for the optical ejecta plotted on top. The X-ray shell has roughly the same axis orientation as the Homunculus, but has a notable gap to the south and southeast.

The spatial association between the soft X-ray shell and the optical features in the outer ejecta has led to a broad consensus that the X-ray emission is the result of shock heating from ejecta interactions (Chlebowski et al., 1984; Corcoran et al., 1998; Seward et al., 2001; Weis et al., 2001; Smith and Morse, 2004). The strongest soft X-ray emission is coincident with the S condensation, upper S ridge, and W arc, where we have measured a mix of ages for the dense optical ejecta. Extremely fast ejecta, with radial speeds of up to $\sim$ 3000 km s^{-1}, have been detected close to the E condensations and coincident with the X-ray shell (Smith and Morse, 2004; Smith, 2008). As described in Section 2.2.2, this very fast material, originating from the Great Eruption in the nineteenth century, is Doppler-shifted out of the narrowband filters used here and is not detected in our images. It is presumably interacting with or approaching the denser, slower blobs measured in this paper. Additional spectral mapping of the outer ejecta is needed to explore the full distribution of the high-velocity material and its relationship to the soft X-ray emission.

Given the limits on the deceleration that we measured for the knots in the E condensations, we can roughly estimate their relative density compared to the very fast ejecta. Over 21 years of *HST* observations, the features in the E condensations change velocity by an average of -0.1 $\pm$ 1.2 km s^{-1} yr^{-1} (consistent with zero). Assuming that the collision between ejecta is fully inelastic and that momentum is conserved, the observed E condensations are thus 10–10^4 times denser than the impacting very fast ejecta, depending on the timescale over which the fast ejecta decelerate.

Returning to Figure 2.11, note that there is no spatial correlation between the sixteenth-century ejecta and the soft X-ray emission. The SE arc falls in the X-ray gap, and the northern ejecta lie outside the X-ray shell altogether. If the inter-

mediate ages of these ejecta were the result of interaction between the thirteenth- and nineteenth-century ejecta, we would expect to see strong X-ray emission from the location of these interactions. We would also expect there to be apparently sixteenth-century ejecta around the E blobs, where very fast ejecta are observed to be hitting the thirteenth-century material. We observe neither of these things, further strengthening the case that there was a distinct eruption in the 1500s.

2.4.3 Alternate ejection histories

In our analysis, we have found approximate ejection dates by assuming that there was no substantial, large-scale deceleration (or acceleration) of the outer ejecta prior to their first detection in 1950. η Car is surrounded by a "cocoon" of less-nitrogen-rich material, likely from pre-eruption mass loss (Smith and Morse, 2004). Here, we explore the hypothesis that all of the observed outer ejecta were decelerated early in their history as they encountered this material, then tapered to their current coasting velocities as the density of the cocoon diminished with radius. In this case, the ejection dates of all the knots move later and closer together. The true timescale between eruptions could then be closer to 100–200 years instead of 300 years. However, our main result, the detection of multiple major mass-loss events in η Car's history, is unaffected. That is the most straightforward scenario to explain our observations.

The most extreme alternate ejection history—that all of the observed outer ejecta date to the Great Eruption of the 1840s, but suffered different amounts of deceleration with an asymmetric wind—is much less likely. It requires a complex pre-existing configuration of mass to decelerate the observed outer ejecta such that they reach their current coasting velocities at their current distances from η Car. A spherically symmetric distribution of pre-eruption circumstellar material (e.g., a stellar wind with a r^{-2} density profile) could not have produced the different coasting velocities seen at the same radii from the star. Compare, for example, the NNE and NW condensations: although both are $\sim$25″ from η Car, the average proper motion of the NNE knots is 380 km s^{-1} while the NW knots are moving at 550 km s^{-1}.

The E condensations provide a particularly firm constraint, as they are already 19–23″ from the central star in the Thackeray (1950) images. To reach that distance by 1950 with an origin in the 1840s would require a minimum initial projected speed of ∼2000 km s^{-1}. The measured projected speeds of the E condensations over the past two decades are 350–600 km s^{-1}. If these features were ejected in the 1840s, there is no way for them to have reached the observed separation from η Car and yet have their current, relatively low speeds without invoking a dense shell located close to their 1950 positions. One could then posit additional pre-existing partial shells that would have decelerated the NW and SE condensations to their present-day coasting velocities. This scenario would still require substantial and episodic prior mass-loss events. It would have much the same consequences for η Car's eruptive history, except it would indicate that the star's surface nitrogen enhancement took place recently, between the older shell-producing events and the 1840s Great Eruption.

From an energy standpoint, we know the Great Eruption did produce ejecta with velocities of 1000 km s^{-1} or more; they are seen in spectra of the equatorial plane of the Homunculus and of near or inside the soft X-ray shell (Smith, 2008). However, as discussed in Section 2.4.2, some of these very fast ejecta are coincident with and appear to be running into the E condensations, likely powering the observed soft X-ray shell. There is no clear mechanism by which two sets of mass should reach the same projected distance over the same time yet have present-day speeds that differ by a factor of ten. Furthermore, the ejection of all of the dense outer ejecta at 1000 km s^{-1} or more would require a dramatic upward revision of the estimated energy budget of the Great Eruption. The discovery of the very fast ejecta roughly doubled the Great Eruption's energy budget (Smith, 2008), and that number assumed that the 3000 km s^{-1} material was about a factor of ten less dense than the slower, named ejecta. (Note that this agrees with our rough estimate of the density ratio in Section 2.4.2.) The explosive amount of kinetic energy required to eject several solar masses of outer ejecta at these speeds approaches that of a core-collapse supernova.

2.4.4 Implications for models of η Car

The proper motions of the outer ejecta thus confirm that η Car has undergone at least two and probably three major mass-loss events over the last millennium, including the nineteenth-century Great Eruption. These results raise a number of interesting questions that are as yet unanswered by existing theories: What mechanism drives these repeating eruptions? Why do they repeat on a several-hundred-year timescale, much longer than the 5.5-year binary orbit? Why was the thirteenth-century eruption so one-sided? Why does the Homunculus have a clear bipolar symmetry that past eruptions lack? Models of η Car's behavior must not treat the Great Eruption in isolation, but should aim to account for all of the observed characteristics of the prior eruptions.

In single-star models (i.e., those in which the companion star plays no significant role), η Car's eruptions are considered to be continuum-driven super-Eddington wind events, where the extra luminosity arises from as-yet-unidentified mechanisms (Davidson and Humphreys, 1997; Owocki et al., 2004). However, it is difficult for a single-star model to explain the observed asymmetry in the outer ejecta and the changes in mass-loss symmetry with time. What could cause a single star to produce the highly one-sided mass loss of the thirteenth-century eruption, then eject the axisymmetric Homunculus several centuries later?

Current models involving a binary or higher-order multiple system may get us closer, but also have difficulty explaining the observed historical mass loss. The time between major eruptive events is much longer than the orbital period of the current binary (5.54 years, Damineli, 1996). If the eruptions are influenced by periastron interactions (Cassinelli, 1999; Soker, 2007; Kashi and Soker, 2010; Smith, 2011), these interactions must be suppressed for long periods of time. Models that invoke a one-time catastrophic event such as a merger (Gallagher, 1989; Iben, 1999; Morris and Podsiadlowski, 2009; Podsiadlowski, 2010; Portegies Zwart and van den Heuvel, 2016) or a dynamical exchange (Livio and Pringle, 1998) require additional unexplained complexities to ac-

count for these repetitive yet discrete events separated by centuries.

The lack of older, more distant outer ejecta rules out additional major mass-loss events prior to the thirteenth century. Bohigas et al. (2000) claimed to detect a much older (10^4 yr) bipolar shell, but this was interpreted by Smith et al. (2005a) as η Car's astropause, modified by the wind of a nearby Of star, as it lacks the nitrogen-rich chemistry or clumpy structure of the other outer ejecta. What, then, caused η Car's eruptive behavior to start in the 1200s? The apparently sudden initiation of mass ejections is probably an important clue, and is another key constraint for models.

An added complication in the story of η Car is the 1890s Lesser Eruption, in which a much smaller amount of mass (0.1 $M_\odot$; Ishibashi et al., 2003; Smith, 2005) was ejected with the same geometry as the Homunculus. Secondary eruptions of this sort, occurring several decades after a major outburst, have been observed in P Cygni and some of the other known eruptive LBVs (Humphreys et al., 1999). Our data are not sensitive to similar small eruptions in the decades after the larger thirteenth- and sixteenth-century events.

2.5 Conclusions

We have aligned eight epochs of *HST* imaging (both WFPC2 and ACS) of η Car's outer ejecta to the same distortion-corrected reference frame and measured the proper motions of 792 ejecta features, many for the first time. We achieve unprecedented time coverage, with each feature measured in up to 16 baselines over 21 years, as well as unprecedented velocity precision (few km s^{-1}) and spatial resolution for these features.

All 792 features measured in η Car's outer ejecta have transverse velocities pointing nearly directly away from the star. The majority have proper motions of 300–600 km s^{-1}, although some are as fast as 1500 km s^{-1}. The fastest-moving material is found in the large feature known as the S ridge and in the broadly jet-shaped N bow. Both date back to η Car's Great Eruption in the 1840s or to a few decades

prior.

Over the 21 years of data, we see no evidence for large-scale acceleration or deceleration of any of the outer ejecta: 94% of the knots are consistent with moving at constant velocity over that time. Comparison to images from 1949–1950 support ballistic motion over a longer time period. Under the assumption of constant velocity, we find that the material in and around the E and NNE condensations was ejected in the mid-1200s A.D., give or take 50–100 years. With the exception of three small knots to the far south of η Car and one to the northwest, the ejecta dating to the mid-1200s are all found to one side of the central star and are blueshifted.

We also see evidence of a third, intermediate eruption that occurred in the sixteenth century. Ejecta dating to the mid-1500s are found in the SE arc, the W condensation, and in and around the NW condensation. From proper motions alone, we cannot rule out that this intermediate date peak is the result of newer ejecta from the Great Eruption hitting the older material from the 1200s. However, the radial velocities of these features place them in a different part of three-dimensional space from the thirteenth-century ejecta. The lack of X-ray emission over the SE arc and the features to the far north also indicates a lack of strong interaction between ejecta at those spots.

In summary, we have shown with distance-independent measurements that η Car erupted at least once, likely twice, before its Great Eruption in the 1800s. Models for this still-enigmatic star must therefore explain the recurrence of these major mass-loss events, along with their several-hundred-year timescale and their various asymmetries.

CHAPTER 3

PROPER MOTIONS OF FIVE OB STARS WITH CANDIDATE DUSTY BOW SHOCKS IN THE CARINA NEBULA[†]

We constrain the proper motions of five OB stars associated with candidate stellar wind bow shocks in the Carina Nebula using *HST* ACS imaging over 9–10 year baselines. These proper motions allow us to directly compare each star's motion to the orientation of its candidate bow shock. Although these stars are saturated in our imaging, we assess their motion by the shifts required to minimize residuals in their Airy rings. The results limit the direction of each star's motion to sectors less than 90° wide. None of the five stars are moving away from the Carina Nebula's central clusters as runaway stars would be, confirming that a candidate bow shock is not necessarily indicative of a runaway star. Two of the five stars are moving tangentially relative to the orientation of their candidate bow shocks, both of which point at the OB cluster Trumpler 14. In these cases, the large-scale flow of the interstellar medium, powered by feedback from the cluster, appears to dominate over the motion of the star in producing the observed candidate bow shock. The remaining three stars all have some component of motion toward the central clusters, meaning that we cannot distinguish whether their candidate bow shocks are indicators of stellar motion, of the flow of ambient gas, or of density gradients in their surroundings. In addition, these stars' lack of outward motion hints that the distributed massive-star population in Carina's South Pillars region formed in place, rather than migrating out from the association's central clusters.

[†]This chapter has been previously published as Kiminki et al. (2017).

3.1 Introduction

Feedback from massive stars impacts their surroundings on scales ranging from the shaping of their immediate circumstellar environment to the reionization of the Universe. Stellar wind bow shocks, falling on the former end of that scale, provide important information about a star's history and environment. Bow shocks are produced when the relative velocity between a star and the surrounding interstellar medium (ISM) is supersonic (Baranov et al., 1971; van Buren and McCray, 1988). They typically appear as arc-shaped features in optical line emission (e.g., Kaper et al., 1997; Bally et al., 2000; Brown and Bomans, 2005; Brownsberger and Romani, 2014) and/or thermal infrared continuum emission from dust (e.g., van Buren et al., 1995; Noriega-Crespo et al., 1997; Comerón and Pasquali, 2007; France et al., 2007; Gáspár et al., 2008; Peri et al., 2012; Winston et al., 2012; Kobulnicky et al., 2016). These features mark the sweeping-up of ambient material between the stellar wind termination shock and a second shock from the supersonic motion. The orientation of the bow shock arc depends on the direction of the relative motion, although it can be skewed by density gradients in the environment (Wilkin, 2000). The arc's standoff distance from the star depends on the pressure balance between the stellar wind and the ISM and hence on the magnitude of their relative motion and the density of the ISM. Bow-shock-like structures may also be produced where dust in a photoevaporative flow is stalled by radiation pressure rather than the stellar wind (Ochsendorf et al., 2014a,b; Ochsendorf and Tielens, 2015; Ochsendorf et al., 2015). The asymmetric stellar wind bubbles of slower-moving stars may also have a similar appearance in the mid-infrared (Mackey et al., 2015, 2016).

Arc-shaped structures around massive stars have commonly been considered a marker of high stellar velocities, under the assumption that the relative motion between star and ISM is dominated by the absolute motion of the star (van Buren et al., 1995; Kaper et al., 1997; Gvaramadze and Bomans, 2008; Gvaramadze et al., 2010; Kobulnicky et al., 2010; Gvaramadze et al., 2011a,b). The typical velocity of an O-type star relative to its surroundings is ~ 10 km s^{-1} (Blaauw,

1961; Cruz-González et al., 1974; Gies and Bolton, 1986; Tetzlaff et al., 2011), comparable to the speed of sound in an H II region, but 20–30% of O-type stars are "runaways" with velocities $\gtrsim 40$ km s^{-1} (Blaauw, 1961; Cruz-González et al., 1974; Stone, 1991; Tetzlaff et al., 2011). The high speeds of runaway stars are imparted through dynamical interactions in a cluster (Poveda et al., 1967; Gies and Bolton, 1986; Fujii and Portegies Zwart, 2011), through the disruption of a binary system when the companion star explodes as a supernova (Blaauw, 1961), or through a two-step scenario involving both processes (Pflamm-Altenburg and Kroupa, 2010). Runaways make up 50–100% of field O-type stars, the O-type population found outside clusters and associations (de Wit et al., 2005; Schilbach and Röser, 2008; Gvaramadze et al., 2012).

The question of whether all field O-type stars are runaways, or whether a small fraction formed in isolation, is of key importance to our understanding of massive star formation. The monolithic collapse model (McKee and Tan, 2003; Krumholz et al., 2005b, 2009) permits truly isolated massive star formation, albeit rarely, while the competitive accretion model (Zinnecker, 1982; Bonnell et al., 2001a,b, 2004) requires that massive stars form exclusively in clusters. In observational studies, the presence of a bow shock or candidate bow shock is sometimes taken as a clue that a given massive field star did not form in situ. For example, HD 48229 and HD 165319 were part of the 4 ± 2% of all O-type stars identified by de Wit et al. (2004, 2005) as likely candidates for isolated massive star formation. Bow shocks were later discovered around both sources (Gvaramadze and Bomans, 2008; Gvaramadze et al., 2012), calling into question their origins in the field.

While 70% of bow shocks and bow-shock-like structures are located in relatively isolated environments consistent with runaway stars (Kobulnicky et al., 2016), the rest are found around OB stars in clusters and associations. These stars have sometimes been interpreted as runaway interlopers from other regions (Gvaramadze et al., 2011b). However, the assumption that the motion of the ambient ISM is negligible relative to that of the star may not always be valid, particularly in and around giant H II regions. In many cases, bow shock orientations

suggest that feedback-driven ISM flows are relevant. Povich et al. (2008) observed that bow shocks in the massive star-forming regions M17 and RCW 49 are oriented toward those regions' central clusters, suggesting that global expansion of the H II regions is the dominant component of the relative star–ISM velocity. Similarly, several bow shocks in Cygnus OB2 point toward the association's interior (Kobulnicky et al., 2010), as do more than half of the candidate bow shocks in the Carina Nebula (Smith et al., 2010c; Sexton et al., 2015). The Galactic Plane survey of Kobulnicky et al. (2016) found that roughly 15% of infrared bow shocks are pointed at H II regions, while another 8% face bright-rimmed clouds; they also noted that bow shock orientations are correlated on small scales, indicative of the influence of external forces. Povich et al. (2008) refer to such feedback-facing bow shocks as "interstellar weather vanes," tracing photoevaporative flows off local dense gas and/or large-scale gas motions driven by cluster feedback. Kobulnicky et al. (2016) call them "in-situ bow shocks," reflecting their origin around presumably non-runaway OB stars.

When the motion of the star dominates over the motion of the surrounding ISM, as it does for runaway stars, the bow shock is expected to point in the direction of the star's motion. van Buren et al. (1995) surveyed bow shocks around known runaway stars and found that the bow shocks were preferentially aligned with their host stars' proper-motion vectors. However, they used proper motions measured in an absolute reference frame, not corrected for Galactic rotation and solar peculiar motion and thus not necessarily representative of a star's motion relative to the surrounding ISM. More recent surveys by Peri et al. (2012, 2015), again of bow shocks around known runaways stars, did correct proper motions for Galactic rotation and noted a similar, albeit qualitative, tendency for alignment. Individual runaway stars are also often observed to be moving in the direction of their bow shocks (e.g., Moffat et al., 1998, 1999; Comerón and Pasquali, 2007). But what about bow shock around stars that have not already been identified as runaways? Kobulnicky et al. (2016) compiled a sample of bow shocks without any selection on their host stars' kinematics. They found that more than 50% of the host stars with

significant measured proper motions had velocity–bow shock misalignments of more than 45°, although again, they were working with absolute proper motions rather than local. The relationship between stellar motion and bow shock orientation for stars in clusters and associations remains largely unexplored.

To further investigate this relationship, we measure *local* proper motions for five massive stars in the Carina Nebula (listed in Table 3.1), each of which is associated with a candidate bow shock from Sexton et al. (2015, which includes objects first identified by Smith et al. 2010c). Smith et al. (2010c) and Sexton et al. (2015) identified a total of 39 "extended red objects" (EROs) in the Carina Nebula. These EROs exhibit extended, often arc-shaped, morphology in *Spitzer* Infrared Array Camera (IRAC) 8.0 μm images. Nine of the Sexton et al. (2015) EROs are clearly resolved arcs and are classified as morphological bow shock candidates; one of our stars (ALS 15206) is associated with one of these sources (ERO 2). Another eight of the Sexton et al. (2015) EROs lack resolved morphologies at 8.0 μm but have infrared colors that rule out emission from young stellar objects (YSOs) and polycyclic aromatic hydrocarbons (PAHs). The remaining four of our stars are associated with sources in this category, known as color bow shock candidates.

Our five target stars reside in the Carina Nebula: their visual magnitudes (see Table 3.1), spectral types, and extinctions (Povich et al., 2011b) confirm that they are unlikely to be foreground or background objects. The Carina Nebula is home to nearly 70 O-type and evolved massive stars (Smith, 2006a), including some of the earliest known O-type stars (Walborn et al., 2002b) and the luminous blue variable η Carinae (Davidson and Humphreys, 1997). At 2.3 kpc (Smith, 2006b), it is one of the closest and least-extincted massive star-forming regions. Its two central clusters, Trumpler (Tr) 14 and Tr 16, contain about half of its massive-star population. The rest is spread across $\sim$30 pc, mostly in a region of ongoing star formation known as the South Pillars (Smith et al., 2000). Emission-line profiles show that feedback from the central clusters is driving the expansion of multiple shells of ionized gas (Damiani et al., 2016), resulting in a global expansion of the H II region at $\pm$15–20 km s^{-1} (Walborn and Hesser, 1975; Walborn et al., 2002a, 2007). It is easy to envi-

Table 3.1: *HST* data log.

ERO No.[a]	Star ID	R.A. (J2000)	Dec. (J2000)	Spectral type	V (mag)	ACS field	Date 1	Exp. time 1 (s)	Date 2	Exp. time 2 (s)
2	ALS 15206	10:44:00.9	-59:35:46	O9.2 V[b]	10.7[d]	TR14	2005 Jul 17	2 × 500	2015 Jun 28	2 × 520
23	TYC 8626-2506-1	10:44:30.2	-59:26:13	O9 V[b]	10.9[e]	TR14	2005 Jul 17	2 × 500	2015 Jun 28	2 × 520
24	CPD-59 2605	10:44:50.4	-59:55:45	B1 V[c]	11.1[f]	POS27	2006 Mar 18	2 × 500	2015 Mar 12	2 × 560
25	HDE 305533	10:45:13.4	-59:57:54	B1 V[a]	10.6[f]	POS26	2006 Mar 16	2 × 500	2015 Mar 12	2 × 560
31	HD 93576	10:46:53.8	-60:04:42	O9.5 IV[b]	9.6[d]	POS20	2006 Mar 15	2 × 500	2015 Mar 11	2 × 455

[a]From Sexton et al. (2015).
[b]From Sota et al. (2014).
[c]From Vijapurkar and Drilling (1993).
[d]From Reed (2003).
[e]From Høg et al. (2000).
[f]From Massey and Johnson (1993).

sion that the inward-facing orientations of many of Carina's candidate bow shocks are the result of this supersonic, feedback-driven ISM expansion (Sexton et al., 2015) or that they are shaped by interaction with dense photoevaporative flows. Here, we explore whether those interpretations are valid and to what degree these bow shocks are shaped by the motion and structure of the ISM versus the motion of their driving stars.

The organization of this paper is as follows: In Section 3.2, we describe our multi-epoch *Hubble Space Telescope* (*HST*) observations, our image alignment procedure, and our method for measuring proper motions. We present our results and compare the stellar motions to the orientations of their associated bow shock candidates in Section 3.3. Section 3.4 discusses the implications and limitations of our results, and Section 3.5 summarizes our conclusions.

3.2 Observations and Analysis

3.2.1 *HST* ACS imaging

We have conducted a large-scale multiepoch survey of the Carina Nebula using the Wide Field Camera (WFC) of *HST*'s Advanced Camera for Surveys (ACS). All observations were made with the F658N filter, which captures emission from Hα and [N II] λ6584. Our imaging coverage is shown in Figure 3.1, where each small rectangle is one orbit made up of three overlapping pairs of `CR-SPLIT` exposures. Orbital pointings were designed to target features of particular interest in star formation (pillars, Herbig-Haro objects, etc.) as well as the central Tr 14 and Tr 16 clusters. The pointings in Figure 3.1 are labelled according to their designations in the *HST* data archive.

The first epoch of our ACS observations was taken in 2005–2006 (GO-10241 and GO-10475, PI: N. Smith; see Smith et al. 2010a). The same set of observations was repeated in 2014–2015 (GO-13390 and GO-13791, PI: N. Smith). This second epoch was designed to replicate the first as closely as possible in pointing and position angle in order to minimize position-dependent systemic errors when measuring proper

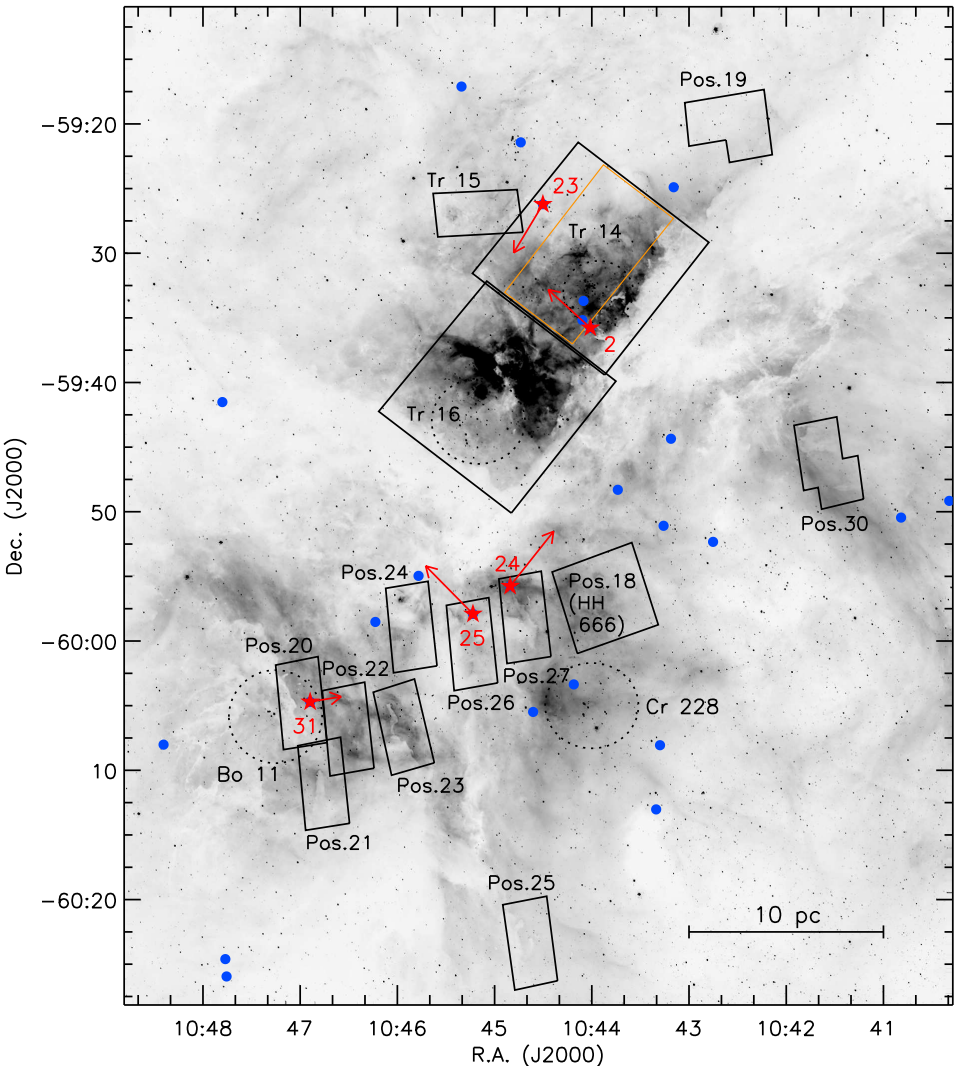

Figure 3.1: Ground-based Hα image of the Carina Nebula from Smith et al. (2010a), with the positions of our *HST* ACS fields outlined in black and labelled by their designations in the *HST* data archive. All fields were observed twice, with a 9–10 year baseline between epochs. The orange box indicates the portion of our Tr 14 mosaic that could not be re-observed at the same position angle due to changes in the *HST* Guide Star Catalog between epochs. Extended red objects (EROs) from Sexton et al. (2015) that fall inside our fields are marked with red stars and labeled with their ERO number; the red arrows show their measured proper motions (Section 3.3) scaled to a travel time of 10^5 yr. The blue filled circles are EROs from Sexton et al. (2015) that fall outside our *HST* fields. The approximate positions of the primary central clusters, Tr 14 and Tr 16, are outlined with dashed circles, as are the positions of Bochum 11 and Collinder 228, two smaller clusters in the South Pillars region.

motions. Owing to changes in the *HST* Guide Star Catalog between epochs, we were unable to duplicate the orientation angle of the central segment of the Tr 14 mosaic (marked in orange in Figure 3.1) and of Positions 25 and 30. Those observations were rotated by ∼180°.

Also marked in Figure 3.1 are the locations of EROs from Sexton et al. (2015). Our survey serendipitously imaged the stars associated with seven EROs. However, as discussed below, we were unable to constrain the proper motions of the two ERO-associated stars in the central part of the Tr 14 mosaic (the part for which the orientation angle changed beween epochs), leaving us with a sample of five. Full details of the observations of each of these five stars are given in Table 3.1.

3.2.2 Image alignment and stacking

Our image alignment procedure, which adapts the methods of Anderson et al. (2008a,b), Anderson and van der Marel (2010), and Sohn et al. (2012), is described in detail in Reiter et al. (2015a,b) and Kiminki et al. (2016). In summary, we find the positions of uncrowded, unsaturated stars in individual exposures and use those positions to relate each image to a master, distortion-free reference frame. We use the program `img2xym_WFC.09x10` (Anderson and King, 2006), which uses an array of effective point spread functions (PSFs) and has the option to fit a spatially constant perturbation PSF to account for telescope breathing and other focus changes. The measured stellar positions were then corrected for geometric distortion (Anderson, 2006).

A master reference frame with a pixel scale of 50 mas was constructed for each orbital pointing, aligned with north in the $+y$ direction. The six overlapping images from each epoch of a given pointing were stacked into two reference-frame master images (one per epoch) using the stacking algorithm of Anderson et al. (2008b). Object positions in the master images are directly comparable between epochs to an alignment accuracy of approximately 1 mas (~ 1 km s^{-1} over a 9–10 year baseline at the distance of the Carina Nebula). We found that including a perturbation PSF in fitting stellar positions did not improve the alignment precision, but we address

other possible effects of *HST* focus changes in Section 3.2.3.

In all cases, the master reference frames are not tied to an absolute proper-motion zero point. Instead, the zero point is based on the average motion of several hundred well-measured stars in the image. In other words, the bulk motion of the Carina Nebula is removed, as are smaller differences in the large-scale motion of Carina's clusters and subclusters. Features that are locally stationary, like bow shocks, are expected to be stationary in our reference frames, allowing direct measurement of the motion of stars relative to their surroundings.

3.2.3 Measuring local proper motions of saturated stars

With the images from two epochs on the same reference frame, measuring local proper motions for unsaturated stars in our stacked images is as simple as comparing their PSF-derived positions between epochs. However, most of the OB stars observed, including those associated with candidate bow shocks, are saturated in our ACS images (which were all ∼500 s long). We were unable to reconstruct the PSF core to perform traditional astrometry. Instead, we used the positions of the extended Airy rings, which are clearly visible for these stars in these deep, high-resolution images. The left column of Figure 3.2 shows the first-epoch image of all five ERO-associated stars for which we measured proper motions.

As marked in Figure 3.2, we identified four regions in the outer PSF of each star, avoiding diffraction spikes, saturation bleeding, and close companions. We then found the pixel offset in x (west-east) and y (north-south) by which the first epoch needed to be shifted in order to minimize the sum over those four regions of the absolute value of the flux difference between epochs. The best-fit offset was computed using the `AMOEBA` algorithm, the IDL implementation of the downhill simplex function minimization method (Nelder and Mead, 1965; Press et al., 1992). `AMOEBA` requires an input estimate. As recommended by Press et al. (1992), we run the algorithm twice, giving it a random starting estimate on the first run and then starting the second run at the best-fit parameters of the first. The resulting best-fit difference images (unshifted second epoch minus best-fit shifted first epoch) are

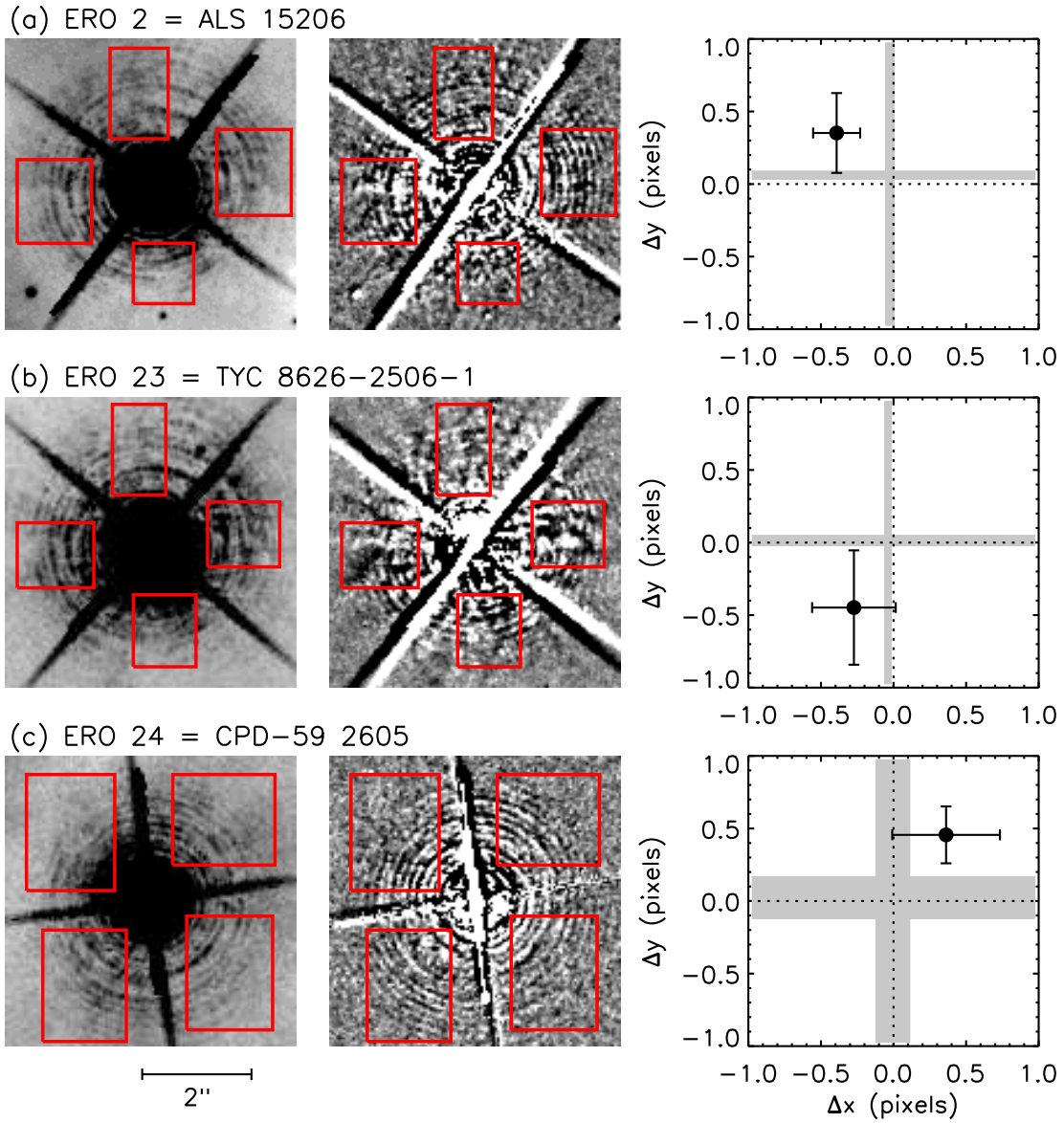

Figure 3.2: Left: first-epoch ACS F658N images of five stars associated with candidate bow shocks in the Carina Nebula. The red boxes mark the sections of the Airy rings used for fitting the offset between epochs. Middle: best-fit difference images (unshifted second epoch minus best-fit shifted first epoch) for each star. Right: best-fit pixel offset between epochs with a 9–10 year baseline. The gray shaded regions mark the space of possible apparent offsets due to focus changes.

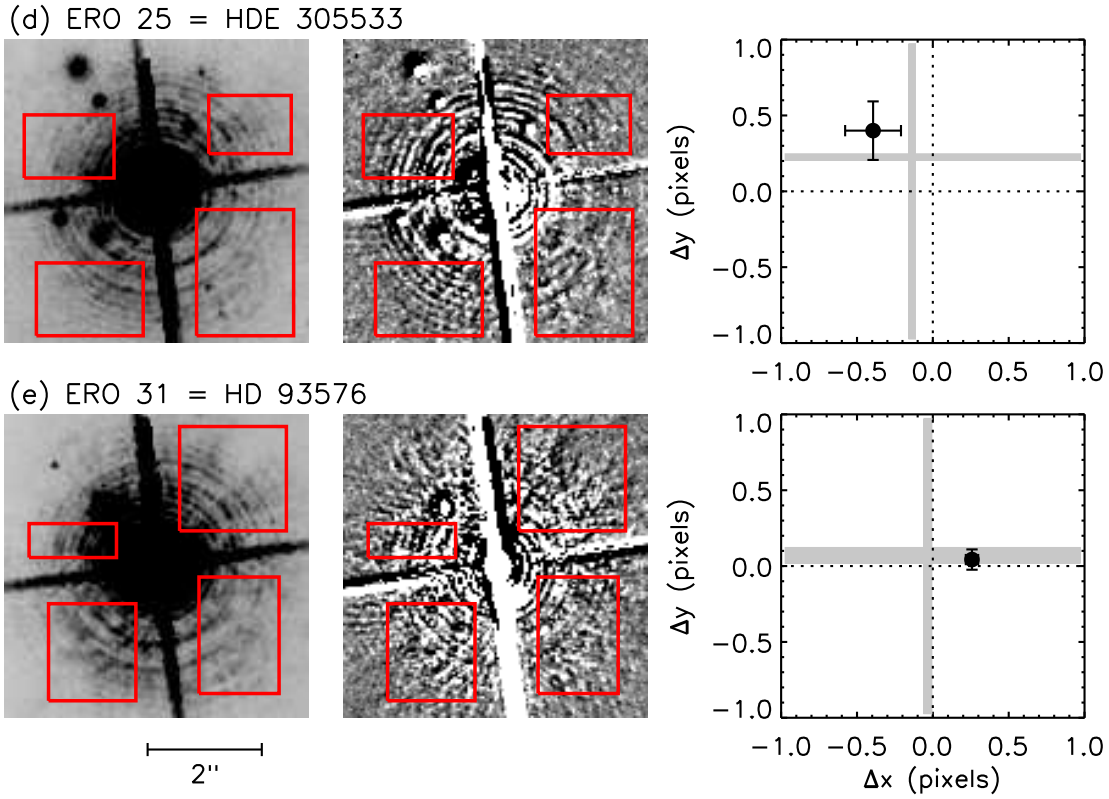

Figure 3.2: Continued.

shown in the middle column of Figure 3.2. Although the Airy rings do not disappear completely in the difference images, there are no systematic differences in residual flux between quadrants. The best-fit offset for each star, in pixels over the 9–10 year baseline, is plotted in the right column of Figure 3.2.

This method does not produce accurate results for saturated stars in fields that experienced significant rotation between epochs. The asymmetry of the ACS WFC PSF (Anderson and King, 2006; Mahmud and Anderson, 2008) causes the flux distribution in the outer PSF to be orientation-dependent. When the fields are rotated into alignment, the asymmetric flux distribution introduces an apparent shift of up to several pixels. Consequently, as mentioned in Section 3.2.1, we were unable to measure the true shifts of the two ERO-associated stars in the central part of our Tr 14 mosaic (see Figure 3.1). These stars were removed from further analysis and are not shown in Figure 3.2; our final sample consists of the five ERO-associated stars listed in Table 3.1.

To characterize the uncertainties in our fits, we ran several different tests. First, we adjusted the size and placement of the boxes used to calculate the residuals, then refit. These adjustments proved to have a negligible effect on the resulting best-fit offset. Second, we repeated the full fitting process 100 times and measured the standard deviation among the results. These ranged from 0.03 to 0.4 pixels depending on the star. Finally, we applied 100 random $[x,y]$ offsets to the first-epoch images and repeated the full fitting process again for each, to determine how well we could recover the expected (artificial + true) offsets. The standard deviation in the offsets recovered via this approach ranged from 0.04 to 0.23 pixels. For each star, we adopt the greater of the two uncertainty values as the formal uncertainty.

Changes in *HST* focus from both short-term thermal breathing and long-term non-thermal effects (e.g., Cox and Lallo, 2012) could induce an apparent offset between epochs by redistributing flux in the PSF. To evaluate the magnitude of this effect, we downloaded a Tiny Tim model PSF (Krist et al., 2011) for each star, at its observed chip position, for the appropriate focus value taken from the *HST* focus model (di Nino et al., 2008; Niemi and Lallo, 2010; Cox and Niemi, 2011). The true

shift between "epochs" of Tiny Tim models is zero, so any measured shift would be a false positive. We ran the pair of Tiny Tim models for each star through our fitting procedure and measured apparent offsets of 0.035 to 0.22 pixels, which are illustrated by the shaded gray regions in the third column of Figure 3.2. In most cases, the focus-induced shifts are small and/or distributed roughly evenly about the origin. For HDE 305533 (ERO 24), however, the focus changes induced a systematic $-x, +y$ offset. Removing this shift would reduce the magnitude of the observed proper motion of HDE 305533 by roughly half, but would have only a small effect on its direction of motion.

3.3 Results

As the plots in the right column of Figure 3.2 demonstrate, each of the five stars associated with candidate bow shocks traveled no more than ∼0.5 pixels (25 mas) in any direction over their 9–10 year baselines. The measured pixel offsets are given in Table 3.2 along with the corresponding proper motion components, the total transverse velocity, and the position angle of the proper motion vector. The best-fit local transverse velocities range from 16 to 35 km s^{-1}; the red arrows in Figure 3.1 show the expected travel distances over 10^5 yr. However, the uncertainties on most of the measured velocities are relatively large: most of the stars have motion consistent with zero within 1–2 σ. Only HD 93576 has motion significant at the 3σ level, in the x direction, although it has negligible y (north–south) motion. We argue in Section 3.4.1 below that the true proper moions are likely on the smaller side of the allowed ranges. Even so, the results for all five stars constrain their directions of motion to sectors less than 90° wide.

In Figure 3.3, we compare the local proper motions of the stars to the orientations of their associated candidate bow shocks. The latter were determined by Sexton et al. (2015) based on the peaks of the 8.0 μm flux. (ERO 25, associated with HDE 305533, does not have a measured orientation.) In these three-color *Spitzer* IRAC images, the candidate stellar wind bow shocks appear as extended

Table 3.2: Local proper motions of stars associated with candidate bow shocks.

ERO No.	Star ID	δx (pixels)	δy (pixels)	$\mu_\alpha \cos\delta$ (mas yr^{-1})	μ_δ (mas yr^{-1})	v_T[a] (km s^{-1})	Position angle (deg E of N)
2	ALS 15206	-0.39 (0.16)	0.35 (0.28)	2.0 (0.8)	1.8 (1.4)	29 (17)	48 (25)
23	TYC 8626-2506-1	-0.27 (0.29)	-0.45 (0.39)	1.4 (1.4)	-2.3 (2.0)	29 (27)	149 (35)
24	CPD-59 2605	0.36 (0.37)	0.46 (0.20)	-2.0 (2.1)	2.5 (1.1)	35 (25)	322 (31)
25	HDE 305533	-0.39 (0.18)	0.40 (0.19)	2.2 (1.0)	2.2 (1.1)	34 (16)	45 (19)
31	HD 93576	0.26 (0.04)	0.04 (0.07)	-1.4 (0.2)	0.2 (0.4)	16 (5)	279 (15)

Uncertainties for each quantity are listed in parentheses.

[a]Total transverse velocity, assuming a distance of 2.3 kpc.

red (8.0 μm) features, while nearby stars are prominent in blue (3.6 μm) and green (4.5 μm). We indicate the stars' motions with white arrows (lengths arbitrarily scaled for visiblity) and show the range of possible directions with dotted white lines. The orientations of the candidate bow shocks, where known, are denoted by cyan arrows, and the outer yellow arrows show the directions to the various OB clusters.

The uppermost panels in Figure 3.3 show ALS 15206 (with ERO 2 from Sexton et al. 2015) and TYC 8626-2506-1 (ERO 23). Both of these stars are closer to Tr 14 than to Tr 16 (see Figure 3.1), both are associated with candidate bow shocks pointing at Tr 14, and both have proper motions directed tangentially to the orientation of their candidate bow shocks. The radial velocity of ALS 15206 is poorly constrained, as it is a probable spectroscopic binary (see Chapter 4), but is consistent with being drawn from the radial velocity distribution of Tr 14 (Penny et al. 1993; García et al. 1998; also see Chapter 4). No radial velocity data exist for TYC 8626-2506-1. Thus based on the proper motions of their associated stars, the relative motion shaping EROs 2 and 23 appears to be dominated by the motion of the surrounding ISM, expanding outward from Tr 14. Unseen density gradients may also play a role, but the motions of the stars themselves do not look to be influencing the directions of these candidate bow shocks. They may truly be acting as "weather vanes," tracing the large-scale flows of the ISM.

The middle row of Figure 3.3 shows CPD-59 2605 (ERO 24) and HDE 305533 (ERO 25). These stars' candidate bow shocks are not arc-shaped at IRAC resolutions; Sexton et al. (2015) were able to measure an orientation for ERO 24 but not for ERO 25. Both stars are in Carina's South Pillars region, and are roughly 7.5 pc northeast of the nominal center (Wu et al., 2009) of the sparse open cluster Collinder 228 (Cr 228). ERO 24 points north toward Tr 16, suggesting that it is influenced by feedback-driven outflows. However, its associated star (CPD-59 2605) has a local proper motion to the northwest, consistent with the orientation of the candidate bow shock within the uncertainties. It is thus not possible to distinguish between the effects of ISM flows and stellar motion in the case of ERO 24, as both

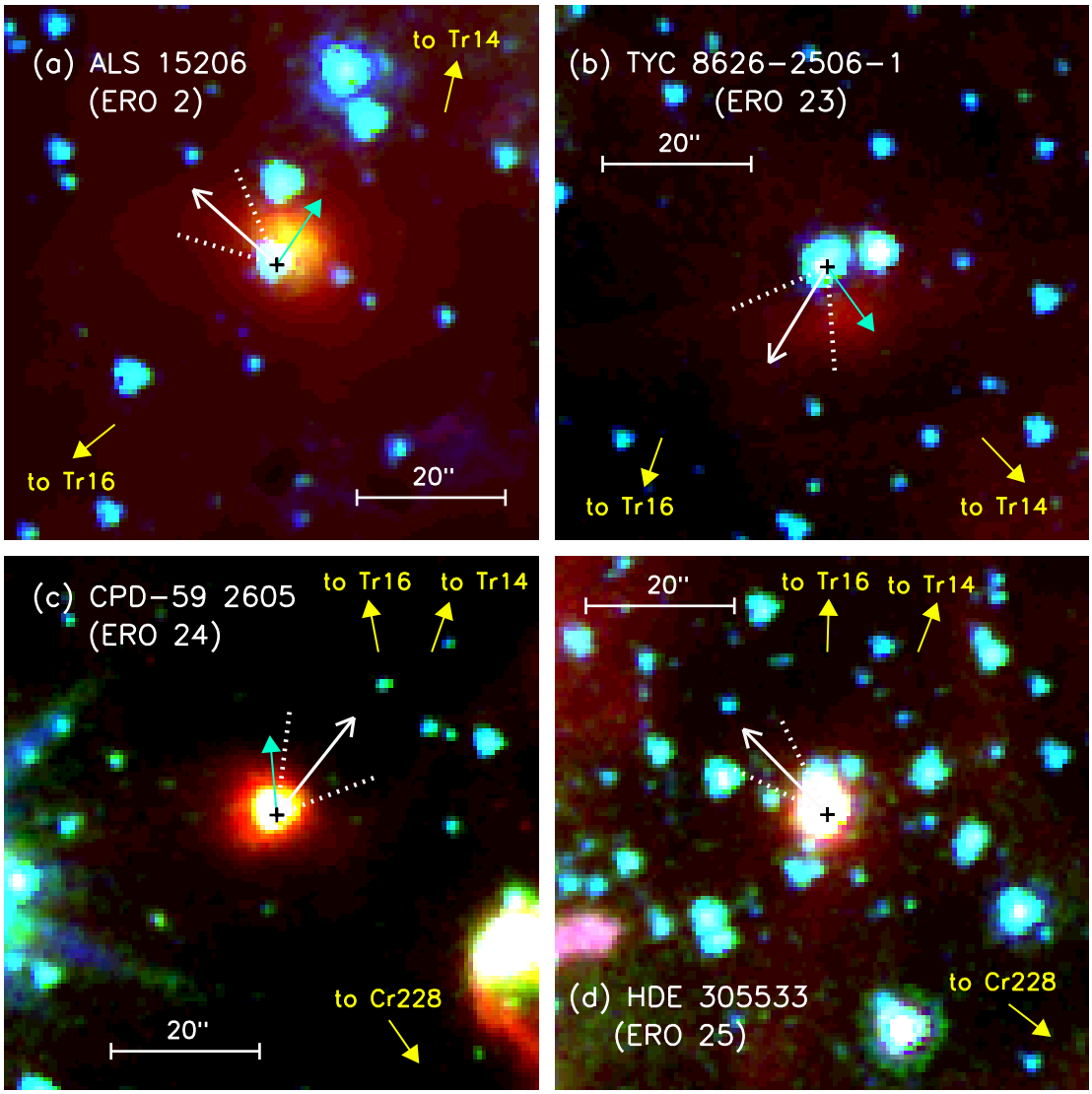

Figure 3.3: Composite three-color *Spitzer* IRAC images of the five OB stars and their associated candidate bow shocks (blue = 3.6 μm, green = 4.5 μm, red = 8.0 μm). The white arrows indicate the direction of the best-fit proper motion of each star, with the dotted white lines bracketing the $\pm 1\sigma$ range of directions. The cyan arrows highlight the orientation of the candidate bow shock, i.e., the direction from the star to the peak of the 8.0 μm emission, where measured by Sexton et al. (2015). Also indicated are the directions to Tr 14 and Tr 16, the largest OB clusters in the Carina Nebula, and to the smaller clusters Bo 11 and Cr 228.

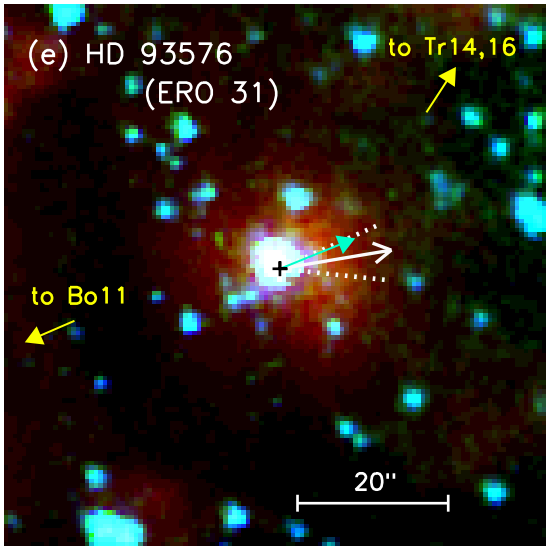

Figure 3.3: Continued.

may be relevant to shaping that feature. No radial velocity data exist for CPD-59 2605.

Relative to its surroundings, HDE 305533 (ERO 25) is moving to the northeast, away from the WNH star HD 93131 and the small group of late O-type stars that make up the center of Cr 228. Its path hints at an ejection from Cr 228, although at its observed speed it would have covered the 7.5 pc from Cr 228 in just 220,000 yr (but see discussion in Section 3.4.1 below on the likelihood that our measured proper motions are upper limits). The age and extent of Cr 228 are also poorly constrained, as it has often been considered an extension of Tr 16 (Walborn, 1995; Smith and Brooks, 2008), while X-ray data show it to be a discrete collection of groups and subclusters without a clear center (Feigelson et al., 2011). The origin of HDE 305533 is therefore not clearly evident. Its radial velocity (-18 km s^{-1}; Levato et al., 1990) is typical for the massive stars in Cr 228 and the South Pillars region (Levato et al. 1990; also see Chapter 4) and comparable to the radial velocity of the surrounding gas pillars (Rebolledo et al., 2016).

Finally, the bottom panel of Figure 3.3 shows HD 93576, the binary system (Levato et al., 1990) associated with ERO 31. HD 93576 lies on the outskirts of

the small open cluster Bochum 11 (Bo 11), located in the southeastern part of the South Pillars. Bo 11 is home to an estimated 1000 stars (Dias et al., 2002), including the O5 supergiant HD 93632 (Sota et al., 2014) and three additional O-type stars besides HD 93576. Photometric analysis indicates that the cluster is 3–5 Myr old (Fitzgerald and Mehta, 1987; Patat and Carraro, 2001; Preibisch et al., 2011a); the presence of an O5I star suggests that 3 Myr is more likely. As Figure 3.3 shows, the proper motion vector of HD 93576 is closely aligned with the orientation of its candidate bow shock, which in turn points nearly directly away from the center of Bo 11. This configuration suggests that HD 93576 was ejected from Bo 11 and that its subsequent supersonic motion produced the observed candidate bow shock. Its systemic radial velocity (-8 km s^{-1}; see Chapter 4) is commensurate with the radial velocities of the other massive members of Bo 11 (Levato et al. 1990; also see Chapter 4) and the nearby dense gas (Rebolledo et al., 2016). But its observed proper motion (15 km s^{-1}) and current position (1.9 pc from the center of Bo 11) indicate an ejection date just 130,000 yr ago. Perhaps HD 93576 was ejected 2–3 Myr after the formation of Bo 11 (possible; see Oh and Kroupa, 2016). Alternately, it could have originated outside the Carina Nebula and have a coincidental agreement in radial velocities, or the magnitude of its proper motion could be smaller than measured (see discussion in Section 3.4.1). In addition, its candidate bow shock is also generally directed toward the interior of the Carina Nebula, so a contribution from ISM flows driven by cluster feedback cannot be ruled out regardless of the origin of the star.

3.4 Discussion

3.4.1 Proper motions as upper limits

For four of the five candidate bow shock host stars in our sample, we measure local proper motions of $\sim$30 km s^{-1}, with associated uncertainties of $>$ 15 km s^{-1}. (This total includes HDE 305533, whose observed motion may include a contribution from focus changes as described in Section 3.2.3.) Several lines of reasoning

support the interpretation of these measured velocities as upper limits, with the true proper motions lying on the small side of the allowed range. First, the typical velocity of an O-type star relative to its surrounding is $\sim$ 10 km s^{-1} (Blaauw, 1961; Cruz-González et al., 1974; Gies and Bolton, 1986; Tetzlaff et al., 2011). Of course, the stars in our sample are arguably not typical, given their association with candidate dusty bow shocks. Space velocities of 30 km s^{-1} may qualify them as runaway stars, depending on the choice of runaway classification criteria. None of the five stars measured here are moving with trajectories that could have originated in Tr 14 or Tr 16, although HDE 305533 (ERO 25) and HD 93576 (ERO 31) may have come from the smaller open clusters Cr 228 and Bo 11, respectively. An object moving at 30 km s^{-1} would cover 60 pc in 2 Myr (the average estimated age of Tr 14/16; Walborn, 1995; Smith, 2006a; Preibisch et al., 2011a), and these stars are all significantly closer than that to any possible clusters of origin in the Carina Nebula. It is possible that all four of the stars with measured proper motions of $\sim$30 km s^{-1} were ejected more recently, but that scenario would still not explain their directions of motion. Similarly, it is possible that all four are interlopers in the Carina Nebula, originating from another cluster, but the chance of encountering four such stars in our small sample is low. And as described in Section 3.3, the radial velocities of our sample stars, where available, agree with the radial motions of the surrounding stars and gas, consistent with more local origins.

In addition, speeds of 30 km s^{-1} are inconsistent with the relative star–ISM velocities computed for Carina's candidate bow shocks by Sexton et al. (2015). The pressure balance governing a standard bow shock makes it possible to estimate the relative star–ISM velocity as a function of measured standoff distance by making reasonable assumptions about stellar wind velocity, mass-loss rate, and ISM density. Sexton et al. (2015) measured the standoff distances of nine EROs in the Carina Nebula and found an average star–ISM velocity of 17 km s^{-1}. For ERO 2 (associated with ALS 15206), the relative star–ISM velocity was a barely-supersonic 7 km s^{-1}. Similar relative velocities for bow shocks in the massive star-forming region RCW 38 were reported by Winston et al. (2012). These numbers have substantial

uncertainties due to the assumptions that go into their calculation, but they still suggest somewhat lower stellar velocities. Consider ERO 2 (ALS 15206): The orientation of the candidate bow shock indicates that the direction of the highest relative star–ISM velocity is to the northwest. We have measured that ALS 15206 is moving to the northeast, tangential to its candidate bow shock. If the relative star–ISM velocity in the direction of the candidate bow shock is on the order of 7 km s^{-1}, the relative star–ISM velocity in a different direction cannot be substantially higher than that, although the picture may be complicated if there are density gradients in the ISM.

For these reasons, it is unlikely that the measured stars associated with candidate bow shocks are moving as fast as 30 km s^{-1} relative to their surroundings. The local proper motions given here should thus be treated as upper limits. HD 93576 may be an exception, as its westward motion is measured at 3σ significance (but this raises questions about its possible origin in Bo 11, as discussed in Section 3.3).

3.4.2 Comparison to absolute proper motions

All five of the stars in our sample have proper motions listed in the USNO CCD Astrograph Catalog (UCAC4; Zacharias et al., 2013), and ALS 15206, TYC 8626-2506-1, and HD 93576 also have proper motions in the Tycho-2 Catalogue (Høg et al., 2000) and *Gaia* Data Release 1 (DR1; Gaia Collaboration et al., 2016a,b; Lindegren et al., 2016). (Note that Tycho-2 and *Gaia* DR 1 are not wholly independent measurements, as the latter incorporates positional information from the former.) The UCAC4, Tycho-2, and *Gaia* DR1 proper motions are measured in an absolute reference frame and are therefore not directly comparable to the local proper motions measured here. We would expect to see a roughly constant offset between these absolute proper motions and our local ones, with that offset representing the bulk motion of the Carina Nebula relative to the Sun. We plot the available absolute proper motions for each star, along with our measured local proper motions, in Figure 3.4. Contrary to expectations, Figure 3.4 does not show a consistent offset between local and absolute proper motions. The UCAC4 proper

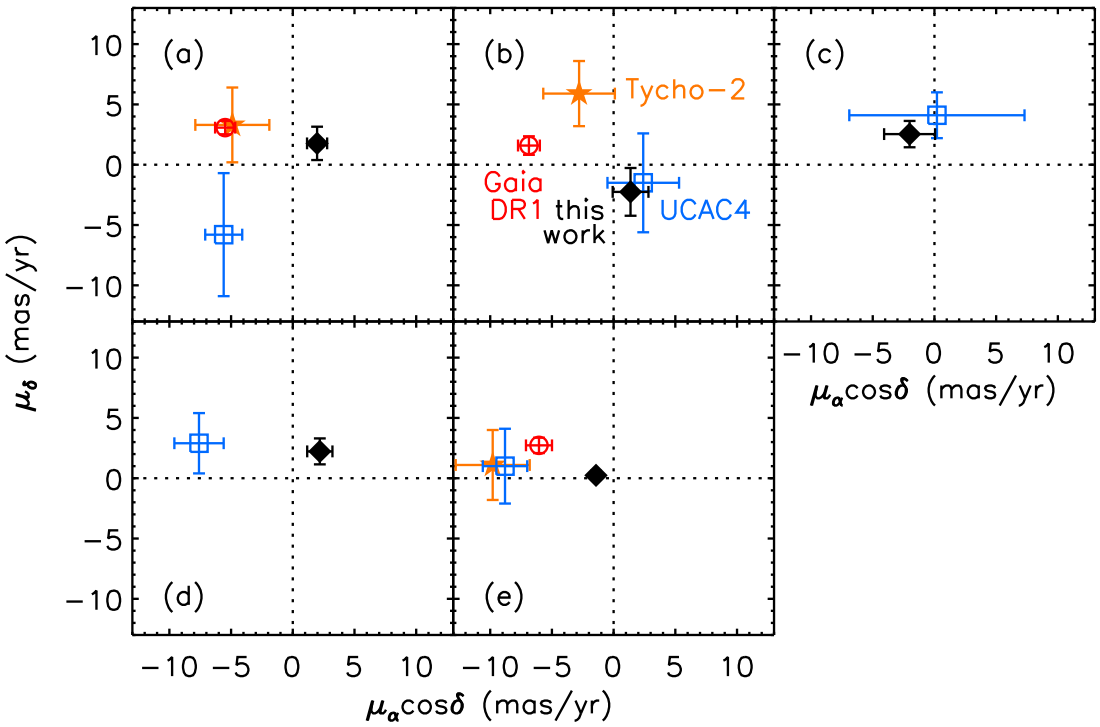

Figure 3.4: Comparison of the *local* proper motion (filled black diamonds) of each star measured here to its *absolute* proper motion from UCAC4 (open blue squares, Zacharias et al., 2013), the Tycho-2 Catalogue (filled orange stars, Høg et al., 2000), and *Gaia* Data Release 1 (open red circles, Gaia Collaboration et al., 2016a,b; Lindegren et al., 2016). (a) ALS 15206 (ERO 2); (b) TYC 8626-2506-1 (ERO 23); (c) CPD-59 2605 (ERO 24); (d) HDE 305533 (ERO 25); (e) HD 93576 (ERO 31).

motions in particular do not follow any apparent trend relative to the local proper motions or the Tycho-2 and *Gaia* DR1 data. The differences between catalogues suggest that there may be systematic effects in the literature measurements that are not taken into account in the published uncertainties.

For further comparison, we correct the *Gaia* proper motions, where available, to the rest frame of the Carina Nebula in two ways. First, we formally correct for Galactic rotation and solar peculiar motion, as in Moffat et al. (1998, 1999) and Comerón and Pasquali (2007). We adopt Oort's constants $A = 15 \pm 1$ km s^{-1} kpc^{-1} and $B = -12 \pm 1$ km s^{-1} kpc^{-1} (Feast and Whitelock, 1997; Elias et al., 2006; Bovy,

2017) and components of the solar peculiar velocity $(U_\odot, V_\odot, W_\odot) = (10 \pm 1, 12 \pm 1, 7 \pm 1)$ km s^{-1} (Feast and Whitelock, 1997; Elias et al., 2006; Schönrich et al., 2010; Tetzlaff et al., 2011). The corrected proper motions are plotted in Figure 3.5. For all three stars, the corrected *Gaia* proper motions are ≤ 1.3 mas yr^{-1} (≤ 14 km s^{-1}), supporting our interpretation that these stars are not runaways. The corrected *Gaia* proper motion of ALS 15206 (ERO 2) is, like our measured motion, directed to the northeast, tangential to the orientation of its candidate bow shock. The corrected *Gaia* motion of TYC 8626-2506-1 (ERO 23) is to the southwest, into its candidate bow shock, although its 1σ uncertainties overlap with those of our measured motion to the southeast. The corrected *Gaia* motion of HD 93576 (ERO 31) is also consistent with our data, although the *Gaia* results indicate a smaller velocity to the west, suggesting a longer time since ejection from Bo 11.

We also perform an empirical correction to the local reference frame: we compute the weighted mean proper motion of the 38 O-type stars in the Carina Nebula in *Gaia* DR1 (which is roughly half the total O-type population of the region; e.g., Smith, 2006a; Gagné et al., 2011; Alexander et al., 2016) and subtract that from the absolute *Gaia* proper motions of the three sample stars. The results are consistently ~ 1.1 mas yr^{-1} (~ 12 km s^{-1}) offset from the results of formally correcting for Galactic rotation and solar peculiar motion. For ALS 15206 (ERO 2) and TYC 8626-2506-1 (ERO 23), the empirical correction brings the corrected *Gaia* proper motions into better agreement with our results. For HD 93576 (ERO 31), the empirical correction produces worse agreement with our results and suggests that the star is moving to the east, away from its candidate bow shock and toward Bo 11. The different parts of the Carina Nebula may have different large-scale motions not properly accounted for in these corrections. Future *Gaia* data releases, extending into Carina's intermediate-mass population, will allow more precise and locally-specific corrections to the local reference frame.

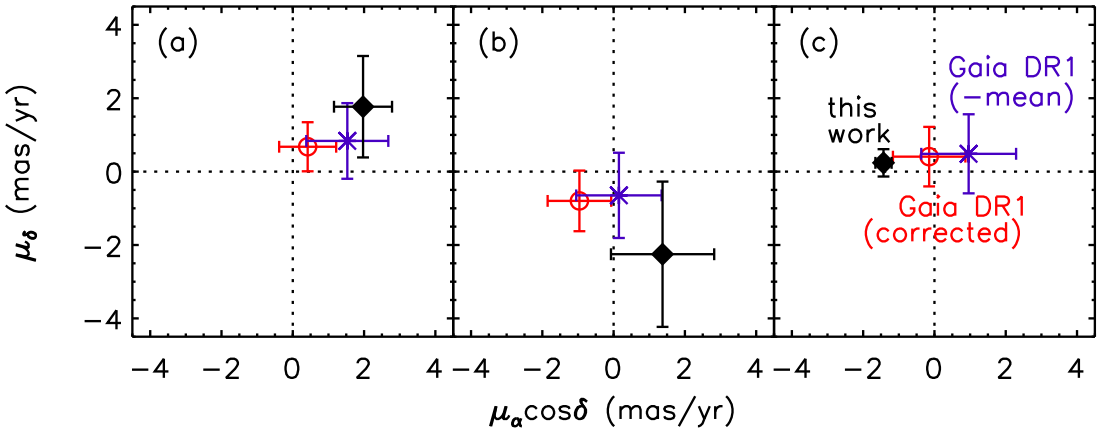

Figure 3.5: Comparison of the local proper motions (filled black diamonds) measured here to proper motions from *Gaia* Data Release 1 (Gaia Collaboration et al., 2016a,b; Lindegren et al., 2016) that have been corrected to a local reference frame. Open red circles are the *Gaia* DR1 data corrected for Galactic rotation and solar peculiar motion as described in Section 3.4.2; purple asterisks are the *Gaia* DR1 data corrected empirically by subtracting the mean proper motion of O-type stars in the Carina Nebula. (a) ALS 15206 (ERO 2); (b) TYC 8626-2506-1 (ERO 23); (c) HD 93576 (ERO 31).

3.4.3 Interpreting bow shocks in giant H II regions

In our subsample of bow shock candidates in the Carina Nebula, EROs 2 and 23 face the OB cluster Tr 14, while EROs 24 and 31 point more generally toward Tr 14 and 16. The majority of bow shock candidates in the full Sexton et al. (2015) sample also point in toward the clusters rather than out as would be expected for runaway stars. Sexton et al. (2015) hypothesized that these candidate bow shocks are markers of large-scale ISM flows driven by cluster feedback. The ionized gas in the Carina Nebula is known to be globally expanding at 15–20 km s^{-1} (Walborn and Hesser, 1975; Walborn et al., 2002a, 2007), with multiple local centers of expansion including Tr 14 (Damiani et al., 2016). Feedback-driven outflows are also thought to explain the orientations of bow shocks in other massive star-forming regions (Povich et al., 2008; Winston et al., 2012) and the correlation of bow shock orientations on small angular scales (Kobulnicky et al., 2016). Our results are broadly compatible with this interpretation, but they indicate that the factors influencing a bow shock or bow-shock-like structure cannot be deduced solely from its orientation.

The associated stars of EROs 2 and 23 are not moving in the direction of their infrared arcs, which are thus likely shaped by feedback from Tr 14. These two objects confirm that, at least in this environment, apparent bow shock orientation does not always follow stellar motion. In contrast, the associated stars of EROs 24, 25, and 31 are moving roughly toward Tr 14 and 16. Both stellar motion and ISM flows could be relevant in setting the orientation of these three candidate bow shocks, demonstrating that cluster-facing bow-shock-like structures are not necessarily clear markers of the motion of the ISM.

Feedback may also be affecting bow shocks in giant H II regions in other ways besides large-scale outflows. For instance, the pile-up of dust in bow shock arcs depends on the presence of dust in the surrounding H II region, as the hot winds of OB stars do not make dust effectively. This dust may originate in photoevaporative flows off nearby molecular pillars, driven globally by ionizing radiation from the central clusters and locally by individual OB stars. Kobulnicky et al. (2016) found that

eight percent of bow shocks across the Galactic Plane face bright-rimmed clouds, suggesting they are shaped by local photoevaporative flows. The arc-shaped dust waves around σ and λ Ori are also thought to be driven by photoevaporative flows off the edge of ionized bubbles (Ochsendorf et al., 2014a,b; Ochsendorf and Tielens, 2015; Ochsendorf et al., 2015). Density gradients in the ISM can also affect bow shock symmetries (Wilkin, 2000) or create infrared arcs via uneven heating.

We inspected *Spitzer* images of the Carina Nebula to assess the relationship between Carina's EROs, its molecular gas, and the distribution of warm dust. There is a possible tendency for EROs to be closer to dense pillars than expected from a random distribution, but there is no correlation between ERO orientation and the direction to the nearest pillar. ERO 31, for example, lies just 45″ (∼0.5 pc) from the edge of a prominent pillar, but points almost directly away from it. Multiband Imaging Photometer (MIPS) images at 24 μm reveal complex warm dust structures throughout the nebula, including around EROs 24 and 31. However, the origin and impact of these structures with respect to the EROs is unclear. Higher-resolution mid-infrared imaging is required to tease out the effects of density gradients and photoevaporative flows in shaping Carina's EROs.

In any case, our main result is unaffected: in a giant H II region, the orientation of bow-shock-like structures may be determined by the ISM, by stellar motion, or by some combination of factors. It is worth reiterating that none of the five stars in our study are runaways from Tr 14 or 16. While this result is unsurprising given the orientation of their candidate bow shocks, it confirms that stars with bow-shock-like structures are not automatically runaways. The statistical preference for alignment between stellar motion and bow shock orientation, particularly among known runaway stars (van Buren et al., 1995; Kobulnicky et al., 2016) suggests that stellar motion does dominate over ISM flows for bow shocks far from feedback-generating clusters. But within associations, assumptions about the implications of bow shocks and bow-shock-like structures (e.g., Kobulnicky et al., 2010; Gvaramadze et al., 2011b) should be made with caution.

3.4.4 Implications for the origins of OB associations

The local proper motions of CPD-59 2605 (ERO 24), HDE 305533 (ERO 25), and HD 93576 (ERO 31) can also shed light on the origins of the distributed massive-star population in the Carina Nebula. Nearly half of Carina's massive stars, including the WNH star HD 93131, are spread across roughly 20 pc in the South Pillars (Smith, 2006a). Some of these massive stars are associated with small open clusters (Bo 11, Cr 228) and other groups and subclusters of young stars (Smith et al., 2010c; Feigelson et al., 2011). However, *Herschel* imaging detected no massive protostars in the region, suggesting that the ongoing star formation in the South Pillars is limited to low- and intermediate-mass stars (Gaczkowski et al., 2013).

In the classic picture of clustered star formation (e.g., Lada and Lada, 2003), massive stars rarely form in a distributed mode as seen in the South Pillars. Instead, massive stars are born in clusters that may subsequently become unbound after gas dispersal and expand into OB associations (Tutukov, 1978; Hills, 1980; Lada and Lada, 1991, 2003). In this picture, one would expect the Carina Nebula's distributed massive stars to have formed in the central Trumpler clusters and drifted out to their current locations over several Myr.

Our proper motion results are inconsistent with this expectation, as all three of the massive South Pillars stars measured here are moving toward the Trumpler clusters, not away. These stars' kinematics suggest that they were born in the South Pillars, possibly in one of the smaller open clusters, and support a model of star formation in which OB associations form directly as loose aggregates (e.g., Efremov and Elmegreen, 1998a; Clark et al., 2005). A similar result has been observed for the Cyg OB2 association based on its substructure and lack of global expansion (Wright et al., 2014, 2016). Further investigation of stellar kinematics in the South Pillars is needed to confirm this interpretation of the Carina Nebula's distributed population.

3.5 Conclusions

Using *HST* ACS imaging with 9–10 year baselines, we have measured the local proper motions (i.e., relative to the surrounding stars) of five OB stars associated with candidate bow shocks in the Carina Nebula. Because these stars are highly saturated in our data, we use precisely-aligned images to measure the shift in each star's Airy rings between epochs. The results are largely upper limits, but we are able to constrain the direction of each star's motion for comparison to the orientation of its candidate bow shock.

Stellar wind bow shocks are formed when the relative velocity between star and ISM is supersonic, but the bow shock alone does not indicate which component of the relative velocity dominates. Are bow shocks indicators of fast-moving runaway stars or do they mark the large-scale flow of the ISM? In our sample of five, we find two cases where the latter is likely the case, as the stars are moving at a tangent to the arc of their candidate bow shocks. In the other three cases, we conclude that the possible influences of ISM flows, ISM structure, and stellar motion cannot be separated, and that multiple factors could be relevant for each object. We consequently caution against overinterpreting the orientation of bow shocks and bow-shock-like structures in giant H II regions like the Carina Nebula.

In addition, none of the five stars measured here are runaways from the central OB clusters of the Carina Nebula, although two may have been ejected from smaller open clusters in the South Pillars. This finding emphasizes that bow shocks and bow-shock-like structures in giant H II regions are not definite markers of runaway stars. It also suggests that the distributed massive-star population in the Carina's South Pillars formed along with the distributed low- and intermediate-mass population; the resulting OB association is not the expanding remnant of an embedded cluster but a loose collection of many small groups and clusters.

CHAPTER 4

A RADIAL VELOCITY SURVEY OF THE CARINA NEBULA'S O-TYPE STARS[†]

We have obtained multi-epoch observations of 31 O-type stars in the Carina Nebula using the CHIRON spectrograph on the CTIO/SMARTS 1.5-m telescope. We measure their radial velocities to 1–2 km s^{-1} precision and present new or updated orbital solutions for the binary systems HD 92607, HD 93576, HDE 303312, and HDE 305536. We also compile radial velocities from the literature for 32 additional O-type and evolved massive stars in the region. The combined data set shows a mean heliocentric radial velocity of 0.6 km s^{-1}. We calculate a velocity dispersion of $\leq$ 9.1 km s^{-1}, consistent with an unbound, substructured OB association. The Tr 14 cluster shows a marginally significant 5 km s^{-1} radial velocity offset from its neighbor Tr 16, but there are otherwise no correlations between stellar position and velocity. The O-type stars in Cr 228 and the South Pillars region have a lower velocity dispersion than the region as a whole, supporting a model of distributed massive-star formation rather than migration from the central clusters. We compare our stellar velocities to the Carina Nebula's molecular gas and find that Tr 14 shows a close kinematic association with the Northern Cloud. In contrast, Tr 16 has accelerated the Southern Cloud by 10–15 km s^{-1}, possibly triggering further massive-star formation. The expansion of the surrounding H II region is not symmetric about the O-type stars in radial velocity space, indicating that the ionized gas is constrained by denser material on the far side.

[†]This chapter has been submitted for publication in the *Monthly Notices of the Royal Astronomical Society* as Kiminki and Smith (2017).

4.1 Introduction

The Carina Nebula is one of the most dramatic star-forming regions in the nearby Galaxy. It is home to more than 70 O-type stars (Smith, 2006a; Gagné et al., 2011; Alexander et al., 2016), including the defining star of the O2 spectral type (Walborn et al., 2002b), as well as three late-type hydrogen-rich Wolf-Rayet stars (WNH stars; Smith and Conti, 2008) and the remarkable luminous blue variable η Carinae (Davidson and Humphreys, 1997). The distribution of these O-type and evolved massive stars is shown in Figure 4.1. Roughly half belong to two central clusters, Trumpler (Tr) 14 and Tr 16, while the rest are spread across an area more than 30 pc in diameter. Most of the more distributed stellar population is found in the South Pillars, a region of active star formation to the south of Tr 16 (Smith et al., 2000, 2010c). The combined ionizing radiation and stellar winds from the clustered and distributed massive stars (Smith and Brooks, 2007) has had a major impact on their surroundings, shaping spectacular dust pillars (Smith et al., 2000, 2010c), powering a developing superbubble (Smith et al., 2000), and potentially triggering the observed ongoing star formation (Megeath et al., 1996; Smith et al., 2000; Rathborne et al., 2004; Smith et al., 2005b, 2010c). The feedback-dominated environment of the Carina Nebula is the closest analogue to giant starburst regions like 30 Doradus (e.g., Doran et al., 2013).

Due to the physical extent and complex structure of the Carina Nebula, the relationships between its various clusters and subclusters have been the subject of considerable debate. Photometric and spectroscopic surveys of the stellar populations of Tr 14 and Tr 16 have usually placed the two clusters at a common distance in the range 2.0 to 3.5 kpc (Feinstein et al., 1973; Walborn, 1982a,b; The et al., 1980a,b; Turner and Moffat, 1980; Tapia et al., 1988; Cudworth et al., 1993; Massey and Johnson, 1993; Tovmassian et al., 1994; Tapia et al., 2003; Hur et al., 2012). Other studies concluded that Tr 14 lies 1–2 kpc behind Tr 16 (Walborn, 1973; Morrell et al., 1988) or vice versa (Carraro et al., 2004). The smaller Tr 15 cluster likewise alternated between being considered a foreground

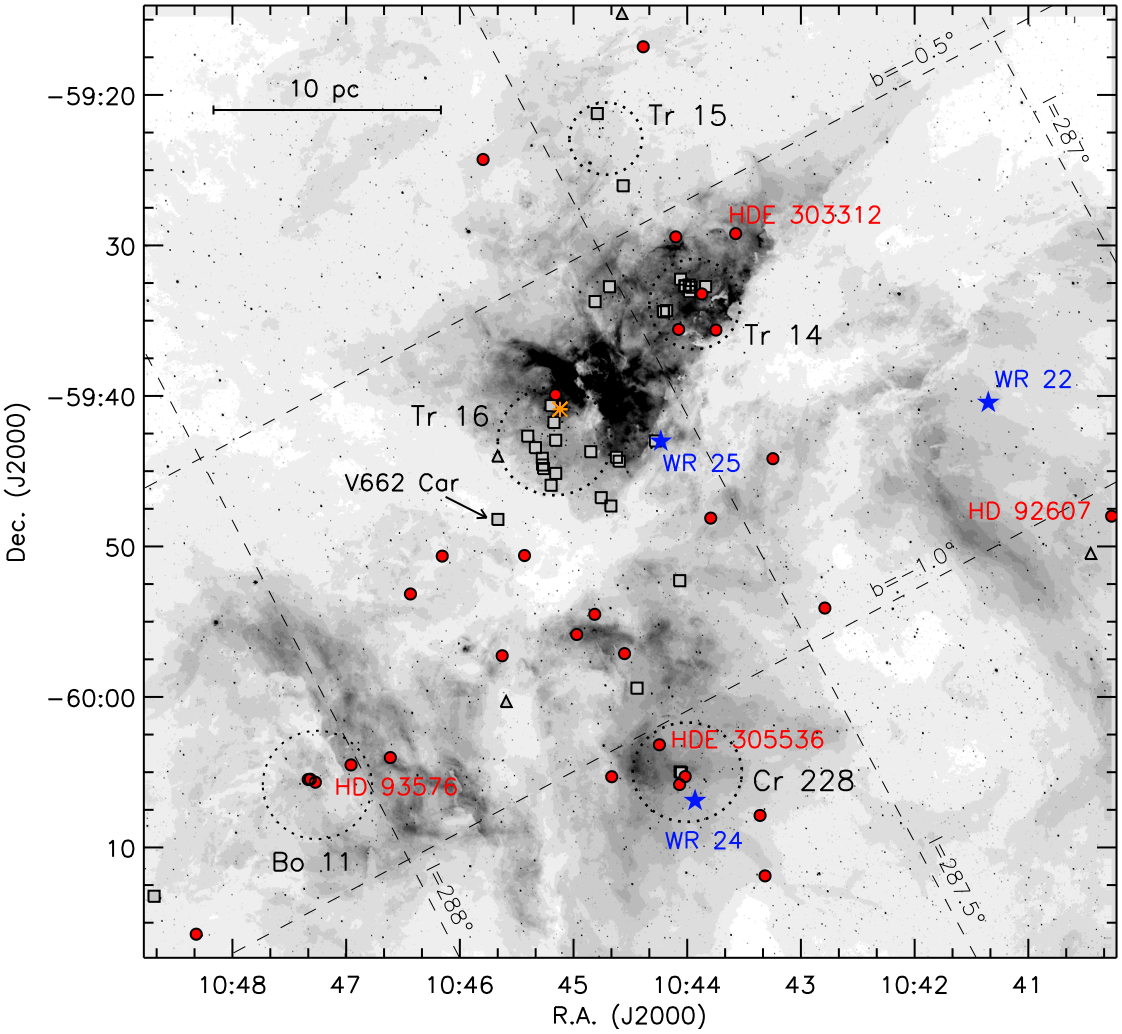

Figure 4.1: The O-type and evolved massive stars in the Carina Nebula, shown over a ground-based Hα image from Smith et al. (2010a) with Galactic coordinates overlaid for reference. Red circles are O-type stars with new CHIRON observations; we identify by name the four spectroscopic binaries with new orbital solutions (see Section 4.3). Gray squares are O-type stars in version 3.1 of the Galactic O-Star Catalog (Maíz Apellániz et al., 2013; Sota et al., 2014) that were not targeted with CHIRON. The V662 Car system (see Section 4.4.3) is highlighted. Gray triangles are additional O-type stars confirmed by Alexander et al. (2016). The three WNH stars are marked with blue stars, and η Car is indicated by an orange asterisk. The large dashed circles mark the approximate locations of the major clusters in the region.

(Thé and Vleeming, 1971) or background (Walborn, 1973) cluster, until recent X-ray data revealed a stellar bridge between Tr 15 and Tr 14 (Feigelson et al., 2011). The open cluster Collinder (Cr) 228 and the distributed massive stars of the South Pillars region have been variously treated as an extension of Tr 16 (Walborn, 1995; Smith and Brooks, 2008), a distinct but same-distance cluster (Herbst, 1976; Turner and Moffat, 1980; Tapia et al., 1988; Tovmassian et al., 1994; Massey et al., 2001, and see also Smith et al. 2010c and Feigelson et al. 2011), or a foreground cluster (Feinstein et al., 1976; Forte, 1978; Carraro and Patat, 2001). The optical studies were complicated by the variable extinction across the region and the unusually high ratio of total-to-selective extinction R_V (Herbst, 1976; Forte, 1978; The et al., 1980a,b; Smith, 1987; Tovmassian et al., 1994; Carraro et al., 2004; Mohr-Smith et al., 2017).

Independent of the many spectrophotometric distance studies of the region, measurements of the expansion of η Car's Homunculus Nebula have placed that star at a firm distance of 2.3 kpc (Allen and Hillier, 1993; Davidson et al., 2001; Smith, 2006a). As there is strong evidence that η Car is a member of Tr 16 (Walborn and Liller, 1977; Allen, 1979) and gas pillars across the Carina Nebula complex show the influence of Tr 16's feedback (Smith et al., 2000, 2010c), a general consensus has arisen that Tr 14, Tr 16, Cr 228, and the rest of the stars in the Carina Nebula belong to a single massive association at 2.3 kpc (e.g., Smith and Brooks 2008, although see Hur et al. 2012). Preliminary results from *Gaia* Data Release 1 (DR1; Gaia Collaboration et al., 2016a,b; Lindegren et al., 2016) support this interpretation, with the parallaxes of the 43 measured O-type stars clustering around 0.5 mas or 2.0 kpc (Smith and Stassun, 2017).

Even with the spatial link between the Carina Nebula's components now relatively secure, the formation of its distributed massive population remains somewhat uncertain. The O-type stars currently seen among the South Pillars may have been born there, a possible example of an OB association forming through distributed, hierarchical star formation (e.g., Efremov and Elmegreen, 1998b; Clark et al., 2005). But no massive protostars have been detected among the forming stellar population

in the South Pillars (Gaczkowski et al., 2013), and Preibisch et al. (2011b) argue that the dense gas clouds in the region are not massive enough to support further massive-star formation. If the distributed O-type stars did not form in situ, they may have migrated out from Tr 16 either through the classic expansion of a cluster after gas dispersal (Tutukov, 1978; Hills, 1980; Lada and Lada, 1991, 2003) or as the result of cluster-cluster interaction (Gieles, 2013) between Tr 14 and Tr 16. Kiminki et al. (2017) did not see any such outward migration in the local proper motions of bow-shock-associated massive stars in the South Pillars, but their sample size was limited.

In this paper, we explore the relationships between the components of the Carina Nebula and the origins of its massive-star populations through a survey of the radial velocities (RVs) of its O-type and evolved massive stars. These stellar RVs can be compared to the kinematics of the Carina Nebula's H II regions (e.g., Damiani et al., 2016) and molecular gas (e.g., Rebolledo et al., 2016), allowing a direct assessment of the impact of massive-star feedback on the intersellar medium. The RVs of massive stars can be strongly affected by stellar binarity (e.g., Gieles et al., 2010), but the effects can be constrained with multi-epoch observations.

The paper is organized as follows: In Section 4.2, we describe our multi-epoch spectroscopic observing campaign and our RV measurements, and summarize the additional data compiled from the literature. In Section 4.3, we discuss the O-type stars with variable RVs and present orbital solutions for four spectroscopic binary systems. Section 4.4 discusses the RV distributions of the various O-star populations in the Carina Nebula and compares the observed stellar kinematics to the motions of the region's molecular and ionized gas. Our conclusions are summarized in Section 4.5.

4.2 Observations and Data Analysis

4.2.1 Target selection

Our list of O-type stars in the Carina Nebula is drawn from version 3.1 of the Galactic O-Star Catalog (GOSC; Maíz Apellániz et al., 2013; Sota et al., 2014). The GOSC v3.1 lists 68 objects, including the Of/WNH system WR 25, with right ascensions between 10:40:00 and 10:49:00 and declinations between −60:20:00 and −59:10:00. An additional four O-type systems in this coordinate range, originally suspected on the basis of their X-ray emission (Povich et al., 2011a), were recently spectroscopically confirmed by Alexander et al. (2016). Adding η Car and the remaining two WNH stars brings the total number of known systems with O-type and evolved massive primaries to 75. These 75 systems are shown in Figure 4.1.

We selected 31 of these systems for new spectroscopic observations. In choosing targets, we prioritized stars that had zero or few prior RV measurements, or whose only existing RV data had high uncertainties. Most of our target stars are thus outside of Tr 14 and Tr 16, as those clusters have been the targets of multiple spectroscopic campaigns and binary fraction analyses (Penny et al., 1993; García et al., 1998; Albacete Colombo et al., 2001, 2002; Morrell et al., 2001; Rauw et al., 2001, 2009; Nazé et al., 2005; Niemela et al., 2006). We also prioritized sources brighter than $V = 11$ mag.

4.2.2 Spectroscopy

We obtained high-resolution spectra of our 31 target stars with the CHIRON echelle spectrograph (Tokovinin et al., 2013) on the CTIO 1.5-m telescope operated by the SMARTS Consortium. Observations were taken in queue operation using the fiber mode configuration, which provides a resolution of R ∼25,000 over a wavelength range of 4100–8900 Å. All 31 stars were observed 2–4 times each in Nov–Dec 2014. Observations of a given star were spaced 7–14 days apart to minimize the chances of catching a short-period binary at the same phase, as there is a relative lack of massive binaries in this period range (Kiminki and Kobulnicky, 2012; Kobulnicky et al.,

2014). Follow-up observations of eight stars showing possible RV variations were obtained in Oct 2015–Jan 2016. Throughout our observing campaign, exposure times were 60–1800 s, designed to achieve signal-to-noise (S/N) ratios of 50–70 at 5500 Å. The resulting S/N ratios ranged from 30 to 150 with a median of 77. ThAr calibration spectra were taken before moving the telescope after observing each star; bias and flat-field observations were taken at the beginning and end of each night as part of CHIRON's standard queue observing protocol.

Data were reduced in `IRAF`[1] using standard procedures, including bias subtraction, flat-fielding, cosmic ray correction, and extraction of 74 echelle orders. Wavelength calibration was performed using the corresponding ThAr spectrum for each star, and wavelengths were corrected to a heliocentric frame. The wavelength scale of each order is good to an rms of 0.01 Å (∼0.6 km s^{-1} at 5000 Å). Echelle orders were continuum-normalized before being combined into a single spectrum for each exposure. A representative sample of reduced spectra is shown in Figure 4.2, focusing on a wavelength region that covers most of the lines used for RV measurement (see Section 4.2.3).

4.2.3 New radial velocities

We adapt the method of Sana et al. (2013) for measuring stellar RVs, performing Gaussian fits to a set of He lines and fitting all lines and epochs for a given star simultaneously. The final fit forces all lines at a given epoch to have the same RV, and assumes that the width and amplitude of a given spectral line are constant across epochs. The uncertainties on initial, single-line fits are used to weight each line in the final overall fit. We use the IDL curve-fitting package `MPFIT` (Markwardt, 2009).

Like Sana et al. (2013), we use He absorption lines because they are relatively unaffected by winds in main-sequence O-type stars (unlike the hydrogen Balmer

[1] `IRAF` is distributed by the National Optical Astronomy Observatory, which is operated by the Association of Universities for Research in Astronomy (AURA) under a cooperative agreement with the National Science Foundation.

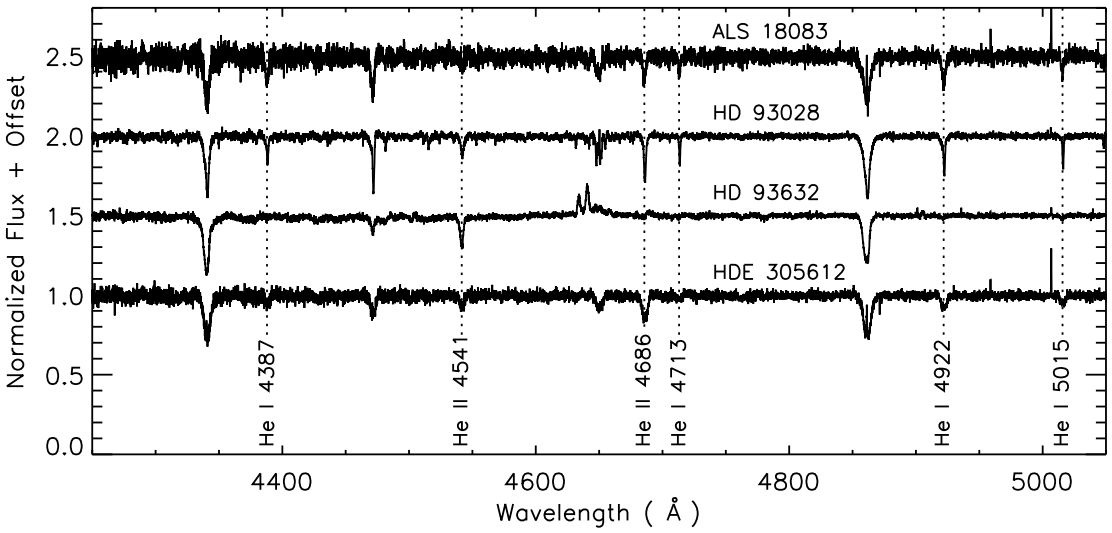

Figure 4.2: Continuum-normalized CHIRON spectra of four O-type stars in our observed sample, illustrating the range of S/N achieved in the wavelength range 4250–5050 Å. Stellar radial velocities were measured using fits to the marked He I and He II absorption lines, where present, along with He I $\lambda\lambda$5876, 7065.

lines; Bohannan and Garmany, 1978), and are present across all O subtypes (unlike most metal lines), allowing us to apply a consistent approach to our full sample of observed stars. Initially, we fit He I $\lambda\lambda$4387, 4471, 4713, 4922, 5015, 5876, 6678, 7065 and He II $\lambda\lambda$4541, 4686. The rest wavelengths for these lines were taken from the NIST Atomic Spectra Database (Kramida et al., 2016) and the Atomic Line List by Peter van Hoof.[2] After the first round of fits, we compared the RVs from individual line fits to the RVs from fitting all lines at once. The triplet blend He I λ4471 was systematically blueshifted by $\sim$10 km s^{-1} relative to the overall results, and the singlet line He I λ6678 was systematically redshifted by a similar amount. We therefore removed those two lines and refit all epochs of the observed stars. On a star-by-star basis, we also excluded lines that were visibly contaminated by nebular emission or, in the case of HD 93190, stellar P Cygni emission. With these exclusions, an average of seven absorption lines were used to fit the RVs of each star. The measured RVs for each star at each epoch are given in Table 4.1. The

[2] http://www.pa.uky.edu/~peter/atomic/

Table 4.1: Heliocentric radial velocities measured from CHIRON observations of O-type stars in the Carina Nebula. Dates are given for the midpoints of the exposures.

Name	HJD −2400000	RV1 (km s^{-1})	σ(RV1) (km s^{-1})	RV2 (km s^{-1})	σ(RV2) (km s^{-1})
ALS 15204	56987.814	-60.0	4.7	...	...
ALS 15204	56994.850	1.0	2.3	...	...
ALS 15204	57003.836	43.1	2.0	...	...
ALS 15206	56992.858	24.5	0.4	...	...
ALS 15206	57000.851	29.8	0.5	...	...
ALS 15206	57008.788	34.1	0.3	...	...
ALS 15207	56972.840	-20.8	1.2	...	...
ALS 15207	56987.838	-6.2	1.6	...	...
ALS 15207	56994.862	3.7	1.8	...	...
ALS 15207	56996.801	7.1	1.7	...	...
ALS 15207	57362.867	15.0	1.9	...	...
ALS 15207	57364.831	3.4	1.3	...	...
ALS 15207	57374.859	-21.5	1.4	...	...
ALS 18083	57004.782	2.3	1.2	...	...
ALS 18083	57011.775	2.2	1.0	...	...
[ARV2008] 206	56995.848	18.0	2.4	...	...
[ARV2008] 206	57004.804	14.3	2.3	...	...
[ARV2008] 206	57011.741	18.8	2.3	...	...
CPD-58 2627	56998.789	-9.2	2.8	...	...
CPD-58 2627	57008.759	-6.3	2.4	...	...
CPD-59 2551	56982.848	-0.2	1.0	...	...
CPD-59 2551	56992.846	-3.2	1.1	...	...
CPD-59 2551	57000.826	-3.2	1.1	...	...
CPD-59 2554	56997.778	-13.7	0.8	...	...
CPD-59 2554	57005.783	-21.1	0.8	...	...
CPD-59 2554	57322.890	63.4	1.5	...	...
CPD-59 2554	57332.875	-11.3	0.9	...	...
CPD-59 2554	57350.865	1.6	1.2	...	...
CPD-59 2554	57352.873	-5.8	1.3	...	...
CPD-59 2554	57361.853	-22.7	1.2	...	...
CPD-59 2554	57362.855	-20.6	1.0	...	...
CPD-59 2554	57364.844	-19.2	1.0	...	...
CPD-59 2610	57000.872	-6.0	1.4	...	...
CPD-59 2610	57008.821	-3.0	1.0	...	...

Table 4.1: Continued.

Name	HJD −2400000	RV1 (km s^{-1})	σ(RV1) (km s^{-1})	RV2 (km s^{-1})	σ(RV2) (km s^{-1})
CPD-59 2673	56980.850	-4.5	3.0	...	...
CPD-59 2673	56994.799	4.5	3.0	...	...
CPD-59 2673	57004.831	-2.1	2.2	...	...
HD 92607	56965.861	11.0	32.5	9.7	30.8
HD 92607	56974.857	-99.2	5.6	131.5	5.3
HD 92607	56986.866	206.2	7.8	-203.6	7.4
HD 92607	57353.877	166.4	6.9	-143.6	6.5
HD 92607	57354.838	-142.6	6.8	165.0	6.5
HD 92607	57361.849	4.0	43.8	1.3	41.5
HD 92607	57362.849	-184.2	8.3	229.3	7.8
HD 92607	57363.860	108.5	6.7	-110.1	6.5
HD 92607	57365.849	-134.9	12.2	160.6	11.5
HD 92607	57374.773	5.1	53.2	5.5	51.0
HD 92607	57378.855	179.6	6.5	-193.6	6.2
HD 92607	57379.723	203.7	7.0	-186.2	6.6
HD 93027	56972.872	-3.3	0.4	...	...
HD 93027	56987.826	-4.9	0.4	...	...
HD 93027	56994.839	-5.5	0.5	...	...
HD 93028	56969.850	30.8	0.3	...	...
HD 93028	56982.831	25.5	0.3	...	...
HD 93028	56991.806	17.4	0.3	...	...
HD 93028	56998.797	8.4	0.3	...	...
HD 93190	56974.832	0.5	1.5	...	...
HD 93190	56988.824	-1.2	1.7	...	...
HD 93190	56996.844	-2.4	1.4	...	...
HD 93222	56966.870	0.0	0.6	...	...
HD 93222	56980.795	0.2	0.8	...	...
HD 93403	56980.827	-17.0	1.2	...	...
HD 93403	56994.777	-30.5	1.2	...	...
HD 93403	57004.821	-30.0	1.1	...	...
HD 93576	57005.793	-97.8	1.4	...	...
HD 93576	57012.844	-16.8	1.9	...	...
HD 93576	57019.783	71.4	1.5	...	...
HD 93576	57354.861	70.7	1.5	...	...
HD 93576	57361.842	-16.9	2.1	...	...
HD 93576	57362.843	-9.9	1.8	...	...

Table 4.1: Continued.

Name	HJD −2400000	RV1 (km s^{-1})	σ(RV1) (km s^{-1})	RV2 (km s^{-1})	σ(RV2) (km s^{-1})
HD 93576	57364.858	-52.5	1.7	...	...
HD 93576	57375.848	-22.1	3.6	...	...
HD 93576	57378.874	64.4	1.7	...	...
HD 93576	57379.754	-74.8	1.9	...	...
HD 93576	57380.763	67.0	1.8	...	...
HD 93576	57389.840	36.5	1.5	...	...
HD 93632	57007.863	-6.5	1.0	...	...
HD 93632	57015.830	-2.7	1.0	...	...
HD 93632	57021.860	-3.4	1.1	...	...
HDE 303308	56966.875	-8.8	1.1	...	...
HDE 303308	56988.846	-2.5	1.1	...	...
HDE 303308	56996.771	-2.0	1.3	...	...
HDE 303308	56997.787	-1.4	1.0	...	...
HDE 303312	56978.835	-1.0	1.4	...	...
HDE 303312	56988.808	-14.5	1.9	...	...
HDE 303312	56996.827	17.0	1.8	...	...
HDE 303312	57354.873	2.6	2.9	...	...
HDE 303312	57361.830	35.8	2.5	...	...
HDE 303312	57362.829	23.2	1.6	...	...
HDE 303312	57363.870	13.7	3.0	...	...
HDE 303312	57365.858	-71.0	4.1	...	...
HDE 303312	57375.835	-118.4	2.8	...	...
HDE 303312	57376.867	3.7	1.5	...	...
HDE 303312	57378.845	24.9	1.8	...	...
HDE 303312	57379.734	29.6	1.6	...	...
HDE 303316	56987.796	0.9	0.6	...	...
HDE 303316	56988.837	0.2	0.8	...	...
HDE 303316	56996.785	0.8	0.7	...	...
HDE 305438	56969.843	-6.4	0.2	...	...
HDE 305438	56982.827	-6.2	0.2	...	...
HDE 305438	56992.826	-5.9	0.2	...	...
HDE 305518	56969.858	-25.6	0.9	...	...
HDE 305518	56992.837	-28.2	1.2	...	...
HDE 305523	56974.827	5.4	0.4	...	...
HDE 305523	56988.828	6.3	0.5	...	...
HDE 305523	56996.849	2.6	0.5	...	...

Table 4.1: Continued.

Name	HJD −2400000	RV1 (km s^{-1})	σ(RV1) (km s^{-1})	RV2 (km s^{-1})	σ(RV2) (km s^{-1})
HDE 305524	56992.818	-2.3	2.8	...	...
HDE 305524	57000.864	-2.0	2.3	...	...
HDE 305524	57008.802	-1.8	1.8	...	...
HDE 305525	56980.835	-59.4	2.3	...	...
HDE 305525	56994.785	1.2	2.7	...	...
HDE 305525	57004.765	49.7	3.0	...	...
HDE 305525	57375.805	20.1	3.8	...	...
HDE 305525	57378.830	-29.7	2.0	...	...
HDE 305525	57379.767	-0.9	2.4	...	...
HDE 305525	57380.753	-29.3	2.2	...	...
HDE 305525	57389.828	-81.7	2.1	...	...
HDE 305532	56980.818	1.7	0.8	...	...
HDE 305532	56994.830	0.5	0.6	...	...
HDE 305532	57003.852	0.5	0.8	...	...
HDE 305536	56974.837	24.9	0.6	...	...
HDE 305536	56988.819	-18.2	0.6	...	...
HDE 305536	56996.838	-31.0	0.6	...	...
HDE 305536	57364.850	3.0	0.6	...	...
HDE 305536	57365.868	-5.3	1.1	...	...
HDE 305536	57375.824	-28.1	1.0	...	...
HDE 305536	57378.859	18.4	0.6	...	...
HDE 305536	57379.744	-15.1	0.6	...	...
HDE 305536	57380.733	19.0	0.6	...	...
HDE 305536	57389.818	41.7	0.5	...	...
HDE 305536	57390.706	-29.6	0.6	...	...
HDE 305536	57394.773	-19.9	2.0	...	...
HDE 305539	56997.802	-3.1	0.9	...	...
HDE 305539	57008.772	-1.1	0.8	...	...
HDE 305539	57015.820	-4.2	1.1	...	...
HDE 305612	56978.851	22.3	1.9	...	...
HDE 305612	56988.868	17.2	2.0	...	...
HDE 305612	56996.868	3.7	2.5	...	...
HDE 305619	56978.862	-2.3	0.7	...	...
HDE 305619	56988.856	-13.2	0.8	...	...
HDE 305619	57364.867	-7.8	0.7	...	...
HDE 305619	57375.817	-9.2	1.3	...	...

Table 4.1: Continued.

Name	HJD −2400000	RV1 (km s^{-1})	σ(RV1) (km s^{-1})	RV2 (km s^{-1})	σ(RV2) (km s^{-1})
HDE 305619	57378.866	-5.5	0.7	...	...
HDE 305619	57379.838	-6.0	0.8	...	...
HDE 305619	57380.742	-1.7	0.8	...	...

median uncertainty in RV for the single-lined spectra is 1.2 km s^{-1}.

One of our observed sources, HD 92607, is a double-lined spectroscopic binary (SB2), first identified by Sexton et al. (2015). We adapted our RV measurement procedure to fit a double Gaussian at all epochs. This process required several steps: First, we fit He I λ5876 for the six epochs in which the components were clearly separated. Then, we fixed the width and amplitude of the He I λ5876 components and fit to the four epochs with blended components. These fits gave us initial estimates for the RVs at all epochs, which we used as the starting point for fits to He I $\lambda\lambda$4922, 5015 and He II λ4686. Again, we fit these lines in the well-separated epochs first, then fixed widths and amplitudes for fits to the blended epochs. The final fit was to all four lines at all epochs. Because the two components of HD 92607 are of similar spectral type, several iterations of line fitting and orbital analysis (see Section 4.3.1) were required to confidently identify which line component was associated with which star at a given epoch. The median uncertainty on the RVs of the components of HD 92607 is 7.1 km s^{-1}, and ranges as high as 30–40 km s^{-1} in epochs where the lines are highly blended.

As a check on our wavelength calibration, we obtained CHIRON spectra of the RV standard stars HIP 51722 (spectral type F7–8 V) and HIP 53719 (K1–2 IV), both from the catalog of Soubiran et al. (2013), in Nov 2014. As the spectra of these standard stars do not have He I lines, their RVs could not be measured by the same method used for our science spectra. Instead, we measured their RVs by cross-correlation with high-resolution stellar spectra from Coelho (2014), using the IRAF task `fxcor`. The measured RVs of both standard stars agree with their expected values within 0.4 km s^{-1}.

4.2.4 Radial velocities from the literature

Where available, we also compiled heliocentric RVs from the literature for the Carina Nebula's O-type and evolved massive stars. The adopted RVs and associated uncertainties for stars not observed with CHIRON are given in Table 4.2 along with the corresponding references. Where there are observations at multiple epochs, we give the weighted mean; where the system is a spectroscopic binary with an orbital solution, we give the systemic velocity. For visual binaries that are resolvable at the few-arcsecond level (e.g., HD 93161AB), we use only data that specifies which component was observed. We also note whether systems were classified as constant-RV or binary in the multiplicity survey of Chini et al. (2012). Additional notes on the spectroscopic multiplicity of a system are given in the references column. We also incorporate literature data for the following CHIRON targets: ALS 15206 (Huang and Gies, 2006), ALS 15207 (García et al., 1998), HD 93028 (Feast et al., 1957; Conti et al., 1977), HDE 303308 (Conti et al., 1977), HDE 305518 (Huang and Gies, 2006), and HDE 305619 (Humphreys, 1973). In no case does the inclusion of these sources' literature RVs shift their overall weighted mean RV by more than 1.5 km s^{-1}.

Table 4.2 also includes RVs for the three WNH stars in the Carina Nebula. Like all Wolf-Rayet stars, these sources have strong stellar winds, and their spectral features are formed at various depths within those winds (e.g., Crowther, 2007). Wolf-Rayet stars tend to show highly blueshifted hydrogen Balmer and He II absorption lines (Conti et al., 1979) and highly redshifted He II emission (Bartzakos et al., 2001; Foellmi et al., 2003). We adopt RVs from narrow metal emission lines (the "Group 1" lines of Conti et al. 1979), which are thought to be formed relatively closer to the star, making them more representative of the sources' true systemic velocities. The reported RVs are likely still impacted by winds (see Moffat and Seggewiss, 1979; Schweickhardt et al., 1999) and so we consider the three WNH stars as a separate group in our analysis. Note that although η Car is also an evolved massive star with a high mass-loss rate, its RV was measured by a different method (Smith, 2004) and it does not suffer from the same bias.

Table 4.2: Mean or systemic heliocentric radial velocities adopted from the literature.

Name	$\overline{\mathrm{RV}}$ or γ (km s^{-1})	$\sigma(\overline{\mathrm{RV}})$ (km s^{-1})	Spectral flag from Chini et al. (2012)[a]	References
ALS 15229	14.7	3.5	...	García et al. (1998)
CPD-58 2611	4.7	5.0	C[b]	Penny et al. (1993); García et al. (1998)
CPD-58 2620	-0.6	5.8	SB1	Penny et al. (1993); García et al. (1998)
CPD-59 2591	-2.9	10.	...	Huang and Gies (2006)
CPD-59 2624	13.5	10.	...	Huang and Gies (2006); SB2 in Alexander et al. (2016)
CPD-59 2626	-22.7	10.	...	Huang and Gies (2006)
CPD-59 2627	-15.9	10.	...	Huang and Gies (2006)
CPD-59 2629	-8.8	12.8	...	SB1 in Williams et al. (2011)
CPD-59 2635	0.	1.	SB2	SB2 solution from Albacete Colombo et al. (2001)
CPD-59 2636	4.0	5.7	SB2	Quadruple system; Albacete Colombo et al. (2002)
CPD-59 2641	-4.5	1.8	SB2	SB2 solution from Rauw et al. (2009)
η Carinae	-8.1	1.	...	Smith (2004)
HD 93128	5.0	5.3	C[b]	Penny et al. (1993); García et al. (1998)
HD 93129A	-10.1	18.7	C[b]	Conti et al. (1979); Penny et al. (1993)
HD 93129B	7.1	2.2	...	Penny et al. (1993)
HD 93160	-12.9	17.9	SB1	Thackeray et al. (1973); Conti et al. (1977)
HD 93161A	1.1	3.6	SB2	SB2 data from Nazé et al. (2005)
HD 93161B	-25.4	28.4	...	Nazé et al. (2005)
HD 93130	59.9	3.1	SB2	Conti et al. (1977)
HD 93204	8.5	3.8	C	Conti et al. (1977)
HD 93205	-2.9	0.9	SB2	SB2 solution from Morrell et al. (2001)
HD 93250	-5.2	7.6	C[b]	Thackeray et al. (1973); Rauw et al. (2009); Williams et al. (2011)
HD 93343	-2.8	54.4	SB2	SB2 data from Rauw et al. (2009)
HD 93403	-14.2	5.4	SB2	SB2 solution from Rauw et al. (2000)
HD 93843	-9.9	0.4	C	Feast et al. (1957); Conti et al. (1977)
QZ Car	-8.7	15.5	SB2	Quadruple system; Morrison and Conti (1980); Mayer et al. (2001)
Trumpler 14-9	5.6	3.8	...	Penny et al. (1993); García et al. (1998)
V572 Car	-3.4	3.7	SB2	Triple system; Rauw et al. (2001)
V573 Car	-5.	4.	...	SB2 solution from Solivella and Niemela (1999)

Table 4.2: Continued.

Name	$\overline{\text{RV}}$ or γ (km s^{-1})	$\sigma(\overline{\text{RV}})$ (km s^{-1})	Spectral flag from Chini et al. (2012)[a]	References
V662 Car	-15.	2.	...	SB2 solution from Niemela et al. (2006)
WR 22[c]	-23.8	12.5	...	SB1 solution from Schweickhardt et al. (1999)
WR 24[c]	-34.4	15.7	...	Conti et al. (1979)
WR 25[c]	-33.5	2.2	...	SB1 solution from Gamen et al. (2006)

[a]C = constant; SB1 = single-lined spectroscopic binary; SB2 = double-lined spectroscopic binary.
[b]Although classified as constant in Chini et al. (2012), these stars meet our criteria for significant RV variability ($P(\chi^2, \nu) < 0.01$; see Section 4.3) and have RV amplitudes > 20 km s^{-1}.
[c]As discussed in Section 4.2.4, the reported RVs of Wolf-Rayet stars are likely more negative than their true systemic velocities.

In compiling literature RVs for Table 4.2, we discovered that the RVs in Levato et al. (1990, 1991a,b) are notably discrepant with later observations, including our own. These three studies measured RVs for a total of 92 candidate members of Cr 228, Tr 14, and Tr 16, using the spectrograph on the 1-m Yale CTIO telescope (see Levato et al., 1986). Levato et al. (1991a) report that the mean RV of Tr 14 is -29 km s^{-1}, where Penny et al. (1993) and García et al. (1998) measure 2.8 and 6.0 km s^{-1}, respectively. For individual stars across the region, even those that otherwise show little to no variation in RV, the Levato et al. (1990, 1991a,b) data are 10–60 km s^{-1} more negative than subsequent observations. We therefore decided to exclude all data from the Levato et al. studies, except for specific binary orbits as discussed in Section 4.3.

With the inclusion of the literature data in Table 4.2, we have RVs for 63 of the 75 O-type and evolved massive stars in the Carina Nebula. Four of the twelve stars without RV data are those that were newly confirmed by Alexander et al. (2016). These four are relatively highly extincted, with a median A_V of 5.7 mag compared to the median A_V of 2.2 mag for the rest of the O-type stars in the region (Gagné et al., 2011; Povich et al., 2011b). Alexander et al. (2016) postulate that one of these, OBc 3, is a coincidentally-aligned background star. The other eight stars without RV data are neither systematically more extincted nor systematically fainter at visual wavelengths than the 63 sources with RV data. Some of these eight have been observed as part of the OWN RV survey (Barbá et al. 2010; see Sota et al. 2014; Maíz Apellániz et al. 2016) but currently lack published RVs.

4.3 New and Updated Binary Orbits

Multiplicity is ubiquitous among O-type stars (Garmany et al., 1980; Mason et al., 2009; Chini et al., 2012; Sana et al., 2012, 2013, 2014; Kobulnicky et al., 2014; Moe and Di Stefano, 2017) and must be considered when determining their systemic RVs. For each of our CHIRON sources, we compute $P(\chi^2, \nu)$, the probability that the χ^2 about the weighted mean would be exceeded by random chance given

$\nu = N_{obs} - 1$ degrees of freedom. Nine of the 31 observed stars display significant ($P(\chi^2, \nu) < 0.01$) RV variations with amplitudes > 20 km s^{-1} in our CHIRON data. As discussed below, we are able to find periods and fit orbital solutions to four of these spectroscopic binaries. Two additional observed sources meet the criteria for significant, high-amplitude variations when their literature RVs are included. One of these sources is HD 93403, a known SB2 with a full orbital solution in Rauw et al. (2000). Our CHIRON observations are in good agreement with the orbit of the primary star, and we adopt the systemic velocity for HD 93403 from the Rauw et al. (2000) solution.

An additional five CHIRON targets display significant ($P(\chi^2, \nu) < 0.01$) but low-amplitude (ΔRV $<$ 20 km s^{-1}) RV variations. These stars include HDE 305619, which was flagged as an SB1 by Chini et al. (2012) but lacks published RV data. The other four stars may have undetected long-period companions or may be showing photospheric variability (e.g., Garmany et al., 1980; Gies and Bolton, 1986; Fullerton et al., 1996; Ritchie et al., 2009; Martins et al., 2015).

We search for periodicity in stars with significant, high-amplitude RV variations and $N_{obs} \geq 7$. We compute the frequency power spectrum for each source using A. W. Fullerton's IDL implementation of the one-dimensional `CLEAN` algorithm (Högbom, 1974; Roberts et al., 1987). We also, without any constraint on the period, input the RV data into the IDL package `rvfit` (Iglesias-Marzoa et al., 2015), which solves for the orbital parameters P (orbital period), e (eccentricity), γ (systemic velocity), ω (argument of periastron), T_p (epoch of periastron), K_1 (primary semi-amplitude), and K_2 (secondary semi-amplitude, where applicable). `rvfit` will provide orbital parameters for any set of input data, but poor fits have high χ^2 values and are not replicable. In four cases, described in further detail below, we found reasonable, replicable orbital solutions with `rvfit`, with periods that agreed with those determined by `CLEAN`. After convergence on a solution, we computed uncertainties for each orbital parameter using `rvfit`'s Markov Chain Monte Carlo implementation.

Table 4.3: Orbital and physical parameters of new and updated binary solutions.

Element	HD 92607	HD 93576	HDE 303312—RV only	HDE 303312—higher K_1	HDE 305536
P (d)	3.6993 (0.0001)	1.852102 (0.000002)	9.4111 (fixed)	9.4111 (fixed)	1.88535 (0.00002)
e	0.00 (fixed)	0.075 (0.009)	0.57 (fixed)	0.57 (fixed)	0.129 (0.008)
γ (km s^{-1})	8.8 (1.6)	-8.4 (0.6)	2.4 (0.6)	-0.5 (0.6)	2.3 (0.2)
ω ($^\circ$)	90 (fixed)	201 (9)	192 (2)	192 (fixed)	56 (3)
T_p (HJD−2400000)	56965.910 (0.009)	57005.94 (0.05)	56980.58 (0.03)	56980.58 (fixed)	56975.34 (0.02)
K_1 (km s^{-1})	224 (3)	85.0 (0.8)	70 (1)	125 (fixed)	37.3 (0.3)
K_2 (km s^{-1})	242 (3)	...	...	...	...
$f(M_1, M_2)$ (M$_\odot$)	...	0.117 (0.004)	0.19 (0.01)	1.06	0.0099 (0.0004)
$M_1 \sin^3 i$ (M$_\odot$)	20.2 (0.7)	...	...	...	...
$M_2 \sin^3 i$ (M$_\odot$)	18.7 (0.6)	...	...	...	...
$a_1 \sin i$ (R$_\odot$)	16.4 (0.3)	3.10 (0.03)	10.7 (0.2)	19.1	1.38 (0.01)
$a_2 \sin i$ (R$_\odot$)	17.7 (0.3)	...	...	...	...
rms$_1$ (km s^{-1})	19.7	10.9	6.1	31.0	2.8
rms$_2$ (km s^{-1})	23.7	...	...	...	...

Uncertainties for each quantity are listed in parentheses.

4.3.1 HD 92607

HD 92607 was first noted as an SB2 by Sexton et al. (2015), who classified its components as O8.5 V + O9 V. It is on the far western side of the Carina Nebula, approximately 25 pc from Tr 14 and 16 (see Figure 4.1). The lower-mass stellar population in this area, by the edge of the Carina Nebula's northern molecular cloud, is relatively young (< 1 Myr; Kumar et al., 2014). HD 92607 is associated with an extended arc of 24 μm emission, suggestive of a stellar wind bow shock, that points to the southeast (Sexton et al., 2015).

We obtained 12 CHIRON spectra of HD 92607 in 2014–2015. As described in Section 4.2.3, we adapted our RV-fitting procedure to fit two Gaussian profiles to He I $\lambda\lambda$4922, 5015, 5876 and He II λ4686 across all 12 epochs, using fits to the well-separated epochs to fix the widths and amplitudes of the lines. We used `rvfit` to fit an orbit to the primary and secondary RVs simultaneously.

The best-fitting period for HD 92607 is 3.6993 ± 0.0001 d. Figure 4.3 shows the progression of He I λ5876 over this period. After our initial orbital fit converged on an eccentricity of zero, we fixed $e = 0$ for further fitting, allowing `rvfit` to treat ω and T_p (which are ill-defined at very low eccentricities) in a consistent manner (see Iglesias-Marzoa et al., 2015). The final best-fitting orbital solution is shown in Figure 4.4, and the orbital parameters are listed in Table 4.3. In the best-fitting orbit, the minimum masses of the primary and secondary stars are $M_1 \sin^3 i = 20.2 \pm 0.7$ M$_\odot$ and $M_2 \sin^3 i = 18.7 \pm 0.6$ M$_\odot$, respectively, giving a mass ratio of $q = 0.93 \pm 0.04$. But their spectral types of O8.5 V and O9 V (Sexton et al., 2015), according to the "observational" scale of Martins et al. (2005), have somewhat lower expected masses of $M_1 = 18.8$ M$_\odot$ and $M_2 = 17.1$ M$_\odot$. The apparent discrepancy could be the result of the normal uncertainties on spectral-type classification; for instance, Gagné et al. (2011) list HD 92607 as an O8 V star, although they do not account for its spectroscopic binarity. Or perhaps the components of HD 92607 are slightly older, and hence cooler for their masses, than average main-sequence stars of their types. In any case, the HD 92607 system is likely close to edge-on ($i \sim 90°$), as

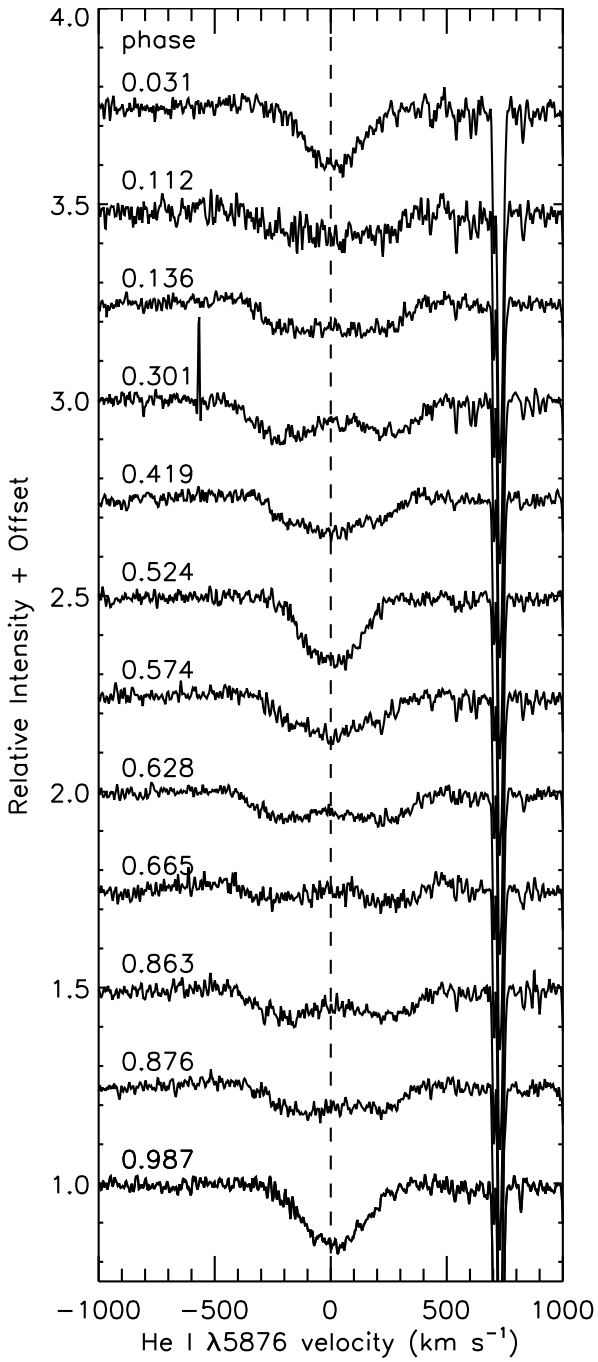

Figure 4.3: He I λ5876 in velocity space and in order of phase for CHIRON observations of the SB2 HD 92607, for an orbital period of 3.6993 d. The narrow absorption line on the right is interstellar Na I λ5890.

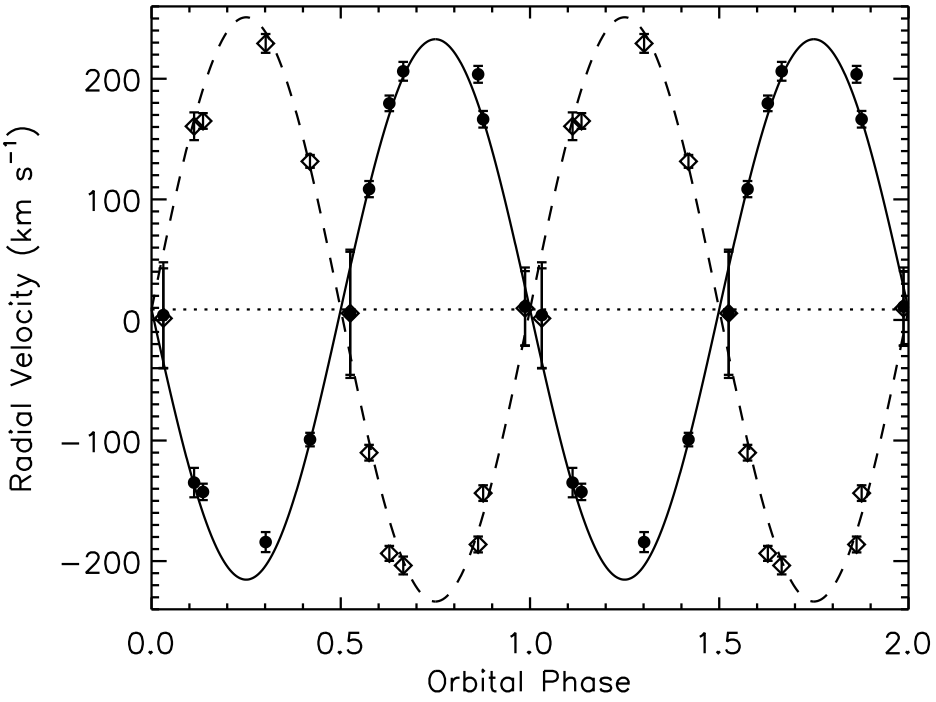

Figure 4.4: Radial velocity curve and orbital solution for the SB2 HD 92607 at the best-fitting orbital period of 3.6993 d. Filled circles and open diamonds correspond to the primary and secondary components, respectively. The dotted line marks the systemic velocity.

a smaller inclination would imply implausibly large masses for its component stars.

As can be seen in Figure 4.3, the He I line depths for the two components of HD 92607 are very similar due to their close spectral types. If, when measuring RVs, we swap the component assignments in some of the widely-separated phases, we find a plausible if less elegant orbital solution at the alias period of 1.84957 ± 0.00005 d (almost exactly half the best-fitting period). The fit to the alias period requires a substantial eccentricity ($e = 0.35$) and has an estimated inclination of $\sim 45°$.

4.3.2 HD 93576

HD 93576 is one of five O-type systems in the open cluster Bochum (Bo) 11 in Carina's South Pillars region. Its primary is of type O9–9.5 IV–V (Sota et al., 2014; Sexton et al., 2015). It is associated with an extended arc of 8 μm emission, which points away from Bo 11 and has infrared colors indicative of a stellar wind bow shock (Sexton et al., 2015). Its local proper motion confirms that it is moving away from Bo 11 at $\lesssim 15$ km s^{-1}; it may have been recently ejected from the cluster (Kiminki et al., 2017).

Levato et al. (1990) first noted periodic RV variations in the spectra of HD 93576, and fit an orbital solution with a period of 2.020 d. We obtained 12 CHIRON observations of this system in 2014–2016, in which we identified a periodicity of 1.852 d. We used `rvfit` to compute orbital solutions both with and without the Levato et al. (1990) data. The final best-fitting orbital parameters given in Table 4.3 are from the combined data set; excluding the older data has a negligible effect on our derived period, eccentricity, systemic velocity, and semi-amplitude. The phase-folded RV curve is shown in Figure 4.5. Note that the systemic velocity from our fits is substantially less negative than the $\gamma = -21$ km s^{-1} reported by Levato et al. (1990). As can be seen in Figure 4.5, many but not all of the Levato et al. (1990) RVs for this system are 10–20 km s^{-1} blueshifted relative to CHIRON data at the same phase.

The orbit of HD 93576 is minimally but significantly non-circular, with an eccentricity of 0.075 ± 0.009. The resulting mass function is $f(M_1, M_2) = 0.117 \pm$

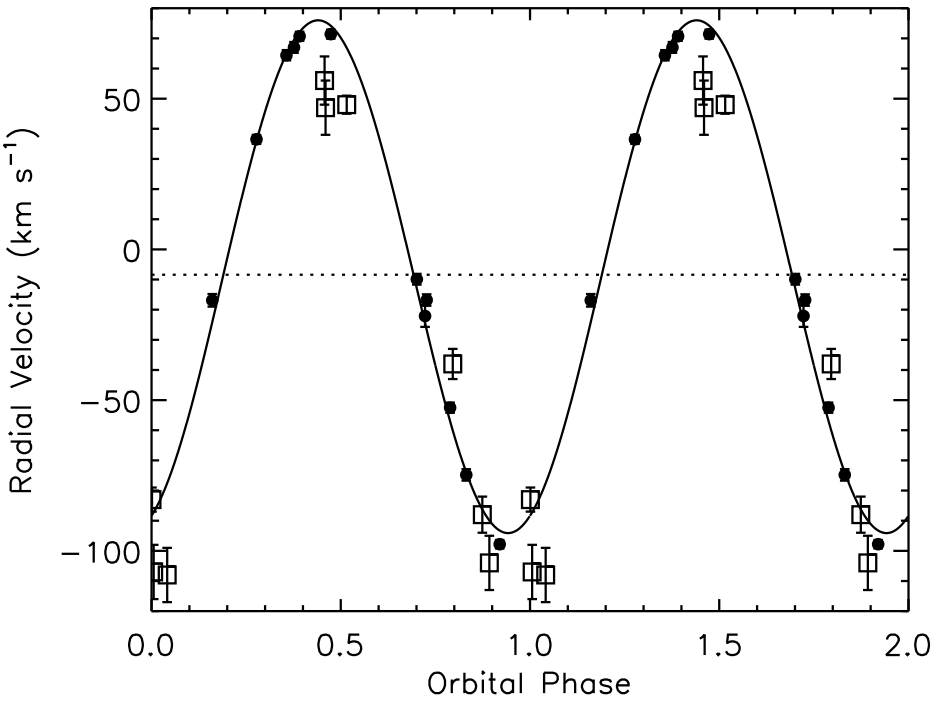

Figure 4.5: Radial velocity curve and orbital solution for the SB1 HD 93576 at the best-fitting orbital period of 1.852102 d. Solid circles are measurements from our CHIRON spectra and open squares are data from Levato et al. (1990). Both data sets were used in computing the orbital solution. The dotted line marks the systemic velocity.

0.004 $M_\odot$. Assuming the primary star has a mass of 16–18 $M_\odot$, as appropriate for its spectral type per Martins et al. (2005), the minimum mass of the secondary star is ∼3.7 $M_\odot$, roughly the mass of a B8 V star (Drilling and Landolt, 2000).

4.3.3 HDE 303312

HDE 303312 is an O9.7 IV star (Sota et al., 2014) located on the outskirts of Tr 14 (see Figure 4.1). There are no RVs for this source in the literature, but Otero (2006) discovered that it is an eclipsing binary with a period of 9.4109 d. Otero (2006) also noted from the light curve that it is an "extremely eccentric" system. We obtained a total of 12 CHIRON observations of HDE 303312 over 2014–2015, and downloaded all available V-band photometry for this source from the All Sky Automated Survey (ASAS; Pojmanski, 1997). In addition to using `rvfit` on the velocity data, we use the eclipsing binary modeling program `NIGHTFALL`[3] to synthesize and compare photometric light curves.

The orbital period of HDE 303312 is constrained by its V-band light curve, which we find to be best fit by a period of 9.4111 d. The light curve also constrains the eccentricity to 0.57 ± 0.01, consistent with the analysis of Otero (2006). With the period and eccentricity fixed at these values, we fit an orbital solution to the RV data, shown as the solid line in Figure 4.6 and listed as the first set of parameters for this system in Table 4.3. The semi-amplitude of this fit is $K_1 = 70$ km s^{-1}, resulting in a mass function of $f(M_1, M_2) = 0.19$ $M_\odot$. Because the system is eclipsing, its inclination must be relatively high; we find that the eclipse shapes are best reproduced in `NIGHTFALL` with $i \approx 80°$. If we take the mass of the primary star to be 15–18 $M_\odot$, based on its spectral type (see Martins et al., 2005), the mass of the secondary star is 4–5 $M_\odot$. Assuming the secondary star is on the main sequence, that mass corresponds to a spectral type of B6–7 V (Drilling and Landolt, 2000).

However, the V-band light curve is inconsistent with a B6–7 V companion ($T_{\rm eff} \approx 13,000$–$14,000$ K; Kenyon and Hartmann, 1995), given that the primary star has an effective temperature of $\approx 30,000$ K (Martins et al., 2005). The noise in

[3] http://www.hs.uni-hamburg.de/DE/Ins/Per/Wichmann/Nightfall

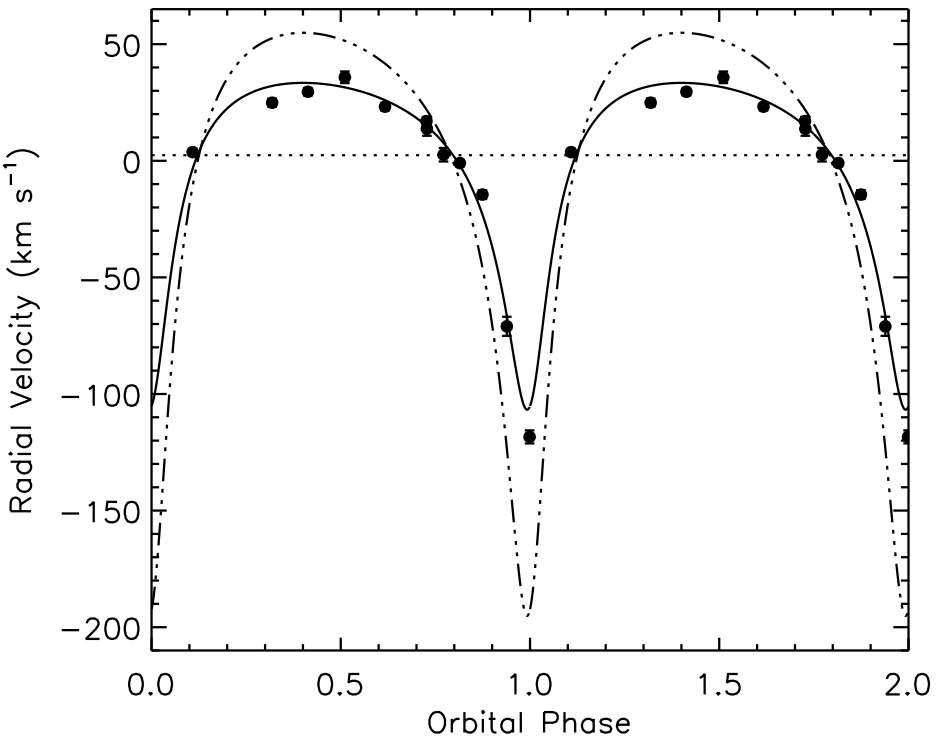

Figure 4.6: Radial velocity curve and orbital solutions for the eclipsing SB1 HDE 303312. The solid line shows the best-fitting orbital solution to the RV data, with the period and eccentricity fixed at 9.4111 d and 0.57, respectively; the horizontal dashed line marks the systemic velocity from this fit. The dot-dash line shows a sample orbit with a higher fixed semi-amplitude (K_1 = 125 km s^{-1}) that better reproduces the observed ASAS V-band eclipse depths.

the ASAS data prevents us from putting strong constraints on the stellar radii, but if we assume values appropriate for those spectral types, the depth of the secondary eclipse would be < 0.01 mag (making it undetectable in the ASAS data). Reproducing the observed secondary eclipse depth of ~ 0.1 mag with a main-sequence companion requires the secondary star to be of spectral type B2–3 V ($T_{\rm eff} \approx 20,000$ K; Kenyon and Hartmann, 1995). That star would have a mass of 8–10 $M_\odot$ (Drilling and Landolt, 2000), giving the system a mass function $f(M_1, M_2) \approx 0.7$–1.5 $M_\odot$. The corresponding semi-amplitude of the RV curve would be 110–140 km s^{-1}. An example of such an orbit, with $K_1 = 125$ km s^{-1}, is shown with a dot-dash line in Figure 4.6, and its parameters are listed in Table 4.3 in the "higher K_1" column for HDE 303312. This orbit is plausibly compatible with the RV observations around periastron, where we may be missing the most extreme RV values, but it is otherwise inconsistent with the RV data.

It is unclear why the photometric and spectroscopic observations of HDE 303312 disagree to this extent. There are no indications from the light curve that the system is currently experiencing mass transfer, but the components may have interacted in the past. In that case, our assumption that the current secondary star is on the main sequence might be incorrect. Otero (2006) also notes that the ASAS photometry of HDE 303312 suffers from contamination by nearby stars, but that would act to decrease the eclipse depths rather than the reverse. However, a close but unresolved component with constant RV could be leading us to underestimate the RVs of the primary star (for an extreme example of this phenomenon, see MT429 in Kiminki et al., 2012). Multi-wavelength photometry and additional spectroscopic phase coverage of this system are needed.

For our subsequent analysis of the Carina Nebula, we adopt the systemic velocity from the best fit to the RV data only. Forcing a higher semi-amplitude changes the systemic velocity by 2–3 km s^{-1}, which does not affect any of our cluster-scale results.

4.3.4 HDE 305536

The O9.5 V star (Sota et al., 2014) HDE 305536 is located close to the optical center of the open cluster Cr 228 (e.g., Wu et al., 2009), a few pc from the WNH star WR 24. Like HD 93576, it is associated with an extended arc of 8 μm emission indicative of a stellar wind bow shock, which in this case points in the general direction of Tr 16 (Sexton et al., 2015). HDE 305536 was observed multiple times by Levato et al. (1990), who detected significant RV variations and fit a rough orbit with a period of 2.018 d.

We obtained 12 CHIRON spectra of this system over 2014–2016, from which we identified a period of 1.88535 $\pm$ 0.00002 d. The parameters of the best-fitting orbital solution to our CHIRON data are given in Table 4.3 and the phase-folded RV curve is shown in Figure 4.7. For comparison, we overplot the Levato et al. (1990) data for this system, folded at our best-fitting period; `rvfit` was unable to converge on a solution when these data were included. Relative to our CHIRON measurements, the Levato et al. (1990) data appear offset by 10–30 km s^{-1} in RV and/or 0.2–0.3 in phase. As discussed in Section 4.2.4, many Levato et al. (1990) sources show unexplained RV offsets relative to later observations. In this case, the apparent phase shift may also suggest orbital precession.

The orbit of HDE 305536 is slightly eccentric with $e = 0.129 \pm 0.008$. The mass function of the system is $f(M_1, M_2) \approx 0.01$ M$_\odot$. Assuming the mass of the O9.5 V primary star is ~ 16 M$_\odot$ (Martins et al., 2005), the minimum mass of the secondary star is ~ 1.4 M$_\odot$, equivalent to a mid F-type dwarf (Drilling and Landolt, 2000).

4.3.5 Additional spectroscopic binaries

In addition to HD 93403 and the four spectroscopic binaries described above, six other stars showed significant ($P(\chi^2, \nu) < 0.01$) RV variations with amplitudes > 20 km s^{-1}. These variations are larger than typical photospheric variability (e.g., Martins et al., 2015), making these stars probable but unconfirmed spectroscopic binaries. We briefly discuss each of these sources below.

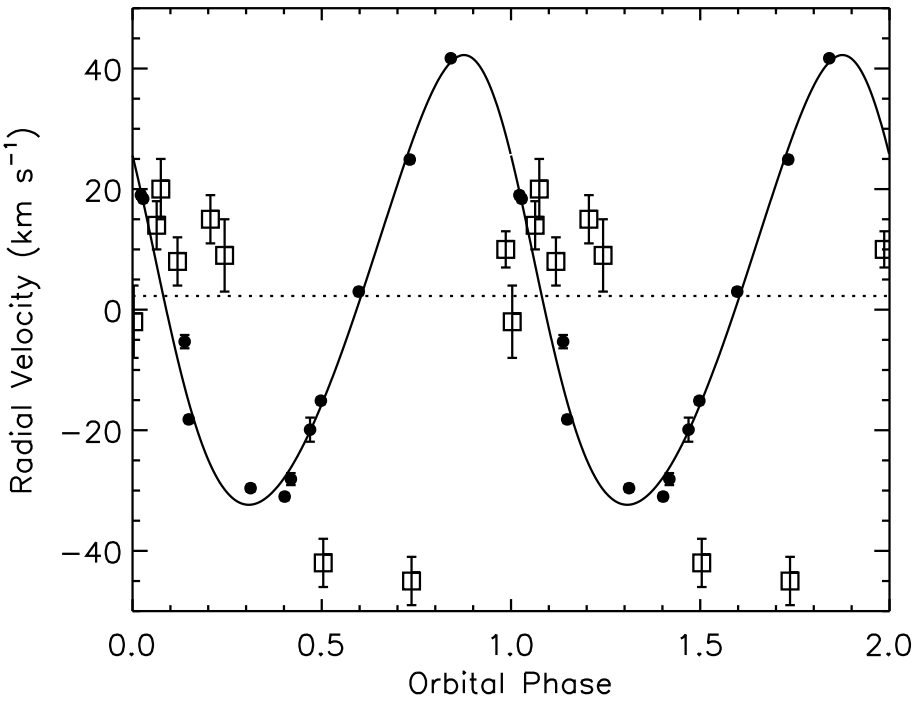

Figure 4.7: Radial velocity curve and orbital solution for the SB1 HDE 305536 at the best-fitting orbital period of 1.88535 d. Solid circles are measurements from our CHIRON spectra. Open squares are data from Levato et al. (1990), shown for comparison but not included in the orbital fit. The dotted line marks the systemic velocity.

ALS 15204: There are no literature RV data for this O7.5 V star (Sota et al., 2014) in Tr 14. We observed it three times with CHIRON in 2014. In spectra taken 16 days apart, its RV changed by more than 100 km s^{-1}. Owing to this star's relative faintness (V = 10.9 mag; Hur et al., 2012), we did not pursue follow-up observations in 2015.

ALS 15206: We observed ALS 15206, an O9.2 V star (Sota et al., 2014) in Tr 14, a total of three times with CHIRON in Dec 2014. Our observations show variability that is significant but low-amplitude (ΔRV$\sim$ 10 km s^{-1}). However, its single-epoch RV from Huang and Gies (2006) is $\sim$ 30 km s^{-1} blueshifted relative to our CHIRON numbers, suggesting a higher degree of variability. ALS 15206 is associated with an extended arc of 8 μm emission, likely a stellar wind bow shock, that points northwest toward the center of Tr 14 (Sexton et al., 2015). It has a local proper motion of $\lesssim$ 30 km s^{-1}, directed to the northeast (Kiminki et al., 2017). As with ALS 15204, we did not pursue follow-up CHIRON observations because this star is relatively faint at visual magnitudes (V = 10.7 mag; Hur et al., 2012)

ALS 15207: This O9 V star (Sota et al., 2014) in Tr 14 was flagged by Levato et al. (1991a) as an SB2; however, García et al. (1998) observed no line doubling nor any significant RV variations. We obtained a total of seven CHIRON spectra of ALS 15207 in 2014–2015; like García et al. (1998), we found that its He I and He II absorption lines were well fit with single Gaussian profiles. We measured RVs ranging from $-$21.5 km s^{-1} to +15.0 km s^{-1} but were unable to constrain the period of the variability.

CPD-59 2554: Although this O9.5 IV star (Sota et al., 2014) in Cr 228 was observed by Levato et al. (1990) to be a constant-RV source, our nine CHIRON spectra from 2014–2015 show significant variability, with RVs ranging from $-$22.7 km s^{-1} to +63.4 km s^{-1}. We were unable to constrain the period of the variability.

HD 93028: This O9 IV star (Sota et al., 2014) is located about 6 pc southwest of the center of Cr 228. Levato et al. (1990) identified it as a spectroscopic binary and fit a rough orbit with a period of 51.554 d. We obtained four CHIRON spectra of this source in 2014, which showed significant RV variations at an amplitude just

above our 20 km s^{-1} cutoff; a larger amplitude is seen when data from Feast et al. (1957) and Conti et al. (1977) are included. Sota et al. (2014) report that HD 93028 is in a long-period ($\sim$ 200 d) spectroscopic binary, but do not provide an orbital solution.

HDE 305525: At about 7 pc southwest of Tr 16, this O5.5 V star (Sota et al., 2014) is part of the distributed population in the South Pillars. Levato et al. (1990) detected significant RV variability in its spectra but were unable to find an orbital solution. Our eight CHIRON spectra from 2014–2015 confirm RV variations with an amplitude of more than 130 km s^{-1}. Like Levato et al. (1990), we were unable to constrain the period of the variability.

4.4 Results and Discussion

4.4.1 Distribution of stellar radial velocities

Combining new spectroscopy with literature data, we have compiled heliocentric RVs for 59 O-type systems in the Carina Nebula, as well as for the LBV η Car and the three WNH stars in the region. We present a histogram of these RVs in Figure 4.8. The stars are divided into three groups, characterizing the likelihood that the observed RVs represent their true systemic motions. The first group, shown in light gray in Figure 4.8, are sources with relatively reliable RVs. These are spectroscopic binaries with well-constrained orbital solutions, for which we plot the computed systemic velocity, as well as stars with no known RV variability or insignificant or low-amplitude RV variability, for which we plot the weighted mean of the observed RVs. In total, this group, which we will henceforth refer to as the "well-constrained sources," consists of η Car and 40 O-type stars. The weighted mean RV of the well-constrained sources is 0.6 km s^{-1}, with a standard deviation of 9.1 km s^{-1}.

The second group of sources, shown in dark gray in Figure 4.8, are those that have been identified as spectroscopic binaries but lack orbital solutions. These include stars that were identified as SB1s or SB2s in the multiplicity survey of Chini et al. (2012), stars with binarity flagged elsewhere in the literature, and stars

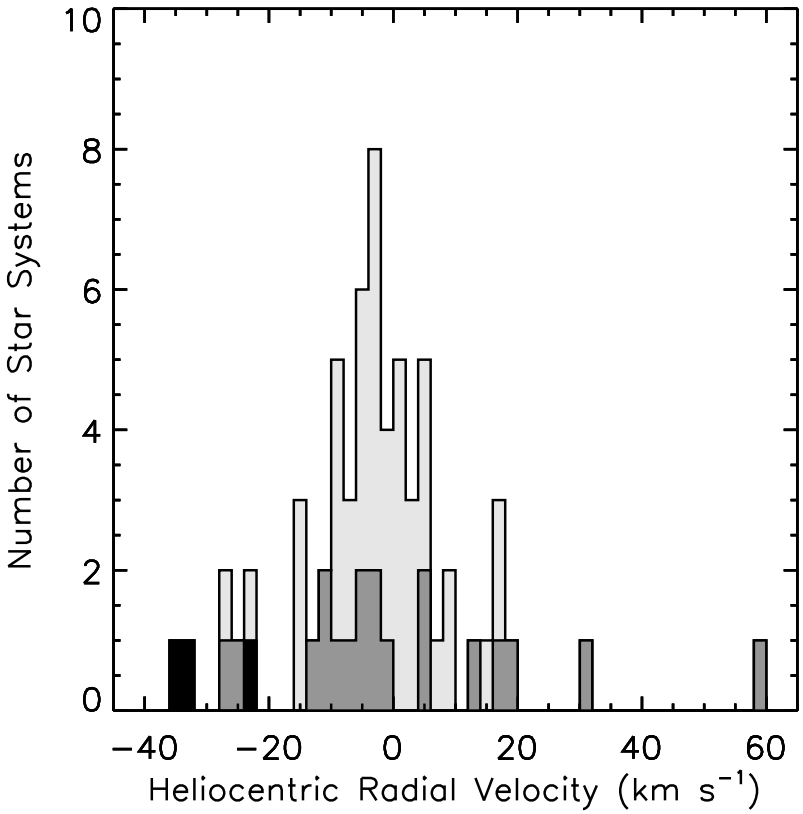

Figure 4.8: Histogram of the heliocentric radial velocities of the O-type and evolved massive stars in the Carina Nebula. Well-constrained sources (solved spectroscopic binaries and stars with little to no RV variation) are shown in light gray. Unsolved binaries are shown in dark gray. The three WNH stars, whose apparent RVs are affected by strong stellar winds, are indicated in black.

whose CHIRON and/or literature RVs display significant variability with amplitudes > 20 km s^{-1}. We refer to this group of 19 O-type systems as the "unsolved binaries." For each system, we plot the weighted mean of its measured RVs, but caution that this number may not be representative of its true systemic velocity, especially for systems with few published RVs. For instance, the most notable outlier in Figure 4.8 is HD 93130, for which there is only a single published RV (59.9 km s^{-1}; Conti et al., 1977). However, Chini et al. (2012) identified HD 93130 as an SB2, making it likely that its outlying RV is the result of its binarity rather than its relationship with the Carina Nebula. The overall weighted mean RV of the well-constrained sources and the unsolved binaries together remains at 0.6 km s^{-1}, while the standard deviation of the distribution increases to 13.5 km s^{-1}.

The third group of sources, shown in black in Figure 4.8, are the WNH stars. As discussed in Section 4.2.4, the strong stellar winds of Wolf-Rayet stars influence their spectral features, often shifting the observed RVs to more negative values. Although we have adopted the RVs of narrow metal emission lines, thought to be among the spectral features least affected by winds (e.g., Conti et al., 1979), the three WNH stars still show an RV offset of ~ 30 km s^{-1} relative to the O-type stars and η Car. The magnitude of this offset is similar to the difference seen by Schweickhardt et al. (1999) between the observed systemic velocities of WR 22 and its O-type companion. Although we cannot rule out the possibility that Carina's three WNH stars are moving toward us at outlying velocities after being ejected from the region's clusters, the consistency of their RV offsets strongly suggests that we are seeing the effect of winds instead.

The overall RV distribution in Figure 4.8 is unimodal, consistent with the various clusters and subclusters of the Carina Nebula being part of a single complex at a common distance. We do not see any probable runaway stars. Aside from WR 24 and WR 25, only HD 93130 has an RV that deviates from the region's mean by ≥ 30 km s^{-1}, and as described above, HD 93130 is a poorly-studied spectroscopic binary and its given RV is unlikely to be its true systemic velocity. However, with RV data, we cannot rule out the presence of runaways with high tangential velocities. Our

region of study extends $\sim$ 20 pc in all directions from Tr 16, meaning a star with a tangential velocity of 30 km s^{-1} would have exited our field in $\sim 600,000$ yr. An O-type star ejected by the recent supernova explosion of its companion (see, e.g., Blaauw, 1961) might still appear to be within the coordinates of the Carina Nebula, but we see no evidence for this in the RV data.

The standard deviation of the RVs of the well-constrained sources, 9.1 km s^{-1}, is an upper limit on the true one-dimensional velocity dispersion of the Carina Nebula, as this group of sources may still contain long-period spectroscopic binaries or other undetected RV variables. Typical OB associations like Scorpius-Centaurus and Perseus OB2 have one-dimensional velocity dispersions of 1–3 km s^{-1} (de Bruijne, 1999; Steenbrugge et al., 2003), but these associations are substantially smaller in mass and extent—and slightly older—than the Carina Nebula complex (see Bally, 2008; Preibisch and Mamajek, 2008). More directly comparable to the Carina Nebula is the Cygnus OB2 association, which contains $>$ 50 O-type stars distributed across tens of parsecs (Massey and Thompson, 1991; Wright et al., 2015). In both tangential and radial velocities, the one-dimensional velocity dispersion of Cyg OB2 is $\sim$ 10 km s^{-1} (Kiminki et al., 2007, 2008; Wright et al., 2016), similar to what we have measured for the O-type stars in the Carina Nebula. This is about a factor of two higher than the velocity dispersions seen in the massive, compact starburst clusters R136 (Hénault-Brunet et al., 2012), NGC 3603 (Rochau et al., 2010), and the Arches Cluster (Clarkson et al., 2012).

4.4.2 Variations between clusters

In Figure 4.9, we separate out and compare the RVs of the O-type and evolved massive stars in Tr 14 and Tr 16. We define membership in each cluster as being within a projected 5′ of the cluster center. This is the observed radius of Tr 14's pre-main-sequence population (Ascenso et al., 2007) and a natural break in its O-star distribution. Tr 14 contains six O-type stars with well-constrained RVs and an additional nine unsolved binaries. Tr 16 is larger and less well-defined than Tr 14, and is elongated rather than spherical (e.g., Feigelson et al., 2011), and so is

poorly defined by a single radius. With a 5′ cutoff, Tr 16 contains 11 sources with well-constrained RVs (including η Car), and three unsolved binaries. As we describe below, increasing the radius of Tr 16 slightly increases its velocity dispersion but has little effect on the weighted mean of its RV distribution.

The cumulative histograms in Figure 4.9 suggest that the O-type stars in Tr 14 might have slightly more positive RVs, on average, than those in Tr 16. The weighted mean of the well-constrained sources in Tr 14 is 2.4 ± 7.3 km s^{-1}, in agreement with the 2.8 ± 4.9 km s^{-1} measured by Penny et al. (1993) and the 6.0 ± 1.4 km s^{-1} found by García et al. (1998). In comparison, the weighted mean of the well-constrained sources within a 5′ radius of Tr 16 is -3.5 ± 8.6 km s^{-1}. Increasing the radius of Tr 16 to 10′ changes this to -3.3 ± 10.4 km s^{-1}. To evaluate the significance of the apparent RV difference between clusters, we ran a two-sided Kolmogorov-Smirnov (K-S) test, which evaluates the probability that the two clusters were drawn from the same RV distribution. We estimated the uncertainty on the K-S probability by drawing 10^4 combinations of each cluster's RVs, randomly permuting each star's RV within a Gaussian distribution with a standard deviation corresponding to that star's observed RV uncertainty. For the well-constrained sources (the top panel of Figure 4.9), the probability that the two clusters come from the same RV distribution is $4 \pm 11\%$, meaning the difference in RVs is marginally significant. Including unsolved binaries (as in the bottom panel of Figure 4.9) brings the probability of a shared RV distribution to $16 \pm 25\%$, indicating that the difference is not significant. Further study of the kinematics of Tr 14 and Tr 16 are needed to determine if any overall RV difference persists in their lower-mass stellar populations. Damiani et al. (2017) found a mean RV of -5 km s^{-1} for the FGK-type populations of Tr 14 and Tr 16 combined, with no apparent bimodality in their RV distribution, but they did not attempt to separate their stars by cluster.

In Figure 4.10, we search for any additional cluster-scale or spatial dependencies by mapping our RVs as a function of position. The circle representing each star is scaled by the magnitude of its mean/systemic RV and color-coded as redshifted (positive RV) or blueshifted (negative RV). The left-hand plot includes only

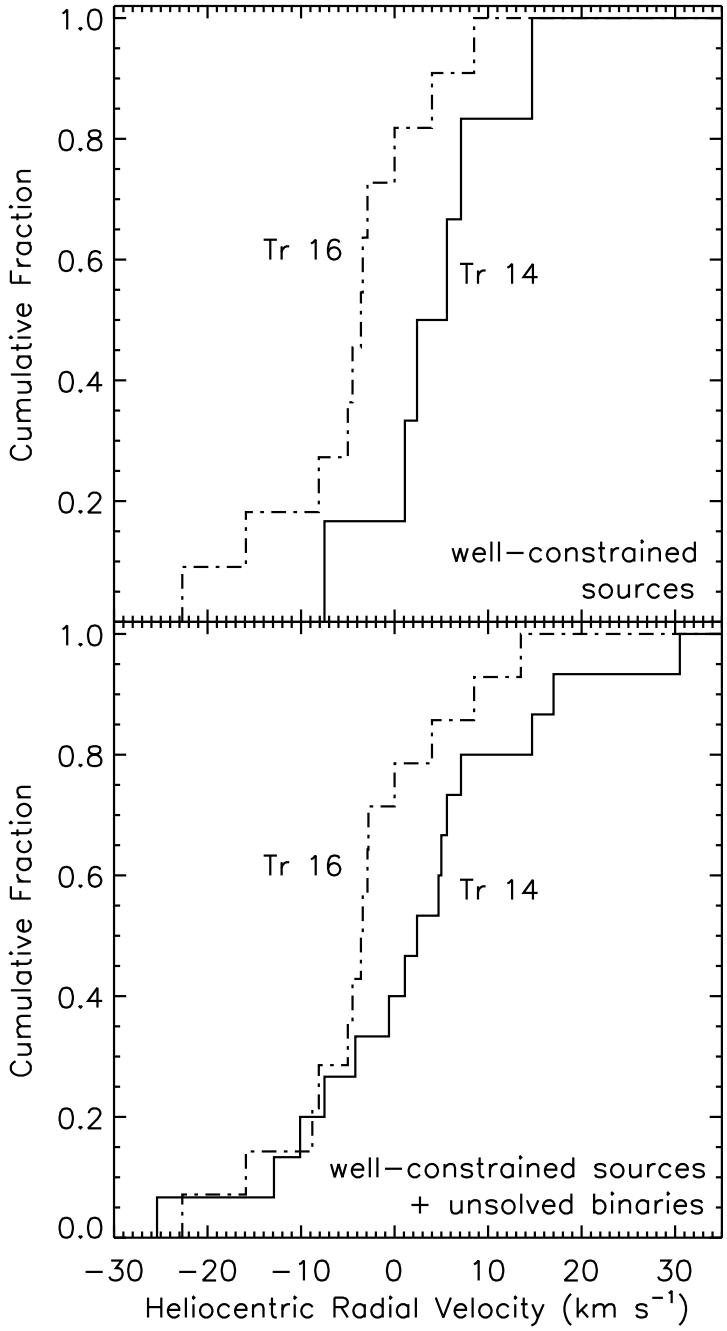

Figure 4.9: Cumulative histograms of the heliocentric radial velocities of O-type stars in Tr 14 (solid line) and O-type stars and η Car in Tr 16 (dot-dash line). Both clusters are defined with a radius of 5′. Top: stellar systems with well-constrained RVs (either solved spectroscopic binaries or sources with little to no RV variation). Bottom: as above, but including the mean RVs of unsolved spectroscopic binaries.

those sources with well-constrained RVs, while the right-hand plot shows both the well-constrained sources and the unsolved binaries. For clarity, we mark only the positions and not the RVs of the three WNH stars.

The apparent velocity difference between Tr 14 and Tr 16 is visible in Figure 4.10, in that the former has more red (positive-RV) sources than the latter. Another notable structure is the grouping of O-type stars extending from the nominal center of Cr 228 up toward Tr 16. These sources have low-magnitude RVs and appear as a sequence of relatively small circles. Their weighted mean RV (0.3 km s^{-1}) is similar to that of the region as a whole, but their velocity dispersion (4.0 km s^{-1}) is comparatively small. This relatively low velocity dispersion suggests that this string of massive stars formed in place; we would expect a population that had migrated out from Tr 16 to have a higher velocity dispersion than the cluster rather than vice versa.

4.4.3 Comparison to molecular gas

The molecular cloud complex associated with the Carina Nebula is composed of three main parts (de Graauw et al., 1981; Brooks et al., 1998; Yonekura et al., 2005; Rebolledo et al., 2016). The Northern Cloud partially surrounds Tr 14 and extends to the northwest (de Graauw et al., 1981; Brooks et al., 2003), where it connects to additional molecular material around the Gum 31 H II region (e.g., Rebolledo et al., 2016). The Southern Cloud coincides with the optically dark lane between Tr 16 and the South Pillars (de Graauw et al., 1981). The South Pillars are themselves composed of molecular gas, shaped by feedback from Carina's OB stars (Rathborne et al., 2004; Yonekura et al., 2005; Rebolledo et al., 2016). Within Tr 16 there are only scattered molecular globules, thought to be the remnants of the gas from which that cluster formed (Cox and Bronfman, 1995; Brooks et al., 2000).

Rebolledo et al. (2016) observed the Carina Nebula in ^{12}CO (1–0) emission as part of the Mopra Southern Galactic Plane CO Survey (Burton et al., 2013). We use their data to compare the kinematics of Carina's molecular gas to the RVs of its O-type and evolved massive stars. For Figures 4.11 and 4.12, we collapse their three-

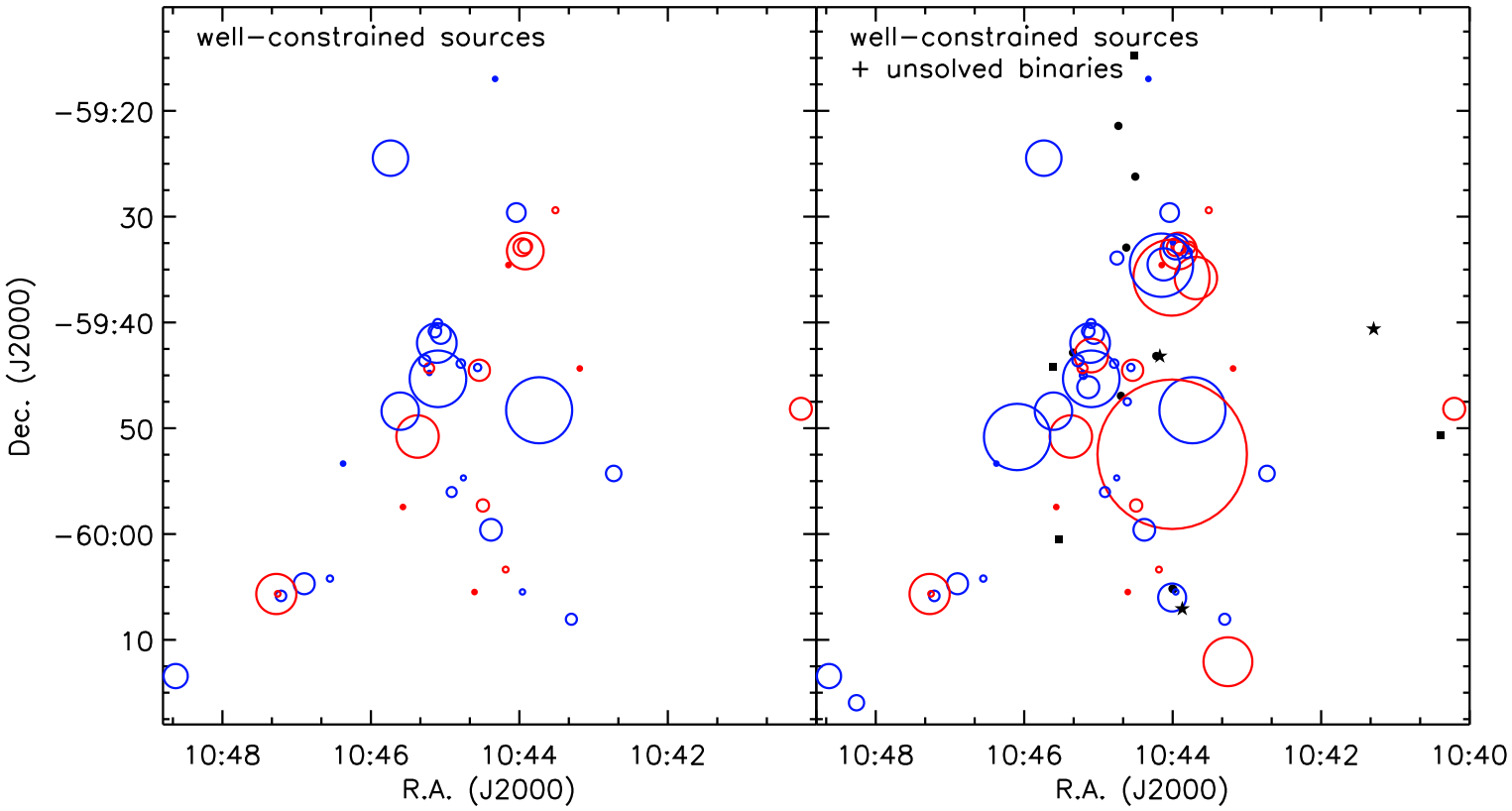

Figure 4.10: Maps of the heliocentric radial velocities of O-type and evolved massive stars in the Carina Nebula. Left: stars (including η Car) with well-constrained RVs as defined in the text. Blue circles indicate negative RVs and red circles indicate positive RVs; circle size scales with the magnitude of the velocity. Right: as left, but including known spectroscopic binaries that lack orbital solutions. The filled black circles and squares show the positions of O-type stars from v3.1 of the GOSC and from Alexander et al. (2016), respectively, that lack RV data. The positions of the three WNH stars are shown by black filled stars.

dimensional data cubes along Galactic latitude and Galactic longitude, respectively, to present two-dimensional position–velocity diagrams of the dense gas in Carina. We convert the gas velocities from the Local Standard of Rest to a heliocentric frame. At the coordinates of the Carina Nebula, $RV_{helio} \approx RV_{LSR} + 11.6$ km s^{-1}. All RVs in the following discussion are heliocentric unless otherwise noted.

Figure 4.11 plots the RVs of the Carina Nebula's O-type stars, evolved massive stars, and ^{12}CO (1–0) emission as a function of Galactic longitude l. The ^{12}CO fluxes from Rebolledo et al. (2016) are summed across Galactic latitudes $-1.4 \leq b \leq 0.1°$. As in Figure 4.8, the stars are divided into three groups: stars (including η Car) with well-constrained systemic velocities, unsolved binaries, and WNH stars. We also indicate the approximate heliocentric velocities of the redshifted and blueshifted components of ionized gas emission lines observed by Damiani et al. (2016) for shells centered on the locations of η Car, WR 25, and Tr 14. In Figure 4.12, we present the same data, but plotted as a function of Galactic latitude b. The ^{12}CO fluxes are summed across Galactic longitudes $287.0 \leq l \leq 288.4°$.

The three components of Carina's molecular cloud complex separate cleanly when plotted against Galactic latitude in Figure 4.11: the Northern Cloud at $l \approx$ 287.0–287.5° with heliocentric RV $\approx (-10)$–0 km s^{-1}; the Southern Cloud at $l \approx$ 287.6–287.8° with heliocentric RV $\approx (-15)$–(-10) km s^{-1}; and the South Pillars at $l \approx$ 287.9–288.2° with heliocentric RV $\approx (-10)$–(-5) km s^{-1} and a smaller part at ~ 0 km s^{-1}. The separation is less notable in Figure 4.12, as the sourthern part of the Northern Cloud overlaps with the Southern Cloud in Galactic longitude, but the RV offset in the Southern Cloud is still apparent. The molecular gas at $l \approx$ 287.7–287.8° , $b \approx -0.4$, with heliocentric RV $\sim +20$ km s^{-1}, is thought to be associated with the far side of the Carina arm, at a greater distance than the Carina Nebula (Damiani et al., 2016).

Figures 4.11 and 4.12 further emphasize that the RVs of the O-type stars in the Carina Nebula are not spatially dependent, as there is no trend in O-star RVs with Galactic longitude or latitude. Rebolledo et al. (2016) applied the four-arm Milky Way model of Vallée (2014) to the rotation curve of McClure-Griffiths and Dickey

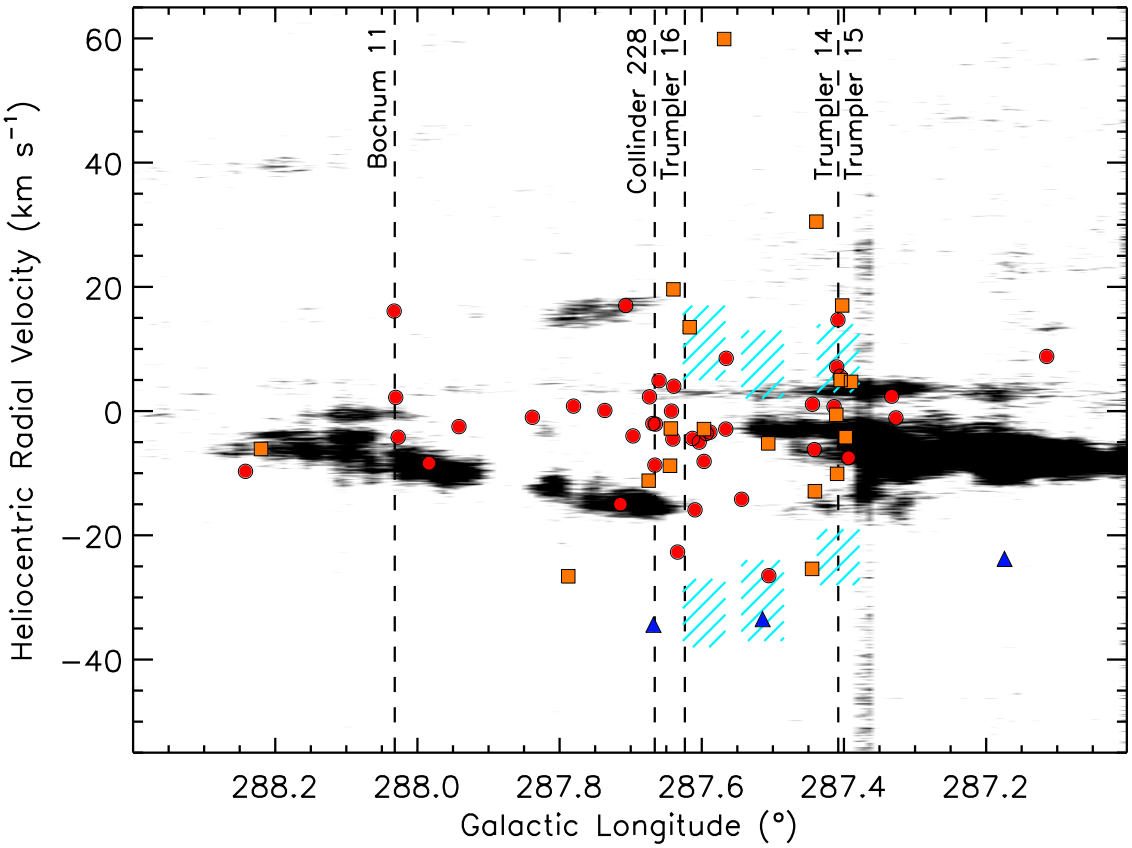

Figure 4.11: Position-velocity diagram of ^{12}CO (1–0) emission (gray-scale) from Rebolledo et al. (2016, converted to a heliocentric frame) compared to O-type and massive evolved stars. Red circles are systems (including η Car) with well-constrained radial velocities, orange squares are known or suspected spectroscopic binaries that lack orbital solutions, and blue triangles are WNH stars. The hatched cyan regions show the RVs of the approaching and receding components of emission from ionized gas (Damiani et al., 2016) centered on the positions of η Car, WR 25, and Tr 14.

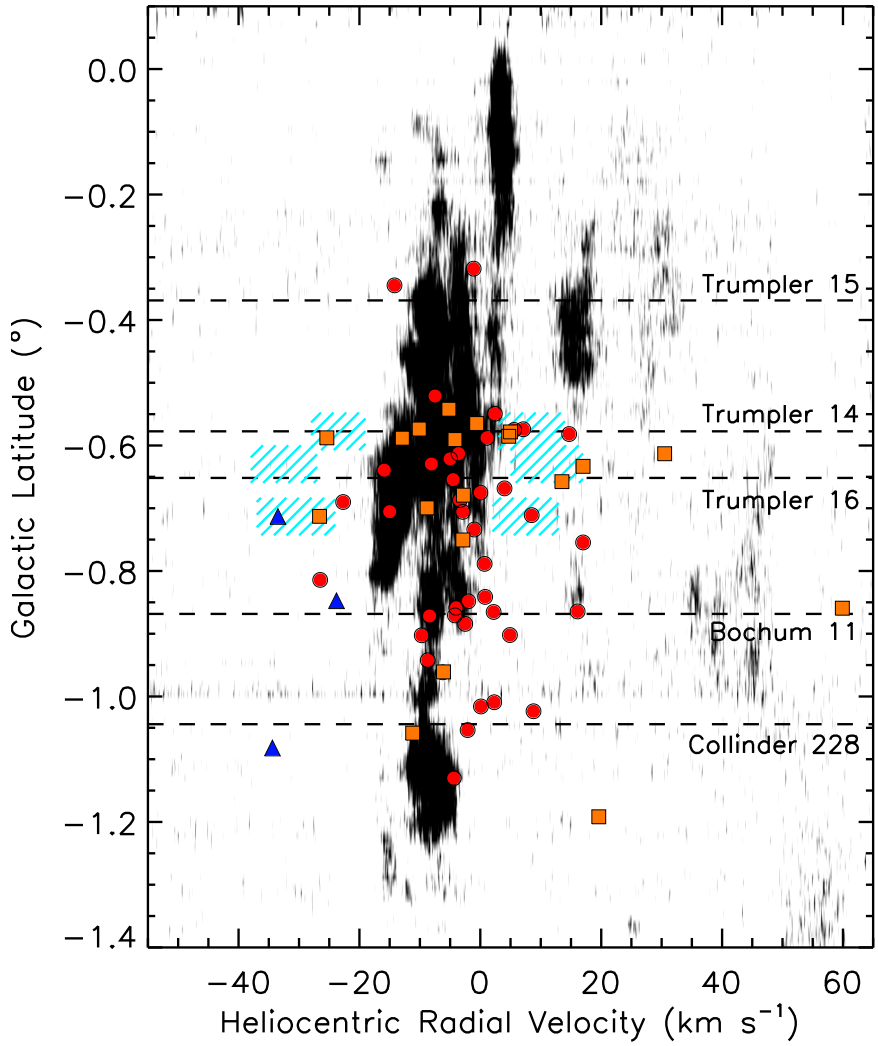

Figure 4.12: Similar to Figure 4.11, but showing the heliocentric radial velocities of ^{12}CO, ionized gas, and stars as a function of Galatic latitude.

(2007) and calculated the expected RV for objects at various distances along the tangent of the Carina spiral arm. For sources on the near side of the arm, at ~ 2 kpc, the expected Local Standard of Rest RV is approximately -10 km s^{-1}, which corresponds to a heliocentric RV of $\approx +2$ km s^{-1}, very close to the observed mean RV of the O-type stars. Objects at greater distances from the Sun would be expected to have more positive RVs (see Rebolledo et al., 2016). Our RV results thus favor the OB clusters and groups in the Carina Nebula being at a common distance of approximately 2 kpc.

Tr 14, Tr 15, and the Northern Cloud:

There is a general consensus that the relatively compact Tr 14 is the youngest of the Carina Nebula's Trumpler clusters, at just 1–2 Myr old (Walborn, 1973, 1982a,b, 1995; Morrell et al., 1988; Vazquez et al., 1996; Smith and Brooks, 2008; Rochau et al., 2011). The case for its youth is strengthened by its close spatial association with the Northern Cloud, which wraps around the west side of the cluster (de Graauw et al., 1981; Brooks et al., 2003; Tapia et al., 2003). Bright radio emission arises from multiple ionization fronts where radiation from Tr 14 impacts dense clumps in the Northern Cloud (Whiteoak, 1994; Brooks et al., 2001). It is clear from Figures 4.11 and 4.12 that the O-type stars in Tr 14 are also kinematically associated with the Northern Cloud, further strengthening the picture of Tr 14 as a young cluster that has not yet dispersed its natal molecular gas.

While Tr 15 has sometimes been considered an unrelated foreground or background cluster (Thé and Vleeming, 1971; Walborn, 1973), its extended X-ray stellar population indicates a connection to Tr 14 (Feigelson et al., 2011; Wang et al., 2011). We have RV data for only two O-type stars around Tr 15, HD 93403 and HD 93190, which appear at $b \sim -0.35°$ in Figure 4.12. Their RVs are consistent with those of the rest of the O-type stars in the Carina Nebula, and span the RV range of the Northern Cloud. Both are 4–5 pc outside the core of Tr 15, and neither is associated with any group or subcluster (see Feigelson et al., 2011). Tr 15 is likely several Myr older than Carina's other Trumpler clusters (Carraro, 2002; Tapia et al., 2003;

Wang et al., 2011), and it seems likely that these two stars drifted out from Tr 15 over the course of their lifetimes.

Off the southern edge of the Northern Cloud, on the far west side of the Carina Nebula (see Figure 4.1), there are several O-type and evolved massive stars, notably WR 22 and HD 92607. There is a young (< 1 Myr) pre-main-sequence population in this region, although it does not show any clustering around the massive stars (Kumar et al., 2014). WR 22 is a particularly puzzling system: it is a very massive binary ($\sim$55-$M_\odot$ primary; Schweickhardt et al., 1999) approximately 21′ (15 pc) from Tr 14, without any subcluster or group of its own. Its observed RV is roughly 10 km s^{-1} less negative than the RVs of WR 24 and WR 25, but it is unclear whether this represents a true difference in their systemic motions or whether it is the result of uncharacterized wind effects.

The SB2 HD 92607 (see Section 4.3.1), evident on the far right side of Figure 4.11, is less extreme in mass but still somewhat puzzling in origin. Its systemic RV (8.7 km s^{-1}) is relatively positive for an O-type system in the Carina Nebula, although still within one standard deviation of the mean. And despite its proximity to the Northern Cloud, it lacks a kinematic association with the molecular gas—perhaps a hint that it did not form in its currently observed location. HD 92607 is associated with a candidate bow shock in the form of a resolved 24 μm arc pointing to the southeast (Sexton et al., 2015), which might suggest an origin outside the Carina Nebula. However, in the active environment of this giant H II region, bow shocks are not clear indicators of stellar motion (Kiminki et al., 2017). Its spectroscopic parallax (using data from Martins et al., 2005; Gagné et al., 2011; Povich et al., 2011a) and preliminary geometric parallax from *Gaia* DR1 (Gaia Collaboration et al., 2016a,b; Lindegren et al., 2016) are both consistent with HD 92607 being part of the Carina Nebula at a distance of around 2 kpc.

Tr 16 and the Southern Cloud:

Unlike the Northern Cloud, which has a close kinematic association with the Tr 14 cluster, the Southern Cloud is offset by 10–15 km s^{-1} in RV from its neighbor

Tr 16. The Southern Cloud has the most negative RVs of the molecular gas in Carina, being 5–10 km s^{-1} blueshifted relative to both the Northern Cloud and the molecular gas in the South Pillars. It coincides with a prominent, optically dark dust lane, indicating that it lies in front of the southeastern edge of Tr 16 (Dickel, 1974; de Graauw et al., 1981; Brooks et al., 1998). Inside Tr 16 itself, there are only small clumps of molecular gas (not visible in the Rebolledo et al. 2016 data), and these have RVs more consistent with those of the O-type stars in the cluster (Cox and Bronfman, 1995; Brooks et al., 2000).

One of the key arguments in favor of Tr 16 being 1–2 Myr older than Tr 14 (e.g., de Graauw et al., 1981; Walborn, 1995) is that the latter (in addition to being more compact) is still partially enclosed by its natal molecular cloud, while the former appears to have disrupted the gas from which it formed. The distribution of gas RVs in Figure 4.11 suggests that the Nothern Cloud, Southern Cloud, and Southern Pillars were originally part of a single continuous molecular cloud, with the massive stars in Tr 16 having since blown out the central part of that cloud. The Northern Cloud, currently being eroded by Tr 14, has not been accelerated along our line-of-sight, while the molecular gas in the South Pillars has undergone some acceleration at its closest approach to Tr 16.

The acceleration of the Southern Cloud by the O-type stars in Tr 16 is readily explained by the rocket effect (Oort and Spitzer, 1955; Bally and Scoville, 1980; Bertoldi and McKee, 1990). As the neutral gas facing Tr 16 is ionized by the strong ultraviolet radition of the cluster (Smith, 2006a), it flows away from the surface of the molecular cloud at roughly its sound speed. The recoil force on the molecular cloud causes it to accelerate away from the ionizing source at a rate proportional to the rate at which it loses mass through ionization. In the simplest scenario, assuming the cloud is initially at rest relative to the ionizing source, the cloud mass and velocity are connected through (Spitzer, 1978):

$$M_c = M_0 e^{-v_c/V_{ion}}, \tag{4.1}$$

where M_0 and M_c are the initial and current masses of the molecular cloud, respec-

tively, v_c is the current velocity of the cloud, and V_{ion} is the velocity with which the newly ionized material flows away from the cloud. For the molecular cloud to have been accelerated to ∼10 km s^{-1}, roughly the speed of sound in ionized gas, the cloud's mass must have decreased by ∼60%. The current mass of the Southern Cloud is $\sim 5 \times 10^4$ M$_\odot$ (Rebolledo et al., 2016). Accounting only for mass loss through ionization, its initial mass would have been on the order of 1.3×10^5 M$_\odot$, comparable to the current mass of the Northern Cloud (Yonekura et al., 2005; Rebolledo et al., 2016).

Noteworthy among the O-type stars in Tr 16 is V662 Car at $l = 287.7°$, $b = -0.7°$, an eclipsing spectroscopic binary with a systemic velocity of -15 ± 2 km s^{-1} (Niemela et al., 2006). V662 Car is the only O-type star to coincide with the Southern Cloud in three-dimensional position–velocity space, and its relatively high visual extinction (Smith, 1987; Povich et al., 2011b) suggests that it is behind or within the molecular gas. The primary star's spectrum has unusually strong He II λ4686 (Niemela et al., 2006), leading it to be assigned to the luminosity class Vz (Sota et al., 2014), which is associated with very young O-type stars close to the zero-age main sequence (Walborn, 2009; Sabín-Sanjulián et al., 2014; Walborn et al., 2014; Arias et al., 2016). Roughly a dozen of the O-type stars in the Carina Nebula are of class Vz (Sota et al., 2014), with the highest fraction relative to non-z O dwarfs found in Tr 14 (Arias et al., 2016). In addition, Niemela et al. (2006) found that both components of V662 Car have smaller radii and luminosities than expected for their spectral types, another indicator of youth. The combination of V662 Car's young age, its deviation from the mean RV of the O-type stars in Tr 16, and its kinematic association with the Southern Cloud suggest that it was formed separately from and more recently than the body of Tr 16. We propose that its formation may have been triggered by the feedback-induced acceleration of the Southern Cloud.

Cr 228, Bo 11, and the molecular gas in the South Pillars:

The relationship between the O-type stars in Bo 11 and Cr 228 and the molec-

ular gas in the South Pillars is difficult to interpret, because the gas detected in ^{12}CO is spatially separate from the O-type stars. Most of the ^{12}CO (1–0) emission in the South Pillars comes from the so-called Giant Pillar (Smith et al., 2000; Yonekura et al., 2005; Smith et al., 2010c), a dusty structure that points toward Tr 16 from the southernmost part of the region, lying roughly halfway between Bo 11 and the nominal center of Cr 228. The Giant Pillar is the site of current star formation (Smith et al., 2010c; Gaczkowski et al., 2013), but is $\geq$ 4 pc from any O-type stars. Its gas has heliocentric RVs of (−10)–(−5) km s^{-1}, similar to the Nothern Cloud. Another dusty structure, whose ionization fronts also face Tr 16, is spatially coincident with Bo 11. Some ^{12}CO (1–0) emission, too faint to appear in Figures 4.11 and 4.12, is detected in this region (Rebolledo et al., 2016), but it has a heliocentric RV of $\gtrsim$ 30 km s^{-1} and likely belongs to the far side of the Carina spiral arm.

Most of the O-type stars in Bo 11 have RVs similar to the rest of the O-type stars in the Carina Nebula and comparable to the gas in the South Pillars. The exception is HDE 305612, which, with a measured mean RV of 16.1 km s^{-1}, appears to be a notable outlier. However, HDE 305612 shows significant RV variation over three epochs of CHIRON data—but was not flagged as an unsolved binary because the amplitude of that variation is $<$ 20 km s^{-1}.

The O-star population of Cr 228 also has similar RVs to the rest of the region; in Figure 4.11, it is indistinguishable from the O-star population of Tr 16. None of the many smaller dust pillars around Cr 228 (Smith et al., 2010c) are detected in ^{12}CO (1–0) emission (Rebolledo et al., 2016), ruling out a direct comparison between the RVs of stars and gas in this part of the Carina Nebula. As discussed in Section 4.4.2, the O-type stars in and around Cr 228 have a lower velocity dispersion than the region as a whole, suggesting that they were not scattered out of Tr 16.

In the far southeast corner of the Carina Nebula, approximately 12.5′ ($\sim$8 pc) from Bo 11, are HD 93843 and HDE 305619. These two stars are clearly visible on the left side of Figure 4.11 as the two O-type systems with the highest Galactic longitudes. They are typically treated as members of the Carina Neb-

ula complex (e.g., Gagné et al., 2011), although there are no known gas structures or lower-mass stellar populations connecting them to the rest of the South Pillars (e.g., Smith et al., 2010c). The spectroscopic parallax of HDE 305619 (using data from Kharchenko, 2001; Martins et al., 2005; Kharchenko and Roeser, 2009; Gagné et al., 2011; Sota et al., 2014) suggests that it might be in the background at a distance of > 3 kpc, but the *Gaia* DR1 parallaxes of both it and HD 93843 (Gaia Collaboration et al., 2016a,b; Lindegren et al., 2016) place both systems at 2.0–2.5 kpc. Their observed RVs are also consistent with being part of the Carina Nebula complex, although HDE 305619 is an SB1 (Chini et al., 2012) with limited published RV data.

4.4.4 Comparison to ionized gas

The ionized gas in the Carina Nebula is globally expanding at ±15–20 km s^{-1}, as seen in radio recombination lines (Gardner et al., 1970; Huchtmeier and Day, 1975; Azcarate et al., 1981; Brooks et al., 2001) and optical line emission (Deharveng and Maucherat, 1975; Walborn and Hesser, 1975; Walsh, 1984; Smith et al., 2004). This expansion is driven by feedback from Carina's O-type and evolved massive stars (Smith and Brooks, 2007). It was most recently mapped by Damiani et al. (2016), who observed more than 650 optical sightlines across Tr 14 and Tr 16. They identified three non-spherical expanding shells, roughly centered on the positions of η Car, WR 25, and Tr 14. We represent these shells in Figures 4.11 and 4.12 with hatched regions showing the range of observed approaching and receding RVs for each shell. Damiani et al. (2016) estimate that the overall expansion is centered around an RV of -12.5 km s^{-1}. Their Tr 14 shell is centered around a slightly less negative -8 km s^{-1}. These values agree with prior results: Walborn (1973); Walborn et al. (2002a, 2007) place the kinematic center of the expansion at -14 km s^{-1}, and radio data (Gardner et al., 1970; Huchtmeier and Day, 1975; Azcarate et al., 1981) consistently centers the expansion at a heliocentric RV of -9 km s^{-1}.

However, the RV distribution of Carina's O-type and evolved massive stars is

not aligned with the expansion of the ionized gas. As described in Section 4.4.1, the weighted mean RV of the well-constrained O-type stars is 0.6 ± 9.1 km s^{-1}, putting the kinematic center of the ionized gas expansion roughly one standard deviation blueward of the mean O-star RV. Figures 4.11 and 4.12 show that the receding/redshifted components of the gas overlap in RV space with the positive-RV tail of the O-star distribution, while the approaching/blueshifted components of the gas have more negative RVs than nearly all of the O-type stars. The observed RVs of the WNH stars, including WR 25, agree with the RVs of the approaching gas, but this is due to wind effects in the WNH spectra and not due to a physical association.

The most likely explanation for the kinematic asymmetry between the gas and the O-type stars is that the receding/redshifted ionized gas is bounded by dense, neutral material behind the Carina Nebula, while the approaching/blueshifted ionized gas moves freely along our line of sight. In addition, the approaching gas around Tr 16 may be partially composed of a photoevaporative flow off the Southern Cloud, which has already been accelerated toward us by feedback from Tr 16 (see discussion above). Damiani et al. (2016) noted a number of smaller-scale kinematic asymmetries in the ionized gas shells, confirming that the expansion of the H II region is non-spherical and is affected by density variations in the surrounding medium. We consequently caution against using the kinematic center of the ionized gas to define the systemic RV of the Carina Nebula.

4.5 Conclusions

We have conducted a radial velocity survey of the O-type and evolved massive stars in the Carina Nebula. We obtained multi-epoch echelle spectroscopy for 31 O-type stars, and compiled published RVs for an additional 32 systems including three WNH stars and the LBV η Car. With these data, we find the first spectroscopic orbital solutions for the near-twin system HD 92607 and the eclipsing binary HDE 303312 and provide updated orbital solutions for HD 93576 and HDE 305536. Our

further results are summarized as follows:

(1) Of the 63 O-type and evolved massive star systems with RV data, 41 have well-constrained systemic velocities. These well-constrained sources have a weighted mean RV of 0.6 km s^{-1}, comparable to prior results for the Tr 14 cluster and to the expected radial motion for sources at a distance of ~ 2 kpc along the Carina spriral arm.

(2) The one-dimensional velocity dispersion is ≤ 9.1 km s^{-1}, the standard deviation of the sources with well-constrained RVs. This value is high compared to typical, less massive OB associations and is roughly twice that of massive bound starburst clusters. However, it is similar to the velocity dispersion of the large, unbound Cyg OB2 association, and is not unexpected for a region with the content and substructure of the Carina Nebula.

(3) The overall O-star RV distribution is unimodal, favoring a common distance to the various clusters of the Carina Nebula.

(4) There is a possible but marginally significant difference between the RV distributions of the Tr 16 and Tr 14 clusters, with the latter's O-star RVs ~ 5 km s^{-1} more positive, on average, than the former's. Kinematic study of the intermediate-mass populations in these clusters is needed to confirm the offset.

(5) We do not detect any line-of-sight runaway O-type stars, nor do we see evidence that the distributed O-type population migrated out from Tr 14 and Tr 16. On the contrary, the O-type stars in Cr 228 and the South Pillars have a low velocity dispersion compared to the region as a whole.

(6) The Tr 14 cluster is kinematically associated with the molecular gas of the Northern Cloud, consistent with its young age.

(7) Feedback from Tr 16 has accelerated the molecular gas of the Southern Cloud toward us, relative to the stellar population, by 10–15 km s^{-1}. V662 Car, an O-type star on the outskirts of Tr 16, may belong to a younger generation of stars triggered by this feedback.

(8) The approaching components of the ionized gas around Tr 14 and Tr 16 show higher velocities, relative to the O-type stars, than the receding components. This

kinematic asymmetry indicates that the expansion of the H II region is not spherical and is likely impacted by the distribution of dense neutral gas.

Our observations set the stage for the analysis of future *Gaia* data releases, which will add further kinematic dimensions to our understanding of the Carina Nebula. This region continues to be a laboratory for the study of massive-star formation and the interplay between stellar feedback and the interstellar medium.

CHAPTER 5

SUMMARY AND FUTURE PROSPECTS

Feedback from massive stars throughout their evolution is a critical contributor to the energy budget of molecular clouds and galaxies. In this dissertation, I have investigated three aspects of massive stars in the Carina Nebula, exploring how those stars have interacted with the interstellar medium and discussing the implications for our understanding of massive stars and OB associations. Below, I summarize my results and describe avenues for future research.

Chapter 2 probed the eruptive history of η Carinae, the very massive LBV at the heart of the Carina Nebula. Nineteenth-century astronomers witnessed an extraordinary mass-loss event from this system, but exactly what happened—and how it relates to the evolution of very massive stars in general—remains a mystery. I used eight epochs of *HST* imaging to measure the transverse velocities of nearly 800 features in η Car's outer ejecta. I determined that these gas knots, traveling at 300 to $>$ 1000 km s^{-1}, did not decelerate or accelerate over the 21 years of data, a conclusion supported by comparison to images from half a century ago. I used their constant motion to estimate the dates they were ejected from η Car and discovered that they fall into three spatially distinct groups. The ejecta to the east and northeast of the star were ejected in the mid-1200s, in a highly asymmetric mass-loss event, while arcs of ejecta to the southeast and northwest likely originated in the mid-1500s. The third group of ejecta came from the known Great Eruption of the mid-1800s, although my results suggest that one or more smaller mass-loss episodes may have occurred in the decades leading up to the main event.

These results show that η Car has had not just one but multiple major eruptions, with several hundred years between them. This raises many questions for theoretical models of this star and of LBVs in general, as these models must now explain the repetition, timescales, and various (a)symmetries involved. It seems difficult to

reproduce the observations with single-star models, but no binary or merger model has yet provided a fully satisfactory explanation either.

Key to my interpretation of the three groups of outer ejecta was the comparison to existing radial velocities, which confirmed that the thirteenth-century ejecta were well separated from the sixteenth-century ejecta. An immediate next step in η Car research is to obtain spatially complete, high-resolution spectra of the ejecta and model their three-dimensional kinematics in further detail. This will be especially valuable along the S ridge and W arc, where ejecta from multiple events overlap and may be interacting. Mehner et al. (2016) used integral field spectroscopy to reveal the structure of a fast-moving ($\sim$ 2000 km s^{-1}) outer shell. They confirm the hypothesis, described in my Chapter 2, that the soft X-ray emission around η Car is due to the collision of diffuse, fast-moving ejecta from the 1800s with older, outer material.

One of the exciting characteristics of η Car, of course, is that it changes on human timescales, so we can continue to watch and wait and see what happens next! Its secondary star next reaches periastron in early 2020, and multi-wavelength observational campaigns are already being planned. If the $\sim$ 300-year cycle seen in the outer ejecta continues, we may have another hundred years before this star's next major eruption—or it might very soon explode in a true supernova. In the meantime, large-scale photometric surveys, like those conducted by the under-construction Large Synoptic Survey Telescope (Ivezic et al., 2008), will reveal more about η-Car-like "supernova impostors" in other galaxies.

Chapter 3 looked at five of the Carina Nebula's massive stars that exhibit stellar wind bow shocks, a sign that their velocities relative to the ISM are supersonic. I used shifts in these stars' outer PSFs across pairs of *HST* images to constrain their proper motions, finding that none are likely runaway sources. Two of the stars are moving at tangents to the orientation of their bow shock arcs, which point toward the Carina Nebula's clusters, strongly suggesting that feedback-driven gas flows—rather than fast-moving stars—are responsible for the supersonic relative motion that produced these bow shocks. For the other three stars, both factors may be

relevant. The key conclusion is that bow shocks can be a tool for investigating the origins and environments of massive stars, but should not be overinterpreted.

More precise proper motions of massive stars, both with and without bow shocks, inside and outside of the Carina Nebula, will come from the *Gaia* spacecraft. Launched in late 2013, *Gaia* is busily accumulating data on the positions of more than a billion stars in the Milky Way (Perryman et al., 1997; Gaia Collaboration et al., 2016b). Its first data release came in September 2016 and provided some early comparison measurements for my results in Chapter 3. Like prior astrometric surveys, *Gaia* determines motions in an absolute reference frame, carefully calibrated against the positions of extragalactic sources. For now, converting these motions to the reference frame of the Carina Nebula (or any given cluster or association) carries non-negligible uncertainties. The full *Gaia* catalog will change that; for the Carina Nebula, it will provide proper motions for thousands of stars at sub-km s^{-1} precision, firmly establishing the overall region's motion relative to our Sun. *Gaia*'s next data release is scheduled for April 2018, with subsequent releases culminating in its final catalog in 2022.[1]

Chapter 4 presented a radial velocity survey of the O-type and evolved massive stars in the Carina Nebula. I measured new radial velocities at multiple epochs for 31 sources (about half of the complex's O-star population), assembled the available literature data for the rest, and compared the results to the motions of the ionized and molecular gas across the region. The Tr 14 cluster remains closely associated with molecular material, while feedback from the Tr 16 cluster has accelerated the remnants of its natal cloud and possibly triggered the formation of additional massive stars. The feedback-driven expansion of the ionized gas around the clusters appears to be bounded by dense material on the far side.

In addition to the larger-scale conclusions, Chapter 4 also included an analysis of four spectroscopic binary systems and discussed several other sources with significant, high-amplitude radial velocity variations. It would be interesting to obtain further observations of all of these systems and particularly HDE 303312, where the

[1] See https://www.cosmos.esa.int/web/gaia/release.

radial velocity orbit and light curve disagree on the properties of the secondary star. The CHIRON spectrograph on the CTIO/SMARTS 1.5-m telescope was the perfect instrument for my radial velocity observations; unfortunately, it is not currently operating due to funding constraints.

Both Chapter 3 and Chapter 4 considered the implications of my results for models of the formation of OB associations. Three of the measured bow shock host stars belong to the distributed massive-star population in the Carina Nebula's South Pillars region; none have proper motions directed away from the central Trumpler clusters. In addition, the radial velocity dispersion of the O-type stars in the South Pillars is low compared to that of the region as a whole. Together, these data indicate that the massive stars of the South Pillars formed there and not in the central clusters. The Carina Nebula is thus more consistent with a hierarchical star formation scenario for the origin of OB associations, with some contribution from triggered star formation.

Some of the remaining open questions about the Carina Nebula could be addressed with a radial velocity survey of its intermediate-mass stellar population. Is the small radial velocity offset between the massive stars of Tr 14 and Tr 16 real or just a statistical quirk? (The results of Damiani et al. 2017 suggest the latter, although they did not delve into that particular issue.) Are the massive stars in the South Pillars kinematically associated with the many subclusters of lower-mass objects? Here, too, *Gaia* proper motions will be enormously useful. *Gaia* data, which are entirely unaffected by stellar winds, might also finally reveal the origins of the Carina Nebula's WNH stars.

REFERENCES

Adams, F. C. and M. Fatuzzo (1996). A Theory of the Initial Mass Function for Star Formation in Molecular Clouds. *The Astrophysical Journal*, **464**, p. 256. doi:10.1086/177318.

Adams, F. C., D. Hollenbach, G. Laughlin, and U. Gorti (2004). Photoevaporation of Circumstellar Disks Due to External Far-Ultraviolet Radiation in Stellar Aggregates. *The Astrophysical Journal*, **611**, pp. 360–379. doi:10.1086/421989.

Agertz, O. and A. V. Kravtsov (2015). On the Interplay between Star Formation and Feedback in Galaxy Formation Simulations. *The Astrophysical Journal*, **804**, 18. doi:10.1088/0004-637X/804/1/18.

Albacete Colombo, J. F., N. I. Morrell, V. S. Niemela, and M. F. Corcoran (2001). Optical spectroscopy of X-Mega targets - I. CPD -59°2635: a new double-lined O-type binary in the Carina Nebula. *Monthly Notices of the Royal Astronomical Society*, **326**, pp. 78–84. doi:10.1046/j.1365-8711.2001.04497.x.

Albacete Colombo, J. F., N. I. Morrell, G. Rauw, M. F. Corcoran, V. S. Niemela, and H. Sana (2002). Optical spectroscopy of X-Mega targets - IV. CPD - 59°2636: a new O-type multiple system in the Carina Nebula. *Monthly Notices of the Royal Astronomical Society*, **336**, pp. 1099–1108. doi:10.1046/j.1365-8711.2002.05755.x.

Alexander, M. J., R. J. Hanes, M. S. Povich, and M. V. McSwain (2016). A Catalog of New Spectroscopically Confirmed Massive OB Stars in Carina. *The Astronomical Journal*, **152**, 190. doi:10.3847/0004-6256/152/6/190.

Allen, D. A. (1979). The location of η Carinae in NGC 3372. *Monthly Notices of the Royal Astronomical Society*, **189**, pp. 1P–4P. doi:10.1093/mnras/189.1.1P.

Allen, D. A. and D. J. Hillier (1993). The Shape of the Homunchulus Nebula around Eta Carinae. *Proceedings of the Astronomical Society of Australia*, **10**, p. 338.

Ambartsumian, V. A. (1947). *Stellar Evolution and Astrophysics*. Armenian Academy of Science, Yerevan.

Ambartsumian, V. A. (1955). Stellar systems of positive total energy. *The Observatory*, **75**, pp. 72–78.

Anderson, J. (2006). Empirical PSFs and Distortion in the WFC Camera. In Koekemoer, A. M., P. Goudfrooij, and L. L. Dressel (eds.) *The 2005 HST Calibration Workshop: Hubble After the Transition to Two-Gyro Mode*, p. 11. Space Telescope Science Institute, Baltimore, MD.

Anderson, J. and I. R. King (1999). Astrometric and Photometric Corrections for the 34th Row Error in HST's WFPC2 Camera. *Publications of the Astronomical Society of the Pacific*, **111**, pp. 1095–1098. doi:10.1086/316432.

Anderson, J. and I. R. King (2000). Toward High-Precision Astrometry with WFPC2. I. Deriving an Accurate Point-Spread Function. *Publications of the Astronomical Society of the Pacific*, **112**, pp. 1360–1382. doi:10.1086/316632.

Anderson, J. and I. R. King (2006). PSFs, Photometry, and Astronomy for the ACS/WFC. Technical report, Space Telescope Science Institute, Baltimore, MD.

Anderson, J., I. R. King, H. B. Richer, G. G. Fahlman, B. M. S. Hansen, J. Hurley, J. S. Kalirai, R. M. Rich, and P. B. Stetson (2008a). Deep Advanced Camera for Surveys Imaging in the Globular Cluster NGC 6397: Reduction Methods. *The Astronomical Journal*, **135**, pp. 2114–2128. doi:10.1088/0004-6256/135/6/2114.

Anderson, J., A. Sarajedini, L. R. Bedin, I. R. King, G. Piotto, I. N. Reid, M. Siegel, S. R. Majewski, N. E. Q. Paust, A. Aparicio, A. P. Milone, B. Chaboyer, and A. Rosenberg (2008b). The ACS Survey of Globular Clusters. V. Generating a Comprehensive Star Catalog for each Cluster. *The Astronomical Journal*, **135**, pp. 2055–2073. doi:10.1088/0004-6256/135/6/2055.

Anderson, J. and R. P. van der Marel (2010). New Limits on an Intermediate-Mass Black Hole in Omega Centauri. I. Hubble Space Telescope Photometry and Proper Motions. *The Astrophysical Journal*, **710**, pp. 1032–1062. doi:10.1088/0004-637X/710/2/1032.

Arias, J. I., N. R. Walborn, S. Simón Díaz, R. H. Barbá, J. Maíz Apellániz, C. Sabín-Sanjulián, R. C. Gamen, N. I. Morrell, A. Sota, A. Marco, I. Negueruela, J. R. S. Leão, A. Herrero, and E. J. Alfaro (2016). Spectral Classification and Properties of the OVz Stars in the Galactic O Star Spectroscopic Survey (GOSSS). *The Astronomical Journal*, **152**, 31. doi:10.3847/0004-6256/152/2/31.

Ascenso, J., J. Alves, S. Vicente, and M. T. V. T. Lago (2007). NTT and VLT diffraction limited imaging of Trumpler 14: revealing a massive core-halo cluster. *Astronomy & Astrophysics*, **476**, pp. 199–215. doi:10.1051/0004-6361:20077210.

Azcarate, I. N., J. C. Cersosimo, and F. R. Colomb (1981). The H 166 alpha recombination line in the Carina Nebula. *Revista Mexicana de Astronomía y Astrofísica*, **6**, pp. 269–272.

Bally, J. (2008). Overview of the Orion Complex. In Reipurth, B. (ed.) *Handbook of Star Forming Regions, Volume I*, p. 459. ASP, San Francisco, CA.

Bally, J. (2016). Protostellar Outflows. *Annual Review of Astronomy and Astrophysics*, **54**, pp. 491–528. doi:10.1146/annurev-astro-081915-023341.

Bally, J., C. R. O'Dell, and M. J. McCaughrean (2000). Disks, Microjets, Windblown Bubbles, and Outflows in the Orion Nebula. *The Astronomical Journal*, **119**, pp. 2919–2959. doi:10.1086/301385.

Bally, J. and N. Z. Scoville (1980). Structure and evolution of molecular clouds near H II regions. I - CO observations of an expanding molecular shell surrounding the Pelican Nebula. *The Astrophysical Journal*, **239**, pp. 121–136. doi:10.1086/158094.

Balog, Z., J. Muzerolle, G. H. Rieke, K. Y. L. Su, E. T. Young, and S. T. Megeath (2007). Spitzer/IRAC-MIPS Survey of NGC 2244: Protostellar Disk Survival in the Vicinity of Hot Stars. *The Astrophysical Journal*, **660**, pp. 1532–1540. doi:10.1086/513311.

Balog, Z., G. H. Rieke, J. Muzerolle, J. Bally, K. Y. L. Su, K. Misselt, and A. Gáspár (2008). Photoevaporation of Protoplanetary Disks. *The Astrophysical Journal*, **688**, 408-417. doi:10.1086/592063.

Balona, L. A., W. A. Dziembowski, and A. Pamyatnykh (1997). The structure of the instability strip and mode identification for beta Cep stars in three young open clusters. *Monthly Notices of the Royal Astronomical Society*, **289**, pp. 25–36. doi:10.1093/mnras/289.1.25.

Baranov, V. B., K. V. Krasnobaev, and A. G. Kulikovskii (1971). A Model of the Interaction of the Solar Wind with the Interstellar Medium. *Soviet Physics Doklady*, **15**, p. 791.

Barbá, R. H., R. Gamen, J. I. Arias, N. Morrell, J. Maíz Apellániz, E. Alfaro, N. Walborn, and A. Sota (2010). Spectroscopic survey of galactic O and WN stars. OWN Survey: new binaries and trapezium-like systems. In Rivinius, T. and M. Curé (eds.) *The Interferometric View on Hot Stars*, volume 38 of *Revista Mexicana de Astronomia y Astrofisica Conference Series*, pp. 30–32.

Bartzakos, P., A. F. J. Moffat, and V. S. Niemela (2001). Magellanic Cloud WC/WO Wolf-Rayet stars - I. Binary frequency and Roche lobe overflow formation. *Monthly Notices of the Royal Astronomical Society*, **324**, pp. 18–32. doi:10.1046/j.1365-8711.2001.04126.x.

Bastian, N., B. Ercolano, M. Gieles, E. Rosolowsky, R. A. Scheepmaker, R. Gutermuth, and Y. Efremov (2007). Hierarchical star formation in M33: fundamental properties of the star-forming regions. *Monthly Notices of the Royal Astronomical Society*, **379**, pp. 1302–1312. doi:10.1111/j.1365-2966.2007.12064.x.

Bastian, N. and S. P. Goodwin (2006). Evidence for the strong effect of gas removal on the internal dynamics of young stellar clusters. *Monthly Notices of the Royal Astronomical Society*, **369**, pp. L9–L13. doi:10.1111/j.1745-3933.2006.00162.x.

Battinelli, P. and R. Capuzzo-Dolcetta (1991). Formation and evolutionary properties of the Galactic open cluster system. *Monthly Notices of the Royal Astronomical Society*, **249**, pp. 76–83. doi:10.1093/mnras/249.1.76.

Baume, G., R. A. Vázquez, G. Carraro, and A. Feinstein (2003). Photometric study of the young open cluster NGC 3293. *Astronomy & Astrophysics*, **402**, pp. 549–564. doi:10.1051/0004-6361:20030223.

Benetti, S., E. Cappellaro, I. J. Danziger, M. Turatto, F. Patat, and M. della Valle (1998). Supernova 1994aj - A probe for pre-supernova evolution and mass-loss from the progenitor. *Monthly Notices of the Royal Astronomical Society*, **294**, p. 448. doi:10.1046/j.1365-8711.1998.01198.x.

Bertoldi, F. (1989). The photoevaporation of interstellar clouds. I - Radiation-driven implosion. *The Astrophysical Journal*, **346**, pp. 735–755. doi:10.1086/168055.

Bertoldi, F. and C. F. McKee (1990). The photoevaporation of interstellar clouds. II - Equilibrium cometary clouds. *The Astrophysical Journal*, **354**, pp. 529–548. doi:10.1086/168713.

Bisbas, T. G., R. Wünsch, A. P. Whitworth, D. A. Hubber, and S. Walch (2011). Radiation-driven Implosion and Triggered Star Formation. *The Astrophysical Journal*, **736**, 142. doi:10.1088/0004-637X/736/2/142.

Blaauw, A. (1961). On the origin of the O- and B-type stars with high velocities (the "run-away" stars), and some related problems. *Bulletin of the Astronomical Institutes of the Netherlands*, **15**, p. 265.

Blaauw, A. (1964). The O Associations in the Solar Neighborhood. *Annual Review of Astronomy and Astrophysics*, **2**, p. 213. doi:10.1146/annurev.aa.02.090164.001241.

Bohannan, B. and C. D. Garmany (1978). A search for binaries and stellar winds among the O-type stars. *The Astrophysical Journal*, **223**, pp. 908–919. doi:10.1086/156323.

Bohigas, J., M. Tapia, M. T. Ruiz, and M. Roth (2000). Possible detection of an old bipolar shell associated with η Carinae. *Monthly Notices of the Royal Astronomical Society*, **312**, pp. 295–300. doi:10.1046/j.1365-8711.2000.03217.x.

Boily, C. M. and P. Kroupa (2003). The impact of mass loss on star cluster formation - I. Analytical results. *Monthly Notices of the Royal Astronomical Society*, **338**, pp. 665–672. doi:10.1046/j.1365-8711.2003.06076.x.

Bok, B. J. (1934). The Stability of Moving Clusters. *Harvard College Observatory Circular*, **384**, pp. 1–41.

Bonnell, I. A., M. R. Bate, C. J. Clarke, and J. E. Pringle (2001a). Competitive accretion in embedded stellar clusters. *Monthly Notices of the Royal Astronomical Society*, **323**, pp. 785–794. doi:10.1046/j.1365-8711.2001.04270.x.

Bonnell, I. A., M. R. Bate, and S. G. Vine (2003). The hierarchical formation of a stellar cluster. *Monthly Notices of the Royal Astronomical Society*, **343**, pp. 413–418. doi:10.1046/j.1365-8711.2003.06687.x.

Bonnell, I. A., C. J. Clarke, M. R. Bate, and J. E. Pringle (2001b). Accretion in stellar clusters and the initial mass function. *Monthly Notices of the Royal Astronomical Society*, **324**, pp. 573–579. doi:10.1046/j.1365-8711.2001.04311.x.

Bonnell, I. A., S. G. Vine, and M. R. Bate (2004). Massive star formation: nurture, not nature. *Monthly Notices of the Royal Astronomical Society*, **349**, pp. 735–741. doi:10.1111/j.1365-2966.2004.07543.x.

Bontemps, S., P. Andre, S. Terebey, and S. Cabrit (1996). Evolution of outflow activity around low-mass embedded young stellar objects. *Astronomy & Astrophysics*, **311**, pp. 858–872.

Bouret, J.-C., T. Lanz, and D. J. Hillier (2005). Lower mass loss rates in O-type stars: Spectral signatures of dense clumps in the wind of two Galactic O4 stars. *Astronomy & Astrophysics*, **438**, pp. 301–316. doi:10.1051/0004-6361:20042531.

Bovy, J. (2017). Galactic rotation in Gaia DR1. *Monthly Notices of the Royal Astronomical Society*, **468**, pp. L63–L67. doi:10.1093/mnrasl/slx027.

Bresolin, F., R. C. Kennicutt, Jr., L. Ferrarese, B. K. Gibson, J. A. Graham, L. M. Macri, R. L. Phelps, D. M. Rawson, S. Sakai, N. A. Silbermann, P. B. Stetson, and A. M. Turner (1998). A Hubble Space Telescope Study of Extragalactic OB Associations. *The Astronomical Journal*, **116**, pp. 119–130. doi:10.1086/300424.

Bresolin, F., R. C. Kennicutt, Jr., and P. B. Stetson (1996). An HST Study of OB Associations and Star Clusters in M101. *The Astronomical Journal*, **112**, p. 1009. doi:10.1086/118073.

Bressan, A., P. Marigo, L. Girardi, B. Salasnich, C. Dal Cero, S. Rubele, and A. Nanni (2012). PARSEC: stellar tracks and isochrones with the PAdova and TRieste Stellar Evolution Code. *Monthly Notices of the Royal Astronomical Society*, **427**, pp. 127–145. doi:10.1111/j.1365-2966.2012.21948.x.

Bressert, E., N. Bastian, R. Gutermuth, S. T. Megeath, L. Allen, N. J. Evans, II, L. M. Rebull, J. Hatchell, D. Johnstone, T. L. Bourke, L. A. Cieza, P. M. Harvey, B. Merin, T. P. Ray, and N. F. H. Tothill (2010). The spatial distribution of star formation in the solar neighbourhood: do all stars form in dense clusters? *Monthly Notices of the Royal Astronomical Society*, **409**, pp. L54–L58. doi:10.1111/j.1745-3933.2010.00946.x.

Briceño, C., T. Preibisch, W. H. Sherry, E. A. Mamajek, R. D. Mathieu, F. M. Walter, and H. Zinnecker (2007). The Low-Mass Populations in OB Associations. *Protostars and Planets V*, pp. 345–360.

Brooks, K. J., M. G. Burton, J. M. Rathborne, M. C. B. Ashley, and J. W. V. Storey (2000). Unlocking the Keyhole: H_2 and PAH emission from molecular clumps in the Keyhole Nebula. *Monthly Notices of the Royal Astronomical Society*, **319**, pp. 95–102. doi:10.1046/j.1365-8711.2000.03798.x.

Brooks, K. J., P. Cox, N. Schneider, J. W. V. Storey, A. Poglitsch, N. Geis, and L. Bronfman (2003). The Trumpler 14 photodissociation region in the Carina Nebula. *Astronomy & Astrophysics*, **412**, pp. 751–765. doi:10.1051/0004-6361:20031406.

Brooks, K. J., J. W. V. Storey, and J. B. Whiteoak (2001). H110α recombination-line emission and 4.8-GHz continuum emission in the Carina nebula. *Monthly Notices of the Royal Astronomical Society*, **327**, pp. 46–54. doi:10.1046/j.1365-8711.2001.04590.x.

Brooks, K. J., J. B. Whiteoak, and J. W. V. Storey (1998). An Investigation of the Molecular Clouds of the Carina HII Region/Molecular Cloud Complex - First Results. *Publications of the Astronomical Society of Australia*, **15**, pp. 202–207. doi:10.1071/AS98202.

Brown, D. and D. J. Bomans (2005). To see or not to see a bow shock. Identifying bow shocks with Hα allsky surveys. *Astronomy & Astrophysics*, **439**, pp. 183–194. doi:10.1051/0004-6361:20041054.

Brownsberger, S. and R. W. Romani (2014). A Survey for Hα Pulsar Bow Shocks. *The Astrophysical Journal*, **784**, 154. doi:10.1088/0004-637X/784/2/154.

Burton, M. G., C. Braiding, C. Glueck, P. Goldsmith, J. Hawkes, D. J. Hollenbach, C. Kulesa, C. L. Martin, J. L. Pineda, G. Rowell, R. Simon, A. A. Stark, J. Stutzki, N. J. H. Tothill, J. S. Urquhart, C. Walker, A. J. Walsh, and M. Wolfire (2013). The Mopra Southern Galactic Plane CO Survey. *Publications of the Astronomical Society of Australia*, **30**, e044. doi:10.1017/pasa.2013.22.

Cameron, A. G. W., P. Hoeflich, P. C. Myers, and D. D. Clayton (1995). Massive Supernovae, Orion Gamma Rays, and the Formation of the Solar System. *The Astrophysical Journal*, **447**, p. L53. doi:10.1086/309554.

Cameron, A. G. W. and J. W. Truran (1977). The supernova trigger for formation of the solar system. *Icarus*, **30**, pp. 447–461. doi:10.1016/0019-1035(77)90101-4.

Cannon, R. D., T. G. Hawarden, and S. B. Tritton (1977). A new Sculptor-type dwarf elliptical galaxy in Carina. *Monthly Notices of the Royal Astronomical Society*, **180**, pp. 81P–82P. doi:10.1093/mnras/180.1.81P.

Cardelli, J. A. and G. C. Clayton (1988). An environmental impact study of Orion Nebula dust. *The Astronomical Journal*, **95**, pp. 516–525. doi:10.1086/114651.

Cardelli, J. A., G. C. Clayton, and J. S. Mathis (1989). The relationship between infrared, optical, and ultraviolet extinction. *The Astrophysical Journal*, **345**, pp. 245–256. doi:10.1086/167900.

Carraro, G. (2002). A photometric investigation of the young open cluster Trumpler 15. *Monthly Notices of the Royal Astronomical Society*, **331**, pp. 785–794. doi:10.1046/j.1365-8711.2002.05249.x.

Carraro, G. and F. Patat (2001). Star clusters in the Carina complex: UBVRI photometry of NGC 3114, Collinder 228 and vdB-Hagen 99. *Astronomy & Astrophysics*, **379**, pp. 136–146. doi:10.1051/0004-6361:20011314.

Carraro, G., F. Patat, and H. Baumgardt (2001). Star clusterings in the Carina complex: UBVRI photometry of NGC 3324 and Loden 165. *Astronomy & Astrophysics*, **371**, pp. 107–114. doi:10.1051/0004-6361:20010307.

Carraro, G., M. Romaniello, P. Ventura, and F. Patat (2004). The star cluster Collinder 232 in the Carina complex and its relation to Trumpler 14/16. *Astronomy & Astrophysics*, **418**, pp. 525–537. doi:10.1051/0004-6361:20034335.

Cassinelli, J. P. (1999). A Near-Eddington Limit Wind Scenario for the Great Eruption of η Carinae. In Morse, J. A., R. M. Humphreys, and A. Damineli (eds.) *Eta Carinae at The Millennium*, volume 179 of *Astronomical Society of the Pacific Conference Series*, p. 358.

Castor, J. I., D. C. Abbott, and R. I. Klein (1975). Radiation-driven winds in Of stars. *The Astrophysical Journal*, **195**, pp. 157–174. doi:10.1086/153315.

Chatzopoulos, E., J. C. Wheeler, J. Vinko, R. Quimby, E. L. Robinson, A. A. Miller, R. J. Foley, D. A. Perley, F. Yuan, C. Akerlof, and J. S. Bloom (2011). SN 2008am: A Super-luminous Type IIn Supernova. *The Astrophysical Journal*, **729**, 143. doi:10.1088/0004-637X/729/2/143.

Chen, Y., A. Bressan, L. Girardi, P. Marigo, X. Kong, and A. Lanza (2015). PARSEC evolutionary tracks of massive stars up to 350 $M_\odot$ at metallicities $0.0001 \leq Z \leq 0.04$. *Monthly Notices of the Royal Astronomical Society*, **452**, pp. 1068–1080. doi:10.1093/mnras/stv1281.

Chevalier, R. A. (1977). The interaction of supernovae with the interstellar medium. *Annual Review of Astronomy and Astrophysics*, **15**, pp. 175–196. doi:10.1146/annurev.aa.15.090177.001135.

Chevalier, R. A. (2000). Young Circumstellar Disks near Evolved Massive Stars and Supernovae. *The Astrophysical Journal*, **538**, pp. L151–L154. doi:10.1086/312814.

Chevalier, R. A. and A. W. Clegg (1985). Wind from a starburst galaxy nucleus. *Nature*, **317**, p. 44. doi:10.1038/317044a0.

Chini, R., V. H. Hoffmeister, A. Nasseri, O. Stahl, and H. Zinnecker (2012). A spectroscopic survey on the multiplicity of high-mass stars. *Monthly Notices of the Royal Astronomical Society*, **424**, pp. 1925–1929. doi:10.1111/j.1365-2966.2012.21317.x.

Chlebowski, T., F. D. Seward, J. Swank, and A. Szymkowiak (1984). X-rays from Eta Carinae. *The Astrophysical Journal*, **281**, pp. 665–672. doi:10.1086/162143.

Cho, H. and H. Kang (2008). Feedback from multiple supernova explosions inside a wind-blown bubble. *New Astronomy*, **13**, pp. 163–177. doi:10.1016/j.newast.2007.07.006.

Chomiuk, L. and M. S. Povich (2011). Toward a Unification of Star Formation Rate Determinations in the Milky Way and Other Galaxies. *The Astronomical Journal*, **142**, 197. doi:10.1088/0004-6256/142/6/197.

Chugai, N. N., S. I. Blinnikov, R. J. Cumming, P. Lundqvist, A. Bragaglia, A. V. Filippenko, D. C. Leonard, T. Matheson, and J. Sollerman (2004). The Type IIn supernova 1994W: evidence for the explosive ejection of a circumstellar envelope. *Monthly Notices of the Royal Astronomical Society*, **352**, pp. 1213–1231. doi:10.1111/j.1365-2966.2004.08011.x.

Clariá, J. J. (1977). NGC 3324. A very young open cluster in the Carina spiral feature. *Astronomy and Astrophysics Supplement Series*, **27**, pp. 145–153.

Clark, P. C., I. A. Bonnell, H. Zinnecker, and M. R. Bate (2005). Star formation in unbound giant molecular clouds: the origin of OB associations? *Monthly Notices of the Royal Astronomical Society*, **359**, pp. 809–818. doi:10.1111/j.1365-2966.2005.08942.x.

Clarkson, W. I., A. M. Ghez, M. R. Morris, J. R. Lu, A. Stolte, N. McCrady, T. Do, and S. Yelda (2012). Proper Motions of the Arches Cluster with Keck Laser Guide Star Adaptive Optics: The First Kinematic Mass Measurement of the Arches. *The Astrophysical Journal*, **751**, 132. doi:10.1088/0004-637X/751/2/132.

Coelho, P. R. T. (2014). A new library of theoretical stellar spectra with scaled-solar and α-enhanced mixtures. *Monthly Notices of the Royal Astronomical Society*, **440**, pp. 1027–1043. doi:10.1093/mnras/stu365.

Colgate, S. A. and R. H. White (1966). The Hydrodynamic Behavior of Supernovae Explosions. *The Astrophysical Journal*, **143**, p. 626. doi:10.1086/148549.

Comerón, F. and A. Pasquali (2007). A very massive runaway star from Cygnus OB2. *Astronomy & Astrophysics*, **467**, pp. L23–L27. doi:10.1051/0004-6361:20077304.

Conti, P. S., E. M. Leep, and J. J. Lorre (1977). Spectroscopic studies of O-type stars. VIII - Radial velocities and the K-term. *The Astrophysical Journal*, **214**, pp. 759–772. doi:10.1086/155305.

Conti, P. S., V. S. Niemela, and N. R. Walborn (1979). A radial velocity study of three WN stars and an O3f star in the Carina Nebula. *The Astrophysical Journal*, **228**, pp. 206–219. doi:10.1086/156837.

Corcoran, M. F., K. Ishibashi, J. H. Swank, and R. Petre (2001). The X-Ray Light Curve of η Carinae: Refinement of the Orbit and Evidence for Phase-dependent Mass Loss. *The Astrophysical Journal*, **547**, pp. 1034–1039. doi:10.1086/318416.

Corcoran, M. F., R. Petre, J. H. Swank, S. A. Drake, K. Koyama, Y. Tsuboi, R. Viotti, A. Damineli, K. Davidson, K. Ishibashi, S. White, and D. Currie (1998). The ASCA X-Ray Spectrum of η Carinae. *The Astrophysical Journal*, **494**, pp. 381–395. doi:10.1086/305190.

Cox, C. and M. Lallo (2012). Keeping the Hubble Space Telescope in focus. In Clampin, M. C., G. G. Fazio, H. A. MacEwen, and J. M. Oschmann (eds.) *Space Telescopes and Instrumentation 2012: Optical, Infrared, and Millimeter Wave*, volume 8442 of *Proc. SPIE*, p. 844237. SPIE, Bellingham, WA. doi:10.1117/12.924900.

Cox, C. and S.-M. Niemi (2011). Evaluation of a temperature-based HST focus model. Technical report, Space Telescope Science Institute, Baltimore, MD.

Cox, P. and L. Bronfman (1995). The molecular gas content of the Keyhole nebula. *Astronomy & Astrophysics*, **299**, p. 583.

Creasey, P., T. Theuns, and R. G. Bower (2013). How supernova explosions power galactic winds. *Monthly Notices of the Royal Astronomical Society*, **429**, pp. 1922–1948. doi:10.1093/mnras/sts439.

Crowther, P. A. (2007). Physical Properties of Wolf-Rayet Stars. *Annual Review of Astronomy and Astrophysics*, **45**, pp. 177–219. doi:10.1146/annurev.astro.45.051806.110615.

Crowther, P. A., L. J. Smith, D. J. Hillier, and W. Schmutz (1995). Fundamental parameters of Wolf-Rayet stars. III. The evolutionary status of WNL stars. *Astronomy & Astrophysics*, **293**, pp. 427–445.

Cruz-González, C., E. Recillas-Cruz, R. Costero, M. Peimbert, and S. Torres-Peimbert (1974). A catalogue of galactic O stars and the ionization of the low density interstellar medium by runaway stars. *Revista Mexicana de Astronomía y Astrofísica*, **1**, pp. 211–259.

Cudworth, K. M., S. C. Martin, and K. Degioia-Eastwood (1993). Proper motions, membership, and photometry of open clusters near eta Carinae. *The Astronomical Journal*, **105**, pp. 1822–1830. doi:10.1086/116557.

Cunningham, A. J., R. I. Klein, M. R. Krumholz, and C. F. McKee (2011). Radiation-hydrodynamic Simulations of Massive Star Formation with Protostellar Outflows. *The Astrophysical Journal*, **740**, 107. doi:10.1088/0004-637X/740/2/107.

Currie, D. G., B. N. Dorland, and A. Kaufer (2002). Discovery of a high velocity, spatially extended emission "shell" in front of the southeast lobe of the η Carinae Homunculus. *Astronomy & Astrophysics*, **389**, pp. L65–L68. doi:10.1051/0004-6361:20020805.

Currie, D. G., D. M. Dowling, E. J. Shaya, J. Hester, P. Scowen, E. J. Groth, R. Lynds, E. J. O'neil, Jr., and Wide Field/Planetary Camera Instrument Definition Team (1996). Astrometric Analysis of the Homunculus of eta Carinae With the Hubble Space Telescope. *The Astronomical Journal*, **112**, p. 1115. doi:10.1086/118083.

Dale, J. E. (2017). The effect of the virial state of molecular clouds on the influence of feedback from massive stars. *Monthly Notices of the Royal Astronomical Society*, **467**, pp. 1067–1082. doi:10.1093/mnras/stx028.

Dale, J. E. and I. A. Bonnell (2012). Ionization-induced star formation - III. Effects of external triggering on the initial mass function in clusters. *Monthly Notices of the Royal Astronomical Society*, **422**, pp. 1352–1362. doi:10.1111/j.1365-2966.2012.20709.x.

Dale, J. E., I. A. Bonnell, and A. P. Whitworth (2007a). Ionization-induced star formation - I. The collect-and-collapse model. *Monthly Notices of the Royal Astronomical Society*, **375**, pp. 1291–1298. doi:10.1111/j.1365-2966.2006.11368.x.

Dale, J. E., P. C. Clark, and I. A. Bonnell (2007b). Ionization-induced star formation - II. External irradiation of a turbulent molecular cloud. *Monthly Notices of the Royal Astronomical Society*, **377**, pp. 535–544. doi:10.1111/j.1365-2966.2007.11515.x.

Dale, J. E., B. Ercolano, and I. A. Bonnell (2012). Ionization-induced star formation - IV. Triggering in bound clusters. *Monthly Notices of the Royal Astronomical Society*, **427**, pp. 2852–2865. doi:10.1111/j.1365-2966.2012.22104.x.

Dale, J. E., B. Ercolano, and I. A. Bonnell (2013a). Ionization-induced star formation - V. Triggering in partially unbound clusters. *Monthly Notices of the Royal Astronomical Society*, **431**, pp. 1062–1076. doi:10.1093/mnras/stt236.

Dale, J. E., T. J. Haworth, and E. Bressert (2015). The dangers of being trigger-happy. *Monthly Notices of the Royal Astronomical Society*, **450**, pp. 1199–1211. doi:10.1093/mnras/stv396.

Dale, J. E., J. Ngoumou, B. Ercolano, and I. A. Bonnell (2013b). Massive stars in massive clusters - IV. Disruption of clouds by momentum-driven winds. *Monthly Notices of the Royal Astronomical Society*, **436**, pp. 3430–3445. doi:10.1093/mnras/stt1822.

Dale, J. E., J. Ngoumou, B. Ercolano, and I. A. Bonnell (2014). Before the first supernova: combined effects of H II regions and winds on molecular clouds. *Monthly Notices of the Royal Astronomical Society*, **442**, pp. 694–712. doi:10.1093/mnras/stu816.

Damiani, F., R. Bonito, L. Magrini, L. Prisinzano, M. Mapelli, G. Micela, V. Kalari, J. Maíz Apellániz, G. Gilmore, S. Randich, E. Alfaro, E. Flaccomio, S. Koposov, A. Klutsch, A. C. Lanzafame, E. Pancino, G. G. Sacco, A. Bayo, G. Carraro, A. R. Casey, M. T. Costado, E. Franciosini, A. Hourihane, C. Lardo, J. Lewis, L. Monaco, L. Morbidelli, C. Worley, S. Zaggia, T. Zwitter, and R. Dorda (2016). Gaia-ESO Survey: Gas dynamics in the Carina nebula through optical emission lines. *Astronomy & Astrophysics*, **591**, A74. doi:10.1051/0004-6361/201628169.

Damiani, F., A. Klutsch, R. D. Jeffries, S. Randich, L. Prisinzano, J. Maíz Apellániz, G. Micela, V. Kalari, A. Frasca, T. Zwitter, R. Bonito, G. Gilmore, E. Flaccomio, P. Francois, S. Koposov, A. C. Lanzafame, G. G. Sacco, A. Bayo, G. Carraro, A. R. Casey, E. J. Alfaro, M. T. Costado, P. Donati, E. Franciosini, A. Hourihane, P. Jofré, C. Lardo, J. Lewis, L. Magrini, L. Monaco, L. Morbidelli, C. C. Worley,

J. S. Vink, and S. Zaggia (2017). Gaia-ESO Survey: Global properties of clusters Trumpler 14 and 16 in the Carina nebula. *Astronomy & Astrophysics*, **603**, A81. doi:10.1051/0004-6361/201629020.

Damineli, A. (1996). The 5.52 Year Cycle of Eta Carinae. *The Astrophysical Journal*, **460**, p. L49. doi:10.1086/309961.

Damineli, A., P. S. Conti, and D. F. Lopes (1997). Eta Carinae: a long period binary? *New Astronomy*, **2**, pp. 107–117. doi:10.1016/S1384-1076(97)00008-0.

Damineli, A., A. Kaufer, B. Wolf, O. Stahl, D. F. Lopes, and F. X. de Araújo (2000). η Carinae: Binarity Confirmed. *The Astrophysical Journal*, **528**, pp. L101–L104. doi:10.1086/312441.

Davidson, K. (1971). On the nature of Eta Carinae. *Monthly Notices of the Royal Astronomical Society*, **154**, pp. 415–427. doi:10.1093/mnras/154.4.415.

Davidson, K., R. J. Dufour, N. R. Walborn, and T. R. Gull (1986). Ultraviolet and visual wavelength spectroscopy of gas around Eta Carinae. *The Astrophysical Journal*, **305**, pp. 867–879. doi:10.1086/164301.

Davidson, K. and R. M. Humphreys (1997). Eta Carinae and Its Environment. *Annual Review of Astronomy and Astrophysics*, **35**, pp. 1–32. doi:10.1146/annurev.astro.35.1.1.

Davidson, K., A. Mehner, R. M. Humphreys, J. C. Martin, and K. Ishibashi (2015). Eta Carinae's 2014.6 Spectroscopic Event: The Extraordinary He II and N II Features. *The Astrophysical Journal*, **801**, L15. doi:10.1088/2041-8205/801/1/L15.

Davidson, K., N. Smith, T. R. Gull, K. Ishibashi, and D. J. Hillier (2001). The Shape and Orientation of the Homunculus Nebula Based on Spectroscopic Velocities. *The Astronomical Journal*, **121**, pp. 1569–1577. doi:10.1086/319419.

Davidson, K., N. R. Walborn, and T. R. Gull (1982). The remarkable spectrum of some material ejected by Eta Carinae. *The Astrophysical Journal*, **254**, pp. L47–L51. doi:10.1086/183754.

de Bruijne, J. H. J. (1999). Structure and colour-magnitude diagrams of Scorpius OB2 based on kinematic modelling of Hipparcos data. *Monthly Notices of the Royal Astronomical Society*, **310**, pp. 585–617. doi:10.1046/j.1365-8711.1999.02953.x.

de Graauw, T., S. Lidholm, B. Fitton, J. Beckman, F. P. Israel, H. Nieuwenhuijzen, and J. Vermue (1981). CO J = 2-1 observations of southern H II regions. *Astronomy & Astrophysics*, **102**, pp. 257–264.

de Groot, M. J. H. and H. J. G. L. M. Lamers (1992). Observation of gradual brightening of P Cygni due to stellar evolution. *Nature*, **355**, p. 422. doi:10.1038/355422a0.

de Jager, C. (1984). The stability limit of hypergiant photospheres. *Astronomy & Astrophysics*, **138**, pp. 246–252.

de Jager, C., H. Nieuwenhuijzen, and K. A. van der Hucht (1988). Mass loss rates in the Hertzsprung-Russell diagram. *Astronomy and Astrophysics Supplement Series*, **72**, pp. 259–289.

de Mink, S. E., H. Sana, N. Langer, R. G. Izzard, and F. R. N. Schneider (2014). The Incidence of Stellar Mergers and Mass Gainers among Massive Stars. *The Astrophysical Journal*, **782**, 7. doi:10.1088/0004-637X/782/1/7.

de Vaucouleurs, G. and O. J. Eggen (1952). The Brightening of η Carinae. *Publications of the Astronomical Society of the Pacific*, **64**, p. 185. doi:10.1086/126457.

de Wit, W. J., L. Testi, F. Palla, L. Vanzi, and H. Zinnecker (2004). The origin of massive O-type field stars. I. A search for clusters. *Astronomy & Astrophysics*, **425**, pp. 937–948. doi:10.1051/0004-6361:20040454.

de Wit, W. J., L. Testi, F. Palla, and H. Zinnecker (2005). The origin of massive O-type field stars: II. Field O stars as runaways. *Astronomy & Astrophysics*, **437**, pp. 247–255. doi:10.1051/0004-6361:20042489.

DeGioia-Eastwood, K., H. Throop, G. Walker, and K. M. Cudworth (2001). The Star Formation History of Trumpler 14 and Trumpler 16. *The Astrophysical Journal*, **549**, pp. 578–589. doi:10.1086/319047.

Deharveng, L., B. Lefloch, A. Zavagno, J. Caplan, A. P. Whitworth, D. Nadeau, and S. Martín (2003). Triggered massive-star formation at the border of the H II Region Sh 104. *Astronomy & Astrophysics*, **408**, pp. L25–L28. doi:10.1051/0004-6361:20031157.

Deharveng, L. and M. Maucherat (1975). Optical study of the Carina Nebula. *Astronomy & Astrophysics*, **41**, pp. 27–36.

Deharveng, L., A. Zavagno, F. Schuller, J. Caplan, M. Pomarès, and C. De Breuck (2009). Star formation around RCW 120, the perfect bubble. *Astronomy & Astrophysics*, **496**, pp. 177–190. doi:10.1051/0004-6361/200811337.

di Nino, D., R. B. Makidon, M. Lallo, K. C. Sahu, M. Sirianni, and S. Casertano (2008). HST Focus Variations with Temperature. Technical report, Space Telescope Science Institute, Baltimore, MD.

Dias, W. S., B. S. Alessi, A. Moitinho, and J. R. D. Lépine (2002). New catalogue of optically visible open clusters and candidates. *Astronomy & Astrophysics*, **389**, pp. 871–873. doi:10.1051/0004-6361:20020668.

Dickel, H. R. (1974). Carina Nebula: A Possible Interpretation of the Molecular Observations. *Astronomy & Astrophysics*, **31**, p. 11.

Doran, E. I., P. A. Crowther, A. de Koter, C. J. Evans, C. McEvoy, N. R. Walborn, N. Bastian, J. M. Bestenlehner, G. Gräfener, A. Herrero, K. Köhler, J. Maíz Apellániz, F. Najarro, J. Puls, H. Sana, F. R. N. Schneider, W. D. Taylor, J. T. van Loon, and J. S. Vink (2013). The VLT-FLAMES Tarantula Survey. XI. A census of the hot luminous stars and their feedback in 30 Doradus. *Astronomy & Astrophysics*, **558**, A134. doi:10.1051/0004-6361/201321824.

Draine, B. T. (2003). Interstellar Dust Grains. *Annual Review of Astronomy and Astrophysics*, **41**, pp. 241–289. doi:10.1146/annurev.astro.41.011802.094840.

Drilling, J. S. and A. U. Landolt (2000). Normal Stars. In Cox, A. N. (ed.) *Allen's Astrophysical Quantities*, pp. 381–396. Springer.

Dufour, R. J., T. W. Glover, J. J. Hester, D. G. Curie, D. van Orsow, and D. K. Walter (1997). New HST Results on the Outer Nebula of Eta Carinae. In Nota, A. and H. Lamers (eds.) *Luminous Blue Variables: Massive Stars in Transition*, volume 120 of *Astronomical Society of the Pacific Conference Series*, p. 255.

Dufton, P. L., S. J. Smartt, J. K. Lee, R. S. I. Ryans, I. Hunter, C. J. Evans, A. Herrero, C. Trundle, D. J. Lennon, M. J. Irwin, and A. Kaufer (2006). The VLT-FLAMES survey of massive stars: stellar parameters and rotational velocities in NGC 3293, NGC 4755 and NGC 6611. *Astronomy & Astrophysics*, **457**, pp. 265–280. doi:10.1051/0004-6361:20065392.

Ebbets, D., E. Malumuth, K. Davidson, R. White, and N. Walborn (1993). Proper Motions of the N Condensations of Eta Carinae. In Cassinelli, J. P. and E. B. Churchwell (eds.) *Massive Stars: Their Lives in the Interstellar Medium*, volume 35 of *Astronomical Society of the Pacific Conference Series*, p. 263.

Eddington, A. S. (1916). On the radiative equilibrium of the stars. *Monthly Notices of the Royal Astronomical Society*, **77**, pp. 16–35. doi:10.1093/mnras/77.1.16.

Efremov, Y. N. and B. G. Elmegreen (1998a). Hierarchical star formation from the time-space distribution of star clusters in the Large Magellanic Cloud. *Monthly Notices of the Royal Astronomical Society*, **299**, pp. 588–594. doi: 10.1046/j.1365-8711.1998.01819.x.

Efremov, Y. N. and B. G. Elmegreen (1998b). Triggered star formation in the LMC4/Constellation III region of the Large Magellanic Cloud. *Monthly Notices of the Royal Astronomical Society*, **299**, pp. 643–652. doi:10.1046/j.1365-8711.1998.01745.x.

Ekström, S., C. Georgy, P. Eggenberger, G. Meynet, N. Mowlavi, A. Wyttenbach, A. Granada, T. Decressin, R. Hirschi, U. Frischknecht, C. Charbonnel, and A. Maeder (2012). Grids of stellar models with rotation. I. Models from 0.8 to 120 $M_{\odot}$ at solar metallicity (Z = 0.014). *Astronomy & Astrophysics*, **537**, A146. doi:10.1051/0004-6361/201117751.

Eldridge, J. J., R. G. Izzard, and C. A. Tout (2008). The effect of massive binaries on stellar populations and supernova progenitors. *Monthly Notices of the Royal Astronomical Society*, **384**, pp. 1109–1118. doi:10.1111/j.1365-2966.2007.12738.x.

Eldridge, J. J., N. Langer, and C. A. Tout (2011). Runaway stars as progenitors of supernovae and gamma-ray bursts. *Monthly Notices of the Royal Astronomical Society*, **414**, pp. 3501–3520. doi:10.1111/j.1365-2966.2011.18650.x.

Eldridge, J. J. and E. R. Stanway (2009). Spectral population synthesis including massive binaries. *Monthly Notices of the Royal Astronomical Society*, **400**, pp. 1019–1028. doi:10.1111/j.1365-2966.2009.15514.x.

Eldridge, J. J. and E. R. Stanway (2012). The effect of stellar evolution uncertainties on the rest-frame ultraviolet stellar lines of C IV and He II in high-redshift Lyman-break galaxies. *Monthly Notices of the Royal Astronomical Society*, **419**, pp. 479–489. doi:10.1111/j.1365-2966.2011.19713.x.

Elias, F., E. J. Alfaro, and J. Cabrera-Caño (2006). OB Stars in the Solar Neighborhood. II. Kinematics. *The Astronomical Journal*, **132**, pp. 1052–1060. doi:10.1086/505941.

Elmegreen, B. G. (2011). Triggered Star Formation. In Charbonnel, C. and T. Montmerle (eds.) *Star Formation in the Local Universe*, volume 51 of *EAS Publications Series*, pp. 45–58. doi:10.1051/eas/1151004.

Elmegreen, B. G. and Y. N. Efremov (1996). An Extension of Hierarchical Star Formation to Galactic Scales. *The Astrophysical Journal*, **466**, p. 802. doi:10.1086/177554.

Elmegreen, B. G. and Y. N. Efremov (1998). Hierarchy of Interstellar and Stellar Structures and the Case of the Orion Star-Forming Region. *ArXiv e-prints*.

Elmegreen, B. G. and D. M. Elmegreen (2001). Fractal Structure in Galactic Star Fields. *The Astronomical Journal*, **121**, pp. 1507–1511. doi:10.1086/319416.

Elmegreen, B. G. and C. J. Lada (1977). Sequential formation of subgroups in OB associations. *The Astrophysical Journal*, **214**, pp. 725–741. doi:10.1086/155302.

Fabian, A. C. (2012). Observational Evidence of Active Galactic Nuclei Feedback. *Annual Review of Astronomy and Astrophysics*, **50**, pp. 455–489. doi:10.1146/annurev-astro-081811-125521.

Fall, S. M., R. Chandar, and B. C. Whitmore (2005). The Age Distribution of Massive Star Clusters in the Antennae Galaxies. *The Astrophysical Journal*, **631**, pp. L133–L136. doi:10.1086/496878.

Fall, S. M., M. R. Krumholz, and C. D. Matzner (2010). Stellar Feedback in Molecular Clouds and its Influence on the Mass Function of Young Star Clusters. *The Astrophysical Journal*, **710**, pp. L142–L146. doi:10.1088/2041-8205/710/2/L142.

Fan, X., C. L. Carilli, and B. Keating (2006). Observational Constraints on Cosmic Reionization. *Annual Review of Astronomy and Astrophysics*, **44**, pp. 415–462. doi:10.1146/annurev.astro.44.051905.092514.

Feast, M. and P. Whitelock (1997). Galactic kinematics of Cepheids from HIPPARCOS proper motions. *Monthly Notices of the Royal Astronomical Society*, **291**, p. 683. doi:10.1093/mnras/291.4.683.

Feast, M., P. Whitelock, and F. Marang (2001). Variability of η Carinae - III. *Monthly Notices of the Royal Astronomical Society*, **322**, pp. 741–748. doi:10.1046/j.1365-8711.2001.04163.x.

Feast, M. W., A. D. Thackeray, and A. J. Wesselink (1957). Radial velocities of southern B stars determined at the Radcliffe Observatory. *Memoirs of the Royal Astronomical Society*, **68**, pp. 1–35.

Federrath, C., M. Schrön, R. Banerjee, and R. S. Klessen (2014). Modeling Jet and Outflow Feedback during Star Cluster Formation. *The Astrophysical Journal*, **790**, 128. doi:10.1088/0004-637X/790/2/128.

Feigelson, E. D., K. V. Getman, L. K. Townsley, P. S. Broos, M. S. Povich, G. P. Garmire, R. R. King, T. Montmerle, T. Preibisch, N. Smith, K. G. Stassun, J. Wang, S. Wolk, and H. Zinnecker (2011). X-ray Star Clusters in the Carina Complex. *The Astrophysical Journal Supplement Series*, **194**, 9. doi:10.1088/0067-0049/194/1/9.

Feinstein, A. (1981). The region of the open cluster Bo 10. *Publications of the Astronomical Society of the Pacific*, **93**, pp. 202–206. doi:10.1086/130805.

Feinstein, A., H. G. Marraco, and J. C. Forte (1976). Collinder 228 and the η Carinae complex. *Astronomy and Astrophysics Supplement Series*, **24**, pp. 389–397.

Feinstein, A., H. G. Marraco, and J. C. Muzzio (1973). A single young open cluster comprising Tr 14 and Tr 16. *Astronomy and Astrophysics Supplement Series*, **12**, p. 331.

Figer, D. F., F. Najarro, D. Gilmore, M. Morris, S. S. Kim, E. Serabyn, I. S. McLean, A. M. Gilbert, J. R. Graham, J. E. Larkin, N. A. Levenson, and H. I. Teplitz (2002). Massive Stars in the Arches Cluster. *The Astrophysical Journal*, **581**, pp. 258–275. doi:10.1086/344154.

Filippenko, A. V. (1997). Optical Spectra of Supernovae. *Annual Review of Astronomy and Astrophysics*, **35**, pp. 309–355. doi:10.1146/annurev.astro.35.1.309.

Fitzgerald, M. P. and S. Mehta (1987). Spectroscopic and photometric observations in Bochum 10 and 11. *Monthly Notices of the Royal Astronomical Society*, **228**, pp. 545–555. doi:10.1093/mnras/228.3.545.

Foellmi, C., A. F. J. Moffat, and M. A. Guerrero (2003). Wolf-Rayet binaries in the Magellanic Clouds and implications for massive-star evolution - II. Large Magellanic Cloud. *Monthly Notices of the Royal Astronomical Society*, **338**, pp. 1025–1056. doi:10.1046/j.1365-8711.2003.06161.x.

Forte, J. C. (1978). The reddening law in Carina OB 1. *The Astronomical Journal*, **83**, pp. 1199–1205. doi:10.1086/112311.

France, K., S. R. McCandliss, and R. E. Lupu (2007). A Cometary Bow Shock and Mid-Infrared Emission Variations Revealed in Spitzer Observations of HD 34078 and IC 405. *The Astrophysical Journal*, **655**, pp. 920–939. doi:10.1086/510481.

Frew, D. J. (2004). The Historical Record of η Carinae I. The Visual Light Curve, 1595-2000. *Journal of Astronomical Data*, **10**, p. 6.

Freyhammer, L. M., H. Hensberge, C. Sterken, K. Pavlovski, A. Smette, and S. Ilijić (2005). The β Cephei variable in the eclipsing binary HD 92024. I. Determination of the orbit. *Astronomy & Astrophysics*, **429**, pp. 631–643. doi:10.1051/0004-6361:20041527.

Frieman, E. A. (1954). On Elephant-Trunk Structures in the Region of O Associations. *The Astrophysical Journal*, **120**, p. 18. doi:10.1086/145877.

Fujii, M. S. and S. Portegies Zwart (2011). The Origin of OB Runaway Stars. *Science*, **334**, p. 1380. doi:10.1126/science.1211927.

Fullerton, A. W., D. R. Gies, and C. T. Bolton (1996). Absorption Line Profile Variations among the O Stars. I. The Incidence of Variability. *The Astrophysical Journal Supplement Series*, **103**, p. 475. doi:10.1086/192285.

Fullerton, A. W., D. L. Massa, and R. K. Prinja (2006). The Discordance of Mass-Loss Estimates for Galactic O-Type Stars. *The Astrophysical Journal*, **637**, pp. 1025–1039. doi:10.1086/498560.

Gaczkowski, B., T. Preibisch, T. Ratzka, V. Roccatagliata, H. Ohlendorf, and H. Zinnecker (2013). Herschel far-infrared observations of the Carina Nebula complex. II. The embedded young stellar and protostellar population. *Astronomy & Astrophysics*, **549**, A67. doi:10.1051/0004-6361/201219836.

Gagné, M., G. Fehon, M. R. Savoy, D. H. Cohen, L. K. Townsley, P. S. Broos, M. S. Povich, M. F. Corcoran, N. R. Walborn, N. Remage Evans, A. F. J. Moffat, Y. Nazé, and L. M. Oskinova (2011). Carina OB Stars: X-ray Signatures of Wind Shocks and Magnetic Fields. *The Astrophysical Journal Supplement Series*, **194**, 5. doi:10.1088/0067-0049/194/1/5.

Gaia Collaboration, A. G. A. Brown, A. Vallenari, T. Prusti, J. H. J. de Bruijne, F. Mignard, R. Drimmel, C. Babusiaux, C. A. L. Bailer-Jones, U. Bastian, and et al. (2016a). Gaia Data Release 1. Summary of the astrometric, photometric, and survey properties. *Astronomy & Astrophysics*, **595**, A2. doi:10.1051/0004-6361/201629512.

Gaia Collaboration, T. Prusti, J. H. J. de Bruijne, A. G. A. Brown, A. Vallenari, C. Babusiaux, C. A. L. Bailer-Jones, U. Bastian, M. Biermann, D. W. Evans, and et al. (2016b). The Gaia mission. *Astronomy & Astrophysics*, **595**, A1. doi:10.1051/0004-6361/201629272.

Gal-Yam, A., D. C. Leonard, D. B. Fox, S. B. Cenko, A. M. Soderberg, D.-S. Moon, D. J. Sand, Caltech Core Collapse Program, W. Li, A. V. Filippenko, G. Aldering, and Y. Copin (2007). On the Progenitor of SN 2005gl and the Nature of Type IIn Supernovae. *The Astrophysical Journal*, **656**, pp. 372–381. doi:10.1086/510523.

Gallagher, J. S. (1989). Close binary models for luminous blue variables stars. In Davidson, K., A. F. J. Moffat, and H. J. G. L. M. Lamers (eds.) *IAU Colloq. 113: Physics of Luminous Blue Variables*, volume 157 of *Astrophysics and Space Science Library*, pp. 185–192.

Gamen, R., E. Gosset, N. Morrell, V. Niemela, H. Sana, Y. Nazé, G. Rauw, R. Barbá, and G. Solivella (2006). The first orbital solution for the massive colliding-wind binary HD 93162 (≡WR 25). *Astronomy & Astrophysics*, **460**, pp. 777–782. doi:10.1051/0004-6361:20065618.

García, B., S. Malaroda, H. Levato, N. Morrell, and M. Grosso (1998). Frequency of Binaries in the Open Cluster Trumpler 14. *Publications of the Astronomical Society of the Pacific*, **110**, pp. 53–59. doi:10.1086/316117.

Gardner, F. F., D. K. Milne, P. G. Mezger, and T. L. Wilson (1970). The Carina nebula at 6 cm. *Astronomy & Astrophysics*, **7**, pp. 349–358.

Garmany, C. D. (1994). OB associations: Massive stars in context. *Publications of the Astronomical Society of the Pacific*, **106**, pp. 25–37. doi:10.1086/133338.

Garmany, C. D., P. S. Conti, and P. Massey (1980). Spectroscopic studies of O type stars. IX - Binary frequency. *The Astrophysical Journal*, **242**, pp. 1063–1076. doi:10.1086/158537.

Garmany, C. D. and R. E. Stencel (1992). Galactic OB associations in the northern Milky Way Galaxy. I - Longitudes 55 deg to 150 deg. *Astronomy and Astrophysics Supplement Series*, **94**, pp. 211–244.

Gáspár, A., K. Y. L. Su, G. H. Rieke, Z. Balog, I. Kamp, J. R. Martínez-Galarza, and K. Stapelfeldt (2008). Modeling the Infrared Bow Shock at δ Velorum: Implications for Studies of Debris Disks and λ Boötis Stars. *The Astrophysical Journal*, **672**, 974-983. doi:10.1086/523299.

Gatto, A., S. Walch, M.-M. M. Low, T. Naab, P. Girichidis, S. C. O. Glover, R. Wünsch, R. S. Klessen, P. C. Clark, C. Baczynski, T. Peters, J. P. Ostriker, J. C. Ibáñez-Mejía, and S. Haid (2015). Modelling the supernova-driven ISM in different environments. *Monthly Notices of the Royal Astronomical Society*, **449**, pp. 1057–1075. doi:10.1093/mnras/stv324.

Gaviola, E. (1950). Eta Carinae. I. The Nebulosity. *The Astrophysical Journal*, **111**, p. 408. doi:10.1086/145274.

Geen, S., J. Rosdahl, J. Blaizot, J. Devriendt, and A. Slyz (2015). A detailed study of feedback from a massive star. *Monthly Notices of the Royal Astronomical Society*, **448**, pp. 3248–3264. doi:10.1093/mnras/stv251.

Gehrz, R. D. and N. J. Woolf (1971). Mass Loss from M Stars. *The Astrophysical Journal*, **165**, p. 285. doi:10.1086/150897.

Georgy, C., S. Ekström, P. Eggenberger, G. Meynet, L. Haemmerlé, A. Maeder, A. Granada, J. H. Groh, R. Hirschi, N. Mowlavi, N. Yusof, C. Charbonnel, T. Decressin, and F. Barblan (2013). Grids of stellar models with rotation. III. Models from 0.8 to 120 $M_\odot$ at a metallicity $Z = 0.002$. *Astronomy & Astrophysics*, **558**, A103. doi:10.1051/0004-6361/201322178.

Ghosh, S. K., K. V. K. Iyengar, T. N. Rengarajan, S. N. Tandon, R. P. Verma, and R. R. Daniel (1988). Far-infrared (120-300 micron) observations of the Carina Nebula. *The Astrophysical Journal*, **330**, p. 928. doi:10.1086/166523.

Gieles, M. (2013). Interacting Star Clusters. In *Massive Stars: From alpha to Omega*, p. 7.

Gieles, M. and S. F. Portegies Zwart (2011). The distinction between star clusters and associations. *Monthly Notices of the Royal Astronomical Society*, **410**, pp. L6–L7. doi:10.1111/j.1745-3933.2010.00967.x.

Gieles, M., H. Sana, and S. F. Portegies Zwart (2010). On the velocity dispersion of young star clusters: super-virial or binaries? *Monthly Notices of the Royal Astronomical Society*, **402**, pp. 1750–1757. doi:10.1111/j.1365-2966.2009.15993.x.

Gies, D. R. and C. T. Bolton (1986). The binary frequency and origin of the OB runaway stars. *The Astrophysical Journal Supplement Series*, **61**, pp. 419–454. doi:10.1086/191118.

Girichidis, P., S. Walch, T. Naab, A. Gatto, R. Wünsch, S. C. O. Glover, R. S. Klessen, P. C. Clark, T. Peters, D. Derigs, and C. Baczynski (2016). The SILCC (SImulating the LifeCycle of molecular Clouds) project - II. Dynamical evolution of the supernova-driven ISM and the launching of outflows. *Monthly Notices of the Royal Astronomical Society*, **456**, pp. 3432–3455. doi:10.1093/mnras/stv2742.

Glatzel, W. (1994). On the origin of strange modes and the mechanism of related instabilities. *Monthly Notices of the Royal Astronomical Society*, **271**. doi:10.1093/mnras/271.1.66.

Glatzel, W. and M. Kiriakidis (1993). Stability of Massive Stars and the Humphreys-Davidson Limit. *Monthly Notices of the Royal Astronomical Society*, **263**, p. 375. doi:10.1093/mnras/263.2.375.

Gomez, H. L., C. Vlahakis, C. M. Stretch, L. Dunne, S. A. Eales, A. Beelen, E. L. Gomez, and M. G. Edmunds (2010). Submillimetre variability of Eta Carinae: cool dust within the outer ejecta. *Monthly Notices of the Royal Astronomical Society*, **401**, pp. L48–L52. doi:10.1111/j.1745-3933.2009.00784.x.

Goodwin, S. P. (1997). Residual gas expulsion from young globular clusters. *Monthly Notices of the Royal Astronomical Society*, **284**, pp. 785–802. doi:10.1093/mnras/284.4.785.

Goodwin, S. P. and N. Bastian (2006). Gas expulsion and the destruction of massive young clusters. *Monthly Notices of the Royal Astronomical Society*, **373**, pp. 752–758. doi:10.1111/j.1365-2966.2006.11078.x.

Gouliermis, D., M. Kontizas, E. Kontizas, and R. Korakitis (2003). OB stellar associations in the Large Magellanic Cloud: Survey of young stellar systems. *Astronomy & Astrophysics*, **405**, pp. 111–124. doi:10.1051/0004-6361:20030483.

Gounelle, M. and G. Meynet (2012). Solar system genealogy revealed by extinct short-lived radionuclides in meteorites. *Astronomy & Astrophysics*, **545**, A4. doi: 10.1051/0004-6361/201219031.

Gräfener, G., J. S. Vink, A. de Koter, and N. Langer (2011). The Eddington factor as the key to understand the winds of the most massive stars. Evidence for a Γ-dependence of Wolf-Rayet type mass loss. *Astronomy & Astrophysics*, **535**, A56. doi:10.1051/0004-6361/201116701.

Gritschneder, M., A. Burkert, T. Naab, and S. Walch (2010). Detailed Numerical Simulations on the Formation of Pillars Around H II Regions. *The Astrophysical Journal*, **723**, pp. 971–984. doi:10.1088/0004-637X/723/2/971.

Gritschneder, M., D. N. C. Lin, S. D. Murray, Q.-Z. Yin, and M.-N. Gong (2012). The Supernova Triggered Formation and Enrichment of Our Solar System. *The Astrophysical Journal*, **745**, 22. doi:10.1088/0004-637X/745/1/22.

Groh, J. H., G. Meynet, and S. Ekström (2013). Massive star evolution: luminous blue variables as unexpected supernova progenitors. *Astronomy & Astrophysics*, **550**, L7. doi:10.1051/0004-6361/201220741.

Güdel, M., K. R. Briggs, T. Montmerle, M. Audard, L. Rebull, and S. L. Skinner (2008). Million-Degree Plasma Pervading the Extended Orion Nebula. *Science*, **319**, p. 309. doi:10.1126/science.1149926.

Gull, T. R., G. V. Kober, and K. E. Nielsen (2006). Eta Carinae across the 2003.5 Minimum: The Character and Variability of the Ejecta Absorption in the Near-Ultraviolet. *The Astrophysical Journal Supplement Series*, **163**, pp. 173–183. doi:10.1086/500113.

Gutermuth, R. A., J. L. Pipher, S. T. Megeath, P. C. Myers, L. E. Allen, and T. S. Allen (2011). A Correlation between Surface Densities of Young Stellar Objects and Gas in Eight Nearby Molecular Clouds. *The Astrophysical Journal*, **739**, 84. doi:10.1088/0004-637X/739/2/84.

Gvaramadze, V. V. and D. J. Bomans (2008). Search for OB stars running away from young star clusters. I. NGC 6611. *Astronomy & Astrophysics*, **490**, pp. 1071–1077. doi:10.1051/0004-6361:200810411.

Gvaramadze, V. V., A. Y. Kniazev, P. Kroupa, and S. Oh (2011a). Search for OB stars running away from young star clusters. II. The NGC 6357 star-forming region. *Astronomy & Astrophysics*, **535**, A29. doi:10.1051/0004-6361/201117746.

Gvaramadze, V. V., P. Kroupa, and J. Pflamm-Altenburg (2010). Massive runaway stars in the Large Magellanic Cloud. *Astronomy & Astrophysics*, **519**, A33. doi: 10.1051/0004-6361/201014871.

Gvaramadze, V. V., J. Pflamm-Altenburg, and P. Kroupa (2011b). Massive runaway stars in the Small Magellanic Cloud. *Astronomy & Astrophysics*, **525**, A17. doi: 10.1051/0004-6361/201015656.

Gvaramadze, V. V., C. Weidner, P. Kroupa, and J. Pflamm-Altenburg (2012). Field O stars: formed in situ or as runaways? *Monthly Notices of the Royal Astronomical Society*, **424**, pp. 3037–3049. doi:10.1111/j.1365-2966.2012.21452.x.

Hägele, G. F., J. F. Albacete Colombo, R. H. Barbá, and G. L. Bosch (2004). G287.84-0.82: an infrared star cluster in the Carina nebula. *Monthly Notices of the Royal Astronomical Society*, **355**, pp. 1237–1243. doi:10.1111/j.1365-2966.2004.08403.x.

Harper-Clark, E. and N. Murray (2009). One-Dimensional Dynamical Models of the Carina Nebula Bubble. *The Astrophysical Journal*, **693**, pp. 1696–1712. doi: 10.1088/0004-637X/693/2/1696.

Hartigan, P., J. A. Morse, B. Reipurth, S. Heathcote, and J. Bally (2001). Proper Motions of the HH 111 Jet Observed with the Hubble Space Telescope. *The Astrophysical Journal*, **559**, pp. L157–L161. doi:10.1086/323976.

Hartigan, P., M. Reiter, N. Smith, and J. Bally (2015). A Survey of Irradiated Pillars, Globules, and Jets in the Carina Nebula. *The Astronomical Journal*, **149**, 101. doi:10.1088/0004-6256/149/3/101.

Harvey, P. M., W. F. Hoffmann, and M. F. Campbell (1979). Far-infrared observations of the Carina I and II H II regions. *The Astrophysical Journal*, **227**, pp. 114–120. doi:10.1086/156709.

Hassan, S., R. Davé, S. Mitra, K. Finlator, B. Ciardi, and M. G. Santos (2017). Constraining the contribution of active galactic nuclei to reionisation. *ArXiv e-prints*.

Heiles, C. (1990). Clustered supernovae versus the gaseous disk and halo. *The Astrophysical Journal*, **354**, pp. 483–491. doi:10.1086/168709.

Hénault-Brunet, V., C. J. Evans, H. Sana, M. Gieles, N. Bastian, J. Maíz Apellániz, N. Markova, W. D. Taylor, E. Bressert, P. A. Crowther, and J. T. van Loon (2012). The VLT-FLAMES Tarantula Survey. VII. A low velocity dispersion for the young massive cluster R136. *Astronomy & Astrophysics*, **546**, A73. doi: 10.1051/0004-6361/201219471.

Herbst, W. (1976). On the extinction law in the Carina nebula. *The Astrophysical Journal*, **208**, pp. 923–931. doi:10.1086/154681.

Hester, J. J. and S. J. Desch (2005). Understanding Our Origins: Star Formation in HII Region Environments. In Krot, A. N., E. R. D. Scott, and B. Reipurth (eds.) *Chondrites and the Protoplanetary Disk*, volume 341 of *Astronomical Society of the Pacific Conference Series*, p. 107.

Hillier, D. J., K. Davidson, K. Ishibashi, and T. Gull (2001). On the Nature of the Central Source in η Carinae. *The Astrophysical Journal*, **553**, pp. 837–860. doi:10.1086/320948.

Hills, J. G. (1980). The effect of mass loss on the dynamical evolution of a stellar system - Analytic approximations. *The Astrophysical Journal*, **235**, pp. 986–991. doi:10.1086/157703.

Hoffman, J. L., D. C. Leonard, R. Chornock, A. V. Filippenko, A. J. Barth, and T. Matheson (2008). The Dual-Axis Circumstellar Environment of the Type IIn Supernova 1997eg. *The Astrophysical Journal*, **688**, 1186-1209. doi:10.1086/592261.

Høg, E., C. Fabricius, V. V. Makarov, S. Urban, T. Corbin, G. Wycoff, U. Bastian, P. Schwekendiek, and A. Wicenec (2000). The Tycho-2 catalogue of the 2.5 million brightest stars. *Astronomy & Astrophysics*, **355**, pp. L27–L30.

Högbom, J. A. (1974). Aperture Synthesis with a Non-Regular Distribution of Interferometer Baselines. *Astronomy and Astrophysics Supplement Series*, **15**, p. 417.

Hopkins, P. F., D. Kereš, J. Oñorbe, C.-A. Faucher-Giguère, E. Quataert, N. Murray, and J. S. Bullock (2014). Galaxies on FIRE (Feedback In Realistic Environments): stellar feedback explains cosmologically inefficient star formation. *Monthly Notices of the Royal Astronomical Society*, **445**, pp. 581–603. doi:10.1093/mnras/stu1738.

Hopkins, P. F., E. Quataert, and N. Murray (2011). Self-regulated star formation in galaxies via momentum input from massive stars. *Monthly Notices of the Royal Astronomical Society*, **417**, pp. 950–973. doi:10.1111/j.1365-2966.2011.19306.x.

Hopkins, P. F., E. Quataert, and N. Murray (2012). The structure of the interstellar medium of star-forming galaxies. *Monthly Notices of the Royal Astronomical Society*, **421**, pp. 3488–3521. doi:10.1111/j.1365-2966.2012.20578.x.

Hosokawa, T. and S.-i. Inutsuka (2005). Dynamical Expansion of Ionization and Dissociation Fronts around a Massive Star. I. A Mode of Triggered Star Formation. *The Astrophysical Journal*, **623**, pp. 917–921. doi:10.1086/428648.

Huang, W. and D. R. Gies (2006). Stellar Rotation in Young Clusters. I. Evolution of Projected Rotational Velocity Distributions. *The Astrophysical Journal*, **648**, pp. 580–590. doi:10.1086/505782.

Huchtmeier, W. K. and G. A. Day (1975). The Carina Nebula at 3.4 and 6 cm. *Astronomy & Astrophysics*, **41**, pp. 153–164.

Humphreys, R. M. (1973). Spectroscopic and photometric observations of luminous stars in Carina-Centaurus (l=282d - 305d). *Astronomy and Astrophysics Supplement Series*, **9**, p. 85.

Humphreys, R. M. (1978). Studies of luminous stars in nearby galaxies. I. Supergiants and O stars in the Milky Way. *The Astrophysical Journal Supplement Series*, **38**, pp. 309–350. doi:10.1086/190559.

Humphreys, R. M. and K. Davidson (1994). The luminous blue variables: Astrophysical geysers. *Publications of the Astronomical Society of the Pacific*, **106**, pp. 1025–1051. doi:10.1086/133478.

Humphreys, R. M., K. Davidson, and N. Smith (1999). Eta Carinae's Second Eruption and the Light Curves of the eta Carinae Variables. *Publications of the Astronomical Society of the Pacific*, **111**, pp. 1124–1131. doi:10.1086/316420.

Humphreys, R. M., K. Weis, K. Davidson, and M. S. Gordon (2016). On the Social Traits of Luminous Blue Variables. *The Astrophysical Journal*, **825**, 64. doi:10.3847/0004-637X/825/1/64.

Hur, H., H. Sung, and M. S. Bessell (2012). Distance and the Initial Mass Function of Young Open Clusters in the η Carina Nebula: Tr 14 and Tr 16. *The Astronomical Journal*, **143**, 41. doi:10.1088/0004-6256/143/2/41.

Ibeling, D. and A. Heger (2013). The Metallicity Dependence of the Minimum Mass for Core-collapse Supernovae. *The Astrophysical Journal*, **765**, L43. doi:10.1088/2041-8205/765/2/L43.

Iben, I., Jr. (1999). The Effects of Possible Binary and Tertiary Companions on the Behavior of Eta Carinae. In Morse, J. A., R. M. Humphreys, and A. Damineli (eds.) *Eta Carinae at The Millennium*, volume 179 of *Astronomical Society of the Pacific Conference Series*, p. 367.

Iglesias-Marzoa, R., M. López-Morales, and M. Jesús Arévalo Morales (2015). The rvfit Code: A Detailed Adaptive Simulated Annealing Code for Fitting Binaries and Exoplanets Radial Velocities. *Publications of the Astronomical Society of the Pacific*, **127**, pp. 567–582. doi:10.1086/682056.

Innes, R. T. A. (1903). Observations of variable stars, η Argus. *Annals of the Cape Observatory*, **9**, pp. 75B–78B.

Ishibashi, K., T. R. Gull, K. Davidson, N. Smith, T. Lanz, D. Lindler, K. Feggans, E. Verner, B. E. Woodgate, R. A. Kimble, C. W. Bowers, S. Kraemer, S. R. Heap, A. C. Danks, S. P. Maran, C. L. Joseph, M. E. Kaiser, J. L. Linsky, F. Roesler, and D. Weistrop (2003). Discovery of a Little Homunculus within the Homunculus Nebula of η Carinae. *The Astronomical Journal*, **125**, pp. 3222–3236. doi:10.1086/375306.

Ivanov, G. R. (1996). OB associations in nearby galaxies. *Astronomy & Astrophysics*, **305**, p. 708.

Ivezic, Z., J. A. Tyson, B. Abel, E. Acosta, R. Allsman, Y. AlSayyad, S. F. Anderson, J. Andrew, R. Angel, G. Angeli, R. Ansari, P. Antilogus, K. T. Arndt, P. Astier, E. Aubourg, T. Axelrod, D. J. Bard, J. D. Barr, A. Barrau, J. G. Bartlett, B. J. Bauman, S. Beaumont, A. C. Becker, J. Becla, C. Beldica, S. Bellavia, G. Blanc, R. D. Blandford, J. S. Bloom, J. Bogart, K. Borne, J. F. Bosch, D. Boutigny, W. N. Brandt, M. E. Brown, J. S. Bullock, P. Burchat, D. L. Burke, G. Cagnoli, D. Calabrese, S. Chandrasekharan, S. Chesley, E. C. Cheu, J. Chiang, C. F. Claver, A. J. Connolly, K. H. Cook, A. Cooray, K. R. Covey, C. Cribbs, W. Cui, R. Cutri, G. Daubard, G. Daues, F. Delgado, S. Digel, P. Doherty, R. Dubois, G. P. Dubois-Felsmann, J. Durech, M. Eracleous, H. Ferguson, J. Frank, M. Freemon, E. Gangler, E. Gawiser, J. C. Geary, P. Gee, M. Geha, R. R. Gibson, D. K. Gilmore, T. Glanzman, I. Goodenow, W. J. Gressler, P. Gris, A. Guyonnet, P. A. Hascall, J. Haupt, F. Hernandez, C. Hogan, D. Huang, M. E. Huffer, W. R. Innes, S. H. Jacoby, B. Jain, J. Jee, J. G. Jernigan, D. Jevremovic, K. Johns, R. L. Jones, C. Juramy-Gilles, M. Juric, S. M. Kahn, J. S. Kalirai, N. Kallivayalil, B. Kalmbach, J. P. Kantor, M. M. Kasliwal, R. Kessler, D. Kirkby, L. Knox, I. Kotov, V. L. Krabbendam, S. Krughoff, P. Kubanek, J. Kuczewski, S. Kulkarni, R. Lambert, L. Le Guillou, D. Levine, M. Liang, K. Lim, C. Lintott, R. H. Lupton, A. Mahabal, P. Marshall, S. Marshall, M. May, R. McKercher, M. Migliore, M. Miller, D. J. Mills, D. G. Monet, M. Moniez, D. R. Neill, J. Nief, A. Nomerotski, M. Nordby, P. O'Connor, J. Oliver, S. S. Olivier, K. Olsen, S. Ortiz, R. E. Owen, R. Pain, J. R. Peterson, C. E. Petry, F. Pierfederici, S. Pietrowicz, R. Pike, P. A. Pinto, R. Plante, S. Plate, P. A. Price, M. Prouza, V. Radeka, J. Rajagopal, A. Rasmussen, N. Regnault, S. T. Ridgway, S. Ritz, W. Rosing, C. Roucelle, M. R. Rumore, S. Russo, A. Saha, B. Sassolas, T. L. Schalk, R. H. Schindler, D. P. Schneider, G. Schumacher, J. Sebag, G. H. Sembroski, L. G. Seppala, I. Shipsey, N. Silvestri, J. A. Smith, R. C. Smith, M. A. Strauss, C. W. Stubbs, D. Sweeney, A. Szalay, P. Takacs, J. J. Thaler, R. Van Berg, D. Vanden Berk, K. Vetter, F. Virieux, B. Xin, L. Walkowicz, C. W. Walter, D. L. Wang, M. Warner, B. Willman, D. Wittman, S. C. Wolff, W. M. Wood-Vasey, P. Yoachim, H. Zhan, and for the LSST Collaboration (2008). LSST:

from Science Drivers to Reference Design and Anticipated Data Products. *ArXiv e-prints*.

Johnstone, D., D. Hollenbach, and J. Bally (1998). Photoevaporation of Disks and Clumps by Nearby Massive Stars: Application to Disk Destruction in the Orion Nebula. *The Astrophysical Journal*, **499**, pp. 758–776. doi:10.1086/305658.

Justham, S., P. Podsiadlowski, and J. S. Vink (2014). Luminous Blue Variables and Superluminous Supernovae from Binary Mergers. *The Astrophysical Journal*, **796**, 121. doi:10.1088/0004-637X/796/2/121.

Kaltcheva, N. T. and V. K. Golev (2012). Galactic Structure Toward the Carina Tangent. *Publications of the Astronomical Society of the Pacific*, **124**, p. 128. doi:10.1086/664697.

Kaper, L., J. T. van Loon, T. Augusteijn, P. Goudfrooij, F. Patat, L. B. F. M. Waters, and A. A. Zijlstra (1997). Discovery of a Bow Shock around VELA X-1. *The Astrophysical Journal*, **475**, pp. L37–L40. doi:10.1086/310454.

Karr, J. L. and P. G. Martin (2003). Triggered Star Formation in the W5 H II Region. *The Astrophysical Journal*, **595**, pp. 900–912. doi:10.1086/376590.

Kashi, A. and N. Soker (2010). Periastron Passage Triggering of the 19th Century Eruptions of Eta Carinae. *The Astrophysical Journal*, **723**, pp. 602–611. doi:10.1088/0004-637X/723/1/602.

Kendrew, S., R. Simpson, E. Bressert, M. S. Povich, R. Sherman, C. J. Lintott, T. P. Robitaille, K. Schawinski, and G. Wolf-Chase (2012). The Milky Way Project: A Statistical Study of Massive Star Formation Associated with Infrared Bubbles. *The Astrophysical Journal*, **755**, 71. doi:10.1088/0004-637X/755/1/71.

Kenyon, S. J. and L. Hartmann (1995). Pre-Main-Sequence Evolution in the Taurus-Auriga Molecular Cloud. *The Astrophysical Journal Supplement Series*, **101**, p. 117. doi:10.1086/192235.

Kessel-Deynet, O. and A. Burkert (2003). Radiation-driven implosion of molecular cloud cores. *Monthly Notices of the Royal Astronomical Society*, **338**, pp. 545–554. doi:10.1046/j.1365-8711.2003.05737.x.

Kharchenko, N. V. (2001). All-sky compiled catalogue of 2.5 million stars. *Kinematika i Fizika Nebesnykh Tel*, **17**, pp. 409–423.

Kharchenko, N. V. and S. Roeser (2009). VizieR Online Data Catalog: All-Sky Compiled Catalogue of 2.5 million stars (Kharchenko+ 2009). *VizieR Online Data Catalog*, **1280**.

Kiewe, M., A. Gal-Yam, I. Arcavi, D. C. Leonard, J. Emilio Enriquez, S. B. Cenko, D. B. Fox, D.-S. Moon, D. J. Sand, A. M. Soderberg, and T. CCCP (2012). Caltech Core-Collapse Project (CCCP) Observations of Type IIn Supernovae: Typical Properties and Implications for Their Progenitor Stars. *The Astrophysical Journal*, **744**, 10. doi:10.1088/0004-637X/744/1/10.

Kiminki, D. C. and H. A. Kobulnicky (2012). An Updated Look at Binary Characteristics of Massive Stars in the Cygnus OB2 Association. *The Astrophysical Journal*, **751**, 4. doi:10.1088/0004-637X/751/1/4.

Kiminki, D. C., H. A. Kobulnicky, I. Ewing, M. M. Bagley Kiminki, M. Lundquist, M. Alexander, C. Vargas-Alvarez, H. Choi, and C. B. Henderson (2012). Additional Massive Binaries in the Cygnus OB2 Association. *The Astrophysical Journal*, **747**, 41. doi:10.1088/0004-637X/747/1/41.

Kiminki, D. C., H. A. Kobulnicky, K. Kinemuchi, J. S. Irwin, C. L. Fryer, R. C. Berrington, B. Uzpen, A. J. Monson, M. J. Pierce, and S. E. Woosley (2007). A Radial Velocity Survey of the Cyg OB2 Association. *The Astrophysical Journal*, **664**, pp. 1102–1120. doi:10.1086/513709.

Kiminki, D. C., H. A. Kobulnicky, K. Kinemuchi, J. S. Irwin, C. L. Fryer, R. C. Berrington, B. Uzpen, A. J. Monson, M. J. Pierce, and S. E. Woosley (2008). Erratum: "A Radial Velocity Survey of the Cygnus OB2 Association" (ApJ, 664, 1102 [2007]). *The Astrophysical Journal*, **681**, 735. doi:10.1086/588464.

Kiminki, M. M., M. Reiter, and N. Smith (2016). Ancient eruptions of η Carinae: a tale written in proper motions. *Monthly Notices of the Royal Astronomical Society*, **463**, pp. 845–857. doi:10.1093/mnras/stw2019.

Kiminki, M. M., N. Smith, M. Reiter, and J. Bally (2017). Proper motions of five OB stars with candidate dusty bow shocks in the Carina Nebula. *Monthly Notices of the Royal Astronomical Society*, **468**, pp. 2469–2481. doi:10.1093/mnras/stx607.

Kobulnicky, H. A., W. T. Chick, J. E. Schurhammer, D. P. an Andrews, M. S. Povich, S. A. Munari, G. M. Olivier, R. L. Sorber, H. N. Wernke, D. A. Dale, and D. M. Dixon (2016). A Comprehensive Search for Stellar Bowshock Nebulae in the Milky Way: A Catalog of 709 Mid-infrared Selected Candidates. *The Astrophysical Journal Supplement Series*, **227**, 18. doi:10.3847/0067-0049/227/2/18.

Kobulnicky, H. A., I. J. Gilbert, and D. C. Kiminki (2010). OB Stars and Stellar Bow shocks in Cygnus-X: A Novel Laboratory Estimating Stellar Mass Loss Rates. *The Astrophysical Journal*, **710**, pp. 549–566. doi:10.1088/0004-637X/710/1/549.

Kobulnicky, H. A., D. C. Kiminki, M. J. Lundquist, J. Burke, J. Chapman, E. Keller, K. Lester, E. K. Rolen, E. Topel, A. Bhattacharjee, R. A. Smullen, C. A. Vargas Álvarez, J. C. Runnoe, D. A. Dale, and M. M. Brotherton (2014). Toward Complete Statistics of Massive Binary Stars: Penultimate Results from the Cygnus OB2 Radial Velocity Survey. *The Astrophysical Journal Supplement Series*, **213**, 34. doi:10.1088/0067-0049/213/2/34.

Kotak, R. and J. S. Vink (2006). Luminous blue variables as the progenitors of supernovae with quasi-periodic radio modulations. *Astronomy & Astrophysics*, **460**, pp. L5–L8. doi:10.1051/0004-6361:20065800.

Kramida, A., Y. Ralchenko, J. Reader, and NIST ASD Team (2016). NIST Atomic Spectra Database (version 5.4).

Krause, M. G. H. and R. Diehl (2014). Dynamics and Energy Loss in Superbubbles. *The Astrophysical Journal*, **794**, L21. doi:10.1088/2041-8205/794/2/L21.

Krebs, J. and W. Hillebrandt (1983). The interaction of supernova shockfronts and nearby interstellar clouds. *Astronomy & Astrophysics*, **128**, pp. 411–419.

Krist, J. E., R. N. Hook, and F. Stoehr (2011). 20 years of Hubble Space Telescope optical modeling using Tiny Tim. In Kahan, M. A. (ed.) *Optical Modeling and Performance Predictions V*, volume 8127 of *Proc. SPIE*, p. 81270J. SPIE, Bellingham, WA. doi:10.1117/12.892762.

Kroupa, P., S. Aarseth, and J. Hurley (2001). The formation of a bound star cluster: from the Orion nebula cluster to the Pleiades. *Monthly Notices of the Royal Astronomical Society*, **321**, pp. 699–712. doi:10.1046/j.1365-8711.2001.04050.x.

Kruijssen, J. M. D. (2012). On the fraction of star formation occurring in bound stellar clusters. *Monthly Notices of the Royal Astronomical Society*, **426**, pp. 3008–3040. doi:10.1111/j.1365-2966.2012.21923.x.

Krumholz, M. R., R. I. Klein, C. F. McKee, S. S. R. Offner, and A. J. Cunningham (2009). The Formation of Massive Star Systems by Accretion. *Science*, **323**, p. 754. doi:10.1126/science.1165857.

Krumholz, M. R. and C. D. Matzner (2009). The Dynamics of Radiation-pressure-dominated H II Regions. *The Astrophysical Journal*, **703**, pp. 1352–1362. doi:10.1088/0004-637X/703/2/1352.

Krumholz, M. R., C. F. McKee, and R. I. Klein (2005a). How Protostellar Outflows Help Massive Stars Form. *The Astrophysical Journal*, **618**, pp. L33–L36. doi:10.1086/427555.

Krumholz, M. R., C. F. McKee, and R. I. Klein (2005b). The formation of stars by gravitational collapse rather than competitive accretion. *Nature*, **438**, pp. 332–334. doi:10.1038/nature04280.

Krumholz, M. R. and T. A. Thompson (2012). Direct Numerical Simulation of Radiation Pressure-driven Turbulence and Winds in Star Clusters and Galactic Disks. *The Astrophysical Journal*, **760**, 155. doi:10.1088/0004-637X/760/2/155.

Kudritzki, R.-P. and J. Puls (2000). Winds from Hot Stars. *Annual Review of Astronomy and Astrophysics*, **38**, pp. 613–666. doi:10.1146/annurev.astro.38.1.613.

Kumar, B., S. Sharma, J. Manfroid, E. Gosset, G. Rauw, Y. Nazé, and R. Kesh Yadav (2014). Investigation of the stellar content in the western part of the Carina nebula. *Astronomy & Astrophysics*, **567**, A109. doi:10.1051/0004-6361/201323027.

Lada, C. J. (1985). Cold outflows, energetic winds, and enigmatic jets around young stellar objects. *Annual Review of Astronomy and Astrophysics*, **23**, pp. 267–317. doi:10.1146/annurev.aa.23.090185.001411.

Lada, C. J., B. G. Elmegreen, H.-I. Cong, and P. Thaddeus (1978). Molecular clouds in the vicinity of W3, W4, and W5. *The Astrophysical Journal*, **226**, pp. L39–L42. doi:10.1086/182826.

Lada, C. J. and E. A. Lada (1991). The nature, origin and evolution of embedded star clusters. In Janes, K. (ed.) *The Formation and Evolution of Star Clusters*, volume 13 of *Astronomical Society of the Pacific Conference Series*, pp. 3–22.

Lada, C. J. and E. A. Lada (2003). Embedded Clusters in Molecular Clouds. *Annual Review of Astronomy and Astrophysics*, **41**, pp. 57–115. doi:10.1146/annurev.astro.41.011802.094844.

Lada, C. J., M. Margulis, and D. Dearborn (1984). The formation and early dynamical evolution of bound stellar systems. *The Astrophysical Journal*, **285**, pp. 141–152. doi:10.1086/162485.

Lamers, H. J. G. L. M. and E. L. Fitzpatrick (1988). The relationship between the Eddington limit, the observed upper luminosity limit for massive stars, and the luminous blue variables. *The Astrophysical Journal*, **324**, pp. 279–287. doi:10.1086/165894.

Larson, R. B. (1995). Star formation in groups. *Monthly Notices of the Royal Astronomical Society*, **272**, pp. 213–220. doi:10.1093/mnras/272.1.213.

Lee, T., D. A. Papanastassiou, and G. J. Wasserburg (1976a). Correction to "Demonstration of ^{26}Mg excess in Allende and evidence for ^{26}Al". *Geophysical Research Letters*, **3**(2), pp. 109–112. ISSN 1944-8007. doi:10.1029/GL003i002p00109.

Lee, T., D. A. Papanastassiou, and G. J. Wasserburg (1976b). Demonstration of ^{26}Mg excess in Allende and evidence for ^{26}Al. *Geophysical Research Letters*, **3**(1), pp. 41–44. ISSN 1944-8007. doi:10.1029/GL003i001p00041.

Lefloch, B. and B. Lazareff (1994). Cometary globules. 1: Formation, evolution and morphology. *Astronomy & Astrophysics*, **289**, pp. 559–578.

Leitherer, C., S. Ekström, G. Meynet, D. Schaerer, K. B. Agienko, and E. M. Levesque (2014). The Effects of Stellar Rotation. II. A Comprehensive Set of Starburst99 Models. *The Astrophysical Journal Supplement Series*, **212**, 14. doi: 10.1088/0067-0049/212/1/14.

Leitherer, C., D. Schaerer, J. D. Goldader, R. M. G. Delgado, C. Robert, D. F. Kune, D. F. de Mello, D. Devost, and T. M. Heckman (1999). Starburst99: Synthesis Models for Galaxies with Active Star Formation. *The Astrophysical Journal Supplement Series*, **123**, pp. 3–40. doi:10.1086/313233.

Levato, H., B. García, C. Loustó, N. Morrell, and P. Saizar (1986). About the stability of the spectrograph of the 1-m Yale telescope at Cerro Tololo. *Revista Mexicana de Astronomía y Astrofísica*, **13**, pp. 3–7.

Levato, H., S. Malaroda, B. Garcia, N. Morrell, and G. Solivella (1990). Spectroscopic binaries in the open cluster Collinder 228. *The Astrophysical Journal Supplement Series*, **72**, pp. 323–333. doi:10.1086/191419.

Levato, H., S. Malaroda, B. Garcia, N. Morrell, G. Solivella, and M. Grosso (1991a). Radial velocities in the open cluster Trumpler 14. *Astrophysics and Space Science*, **183**, pp. 147–153. doi:10.1007/BF00643023.

Levato, H., S. Malaroda, N. Morrell, B. Garcia, and C. Hernandez (1991b). Spectroscopic binaries in the open cluster Trumpler 16. *The Astrophysical Journal Supplement Series*, **75**, pp. 869–875. doi:10.1086/191551.

Li, Z.-Y. and F. Nakamura (2006). Cluster Formation in Protostellar Outflow-driven Turbulence. *The Astrophysical Journal*, **640**, pp. L187–L190. doi:10.1086/503419.

Li, Z.-Y., P. Wang, T. Abel, and F. Nakamura (2010). Lowering the Characteristic Mass of Cluster Stars by Magnetic Fields and Outflow Feedback. *The Astrophysical Journal*, **720**, pp. L26–L30. doi:10.1088/2041-8205/720/1/L26.

Licquia, T. C. and J. A. Newman (2015). Improved Estimates of the Milky Way's Stellar Mass and Star Formation Rate from Hierarchical Bayesian Meta-Analysis. *The Astrophysical Journal*, **806**, 96. doi:10.1088/0004-637X/806/1/96.

Lindegren, L., U. Lammers, U. Bastian, J. Hernández, S. Klioner, D. Hobbs, A. Bombrun, D. Michalik, M. Ramos-Lerate, A. Butkevich, G. Comoretto, E. Joliet, B. Holl, A. Hutton, P. Parsons, H. Steidelmüller, U. Abbas, M. Altmann, A. Andrei, S. Anton, N. Bach, C. Barache, U. Becciani, J. Berthier, L. Bianchi, M. Biermann, S. Bouquillon, G. Bourda, T. Brüsemeister, B. Bucciarelli, D. Busonero, T. Carlucci, J. Castañeda, P. Charlot, M. Clotet, M. Crosta, M. Davidson, F. de Felice, R. Drimmel, C. Fabricius, A. Fienga, F. Figueras, E. Fraile, M. Gai, N. Garralda, R. Geyer, J. J. González-Vidal, R. Guerra, N. C. Hambly, M. Hauser, S. Jordan, M. G. Lattanzi, H. Lenhardt, S. Liao, W. Löffler, P. J. McMillan, F. Mignard, A. Mora, R. Morbidelli, J. Portell, A. Riva, M. Sarasso, I. Serraller, H. Siddiqui, R. Smart, A. Spagna, U. Stampa, I. Steele, F. Taris, J. Torra, W. van Reeven, A. Vecchiato, S. Zschocke, J. de Bruijne, G. Gracia, F. Raison, T. Lister, J. Marchant, R. Messineo, M. Soffel, J. Osorio, A. de Torres, and W. O'Mullane (2016). Gaia Data Release 1. Astrometry: one billion positions, two million proper motions and parallaxes. *Astronomy & Astrophysics*, **595**, A4. doi:10.1051/0004-6361/201628714.

Livio, M. and J. E. Pringle (1998). Can eta Carinae be a triple system? *Monthly Notices of the Royal Astronomical Society*, **295**, pp. L59–L60. doi:10.1046/j.1365-8711.1998.01567.x.

Lopez, L. A., M. R. Krumholz, A. D. Bolatto, J. X. Prochaska, and E. Ramirez-Ruiz (2011). What Drives the Expansion of Giant H II Regions?: A Study of Stellar Feedback in 30 Doradus. *The Astrophysical Journal*, **731**, 91. doi:10.1088/0004-637X/731/2/91.

Lopez, L. A., M. R. Krumholz, A. D. Bolatto, J. X. Prochaska, E. Ramirez-Ruiz, and D. Castro (2014). The Role of Stellar Feedback in the Dynamics of H II Regions. *The Astrophysical Journal*, **795**, 121. doi:10.1088/0004-637X/795/2/121.

Lucy, L. B. and P. M. Solomon (1970). Mass Loss by Hot Stars. *The Astrophysical Journal*, **159**, p. 879. doi:10.1086/150365.

Mac Low, M.-M. and R. S. Klessen (2004). Control of star formation by supersonic turbulence. *Reviews of Modern Physics*, **76**, pp. 125–194. doi:10.1103/RevModPhys.76.125.

Mac Low, M.-M. and R. McCray (1988). Superbubbles in disk galaxies. *The Astrophysical Journal*, **324**, pp. 776–785. doi:10.1086/165936.

Mackey, J., V. V. Gvaramadze, S. Mohamed, and N. Langer (2015). Wind bubbles within H II regions around slowly moving stars. *Astronomy & Astrophysics*, **573**, A10. doi:10.1051/0004-6361/201424716.

Mackey, J., T. J. Haworth, V. V. Gvaramadze, S. Mohamed, N. Langer, and T. J. Harries (2016). Detecting stellar-wind bubbles through infrared arcs in H II regions. *Astronomy & Astrophysics*, **586**, A114. doi:10.1051/0004-6361/201527569.

Mackey, J. and A. J. Lim (2010). Dynamical models for the formation of elephant trunks in HII regions. *Monthly Notices of the Royal Astronomical Society*, **403**, pp. 714–730. doi:10.1111/j.1365-2966.2009.16181.x.

Madura, T. I., T. R. Gull, S. P. Owocki, J. H. Groh, A. T. Okazaki, and C. M. P. Russell (2012). Constraining the absolute orientation of η Carinae's binary orbit: a 3D dynamical model for the broad [Fe III] emission. *Monthly Notices of the Royal Astronomical Society*, **420**, pp. 2064–2086. doi:10.1111/j.1365-2966.2011.20165.x.

Maeder, A. (1983). Evolution of chemical abundances in massive stars. I - OB stars, Hubble-Sandage variables and Wolf-Rayet stars. Changes at stellar surfaces and galactic enrichment by stellar winds. *Astronomy & Astrophysics*, **120**, pp. 113–129.

Magnier, E. A., P. Battinelli, W. H. G. Lewin, Z. Haiman, J. van Paradijs, G. Hasinger, W. Pietsch, R. Supper, and J. Truemper (1993). Automated identification of OB associations in M31. *Astronomy & Astrophysics*, **278**, pp. 36–42.

Mahmud, N. and J. Anderson (2008). Using Resolved Galaxies in Hubble Space Telescope Images to Measure Absolute Proper Motions. *Publications of the Astronomical Society of the Pacific*, **120**, pp. 907–921. doi:10.1086/591290.

Maíz Apellániz, J., A. Sota, J. I. Arias, R. H. Barbá, N. R. Walborn, S. Simón-Díaz, I. Negueruela, A. Marco, J. R. S. Leão, A. Herrero, R. C. Gamen, and E. J. Alfaro (2016). The Galactic O-Star Spectroscopic Survey (GOSSS). III. 142 Additional O-type Systems. *The Astrophysical Journal Supplement Series*, **224**, 4. doi:10.3847/0067-0049/224/1/4.

Maíz Apellániz, J., A. Sota, N. I. Morrell, R. H. Barbá, N. R. Walborn, E. J. Alfaro, R. C. Gamen, J. I. Arias, and A. T. Gallego Calvente (2013). First whole-sky results from the Galactic O-Star Spectroscopic Survey. In *Massive Stars: From alpha to Omega*, p. 198.

Markwardt, C. B. (2009). Non-linear Least-squares Fitting in IDL with MPFIT. In Bohlender, D. A., D. Durand, and P. Dowler (eds.) *Astronomical Data Analysis Software and Systems XVIII*, volume 411 of *Astronomical Society of the Pacific Conference Series*, p. 251.

Martins, F., W. Marcolino, D. J. Hillier, J.-F. Donati, and J.-C. Bouret (2015). Radial dependence of line profile variability in seven O9-B0.5 stars. *Astronomy & Astrophysics*, **574**, A142. doi:10.1051/0004-6361/201423882.

Martins, F., D. Schaerer, and D. J. Hillier (2005). A new calibration of stellar parameters of Galactic O stars. *Astronomy & Astrophysics*, **436**, pp. 1049–1065. doi:10.1051/0004-6361:20042386.

Mason, B. D., W. I. Hartkopf, D. R. Gies, T. J. Henry, and J. W. Helsel (2009). The High Angular Resolution Multiplicity of Massive Stars. *The Astronomical Journal*, **137**, pp. 3358–3377. doi:10.1088/0004-6256/137/2/3358.

Massey, P., K. DeGioia-Eastwood, and E. Waterhouse (2001). The Progenitor Masses of Wolf-Rayet Stars and Luminous Blue Variables Determined from Cluster Turnoffs. II. Results from 12 Galactic Clusters and OB Associations. *The Astronomical Journal*, **121**, pp. 1050–1070. doi:10.1086/318769.

Massey, P. and J. Johnson (1993). Massive stars near Eta Carinae - The stellar content of Tr 14 and Tr 16. *The Astronomical Journal*, **105**, pp. 980–1001. doi:10.1086/116487.

Massey, P., K. E. Johnson, and K. Degioia-Eastwood (1995). The Initial Mass Function and Massive Star Evolution in the OB Associations of the Northern Milky Way. *The Astrophysical Journal*, **454**, p. 151. doi:10.1086/176474.

Massey, P. and A. B. Thompson (1991). Massive stars in Cyg OB2. *The Astronomical Journal*, **101**, pp. 1408–1428. doi:10.1086/115774.

Matzner, C. D. (2007). Protostellar Outflow-driven Turbulence. *The Astrophysical Journal*, **659**, pp. 1394–1403. doi:10.1086/512361.

Matzner, C. D. and C. F. McKee (2000). Efficiencies of Low-Mass Star and Star Cluster Formation. *The Astrophysical Journal*, **545**, pp. 364–378. doi:10.1086/317785.

Mauerhan, J. C., N. Smith, A. V. Filippenko, K. B. Blanchard, P. K. Blanchard, C. F. E. Casper, S. B. Cenko, K. I. Clubb, D. P. Cohen, K. L. Fuller, G. Z. Li, and J. M. Silverman (2013). The unprecedented 2012 outburst of SN 2009ip: a luminous blue variable star becomes a true supernova. *Monthly Notices of the Royal Astronomical Society*, **430**, pp. 1801–1810. doi:10.1093/mnras/stt009.

Mauron, N. and E. Josselin (2011). The mass-loss rates of red supergiants and the de Jager prescription. *Astronomy & Astrophysics*, **526**, A156. doi:10.1051/0004-6361/201013993.

Mayer, P., R. Lorenz, H. Drechsel, and A. Abseim (2001). The early-type multiple system QZ Carinae. *Astronomy & Astrophysics*, **366**, pp. 558–564. doi:10.1051/0004-6361:20000228.

McCall, M. L. (1981). Big grains in the Orion nebula. *Monthly Notices of the Royal Astronomical Society*, **194**, pp. 485–502. doi:10.1093/mnras/194.3.485.

McClure-Griffiths, N. M. and J. M. Dickey (2007). Milky Way Kinematics. I. Measurements at the Subcentral Point of the Fourth Quadrant. *The Astrophysical Journal*, **671**, pp. 427–438. doi:10.1086/522297.

McKee, C. F. and J. C. Tan (2003). The Formation of Massive Stars from Turbulent Cores. *The Astrophysical Journal*, **585**, pp. 850–871. doi:10.1086/346149.

Meaburn, J., P. Boumis, J. R. Walsh, W. Steffen, A. J. Holloway, R. J. R. Williams, and M. Bryce (1996). Highly supersonic motions within the outer features of the eta Carinae nebulosity. *Monthly Notices of the Royal Astronomical Society*, **282**, pp. 1313–1320. doi:10.1093/mnras/282.4.1313.

Meaburn, J., R. D. Wolstencroft, and J. R. Walsh (1987). Echelle and spectropolarimetric observations of the Eta Carinae nebulosity. *Astronomy & Astrophysics*, **181**, pp. 333–342.

Megeath, S. T., P. Cox, L. Bronfman, and P. R. Roelfsema (1996). Evidence for ongoing star formation in the Carina nebula. *Astronomy & Astrophysics*, **305**, p. 296.

Mehner, A., K. Davidson, G. J. Ferland, and R. M. Humphreys (2010). High-excitation Emission Lines near Eta Carinae, and Its Likely Companion Star. *The Astrophysical Journal*, **710**, pp. 729–742. doi:10.1088/0004-637X/710/1/729.

Mehner, A., W. Steffen, J. H. Groh, F. P. A. Vogt, D. Baade, H. M. J. Boffin, K. Davidson, W. J. de Wit, R. M. Humphreys, C. Martayan, R. D. Oudmaijer, T. Rivinius, and F. Selman (2016). Dissecting a supernova impostor's circumstellar medium: MUSEing about the SHAPE of η Carinae's outer ejecta. *Astronomy & Astrophysics*, **595**, A120. doi:10.1051/0004-6361/201628770.

Meynet, G. and A. Maeder (2005). Stellar evolution with rotation. XI. Wolf-Rayet star populations at different metallicities. *Astronomy & Astrophysics*, **429**, pp. 581–598. doi:10.1051/0004-6361:20047106.

Miller, G. E. and J. M. Scalo (1978). On the birthplaces of stars. *Publications of the Astronomical Society of the Pacific*, **90**, pp. 506–513. doi:10.1086/130373.

Mizuta, A., J. O. Kane, M. W. Pound, B. A. Remington, D. D. Ryutov, and H. Takabe (2006). Formation of Pillars at the Boundaries between H II Regions and Molecular Clouds. *The Astrophysical Journal*, **647**, pp. 1151–1158. doi:10.1086/505458.

Moe, M. and R. Di Stefano (2017). Mind Your Ps and Qs: The Interrelation between Period (P) and Mass-ratio (Q) Distributions of Binary Stars. *The Astrophysical Journal Supplement Series*, **230**, 15. doi:10.3847/1538-4365/aa6fb6.

Moffat, A. F. J., M. F. Corcoran, I. R. Stevens, G. Skalkowski, S. V. Marchenko, A. Mücke, A. Ptak, B. S. Koribalski, L. Brenneman, R. Mushotzky, J. M. Pittard, A. M. T. Pollock, and W. Brandner (2002). Galactic Starburst NGC 3603 from X-Rays to Radio. *The Astrophysical Journal*, **573**, pp. 191–198. doi:10.1086/340491.

Moffat, A. F. J., S. V. Marchenko, W. Seggewiss, K. A. van der Hucht, H. Schrijver, B. Stenholm, I. Lundstrom, D. Y. A. Setia Gunawan, W. Sutantyo, E. P. J. van den Heuvel, J.-P. de Cuyper, and A. E. Gomez (1998). Wolf-Rayet stars and O-star runaways with HIPPARCOS. I. Kinematics. *Astronomy & Astrophysics*, **331**, pp. 949–958.

Moffat, A. F. J., S. V. Marchenko, W. Seggewiss, K. A. van der Hucht, H. Schrijver, B. Stenholm, I. Lundstrom, D. Y. A. Setia Gunawan, W. Sutantyo, E. P. J. van den Heuvel, J.-P. de Cuyper, and A. E. Gomez (1999). (Erratum) Wolf-Rayet stars and O-star runaways with HIPPARCOS. I. Kinematics. *Astronomy & Astrophysics*, **345**, pp. 321–322.

Moffat, A. F. J. and W. Seggewiss (1979). The intrinsically bright Wolf-Rayet stars of type WN7. IV - The galactic WN7/WN8 stars as massive O-stars in advanced stages of evolution. *Astronomy & Astrophysics*, **77**, pp. 128–140.

Mohr-Smith, M., J. E. Drew, R. Napiwotzki, S. Simón-Díaz, N. J. Wright, G. Barentsen, J. Eislöffel, H. J. Farnhill, R. Greimel, M. Monguió, V. Kalari, Q. A. Parker, and J. S. Vink (2017). The deep OB star population in Carina from the VST Photometric Hα Survey (VPHAS+). *Monthly Notices of the Royal Astronomical Society*, **465**, pp. 1807–1830. doi:10.1093/mnras/stw2751.

Morrell, N., B. Garcia, and H. Levato (1988). Spectral morphology in the open clusters Trumpler 14 and Trumpler 15. *Publications of the Astronomical Society of the Pacific*, **100**, pp. 1431–1435. doi:10.1086/132344.

Morrell, N. I., R. H. Barbá, V. S. Niemela, M. A. Corti, J. F. Albacete Colombo, G. Rauw, M. Corcoran, T. Morel, J.-F. Bertrand, A. F. J. Moffat, and N. St-Louis (2001). Optical spectroscopy of X-Mega targets - II. The massive double-lined O-type binary HD 93205. *Monthly Notices of the Royal Astronomical Society*, **326**, pp. 85–94. doi:10.1046/j.1365-8711.2001.04500.x.

Morris, T. and P. Podsiadlowski (2009). A binary merger model for the formation of the Supernova 1987A triple-ring nebula. *Monthly Notices of the Royal Astronomical Society*, **399**, pp. 515–538. doi:10.1111/j.1365-2966.2009.15114.x.

Morrison, N. D. and P. S. Conti (1980). Spectroscopic studies of O-type binaries. VI - The quadruple system QZ Carinae (HD 93206). *The Astrophysical Journal*, **239**, pp. 212–219. doi:10.1086/158101.

Morse, J. A. (1999). Setting the Scene: an Imaging Overview of the Eta Carinae System. In Morse, J. A., R. M. Humphreys, and A. Damineli (eds.) *Eta Carinae at The Millennium*, volume 179 of *Astronomical Society of the Pacific Conference Series*, p. 13.

Morse, J. A., K. Davidson, J. Bally, D. Ebbets, B. Balick, and A. Frank (1998). Hubble Space Telescope Wide Field Planetary Camera 2 Observations of eta Carinae. *The Astronomical Journal*, **116**, pp. 2443–2461. doi:10.1086/300581.

Morse, J. A., J. R. Kellogg, J. Bally, K. Davidson, B. Balick, and D. Ebbets (2001). Hubble Space Telescope Proper-Motion Measurements of the η Carinae Nebula. *The Astrophysical Journal*, **548**, pp. L207–L211. doi:10.1086/319092.

Muench, A., K. Getman, L. Hillenbrand, and T. Preibisch (2008). Star Formation in the Orion Nebula I: Stellar Content. In Reipurth, B. (ed.) *Handbook of Star Forming Regions, Volume I*, p. 483. ASP, San Francisco, CA.

Murray, N., B. Ménard, and T. A. Thompson (2011). Radiation Pressure from Massive Star Clusters as a Launching Mechanism for Super-galactic Winds. *The Astrophysical Journal*, **735**, 66. doi:10.1088/0004-637X/735/1/66.

Murray, N., E. Quataert, and T. A. Thompson (2005). On the Maximum Luminosity of Galaxies and Their Central Black Holes: Feedback from Momentum-driven Winds. *The Astrophysical Journal*, **618**, pp. 569–585. doi:10.1086/426067.

Murray, N., E. Quataert, and T. A. Thompson (2010). The Disruption of Giant Molecular Clouds by Radiation Pressure & the Efficiency of Star Formation in Galaxies. *The Astrophysical Journal*, **709**, pp. 191–209. doi:10.1088/0004-637X/709/1/191.

Murray, N. and M. Rahman (2010). Star Formation in Massive Clusters Via the Wilkinson Microwave Anisotropy Probe and the Spitzer Glimpse Survey. *The Astrophysical Journal*, **709**, pp. 424–435. doi:10.1088/0004-637X/709/1/424.

Myers, P. C. (2008). Protostar Mass due to Infall and Dispersal. *The Astrophysical Journal*, **687**, 340-353. doi:10.1086/591664.

Nath, B. B. and J. Silk (2009). Starburst-driven galactic outflows. *Monthly Notices of the Royal Astronomical Society*, **396**, pp. L90–L94. doi:10.1111/j.1745-3933.2009.00670.x.

Nazé, Y., I. I. Antokhin, H. Sana, E. Gosset, and G. Rauw (2005). Optical spectroscopy of X-Mega targets - V. The spectroscopic binary HD 93161 A and its visual companion HD 93161 B. *Monthly Notices of the Royal Astronomical Society*, **359**, pp. 688–698. doi:10.1111/j.1365-2966.2005.08945.x.

Nelan, E. P., N. R. Walborn, D. J. Wallace, A. F. J. Moffat, R. B. Makidon, D. R. Gies, and N. Panagia (2004). Resolving OB Systems in the Carina Nebula with the Hubble Space Telescope Fine Guidance Sensor. *The Astronomical Journal*, **128**, pp. 323–329. doi:10.1086/420716.

Nelan, E. P., N. R. Walborn, D. J. Wallace, A. F. J. Moffat, R. B. Makidon, D. R. Gies, and N. Panagia (2010). Erratum: "Resolving OB Systems in the Carina Nebula with Hubble Space Telescope's Fine Guidance Sensor". *The Astronomical Journal*, **139**, 2714. doi:10.1088/0004-6256/139/6/2714.

Nelder, J. A. and R. Mead (1965). A Simplex Method for Function Minimization. *Computer Journal*, **7**, pp. 308–313.

Nielsen, K. E., M. F. Corcoran, T. R. Gull, D. J. Hillier, K. Hamaguchi, S. Ivarsson, and D. J. Lindler (2007). η Carinae across the 2003.5 Minimum: Spectroscopic Evidence for Massive Binary Interactions. *The Astrophysical Journal*, **660**, pp. 669–686. doi:10.1086/513006.

Niemela, V. S., N. I. Morrell, E. Fernández Lajús, R. Barbá, J. F. Albacete Colombo, and M. Orellana (2006). Optical spectroscopy of X-Mega targets in the Carina nebula - VI. FO15: a new O-type double-lined eclipsing binary. *Monthly Notices of the Royal Astronomical Society*, **367**, pp. 1450–1456. doi:10.1111/j.1365-2966.2006.10046.x.

Niemi, S.-M. and M. Lallo (2010). Phase Retrieval to Monitor HST Focus: II. Results Post-Servicing Mission 4. Technical report, Space Telescope Science Institute, Baltimore, MD.

Noriega-Crespo, A., D. van Buren, and R. Dgani (1997). Bow Shocks Around Runaway Stars. III. The High Resolution Maps. *The Astronomical Journal*, **113**, pp. 780–786. doi:10.1086/118298.

Ochsendorf, B. B., A. G. A. Brown, J. Bally, and A. G. G. M. Tielens (2015). Nested Shells Reveal the Rejuvenation of the Orion-Eridanus Superbubble. *The Astrophysical Journal*, **808**, 111. doi:10.1088/0004-637X/808/2/111.

Ochsendorf, B. B., N. L. J. Cox, S. Krijt, F. Salgado, O. Berné, J. P. Bernard, L. Kaper, and A. G. G. M. Tielens (2014a). Blowing in the wind: The dust wave around σ Orionis AB. *Astronomy & Astrophysics*, **563**, A65. doi:10.1051/0004-6361/201322873.

Ochsendorf, B. B. and A. G. G. M. Tielens (2015). A bimodal dust grain distribution in the IC 434 H II region. *Astronomy & Astrophysics*, **576**, A2. doi:10.1051/0004-6361/201424799.

Ochsendorf, B. B., S. Verdolini, N. L. J. Cox, O. Berné, L. Kaper, and A. G. G. M. Tielens (2014b). Radiation-pressure-driven dust waves inside bursting interstellar bubbles. *Astronomy & Astrophysics*, **566**, A75. doi:10.1051/0004-6361/201423545.

Oey, M. S., A. M. Watson, K. Kern, and G. L. Walth (2005). Hierarchical Triggering of Star Formation by Superbubbles in W3/W4. *The Astronomical Journal*, **129**, pp. 393–401. doi:10.1086/426333.

Ofek, E. O., M. Sullivan, S. B. Cenko, M. M. Kasliwal, A. Gal-Yam, S. R. Kulkarni, I. Arcavi, L. Bildsten, J. S. Bloom, A. Horesh, D. A. Howell, A. V. Filippenko, R. Laher, D. Murray, E. Nakar, P. E. Nugent, J. M. Silverman, N. J. Shaviv, J. Surace, and O. Yaron (2013). An outburst from a massive star 40 days before a supernova explosion. *Nature*, **494**, pp. 65–67. doi:10.1038/nature11877.

Oh, S. and P. Kroupa (2016). Dynamical ejections of massive stars from young star clusters under diverse initial conditions. *Astronomy & Astrophysics*, **590**, A107. doi:10.1051/0004-6361/201628233.

Ohlendorf, H., T. Preibisch, B. Gaczkowski, T. Ratzka, R. Grellmann, and A. F. McLeod (2012). Jet-driving protostars identified from infrared observations of the Carina Nebula complex. *Astronomy & Astrophysics*, **540**, A81. doi:10.1051/0004-6361/201118181.

Ohlendorf, H., T. Preibisch, B. Gaczkowski, T. Ratzka, J. Ngoumou, V. Roccatagliata, and R. Grellmann (2013). Discovering young stars in the Gum 31 region with infrared observations. *Astronomy & Astrophysics*, **552**, A14. doi:10.1051/0004-6361/201220218.

Oort, J. H. and L. Spitzer, Jr. (1955). Acceleration of Interstellar Clouds by O-Type Stars. *The Astrophysical Journal*, **121**, p. 6. doi:10.1086/145958.

Ortega, V. G., E. Jilinski, R. de la Reza, and B. Bazzanella (2009). A Formation Scenario of Young Stellar Groups in the Region of the Scorpio Centaurus OB Association. *The Astronomical Journal*, **137**, pp. 3922–3930. doi:10.1088/0004-6256/137/4/3922.

Otero, S. A. (2006). New and Confirmed Variables in the Field of Eta Carinae. Discovery of New Massive O-type Eclipsing Binaries. *Open European Journal on Variable Stars*, **45**, p. 1.

Ouellette, N., S. J. Desch, and J. J. Hester (2007). Interaction of Supernova Ejecta with Nearby Protoplanetary Disks. *The Astrophysical Journal*, **662**, pp. 1268–1281. doi:10.1086/518102.

Owocki, S. P., K. G. Gayley, and N. J. Shaviv (2004). A Porosity-Length Formalism for Photon-Tiring-limited Mass Loss from Stars above the Eddington Limit. *The Astrophysical Journal*, **616**, pp. 525–541. doi:10.1086/424910.

Owocki, S. P. and N. J. Shaviv (2016). The spectral temperature of optically thick outflows with application to light echo spectra from η Carinae's giant eruption. *Monthly Notices of the Royal Astronomical Society*, **462**, pp. 345–351. doi:10.1093/mnras/stw1642.

Parker, N. D., R. Padman, and P. F. Scott (1991). Outflows in dark clouds - Their role in protostellar evolution. *Monthly Notices of the Royal Astronomical Society*, **252**, pp. 442–461. doi:10.1093/mnras/252.3.442.

Parker, R. J. and J. E. Dale (2016). Did the Solar system form in a sequential triggered star formation event? *Monthly Notices of the Royal Astronomical Society*, **456**, pp. 1066–1072. doi:10.1093/mnras/stv2765.

Patat, F. and G. Carraro (2001). Star clusterings in the Carina complex: UBVRI photometry of Bochum 9, 10 and 11. *Monthly Notices of the Royal Astronomical Society*, **325**, pp. 1591–1602. doi:10.1046/j.1365-8711.2001.04576.x.

Pellegrini, E. W., J. A. Baldwin, and G. J. Ferland (2011). Structure and Feedback in 30 Doradus. II. Structure and Chemical Abundances. *The Astrophysical Journal*, **738**, 34. doi:10.1088/0004-637X/738/1/34.

Penny, L. R., D. R. Gies, W. I. Hartkopf, B. D. Mason, and N. H. Turner (1993). The frequency of binary stars in the young cluster Trumpler 14. *Publications of the Astronomical Society of the Pacific*, **105**, pp. 588–594. doi:10.1086/133200.

Peri, C. S., P. Benaglia, D. P. Brookes, I. R. Stevens, and N. L. Isequilla (2012). E-BOSS: an Extensive stellar BOw Shock Survey. I. Methods and first catalogue. *Astronomy & Astrophysics*, **538**, A108. doi:10.1051/0004-6361/201118116.

Peri, C. S., P. Benaglia, and N. L. Isequilla (2015). E-BOSS: An Extensive stellar BOw Shock Survey. II. Catalogue second release. *Astronomy & Astrophysics*, **578**, A45. doi:10.1051/0004-6361/201424676.

Perryman, M. A. C., L. Lindegren, J. Kovalevsky, E. Hoeg, U. Bastian, P. L. Bernacca, M. Crézé, F. Donati, M. Grenon, M. Grewing, F. van Leeuwen, H. van der Marel, F. Mignard, C. A. Murray, R. S. Le Poole, H. Schrijver, C. Turon, F. Arenou, M. Froeschlé, and C. S. Petersen (1997). The HIPPARCOS Catalogue. *Astronomy & Astrophysics*, **323**, pp. L49–L52.

Pflamm-Altenburg, J. and P. Kroupa (2010). The two-step ejection of massive stars and the issue of their formation in isolation. *Monthly Notices of the Royal Astronomical Society*, **404**, pp. 1564–1568. doi:10.1111/j.1365-2966.2010.16376.x.

Pittard, J. M. and M. F. Corcoran (2002). In hot pursuit of the hidden companion of eta Carinae: An X-ray determination of the wind parameters. *Astronomy & Astrophysics*, **383**, pp. 636–647. doi:10.1051/0004-6361:20020025.

Podsiadlowski, P. (2010). Massive binary evolution. *New Astronomy Reviews*, **54**, pp. 39–44. doi:10.1016/j.newar.2010.09.023.

Pojmanski, G. (1997). The All Sky Automated Survey. *Acta Astronomica*, **47**, pp. 467–481.

Portegies Zwart, S. F. and E. P. J. van den Heuvel (2016). Was the nineteenth century giant eruption of Eta Carinae a merger event in a triple system? *Monthly Notices of the Royal Astronomical Society*, **456**, pp. 3401–3412. doi:10.1093/mnras/stv2787.

Poveda, A., J. Ruiz, and C. Allen (1967). Run-away Stars as the Result of the Gravitational Collapse of Proto-stellar Clusters. *Boletin de los Observatorios Tonantzintla y Tacubaya*, **4**, pp. 86–90.

Povich, M. S. (2012). Beyond Strömgren Spheres and Wind-Blown Bubbles: An Observational Perspective on H II Region Feedback. *ArXiv e-prints*.

Povich, M. S., R. A. Benjamin, B. A. Whitney, B. L. Babler, R. Indebetouw, M. R. Meade, and E. Churchwell (2008). Interstellar Weather Vanes: GLIMPSE Mid-Infrared Stellar Wind Bow Shocks in M17 and RCW 49. *The Astrophysical Journal*, **689**, 242-248. doi:10.1086/592565.

Povich, M. S., N. Smith, S. R. Majewski, K. V. Getman, L. K. Townsley, B. L. Babler, P. S. Broos, R. Indebetouw, M. R. Meade, T. P. Robitaille, K. G. Stassun, B. A. Whitney, Y. Yonekura, and Y. Fukui (2011a). A Pan-Carina Young Stellar Object Catalog: Intermediate-mass Young Stellar Objects in the Carina Nebula Identified Via Mid-infrared Excess Emission. *The Astrophysical Journal Supplement Series*, **194**, 14. doi:10.1088/0067-0049/194/1/14.

Povich, M. S., L. K. Townsley, P. S. Broos, M. Gagné, B. L. Babler, R. Indebetouw, S. R. Majewski, M. R. Meade, K. V. Getman, T. P. Robitaille, and R. H. D. Townsend (2011b). Candidate X-ray-emitting OB Stars in the Carina Nebula Identified Via Infrared Spectral Energy Distributions. *The Astrophysical Journal Supplement Series*, **194**, 6. doi:10.1088/0067-0049/194/1/6.

Preibisch, T. and E. Mamajek (2008). The Nearest OB Association: Scorpius-Centaurus (Sco OB2). In Reipurth, B. (ed.) *Handbook of Star Forming Regions, Volume II*, p. 235. ASP, San Francisco, CA.

Preibisch, T., T. Ratzka, B. Kuderna, H. Ohlendorf, R. R. King, S. Hodgkin, M. Irwin, J. R. Lewis, M. J. McCaughrean, and H. Zinnecker (2011a). Deep wide-field near-infrared survey of the Carina Nebula. *Astronomy & Astrophysics*, **530**, A34. doi:10.1051/0004-6361/201116781.

Preibisch, T., V. Roccatagliata, B. Gaczkowski, and T. Ratzka (2012). Herschel far-infrared observations of the Carina Nebula complex. I. Introduction and global cloud structure. *Astronomy & Astrophysics*, **541**, A132. doi:10.1051/0004-6361/201218851.

Preibisch, T., F. Schuller, H. Ohlendorf, S. Pekruhl, K. M. Menten, and H. Zinnecker (2011b). A deep wide-field sub-mm survey of the Carina Nebula complex. *Astronomy & Astrophysics*, **525**, A92. doi:10.1051/0004-6361/201015425.

Preibisch, T., P. Zeidler, T. Ratzka, V. Roccatagliata, and M. G. Petr-Gotzens (2014). The VISTA Carina Nebula Survey. I. Introduction and source catalog. *Astronomy & Astrophysics*, **572**, A116. doi:10.1051/0004-6361/201424045.

Press, W. H., S. A. Teukolsky, W. T. Vetterling, and B. P. Flannery (1992). *Numerical Recipes in C (2nd Ed.): The Art of Scientific Computing*. Cambridge University Press, New York, NY, USA. ISBN 0-521-43108-5.

Puls, J., N. Markova, S. Scuderi, C. Stanghellini, O. G. Taranova, A. W. Burnley, and I. D. Howarth (2006). Bright OB stars in the Galaxy. III. Constraints on the radial stratification of the clumping factor in hot star winds from a combined H_α, IR and radio analysis. *Astronomy & Astrophysics*, **454**, pp. 625–651. doi:10.1051/0004-6361:20065073.

Puls, J., J. S. Vink, and F. Najarro (2008). Mass loss from hot massive stars. *The Astronomy and Astrophysics Review*, **16**, pp. 209–325. doi:10.1007/s00159-008-0015-8.

Quinn, T. and B. Paczynski (1985). Stellar winds driven by super-Eddington luminosities. *The Astrophysical Journal*, **289**, pp. 634–643. doi:10.1086/162927.

Rathborne, J. M., K. J. Brooks, M. G. Burton, M. Cohen, and S. Bontemps (2004). The giant pillars of the Carina Nebula. *Astronomy & Astrophysics*, **418**, pp. 563–576. doi:10.1051/0004-6361:20031631.

Rauw, G., Y. Nazé, E. Fernández Lajús, A. A. Lanotte, G. R. Solivella, H. Sana, and E. Gosset (2009). Optical spectroscopy of X-Mega targets in the Carina nebula - VII. On the multiplicity of Tr 16-112, HD 93343 and HD 93250. *Monthly Notices of the Royal Astronomical Society*, **398**, pp. 1582–1592. doi:10.1111/j.1365-2966.2009.15226.x.

Rauw, G., H. Sana, I. I. Antokhin, N. I. Morrell, V. S. Niemela, J. F. Albacete Colombo, E. Gosset, and J.-M. Vreux (2001). Optical spectroscopy of XMEGA targets in the Carina Nebula - III. The multiple system Tr 16-104 (≡CPD -59° 2603). *Monthly Notices of the Royal Astronomical Society*, **326**, pp. 1149–1160. doi:10.1046/j.1365-8711.2001.04681.x.

Rauw, G., H. Sana, E. Gosset, J.-M. Vreux, E. Jehin, and G. Parmentier (2000). A new orbital solution for the massive binary system HD 93403. *Astronomy & Astrophysics*, **360**, pp. 1003–1010.

Rebolledo, D., M. Burton, A. Green, C. Braiding, S. Molinari, G. Wong, R. Blackwell, D. Elia, and E. Schisano (2016). The Carina Nebula and Gum 31 molecular complex - I. Molecular gas distribution, column densities, and dust temperatures. *Monthly Notices of the Royal Astronomical Society*, **456**, pp. 2406–2424. doi:10.1093/mnras/stv2776.

Reed, B. C. (2003). Catalog of Galactic OB Stars. *The Astronomical Journal*, **125**, pp. 2531–2533. doi:10.1086/374771.

Reipurth, B. (1983). Star formation in Bok globules and low-mass clouds. I - The cometary globules in the Gum Nebula. *Astronomy & Astrophysics*, **117**, pp. 183–198.

Reiter, M. and N. Smith (2013). HST/WFC3 imaging of protostellar jets in Carina: [Fe II] emission tracing massive jets from intermediate-mass protostars. *Monthly Notices of the Royal Astronomical Society*, **433**, pp. 2226–2239. doi:10.1093/mnras/stt889.

Reiter, M. and N. Smith (2014). Kinematics of powerful jets from intermediate-mass protostars in the Carina nebula. *Monthly Notices of the Royal Astronomical Society*, **445**, pp. 3939–3950. doi:10.1093/mnras/stu1979.

Reiter, M., N. Smith, M. M. Kiminki, and J. Bally (2015a). HH 666: different kinematics from H α and [Fe II] emission provide a missing link between jets and

outflows. *Monthly Notices of the Royal Astronomical Society*, **450**, pp. 564–574. doi:10.1093/mnras/stv634.

Reiter, M., N. Smith, M. M. Kiminki, J. Bally, and J. Anderson (2015b). Disentangling the outflow and protostars in HH 900 in the Carina Nebula. *Monthly Notices of the Royal Astronomical Society*, **448**, pp. 3429–3441. doi:10.1093/mnras/stv177.

Rieke, G. H. and M. J. Lebofsky (1985). The interstellar extinction law from 1 to 13 microns. *The Astrophysical Journal*, **288**, pp. 618–621. doi:10.1086/162827.

Ritchie, B. W., J. S. Clark, I. Negueruela, and P. A. Crowther (2009). A VLT/FLAMES survey for massive binaries in Westerlund 1. I. First observations of luminous evolved stars. *Astronomy & Astrophysics*, **507**, pp. 1585–1595. doi:10.1051/0004-6361/200912686.

Roberts, D. H., J. Lehar, and J. W. Dreher (1987). Time Series Analysis with CLEAN. I. Derivation of a Spectrum. *The Astronomical Journal*, **93**, p. 968. doi:10.1086/114383.

Robitaille, T. P. and B. A. Whitney (2010). The Present-Day Star Formation Rate of the Milky Way Determined from Spitzer-Detected Young Stellar Objects. *The Astrophysical Journal*, **710**, pp. L11–L15. doi:10.1088/2041-8205/710/1/L11.

Rochau, B., W. Brandner, A. Stolte, M. Gennaro, D. Gouliermis, N. Da Rio, N. Dzyurkevich, and T. Henning (2010). Internal Dynamics and Membership of the NGC 3603 Young Cluster from Microarcsecond Astrometry. *The Astrophysical Journal*, **716**, pp. L90–L94. doi:10.1088/2041-8205/716/1/L90.

Rochau, B., W. Brandner, A. Stolte, T. Henning, N. Da Rio, M. Gennaro, F. Hormuth, E. Marchetti, and P. Amico (2011). A benchmark for multiconjugated adaptive optics: VLT-MAD observations of the young massive cluster Trumpler 14. *Monthly Notices of the Royal Astronomical Society*, **418**, pp. 949–959. doi:10.1111/j.1365-2966.2011.19561.x.

Rogers, H. and J. M. Pittard (2013). Feedback from winds and supernovae in massive stellar clusters - I. Hydrodynamics. *Monthly Notices of the Royal Astronomical Society*, **431**, pp. 1337–1351. doi:10.1093/mnras/stt255.

Rogers, H. and J. M. Pittard (2014). Feedback from winds and supernovae in massive stellar clusters - II. X-ray emission. *Monthly Notices of the Royal Astronomical Society*, **441**, pp. 964–982. doi:10.1093/mnras/stu625.

Rosen, A. L., L. A. Lopez, M. R. Krumholz, and E. Ramirez-Ruiz (2014). Gone with the wind: Where is the missing stellar wind energy from massive star clusters?

Monthly Notices of the Royal Astronomical Society, **442**, pp. 2701–2716. doi: 10.1093/mnras/stu1037.

Ruprecht, J. (1966). Tables of Associations. In Pecker, J.-C. (ed.) *Transactions of the International Astronomical Union, Vol. XIIB*, pp. 347–356. Academic Press, London.

Sabín-Sanjulián, C., S. Simón-Díaz, A. Herrero, N. R. Walborn, J. Puls, J. Maíz Apellániz, C. J. Evans, I. Brott, A. de Koter, M. Garcia, N. Markova, F. Najarro, O. H. Ramírez-Agudelo, H. Sana, W. D. Taylor, and J. S. Vink (2014). The VLT-FLAMES Tarantula Survey. XIII: On the nature of O Vz stars in 30 Doradus. *Astronomy & Astrophysics*, **564**, A39. doi:10.1051/0004-6361/201322798.

Sana, H., A. de Koter, S. E. de Mink, P. R. Dunstall, C. J. Evans, V. Hénault-Brunet, J. Maíz Apellániz, O. H. Ramírez-Agudelo, W. D. Taylor, N. R. Walborn, J. S. Clark, P. A. Crowther, A. Herrero, M. Gieles, N. Langer, D. J. Lennon, and J. S. Vink (2013). The VLT-FLAMES Tarantula Survey. VIII. Multiplicity properties of the O-type star population. *Astronomy & Astrophysics*, **550**, A107. doi:10.1051/0004-6361/201219621.

Sana, H., S. E. de Mink, A. de Koter, N. Langer, C. J. Evans, M. Gieles, E. Gosset, R. G. Izzard, J.-B. Le Bouquin, and F. R. N. Schneider (2012). Binary Interaction Dominates the Evolution of Massive Stars. *Science*, **337**, p. 444. doi:10.1126/science.1223344.

Sana, H., J.-B. Le Bouquin, S. Lacour, J.-P. Berger, G. Duvert, L. Gauchet, B. Norris, J. Olofsson, D. Pickel, G. Zins, O. Absil, A. de Koter, K. Kratter, O. Schnurr, and H. Zinnecker (2014). Southern Massive Stars at High Angular Resolution: Observational Campaign and Companion Detection. *The Astrophysical Journal Supplement Series*, **215**, 15. doi:10.1088/0067-0049/215/1/15.

Sandford, M. T., II, R. W. Whitaker, and R. I. Klein (1982). Radiation-driven implosions in molecular clouds. *The Astrophysical Journal*, **260**, pp. 183–201. doi:10.1086/160245.

Sargent, A. I. (1979). Molecular clouds and star formation. II - Star formation in the Cepheus OB3 and Perseus OB2 molecular clouds. *The Astrophysical Journal*, **233**, pp. 163–181. doi:10.1086/157378.

Schilbach, E. and S. Röser (2008). On the origin of field O-type stars. *Astronomy & Astrophysics*, **489**, pp. 105–114. doi:10.1051/0004-6361:200809936.

Schlegel, E. M. (1990). A new subclass of Type II supernovae? *Monthly Notices of the Royal Astronomical Society*, **244**, pp. 269–271.

Schneider, F. R. N., R. G. Izzard, S. E. de Mink, N. Langer, A. Stolte, A. de Koter, V. V. Gvaramadze, B. Hußmann, A. Liermann, and H. Sana (2014). Ages of Young Star Clusters, Massive Blue Stragglers, and the Upper Mass Limit of Stars: Analyzing Age-dependent Stellar Mass Functions. *The Astrophysical Journal*, **780**, 117. doi:10.1088/0004-637X/780/2/117.

Schönrich, R., J. Binney, and W. Dehnen (2010). Local kinematics and the local standard of rest. *Monthly Notices of the Royal Astronomical Society*, **403**, pp. 1829–1833. doi:10.1111/j.1365-2966.2010.16253.x.

Schweickhardt, J., W. Schmutz, O. Stahl, T. Szeifert, and B. Wolf (1999). Revised mass determination of the super massive Wolf-Rayet star WR 22. *Astronomy & Astrophysics*, **347**, pp. 127–136.

Seward, F. D., Y. M. Butt, M. Karovska, A. Prestwich, E. M. Schlegel, and M. Corcoran (2001). Early Chandra X-Ray Observations of η Carinae. *The Astrophysical Journal*, **553**, pp. 832–836. doi:10.1086/320961.

Sexton, R. O., M. S. Povich, N. Smith, B. L. Babler, M. R. Meade, and A. L. Rudolph (2015). Extended red objects and stellar-wind bow shocks in the Carina Nebula. *Monthly Notices of the Royal Astronomical Society*, **446**, pp. 1047–1059. doi:10.1093/mnras/stu2143.

Shaviv, N. J. (2000). The Porous Atmosphere of η Carinae. *The Astrophysical Journal*, **532**, pp. L137–L140. doi:10.1086/312585.

Shepherd, D. S. and E. Churchwell (1996). Bipolar Molecular Outflows in Massive Star Formation Regions. *The Astrophysical Journal*, **472**, p. 225. doi:10.1086/178057.

Silich, S. and G. Tenorio-Tagle (2013). How Significant is Radiation Pressure in the Dynamics of the Gas around Young Stellar Clusters? *The Astrophysical Journal*, **765**, 43. doi:10.1088/0004-637X/765/1/43.

Skinner, M. A. and E. C. Ostriker (2015). Numerical Simulations of Turbulent Molecular Clouds Regulated by Reprocessed Radiation Feedback from Nascent Super Star Clusters. *The Astrophysical Journal*, **809**, 187. doi:10.1088/0004-637X/809/2/187.

Smartt, S. J. (2009). Progenitors of Core-Collapse Supernovae. *Annual Review of Astronomy and Astrophysics*, **47**, pp. 63–106. doi:10.1146/annurev-astro-082708-101737.

Smith, N. (2004). The systemic velocity of Eta Carinae. *Monthly Notices of the Royal Astronomical Society*, **351**, pp. L15–L18. doi:10.1111/j.1365-2966.2004.07943.x.

Smith, N. (2005). Doppler tomography of the Little Homunculus: high-resolution spectra of [FeII]λ16435 around Eta Carinae. *Monthly Notices of the Royal Astronomical Society*, **357**, pp. 1330–1336. doi:10.1111/j.1365-2966.2005.08750.x.

Smith, N. (2006a). A census of the Carina Nebula - I. Cumulative energy input from massive stars. *Monthly Notices of the Royal Astronomical Society*, **367**, pp. 763–772. doi:10.1111/j.1365-2966.2006.10007.x.

Smith, N. (2006b). The Structure of the Homunculus. I. Shape and Latitude Dependence from H_2 and [Fe II] Velocity Maps of η Carinae. *The Astrophysical Journal*, **644**, pp. 1151–1163. doi:10.1086/503766.

Smith, N. (2008). A blast wave from the 1843 eruption of η Carinae. *Nature*, **455**, pp. 201–203. doi:10.1038/nature07269.

Smith, N. (2011). Explosions triggered by violent binary-star collisions: application to Eta Carinae and other eruptive transients. *Monthly Notices of the Royal Astronomical Society*, **415**, pp. 2020–2024. doi:10.1111/j.1365-2966.2011.18607.x.

Smith, N. (2014). Mass Loss: Its Effect on the Evolution and Fate of High-Mass Stars. *Annual Review of Astronomy and Astrophysics*, **52**, pp. 487–528. doi:10.1146/annurev-astro-081913-040025.

Smith, N. (2016). The isolation of luminous blue variables: on subdividing the sample. *Monthly Notices of the Royal Astronomical Society*, **461**, pp. 3353–3360. doi:10.1093/mnras/stw1533.

Smith, N., J. E. Andrews, J. C. Mauerhan, W. Zheng, A. V. Filippenko, M. L. Graham, and P. Milne (2016). The Persistent Eruption of UGC 2773-OT: finally, a decade-long extragalactic Eta Carinae analogue. *Monthly Notices of the Royal Astronomical Society*, **455**, pp. 3546–3560. doi:10.1093/mnras/stv2507.

Smith, N., J. Bally, and K. J. Brooks (2004). HH 666: The Axis of Evil in the Carina Nebula. *The Astronomical Journal*, **127**, pp. 2793–2808. doi:10.1086/383291.

Smith, N., J. Bally, and J. A. Morse (2003a). Numerous Proplyd Candidates in the Harsh Environment of the Carina Nebula. *The Astrophysical Journal*, **587**, pp. L105–L108. doi:10.1086/375312.

Smith, N., J. Bally, and N. R. Walborn (2010a). HST/ACS Hα imaging of the Carina Nebula: outflow activity traced by irradiated Herbig-Haro Jets. *Monthly Notices of the Royal Astronomical Society*, **405**, pp. 1153–1186. doi:10.1111/j.1365-2966.2010.16520.x.

Smith, N. and K. J. Brooks (2007). A census of the Carina Nebula - II. Energy budget and global properties of the nebulosity. *Monthly Notices of the Royal Astronomical Society*, **379**, pp. 1279–1292. doi:10.1111/j.1365-2966.2007.12021.x.

Smith, N. and K. J. Brooks (2008). The Carina Nebula: A Laboratory for Feedback and Triggered Star Formation. In Reipurth, B. (ed.) *Handbook of Star Forming Regions, Volume II*, p. 138. ASP, San Francisco, CA.

Smith, N., R. Chornock, W. Li, M. Ganeshalingam, J. M. Silverman, R. J. Foley, A. V. Filippenko, and A. J. Barth (2008). SN 2006tf: Precursor Eruptions and the Optically Thick Regime of Extremely Luminous Type IIn Supernovae. *The Astrophysical Journal*, **686**, 467-484. doi:10.1086/591021.

Smith, N., R. Chornock, J. M. Silverman, A. V. Filippenko, and R. J. Foley (2010b). Spectral Evolution of the Extraordinary Type IIn Supernova 2006gy. *The Astrophysical Journal*, **709**, pp. 856–883. doi:10.1088/0004-637X/709/2/856.

Smith, N. and P. S. Conti (2008). On the Role of the WNH Phase in the Evolution of Very Massive Stars: Enabling the LBV Instability with Feedback. *The Astrophysical Journal*, **679**, pp. 1467–1477. doi:10.1086/586885.

Smith, N., K. Davidson, T. R. Gull, K. Ishibashi, and D. J. Hillier (2003b). Latitude-dependent Effects in the Stellar Wind of η Carinae. *The Astrophysical Journal*, **586**, pp. 432–450. doi:10.1086/367641.

Smith, N., M. P. Egan, S. Carey, S. D. Price, J. A. Morse, and P. A. Price (2000). Large-Scale Structure of the Carina Nebula. *The Astrophysical Journal*, **532**, pp. L145–L148. doi:10.1086/312578.

Smith, N. and G. J. Ferland (2007). The Structure of the Homunculus. II. Modeling the Physical Conditions in η Carinae's Molecular Shell. *The Astrophysical Journal*, **655**, pp. 911–919. doi:10.1086/510328.

Smith, N. and D. J. Frew (2011). A revised historical light curve of Eta Carinae and the timing of close periastron encounters. *Monthly Notices of the Royal Astronomical Society*, **415**, pp. 2009–2019. doi:10.1111/j.1365-2966.2011.18993.x.

Smith, N. and R. D. Gehrz (1998). Proper Motions in the Ejecta of eta Carinae with a 50 Year Baseline. *The Astronomical Journal*, **116**, pp. 823–828. doi:10.1086/300447.

Smith, N., R. D. Gehrz, P. M. Hinz, W. F. Hoffmann, J. L. Hora, E. E. Mamajek, and M. R. Meyer (2003c). Mass and Kinetic Energy of the Homunculus Nebula around η Carinae. *The Astronomical Journal*, **125**, pp. 1458–1466. doi:10.1086/346278.

Smith, N. and P. Hartigan (2006). Infrared [Fe II] Emission from P Cygni's Nebula: Atomic Data, Mass, Kinematics, and the 1600 AD Outburst. *The Astrophysical Journal*, **638**, pp. 1045–1055. doi:10.1086/498860.

Smith, N., W. Li, R. J. Foley, J. C. Wheeler, D. Pooley, R. Chornock, A. V. Filippenko, J. M. Silverman, R. Quimby, J. S. Bloom, and C. Hansen (2007). SN 2006gy: Discovery of the Most Luminous Supernova Ever Recorded, Powered by the Death of an Extremely Massive Star like η Carinae. *The Astrophysical Journal*, **666**, pp. 1116–1128. doi:10.1086/519949.

Smith, N., W. Li, J. M. Silverman, M. Ganeshalingam, and A. V. Filippenko (2011). Luminous blue variable eruptions and related transients: diversity of progenitors and outburst properties. *Monthly Notices of the Royal Astronomical Society*, **415**, pp. 773–810. doi:10.1111/j.1365-2966.2011.18763.x.

Smith, N. and J. A. Morse (2004). Nitrogen and Oxygen Abundance Variations in the Outer Ejecta of η Carinae: Evidence for Recent Chemical Enrichment. *The Astrophysical Journal*, **605**, pp. 854–863. doi:10.1086/382671.

Smith, N., J. A. Morse, and J. Bally (2005a). The [O III] Veil: Astropause of η Carinae's Wind? *The Astronomical Journal*, **130**, pp. 1778–1783. doi:10.1086/444562.

Smith, N., M. S. Povich, B. A. Whitney, E. Churchwell, B. L. Babler, M. R. Meade, J. Bally, R. D. Gehrz, T. P. Robitaille, and K. G. Stassun (2010c). Spitzer Space Telescope observations of the Carina nebula: the steady march of feedback-driven star formation. *Monthly Notices of the Royal Astronomical Society*, **406**, pp. 952–974. doi:10.1111/j.1365-2966.2010.16792.x.

Smith, N. and K. G. Stassun (2017). The Canonical Luminous Blue Variable AG Car and Its Neighbor Hen 3-519 are Much Closer than Previously Assumed. *The Astronomical Journal*, **153**, 125. doi:10.3847/1538-3881/aa5d0c.

Smith, N., K. G. Stassun, and J. Bally (2005b). Opening the Treasure Chest: A Newborn Star Cluster Emerges from Its Dust Pillar in Carina. *The Astronomical Journal*, **129**, pp. 888–899. doi:10.1086/427249.

Smith, N. and R. Tombleson (2015). Luminous blue variables are antisocial: their isolation implies that they are kicked mass gainers in binary evolution. *Monthly Notices of the Royal Astronomical Society*, **447**, pp. 598–617. doi:10.1093/mnras/stu2430.

Smith, R. G. (1987). An infrared study of the stellar population in the direction of the Carina nebula - NGC 3372. *Monthly Notices of the Royal Astronomical Society*, **227**, pp. 943–965. doi:10.1093/mnras/227.4.943.

Sohn, S. T., J. Anderson, and R. P. van der Marel (2012). The M31 Velocity Vector. I. Hubble Space Telescope Proper-motion Measurements. *The Astrophysical Journal*, **753**, 7. doi:10.1088/0004-637X/753/1/7.

Soker, N. (2007). Comparing η Carinae with the Red Rectangle. *The Astrophysical Journal*, **661**, pp. 490–495. doi:10.1086/513711.

Solivella, G. R. and V. S. Niemela (1999). The massive binaries in Car OB1 association. In Morrell, N. I., V. S. Niemela, and R. H. Barbá (eds.) *Workshop on Hot Stars in Open Clusters of the Galaxy and the Magellenic Clouds*, volume 8 of *Revista Mexicana de Astronomia y Astrofisica Conference Series*, pp. 145–147.

Sota, A., J. Maíz Apellániz, N. I. Morrell, R. H. Barbá, N. R. Walborn, R. C. Gamen, J. I. Arias, and E. J. Alfaro (2014). The Galactic O-Star Spectroscopic Survey (GOSSS). II. Bright Southern Stars. *The Astrophysical Journal Supplement Series*, **211**, 10. doi:10.1088/0067-0049/211/1/10.

Soubiran, C., G. Jasniewicz, L. Chemin, F. Crifo, S. Udry, D. Hestroffer, and D. Katz (2013). The catalogue of radial velocity standard stars for Gaia. I. Prelaunch release. *Astronomy & Astrophysics*, **552**, A64. doi:10.1051/0004-6361/201220927.

Spitzer, L. (1978). *Physical processes in the interstellar medium*. Wiley-Interscience, New York, NY. doi:10.1002/9783527617722.

Spitzer, L., Jr. (1958). Disruption of Galactic Clusters. *The Astrophysical Journal*, **127**, p. 17. doi:10.1086/146435.

Stanway, E. R., J. J. Eldridge, and G. D. Becker (2016). Stellar population effects on the inferred photon density at reionization. *Monthly Notices of the Royal Astronomical Society*, **456**, pp. 485–499. doi:10.1093/mnras/stv2661.

Stanway, E. R., J. J. Eldridge, S. M. L. Greis, L. J. M. Davies, S. M. Wilkins, and M. N. Bremer (2014). Interpreting high [O III]/H β ratios with maturing starbursts. *Monthly Notices of the Royal Astronomical Society*, **444**, pp. 3466–3472. doi:10.1093/mnras/stu1682.

Steenbrugge, K. C., J. H. J. de Bruijne, R. Hoogerwerf, and P. T. de Zeeuw (2003). Radial velocities of early-type stars in the Perseus OB2 association. *Astronomy & Astrophysics*, **402**, pp. 587–605. doi:10.1051/0004-6361:20030277.

Steffen, W., M. Teodoro, T. I. Madura, J. H. Groh, T. R. Gull, A. Mehner, M. F. Corcoran, A. Damineli, and K. Hamaguchi (2014). The three-dimensional structure of the Eta Carinae Homunculus. *Monthly Notices of the Royal Astronomical Society*, **442**, pp. 3316–3328. doi:10.1093/mnras/stu1088.

Stone, R. C. (1991). The space frequency and origin of the runaway O and B stars. *The Astronomical Journal*, **102**, pp. 333–349. doi:10.1086/115880.

Störzer, H. and D. Hollenbach (1999). Photodissociation Region Models of Photoevaporating Circumstellar Disks and Application to the Proplyds in Orion. *The Astrophysical Journal*, **515**, pp. 669–684. doi:10.1086/307055.

Stothers, R. B. and C.-W. Chin (1993). Dynamical instability as the cause of the massive outbursts in Eta Carinae and other luminous blue variables. *The Astrophysical Journal*, **408**, pp. L85–L88. doi:10.1086/186837.

Stritzinger, M., F. Taddia, C. Fransson, O. D. Fox, N. Morrell, M. M. Phillips, J. Sollerman, J. P. Anderson, L. Boldt, P. J. Brown, A. Campillay, S. Castellon, C. Contreras, G. Folatelli, S. M. Habergham, M. Hamuy, J. Hjorth, P. A. James, W. Krzeminski, S. Mattila, S. E. Persson, and M. Roth (2012). Multi-wavelength Observations of the Enduring Type IIn Supernovae 2005ip and 2006jd. *The Astrophysical Journal*, **756**, 173. doi:10.1088/0004-637X/756/2/173.

Strömgren, B. (1939). The Physical State of Interstellar Hydrogen. *The Astrophysical Journal*, **89**, p. 526. doi:10.1086/144074.

Sugitani, K., Y. Fukui, and K. Ogura (1991). A catalog of bright-rimmed clouds with IRAS point sources: Candidates for star formation by radiation-driven implosion. I. The Northern Hemisphere. *The Astrophysical Journal Supplement Series*, **77**, pp. 59–66. doi:10.1086/191597.

Sugitani, K. and K. Ogura (1994). A catalog of bright-rimmed clouds with IRAS point sources: Candidates for star formation by radiation-driven implosion. II. The Southern Hemisphere. *The Astrophysical Journal Supplement Series*, **92**, pp. 163–172. doi:10.1086/191964.

Sugitani, K., M. Tamura, Y. Nakajima, C. Nagashima, T. Nagayama, H. Nakaya, A. J. Pickles, T. Nagata, S. Sato, N. Fukuda, and K. Ogura (2002). Near-Infrared Study of M16: Star Formation in the Elephant Trunks. *The Astrophysical Journal*, **565**, pp. L25–L28. doi:10.1086/339196.

Tachibana, S. and G. R. Huss (2003). The Initial Abundance of ^{60}Fe in the Solar System. *The Astrophysical Journal*, **588**, pp. L41–L44. doi:10.1086/375362.

Tachibana, S., G. R. Huss, N. T. Kita, G. Shimoda, and Y. Morishita (2006). ^{60}Fe in Chondrites: Debris from a Nearby Supernova in the Early Solar System? *The Astrophysical Journal*, **639**, pp. L87–L90. doi:10.1086/503201.

Tang, J., A. Bressan, P. Rosenfield, A. Slemer, P. Marigo, L. Girardi, and L. Bianchi (2014). New PARSEC evolutionary tracks of massive stars at low metallicity:

testing canonical stellar evolution in nearby star-forming dwarf galaxies. *Monthly Notices of the Royal Astronomical Society*, **445**, pp. 4287–4305. doi:10.1093/mnras/stu2029.

Tapia, M., M. Roth, H. Marraco, and M. T. Ruiz (1988). The interstellar extinction in the open clusters Tr 14, Tr 15, Tr 16/Cr 232 and Cr 228 in NGC 3372 - New near-infrared photometry. *Monthly Notices of the Royal Astronomical Society*, **232**, pp. 661–681. doi:10.1093/mnras/232.3.661.

Tapia, M., M. Roth, R. A. Vázquez, and A. Feinstein (2003). Imaging study of NGC 3372, the Carina nebula - I. UBVRIJHK photometry of Tr 14, Tr 15, Tr 16 and Car I. *Monthly Notices of the Royal Astronomical Society*, **339**, pp. 44–62. doi:10.1046/j.1365-8711.2003.06186.x.

Tenorio-Tagle, G., P. Bodenheimer, D. N. C. Lin, and A. Noriega-Crespo (1986). On star formation in stellar systems. I - Photoionization effects in protoglobular clusters. *Monthly Notices of the Royal Astronomical Society*, **221**, pp. 635–658. doi:10.1093/mnras/221.3.635.

Tetzlaff, N., R. Neuhäuser, and M. M. Hohle (2011). A catalogue of young runaway Hipparcos stars within 3 kpc from the Sun. *Monthly Notices of the Royal Astronomical Society*, **410**, pp. 190–200. doi:10.1111/j.1365-2966.2010.17434.x.

Thackeray, A. D. (1949). Nebulosity surrounding eta Carinae. *The Observatory*, **69**, pp. 31–33.

Thackeray, A. D. (1950). Some southern stars involved in nebulosity. *Monthly Notices of the Royal Astronomical Society*, **110**, p. 524.

Thackeray, A. D., S. B. Tritton, and E. N. Walker (1973). Radial velocities of southern B stars determined at the Radcliffe Observatory - VII. *Memoirs of the Royal Astronomical Society*, **77**, p. 199.

The, P. S., R. Bakker, and A. Antalova (1980a). Studies of the Carina Nebula. IV - A new determination of the distances of the open clusters Tr 14, Tr 15, Tr 16 and Cr 228 based on Walraven photometry. *Astronomy and Astrophysics Supplement Series*, **41**, pp. 93–107.

The, P. S., R. Bakker, and H. R. E. Tjin A Djie (1980b). Studies of the Carina Nebula. II - The extinction law in the direction of 14 O-type stars. *Astronomy & Astrophysics*, **89**, pp. 209–213.

Thé, P. S. and G. Vleeming (1971). On the distances of the open clusters Tr 14, Tr 15, Tr 16 and the eta Carinae nebula. *Astronomy & Astrophysics*, **14**, pp. 120–127.

Thompson, M. A., J. S. Urquhart, T. J. T. Moore, and L. K. Morgan (2012). The statistics of triggered star formation: an overdensity of massive young stellar objects around Spitzer bubbles. *Monthly Notices of the Royal Astronomical Society*, **421**, pp. 408–418. doi:10.1111/j.1365-2966.2011.20315.x.

Thornton, K., M. Gaudlitz, H.-T. Janka, and M. Steinmetz (1998). Energy Input and Mass Redistribution by Supernovae in the Interstellar Medium. *The Astrophysical Journal*, **500**, pp. 95–119. doi:10.1086/305704.

Tokovinin, A., D. A. Fischer, M. Bonati, M. J. Giguere, P. Moore, C. Schwab, J. F. P. Spronck, and A. Szymkowiak (2013). CHIRON - A Fiber Fed Spectrometer for Precise Radial Velocities. *Publications of the Astronomical Society of the Pacific*, **125**, pp. 1336–1347. doi:10.1086/674012.

Tovmassian, H. M., R. K. Hovhannessian, and R. A. Epremian (1994). On the extinction law in the Carina nebula. *Astrophysics and Space Science*, **213**, pp. 175–183. doi:10.1007/BF00658208.

Townsley, L. K., P. S. Broos, Y.-H. Chu, M. Gagné, G. P. Garmire, R. A. Gruendl, K. Hamaguchi, M.-M. Mac Low, T. Montmerle, Y. Nazé, M. S. Oey, S. Park, R. Petre, and J. M. Pittard (2011a). The Chandra Carina Complex Project: Deciphering the Enigma of Carina's Diffuse X-ray Emission. *The Astrophysical Journal Supplement Series*, **194**, 15. doi:10.1088/0067-0049/194/1/15.

Townsley, L. K., P. S. Broos, M. F. Corcoran, E. D. Feigelson, M. Gagné, T. Montmerle, M. S. Oey, N. Smith, G. P. Garmire, K. V. Getman, M. S. Povich, N. Remage Evans, Y. Nazé, E. R. Parkin, T. Preibisch, J. Wang, S. J. Wolk, Y.-H. Chu, D. H. Cohen, R. A. Gruendl, K. Hamaguchi, R. R. King, M.-M. Mac Low, M. J. McCaughrean, A. F. J. Moffat, L. M. Oskinova, J. M. Pittard, K. G. Stassun, A. ud-Doula, N. R. Walborn, W. L. Waldron, E. Churchwell, J. S. Nichols, S. P. Owocki, and N. S. Schulz (2011b). An Introduction to the Chandra Carina Complex Project. *The Astrophysical Journal Supplement Series*, **194**, 1. doi:10.1088/0067-0049/194/1/1.

Townsley, L. K., P. S. Broos, E. D. Feigelson, B. R. Brandl, Y.-H. Chu, G. P. Garmire, and G. G. Pavlov (2006). A Chandra ACIS Study of 30 Doradus. I. Superbubbles and Supernova Remnants. *The Astronomical Journal*, **131**, pp. 2140–2163. doi:10.1086/500532.

Tremblin, P., E. Audit, V. Minier, and N. Schneider (2012). 3D simulations of pillar formation around HII regions: the importance of shock curvature. *Astronomy & Astrophysics*, **538**, A31. doi:10.1051/0004-6361/201118031.

Turner, D. G. and A. F. J. Moffat (1980). Anomalous extinction in the Carina Nebula. *Monthly Notices of the Royal Astronomical Society*, **192**, pp. 283–296. doi:10.1093/mnras/192.2.283.

Tutukov, A. V. (1978). Early Stages of Dynamical Evolution of Star Cluster Models. *Astronomy & Astrophysics*, **70**, p. 57.

Vallée, J. P. (2014). The Spiral Arms of the Milky Way: The Relative Location of Each Different Arm Tracer within a Typical Spiral Arm Width. *The Astronomical Journal*, **148**, 5. doi:10.1088/0004-6256/148/1/5.

van Bever, J. and D. Vanbeveren (1998). The rejuvenation of starburst regions due to massive close binary evolution. *Astronomy & Astrophysics*, **334**, pp. 21–28.

van Buren, D. and R. McCray (1988). Bow shocks and bubbles are seen around hot stars by IRAS. *The Astrophysical Journal*, **329**, pp. L93–L96. doi:10.1086/185184.

van Buren, D., A. Noriega-Crespo, and R. Dgani (1995). An IRAS/ISSA Survey of Bow Shocks Around Runaway Stars. *The Astronomical Journal*, **110**, p. 2914. doi:10.1086/117739.

Van Dyk, S. D., A. V. Filippenko, R. Chornock, W. Li, and P. M. Challis (2005). Supernova 1954J (Variable 12) in NGC 2403 Unmasked. *Publications of the Astronomical Society of the Pacific*, **117**, pp. 553–562. doi:10.1086/430238.

van Genderen, A. M. (2001). S Doradus variables in the Galaxy and the Magellanic Clouds. *Astronomy & Astrophysics*, **366**, pp. 508–531. doi:10.1051/0004-6361:20000022.

van Genderen, A. M., C. Sterken, W. H. Allen, and W. S. G. Walker (2006). An overview of the photometric events, trends and brightenings of eta Carinae. *Journal of Astronomical Data*, **12**.

van Loon, J. T., M.-R. L. Cioni, A. A. Zijlstra, and C. Loup (2005). An empirical formula for the mass-loss rates of dust-enshrouded red supergiants and oxygen-rich Asymptotic Giant Branch stars. *Astronomy & Astrophysics*, **438**, pp. 273–289. doi:10.1051/0004-6361:20042555.

Vanhala, H. A. T. and A. P. Boss (2002). Injection of Radioactivities into the Forming Solar System. *The Astrophysical Journal*, **575**, pp. 1144–1150. doi:10.1086/341356.

Vazquez, R. A., G. Baume, A. Feinstein, and P. Prado (1996). Investigation on the region of the open cluster Tr 14. *Astronomy and Astrophysics Supplement Series*, **116**, pp. 75–94.

Veilleux, S., G. Cecil, and J. Bland-Hawthorn (2005). Galactic Winds. *Annual Review of Astronomy and Astrophysics*, **43**, pp. 769–826. doi:10.1146/annurev.astro.43.072103.150610.

Vijapurkar, J. and J. S. Drilling (1993). MK spectral types for OB+ stars in the southern Milky Way. *The Astrophysical Journal Supplement Series*, **89**, pp. 293–297. doi:10.1086/191849.

Vink, J. S. and A. de Koter (2005). On the metallicity dependence of Wolf-Rayet winds. *Astronomy & Astrophysics*, **442**, pp. 587–596. doi:10.1051/0004-6361:20052862.

Vink, J. S., A. de Koter, and H. J. G. L. M. Lamers (2001). Mass-loss predictions for O and B stars as a function of metallicity. *Astronomy & Astrophysics*, **369**, pp. 574–588. doi:10.1051/0004-6361:20010127.

Walborn, N. R. (1971). Some Extremely Early O Stars Near Eta Carinae. *The Astrophysical Journal*, **167**, p. L31. doi:10.1086/180754.

Walborn, N. R. (1973). Some characteristics of the Eta Carinae complex. *The Astrophysical Journal*, **179**, p. 517. doi:10.1086/151891.

Walborn, N. R. (1976). The complex outer shell of Eta Carinae. *The Astrophysical Journal*, **204**, pp. L17–L19. doi:10.1086/182045.

Walborn, N. R. (1982a). The O3 stars. *The Astrophysical Journal*, **254**, pp. L15–L17. doi:10.1086/183747.

Walborn, N. R. (1982b). Two-dimensional spectral classifications for O stars in the southern Milky Way. *The Astronomical Journal*, **87**, pp. 1300–1303. doi:10.1086/113216.

Walborn, N. R. (1995). The Stellar Content of the Carina Nebula. In Niemela, V., N. Morrell, and A. Feinstein (eds.) *The Eta Carinae Region: A Laboratory of Stellar Evolution*, volume 2 of *Revista Mexicana de Astronomia y Astrofisica Conference Series*, p. 51.

Walborn, N. R. (2009). Optically observable zero-age main-sequence O stars. In Livio, M. and E. Villaver (eds.) *Massive Stars: From Pop III and GRBs to the Milky Way*, volume 20 of *Space Telescope Science Institute Symposium Series*, pp. 167–177. Cambridge University Press, Cambridge, UK. doi:10.1017/CBO9780511770593.012.

Walborn, N. R. and B. M. Blanco (1988). Third-epoch proper motions in the outer shell of Eta Carinae. *Publications of the Astronomical Society of the Pacific*, **100**, pp. 797–800. doi:10.1086/132237.

Walborn, N. R., B. M. Blanco, and A. D. Thackeray (1978). Proper motions in the outer shell of Eta Carinae. *The Astrophysical Journal*, **219**, pp. 498–503. doi:10.1086/155806.

Walborn, N. R., A. C. Danks, G. Vieira, and W. B. Landsman (2002a). Space Telescope Imaging Spectrograph Observations of High-Velocity Interstellar Absorption-Line Profiles in the Carina Nebula. *The Astrophysical Journal Supplement Series*, **140**, pp. 407–456. doi:10.1086/339373.

Walborn, N. R. and J. E. Hesser (1975). Complex interstellar calcium line structure in the Carina Nebula. *The Astrophysical Journal*, **199**, pp. 535–543. doi:10.1086/153720.

Walborn, N. R., I. D. Howarth, D. J. Lennon, P. Massey, M. S. Oey, A. F. J. Moffat, G. Skalkowski, N. I. Morrell, L. Drissen, and J. W. Parker (2002b). A New Spectral Classification System for the Earliest O Stars: Definition of Type O2. *The Astronomical Journal*, **123**, pp. 2754–2771. doi:10.1086/339831.

Walborn, N. R. and M. H. Liller (1977). The earliest spectroscopic observations of eta Carinae and its interaction with the Carina Nebula. *The Astrophysical Journal*, **211**, pp. 181–183. doi:10.1086/154917.

Walborn, N. R., H. Sana, S. Simón-Díaz, J. Maíz Apellániz, W. D. Taylor, C. J. Evans, N. Markova, D. J. Lennon, and A. de Koter (2014). The VLT-FLAMES Tarantula Survey. XIV. The O-type stellar content of 30 Doradus. *Astronomy & Astrophysics*, **564**, A40. doi:10.1051/0004-6361/201323082.

Walborn, N. R., N. Smith, I. D. Howarth, G. Vieira Kober, T. R. Gull, and J. A. Morse (2007). Interstellar Absorption-Line Evidence for High-Velocity Expanding Structures in the Carina Nebula Foreground. *Publications of the Astronomical Society of the Pacific*, **119**, pp. 156–169. doi:10.1086/511756.

Walch, S., A. P. Whitworth, T. G. Bisbas, D. A. Hubber, and R. Wünsch (2015). Comparing simulations of ionization triggered star formation and observations in RCW 120. *Monthly Notices of the Royal Astronomical Society*, **452**, pp. 2794–2803. doi:10.1093/mnras/stv1427.

Walsh, J. R. (1984). The emission nebula surrounding CPD -59°2661 in the Carina nebula (NGC 3372). *Astronomy & Astrophysics*, **138**, pp. 380–384.

Wang, J., E. D. Feigelson, L. K. Townsley, P. S. Broos, K. V. Getman, S. J. Wolk, T. Preibisch, K. G. Stassun, A. F. J. Moffat, G. Garmire, R. R. King, M. J. McCaughrean, and H. Zinnecker (2011). A Chandra ACIS Study of the Young Star Cluster Trumpler 15 in Carina and Correlation with Near-infrared Sources.

The Astrophysical Journal Supplement Series, **194**, 11. doi:10.1088/0067-0049/194/1/11.

Wang, P., Z.-Y. Li, T. Abel, and F. Nakamura (2010). Outflow Feedback Regulated Massive Star Formation in Parsec-Scale Cluster-Forming Clumps. *The Astrophysical Journal*, **709**, pp. 27–41. doi:10.1088/0004-637X/709/1/27.

Weis, K. (2012). The Outer Ejecta. In Davidson, K. and R. M. Humphreys (eds.) *Eta Carinae and the Supernova Impostors*, volume 384 of *Astrophysics and Space Science Library*, p. 171. doi:10.1007/978-1-4614-2275-4_8.

Weis, K., W. J. Duschl, and D. J. Bomans (2001). High velocity structures in, and the X-ray emission from the LBV nebula around η Carinae. *Astronomy & Astrophysics*, **367**, pp. 566–576. doi:10.1051/0004-6361:20000460.

Welch, W. J., S. N. Vogel, R. L. Plambeck, M. C. H. Wright, and J. H. Bieging (1985). Gas Jets Associated with Star Formation. *Science*, **228**, pp. 1389–1395. doi:10.1126/science.228.4706.1389.

Westphal, J. A. and G. Neugebauer (1969). Infrared Observations of Eta Carinae to 20 Microns. *The Astrophysical Journal*, **156**, p. L45. doi:10.1086/180346.

Whitelock, P. A., M. W. Feast, F. Marang, and E. Breedt (2004). The 2003 shell event in η Carinae. *Monthly Notices of the Royal Astronomical Society*, **352**, pp. 447–456. doi:10.1111/j.1365-2966.2004.07950.x.

Whiteoak, J. B. Z. (1994). High-resolution images of the dust and ionized gas distributions in the Carina Nebula. *The Astrophysical Journal*, **429**, pp. 225–232. doi:10.1086/174313.

Whitworth, A. (1979). The erosion and dispersal of massive molecular clouds by young stars. *Monthly Notices of the Royal Astronomical Society*, **186**, pp. 59–67. doi:10.1093/mnras/186.1.59.

Whitworth, A. P., A. S. Bhattal, S. J. Chapman, M. J. Disney, and J. A. Turner (1994). The Preferential Formation of High-Mass Stars in Shocked Interstellar Gas Layers. *Monthly Notices of the Royal Astronomical Society*, **268**, p. 291. doi:10.1093/mnras/268.1.291.

Wilkin, F. P. (2000). Modeling Nonaxisymmetric Bow Shocks: Solution Method and Exact Analytic Solutions. *The Astrophysical Journal*, **532**, pp. 400–414. doi:10.1086/308576.

Williams, R. J. R., D. Ward-Thompson, and A. P. Whitworth (2001). Hydrodynamics of photoionized columns in the Eagle Nebula, M 16. *Monthly Notices of*

the Royal Astronomical Society, **327**, pp. 788–798. doi:10.1046/j.1365-8711.2001.04757.x.

Williams, S. J., D. R. Gies, T. C. Hillwig, M. V. McSwain, and W. Huang (2011). Radial Velocities of Galactic O-type Stars. I. Short-term Constant Velocity Stars. *The Astronomical Journal*, **142**, 146. doi:10.1088/0004-6256/142/5/146.

Winston, E., S. J. Wolk, T. L. Bourke, S. T. Megeath, R. Gutermuth, and B. Spitzbart (2012). Spitzer Observations of Bow Shocks and Outflows in RCW 38. *The Astrophysical Journal*, **744**, 126. doi:10.1088/0004-637X/744/2/126.

Wise, J. H., T. Abel, M. J. Turk, M. L. Norman, and B. D. Smith (2012). The birth of a galaxy - II. The role of radiation pressure. *Monthly Notices of the Royal Astronomical Society*, **427**, pp. 311–326. doi:10.1111/j.1365-2966.2012.21809.x.

Wolk, S. J., P. S. Broos, K. V. Getman, E. D. Feigelson, T. Preibisch, L. K. Townsley, J. Wang, K. G. Stassun, R. R. King, M. J. McCaughrean, A. F. J. Moffat, and H. Zinnecker (2011). The Chandra Carina Complex Project View of Trumpler 16. *The Astrophysical Journal Supplement Series*, **194**, 12. doi:10.1088/0067-0049/194/1/12.

Woosley, S. E. and A. Heger (2015). The Remarkable Deaths of 9-11 Solar Mass Stars. *The Astrophysical Journal*, **810**, 34. doi:10.1088/0004-637X/810/1/34.

Wright, N. J., H. Bouy, J. E. Drew, L. M. Sarro, E. Bertin, J.-C. Cuillandre, and D. Barrado (2016). Cygnus OB2 DANCe: A high-precision proper motion study of the Cygnus OB2 association. *Monthly Notices of the Royal Astronomical Society*, **460**, pp. 2593–2610. doi:10.1093/mnras/stw1148.

Wright, N. J., J. E. Drew, and M. Mohr-Smith (2015). The massive star population of Cygnus OB2. *Monthly Notices of the Royal Astronomical Society*, **449**, pp. 741–760. doi:10.1093/mnras/stv323.

Wright, N. J., R. J. Parker, S. P. Goodwin, and J. J. Drake (2014). Constraints on massive star formation: Cygnus OB2 was always an association. *Monthly Notices of the Royal Astronomical Society*, **438**, pp. 639–646. doi:10.1093/mnras/stt2232.

Wu, Z.-Y., X. Zhou, J. Ma, and C.-H. Du (2009). The orbits of open clusters in the Galaxy. *Monthly Notices of the Royal Astronomical Society*, **399**, pp. 2146–2164. doi:10.1111/j.1365-2966.2009.15416.x.

Yonekura, Y., S. Asayama, K. Kimura, H. Ogawa, Y. Kanai, N. Yamaguchi, P. J. Barnes, and Y. Fukui (2005). High-Mass Cloud Cores in the η Carinae Giant Molecular Cloud. *The Astrophysical Journal*, **634**, pp. 476–494. doi:10.1086/496869.

Zacharias, N., C. T. Finch, T. M. Girard, A. Henden, J. L. Bartlett, D. G. Monet, and M. I. Zacharias (2013). The Fourth US Naval Observatory CCD Astrograph Catalog (UCAC4). *The Astronomical Journal*, **145**, 44. doi:10.1088/0004-6256/145/2/44.

Zavagno, A., M. Pomarès, L. Deharveng, T. Hosokawa, D. Russeil, and J. Caplan (2007). Triggered star formation on the borders of the Galactic H II region RCW 120. *Astronomy & Astrophysics*, **472**, pp. 835–846. doi:10.1051/0004-6361:20077474.

Zeidler, P., T. Preibisch, T. Ratzka, V. Roccatagliata, and M. G. Petr-Gotzens (2016). The VISTA Carina Nebula Survey. II. Spatial distribution of the infrared-excess-selected young stellar population. *Astronomy & Astrophysics*, **585**, A49. doi:10.1051/0004-6361/201424376.

Zhang, T., X. Wang, C. Wu, J. Chen, J. Chen, Q. Liu, F. Huang, J. Liang, X. Zhao, L. Lin, M. Wang, M. Dennefeld, J. Zhang, M. Zhai, H. Wu, Z. Fan, H. Zou, X. Zhou, and J. Ma (2012). Type IIn Supernova SN 2010jl: Optical Observations for over 500 Days after Explosion. *The Astronomical Journal*, **144**, 131. doi:10.1088/0004-6256/144/5/131.

Zinnecker, H. (1982). Prediction of the protostellar mass spectrum in the Orion near-infrared cluster. *Annals of the New York Academy of Sciences*, **395**, pp. 226–235. doi:10.1111/j.1749-6632.1982.tb43399.x.